CURVING PERFORMANCE OF RAIL PASSENGER VEHICLES

by

MARK L. NAGURKA

B.S.M.E., University of Pennsylvania, Philadelphia, Pennsylvania (1978)

M.S.E., University of Pennsylvania, Philadelphia, Pennsylvania (1979)

SUBMITTED IN PARTIAL FULFILLMENT
OF THE REQUIREMENTS OF THE DEGREE OF
DOCTOR OF PHILOSOPHY

at the

MASSACHUSETTS INSTITUTE OF TECHNOLOGY

May 1983

© Massachusetts Institute of Technology

Signature of Author _____
Department of Mechanical Engineering
May 1983

Certified by _____
Professor J. Karl Hedrick
Thesis Supervisor

Accepted by _____
Warren M. Rohsenow
Chairman, Departmental Graduate Committee

MASSACHUSETTS INSTITUTE OF TECHNOLOGY
JUN 23 1983
LIBRARIES

CURVING PERFORMANCE OF RAIL PASSENGER VEHICLES

by

MARK L. NAGURKA

Submitted to the Department of Mechanical Engineering on May 13, 1983, in partial fulfillment of the requirements for the degree of Doctor of Philosophy.

ABSTRACT

Rail passenger vehicles are often required to negotiate tight curves, especially in urban transit systems. During curve negotiation, the wheelsets of conventional vehicles generally misalign radially with the track increasing wheel/rail contact forces and resulting in increased wheel and rail wear, fuel consumption, and risk of derailment. To alleviate these problems, modified suspension designs and alternate wheel profiles have been proposed.

This research investigates the steady-state and dynamic curving performance of rail passenger vehicles. The effects of vehicle suspension design and wheel/rail profile are studied using analytical and computational methods. The studies are based upon a generalized, nonlinear vehicle model that can represent conventional and advanced suspension designs including self-steered and forced-steered vehicles. The model accounts for single-point wheel/rail contact as well as two-point contact, which can occur with many common wheel profiles during curving.

The results show that in comparison to conventional designs, vehicles with innovative suspension designs, particularly forced-steered vehicles, offer improved curving performance in terms of decreased contact work without sacrificing dynamic stability. Further, the results emphasize the advantages of using single-point contact wheel/rail profiles, which reduce the work expended during curve negotiation in comparison to two-point contact profiles.

Thesis Supervisor: J. Karl Hedrick
Title: Professor of Mechanical Engineering

ACKNOWLEDGEMENTS

Many people are to be thanked for their direct or indirect contributions to this thesis. The author had the privilege of studying at two great universities and learning from many brilliant teachers and students. Many of these people, as is often the case, receive no accolades. However, their efforts have not gone unnoticed and to them I offer my sincere thanks.

Special recognition is in order to members of my doctoral committee. Professor Hedrick provided valuable guidance and constructive suggestions throughout the research effort. His ability to see the "big picture" and ask the right questions helped inordinately to give focus and meaningful direction to the work. Professor Wormley, with his many important insights and comments and superb engineering judgement, was instrumental in making this thesis a more cohesive document. His help and friendship are very much appreciated. Professor Paynter, with his contagious enthusiasm, provided valuable support and helped shape this work. His ability to immediately grasp the most complex issues has always amazed me. Professor Hayes, whose warm friendship I have had the good fortune to enjoy, supervised my masters research at the University of Pennsylvania and encouraged me to continue my education at M.I.T. He deserves special thanks since from him I have learned much.

I am indebted to Professor Mann for getting me started at M.I.T. and for his continued support throughout the years. I am also indebted to Dr. Weinstock of the U.S. Department of Transportation for

his suggestions and advice during the development of this research. The Department of Transportation and the Association of American Railroads are gratefully acknowledged for providing research funds.

Past and present colleagues in the Vehicle Dynamics Laboratory have provided important peer support. My good friends Charles Bell, Arnon Gilan, and Johny Surjana deserve special recognition. They have all left their mark on the technical content of this document. I have also enjoyed and appreciate the friendship of: Ademola Aderbigbe, Kurt Armbruster, Forrest Buzan, George Celniker, Long Chain, Dan Cho, John Dzielski, Steve Eppinger, Michael Gevelber, Jim Goldie, Gerry Melsky, David O'Conner, Mary Ann Partridge, and Gus de los Reyes. Despite their own preoccupations, they have listened attentively to my problems and offered their help. They also deserve credit for being subjects in my experiments in bad humor.

Uri Tsach, who provided countless technical contributions, and Carlos Hakim have been very special friends during my stay at M.I.T. They have been constant sources of encouragement. Sandy Tepper, Leslie Regan, and Joan Gillis deserve many thanks for innumerable kindnesses and moral support along the way. May all these friendships always survive!

To my friends, family, and relatives, I apologize for neglect, which seems to be an occupational hazard of Ph.D. research.

Finally and most importantly, I wish to thank my parents who have always surrounded me with stability, warmth, and love. They made it possible for me to write this thesis. For their love throughout the years I dedicate this work to them.

TABLE OF CONTENTS

Page

ABSTRACT..... 2

ACKNOWLEDGEMENTS..... 3

TABLE OF CONTENTS..... 5

LIST OF FIGURES..... 10

LIST OF TABLES..... 21

NOMENCLATURE..... 24

1.0 INTRODUCTION..... 29

1.1 Background..... 29
1.2 Literature Review..... 31
1.3 Study Objectives and Methods..... 35
1.4 Organization of Thesis..... 37

2.0 STUDY METHODOLOGY..... 40

2.1 Introduction..... 40
2.2 Performance Criteria..... 43

2.2.1 Curve Negotiation..... 44
2.2.2 Lateral Stability..... 49

2.3 Track Model..... 49

2.3.1 Flexible Rail Model..... 54

2.4 Wheelset Model..... 54

2.4.1 Coordinate Systems..... 57
2.4.2 Wheel/Rail Geometric Constraints..... 61
2.4.3 Wheel/Rail Contact Forces..... 68

2.5 Truck Model..... 69

2.5.1 Conventional Truck..... 71
2.5.2 Self-Steered Radial Truck..... 71
2.5.3 Forced-Steered Radial Truck..... 78
2.5.4 Generic Truck Model..... 88

2.6 Vehicle Model..... 94

2.6.1 Carbody/Bolster Model..... 94

2.7 Numerical Methods..... 99

2.7.1 Dynamic Curving Analysis..... 99

Page

2.7.2 Steady-State Curving Analysis..... 104
2.7.3 Linear Stability Analysis..... 105

2.8 Baseline Rail and Vehicle Parameters..... 105

3.0 STEADY-STATE CURVING STUDIES..... 112

3.1 Introduction..... 112
3.2 Curving Performance of a Single Wheelset..... 116

3.2.1 Effect of Wheel/Rail Profile on Curving Performance of a Single Wheelset..... 126

3.3 Curving Performance of Conventional Trucks..... 131

3.3.1 Effect of Primary Suspension Stiffness on Curving Performance of Conventional Trucks.. 132
3.3.2 Effect of Secondary Yaw Breakaway on Curving Performance of Conventional Trucks..... 146
3.3.3 Effect of Track Curvature and Cant Deficiency on Curving Performance of Conventional Trucks..... 148
3.3.4 Effect of Creep Coefficients and Coefficient of Friction on Curving Performance of Conventional Trucks..... 151
3.3.5 Effect of Axle Drive Torque on Curving Performance of Conventional Trucks..... 153
3.3.6 Effect of Rail Flexibility on Curving Performance of Conventional Trucks..... 156
3.3.7 Effect of Wheel/Rail Profile on Curving Performance of Conventional Trucks..... 158

3.4 Curving Performance of Self-Steered Radial Trucks.. 161

3.4.1 Effect of Primary Longitudinal Suspension Stiffness on Curving Performance of Self-Steered Radial Trucks..... 162
3.4.2 Effect of Wheel/Rail Profile on Curving Performance of Self-Steered Radial Trucks... 164

3.5 Curving Performance of Forced-Steered Radial Trucks..... 168

3.5.1 Effect of Effective Interaxle Bending Stiffness on Curving Performance of Forced-Steered Radial Trucks..... 170
3.5.2 Effect of Wheel/Rail Profile on Curving Performance of Forced-Steered Radial Trucks. 175
3.5.3 Effect of Curvature Steering Gain on Curving Performance of Forced-Steered Radial Trucks..... 181

3.6 Curving Performance of Trucks with Wheelset Misalignments..... 185

Page

4.0 CURVING PERFORMANCE/STABILITY TRADEOFF..... 191

4.1 Introduction..... 191
4.2 Curving Performance/Stability Tradeoff of Conventional Trucks..... 196
4.3 Curving Performance/Stability Tradeoff of Self-Steered Radial Trucks..... 199
4.4 Curving Performance/Stability Tradeoff of Forced-Steered Radial Trucks..... 202
4.5 Comparative Performance of Conventional, Self-Steered, and Forced-Steered Radial Trucks..... 208

4.5.1 Comparative Performance of Baseline Trucks..... 211

5.0 DYNAMIC CURVING STUDIES..... 222

5.1 Introduction..... 222

5.1.1 Dynamic Curving Model Evaluation..... 222
5.1.2 Scope and Approach of Dynamic Curving Study..... 225

5.2 Curve Entry Performance of a Conventional Vehicle.. 231

5.2.1 Effect of Track Curvature on Curve Entry Performance of a Conventional Vehicle..... 236
5.2.2 Effect of Wheel/Rail Profile on Curve Entry Performance of a Conventional Vehicle. 241
5.2.3 Effect of Spiral Length on Curve Entry Performance of a Conventional Vehicle..... 246

5.3 Curve Entry Performance of a Self-Steered Radial Vehicle..... 247

5.3.1 Effect of Wheel/Rail Profile on the Curve Entry Performance of a Self-Steered Radial Vehicle..... 253

5.4 Curve Entry Performance of a Forced-Steered Radial Vehicle..... 257

5.4.1 Effect of Wheel/Rail Profile on the Curve Entry Performance of a Forced-Steered Radial Vehicle..... 263

5.5 Comparative Curve Entry Performance of Conventional, Self-Steered, and Forced-Steered Radial Vehicles..... 266

6.0 CONCLUSIONS..... 271

6.1 Introduction..... 271

Page

6.2 Implications of Steady-State and Dynamic Curving Results..... 272
6.3 Recommendations for Future Work..... 274

REFERENCES..... 278

APPENDIX A - DYNAMIC CURVING EQUATIONS OF MOTION OF A WHEELSET..... 283

A.1 Introduction..... 283
A.2 Coordinate Systems..... 284
A.3 Acceleration of Wheelset Center of Mass..... 289
A.4 Rate of Angular Momentum of Wheelset..... 290
A.5 Wheelset Forces and Moments..... 292

A.5.1 Normal Forces..... 293
A.5.2 Creep Forces and Moments..... 295

A.5.2.1 Heuristic Creep Model..... 297
A.5.2.2 Derivation of Creepages for Dynamic Curving..... 300
A.5.2.3 Definition of Contact Patch Work... 304

A.6 Wheelset Equations of Motion..... 305

A.6.1 Single-Point Contact..... 308
A.6.2 Two-Point Contact..... 314

A.7 Wheelset Numerical Methods..... 323

A.7.1 Single-Point Contact..... 326
A.7.2 Two-Point Contact..... 329

APPENDIX B - DYNAMIC CURVING EQUATIONS OF MOTION OF A RAIL VEHICLE MODEL..... 331

B.1 Introduction..... 331
B.2 Coordinate Systems..... 331
B.3 Acceleration of Center of Mass..... 339

B.3.2 Acceleration of Carbody Center of Mass..... 340

B.4 Rate of Angular Momentum..... 341

B.4.1 Rate of Angular Momentum of Truck Frame and Bolster..... 341
B.4.2 Rate of Angular Momentum of Carbody..... 342

B.5 Forces and Moments..... 343

B.5.1 Wheelset Suspension Forces and Moments..... 345
B.5.2 Truck Frame and Bolster Suspension Forces and Moments..... 352
B.5.3 Carbody Suspension Forces and Moments..... 360

Page

B.6 Equations of Motion..... 363

B.6.1 Wheelset Equations of Motion..... 363
B.6.2 Truck Frame and Bolster Equations of Motion. 364
B.6.3 Carbody Equations of Motion..... 365
B.6.4 Modified Carbody Yaw Equation of Motion..... 366

B.7 Numerical Methods..... 370

B.7.1 Dynamic Curving Program..... 377

APPENDIX C - STEADY-STATE CURVING CONDITIONS..... 384

C.1 Introduction..... 384
C.2 Wheelset Equilibrium Conditions..... 384

C.2.1 Single-Point Contact Conditions..... 387
C.2.2 Two-Point Contact Conditions..... 392

C.3 Wheelset Numerical Methods..... 398

C.3.1 Methods for Single-Point Contact..... 400
C.3.2 Methods for Two-Point Contact..... 401

C.4 Half-Carbody Model..... 403

C.4.1 Primary Suspension Model..... 407
C.4.2 Secondary Suspension Model..... 410
C.4.3 Half-Carbody Model Equilibrium Conditions... 412

C.5 Half-Carbody Model Numerical Methods..... 417

C.5.1 Carbody Roll Calculation..... 417
C.5.2 Vertical Wheel Load Calculation..... 425
C.5.3 Solution Method for Coupled Equations..... 428
C.5.4 Program SSCURV..... 430

LIST OF FIGURES

FIGURE NUMBER	TITLE	PAGE
2.1	Truck Arrangement [18]	41
2.2	Definition of Angle of Attack and Lateral Wheelset Excursion	45
2.3	Definition of (a) Degree Curve and (b) Superelevation Angle	51
2.4	Curved Track Definitions	53
2.5	Track Curvature and Superelevation as a Function of Distance	55
2.6	Lateral Track Model	56
2.7	Typical Wheelset Cross-Section	58
2.8	Track and Wheelset Coordinate Systems	60
2.9	Rolling Radii Vs. Net Wheelset Lateral Excursion for (a) Heumann Wheel and (b) New Wheel on Worn Rails	62
2.10	Contact Angles vs. Net Wheelset Lateral Excursion for (a) Heumann Wheel and (b) New Wheel on Worn Rails	63
2.11	Wheelset Roll Angle vs. Net Wheelset Lateral Excursion for (a) Heumann and (b) New Wheel on Worn Rails	64
2.12	Left Wheel/Rail Contact	67
2.13	Contact Patch Creep Force vs. Creepage	70
2.14	Schematic of Conventional Truck	72
2.15	Schematic of Self-Steering Radial Truck	73
2.16	Alternate Self-Steering Radial Truck Configurations	74
2.17	Shear and Bending Stiffness Definitions	76
2.18	Design Region for Conventional and Radial Trucks in the Truck Shear vs. Bending Stiffness Plane	79

FIGURE NUMBER	TITLE	PAGE
2.19	Schematic Diagram of "S" Forced-Steered Truck	81
2.20	Schematic Diagram of "L" Forced-Steered Truck	82
2.21	Schematic Diagram of "U" Forced-Steered Truck	83
2.22	Forced-Steering Truck Model	85
2.23	Schematic Diagram of a Forced-Steering Truck Model with Cant Deficiency Steering Action	87
2.24	Generic Truck Model	90
2.25	Rail Vehicle Model, Side View	95
2.26	Rail Vehicle Model During Curving, Rear View	96
2.27	Physical Arrangement of the Secondary Yaw Suspension	97
2.28	Model of Secondary Yaw Suspension	98
2.29	Truck Frame/Bolster Yaw Supension Characteristic	100
2.30	Wheel/Rail Contact Possibilities for a Truck with New Wheels	103
3.1	Steady-State Equilibrium Configuration for the Wheelsets of a Flexible Truck	115
3.2	Wheelset Lateral Force and Yaw Moment	118
3.3	Wheelset Lateral Force as a Function of Lateral Excursion and Angle of Attack for a Wheelset with Heumann Wheels on Worn Rails Negotiating a 10° Curve (Axle Load = 25,000 lb; Rigid Rails)	119
3.4	Wheelset Yaw Moment as a Function of Lateral Excursion and Angle of Attack for a Wheelset with Heumann Wheels on Worn Rails Negotiating a 10° Curve (Axle Load = 25,000 lb; Rigid Rails)	120

FIGURE NUMBER	TITLE	PAGE
3.5	Wheelset Yaw Moment as a Function of Lateral Excursion and Angle of Attack for a Wheelset with Heumann Wheels on Worn Rails Negotiating Tangent Track (Axle Load = 25,000 lb; Rigid Rails).....	123
3.6	Maximum L/V Ratio at Flanging Wheel vs. Wheelset Angle of Attack (Axle Load = 25,000 lb; Rigid Rails).....	124
3.7	Wheelset Yaw Moment vs. Wheelset Lateral Force for New and Heumann Wheels.....	127
3.8	Flanging Wheel Work vs. (L/V) Ratio for New and Heumann Wheels.....	129
3.9	Work at Flanging Wheel vs. Primary Longitudinal Stiffness of a Conventional Truck with New Wheels Negotiating 2.5°, 5°, 10°, and 20° Curves.....	134
3.10	Effect of Increasing Primary Longitudinal Stiffnesses on the Curving Behavior of a Conventional Truck Negotiating a Tight Curve.	136
3.11	Leading Wheelset Angle of Attack vs Primary Longitudinal Longitudinal Stiffness of a Conventional Truck with New Wheels Negotiating 2.5°, 5°, 10°, and 20° Curves....	138
3.12	Effect of Curvature and Primary Longitudinal Stiffness on the Leading Wheelset Angle of Attack and Yaw Moment of a Conventional Truck with New Wheels.....	140
3.13	Leading Outer Wheel Lateral Force vs. Primary Longitudinal Stiffness of a Conventional Truck with New Wheels Negotiating 2.5°, 5°, 10°, and 20° Curves.....	142
3.14	Direction of Secondary Yaw Moment on Front and Rear Trucks During Curve Negotiation.....	143
3.15	Work at Flanging Wheel vs. Primary Lateral Stiffness of a Conventional Truck with New Wheels Negotiating a 10° Curve.....	145

FIGURE NUMBER	TITLE	PAGE
3.16	Effect of Secondary Yaw Breakaway Torque on the Work at the Flanging Wheel of a Conventional Truck with New Wheels Negotiating a 10° Curve	147
3.17	Effect of Curvature on the Work at the Flanging Wheel of a Conventional Truck with New Wheels at Balanced Running	149
3.18	Effect of Cant Deficiency on the Work at the Flanging Wheel of a Conventional Truck with New Wheels Negotiating a 10° Curve	150
3.19	Work at Flanging Wheel vs. Fraction of Full Kalker Creep Coefficients for a Conventional Truck with New Wheels Negotiating a 10° Curve	152
3.20	Effect of Coefficient of Friction on the Work at the Flanging Wheel of a Conventional Truck with New Wheels Negotiating a 10° Curve	154
3.21	Effect of Axle Drive Torque on the Work at the Flanging Wheel of a Conventional Truck with New Wheels Negotiating a 10° Curve	15[illegible]
3.22	Work at Flanging Wheel vs. Primary Longitudinal Stiffness of a Conventional Truck with Heumann Wheels Negotiating 2.5°, 5°, 10°, and 20° Curves	159
3.23	Work at Flanging Wheel vs. Primary Longitudinal Stiffness of a Self-Steered Radial Truck with New Wheels Negotiating 2.5°, 5", 10°, and 20° Curves	163
3.24	Work at Flanging Wheel vs. Primary Longitudinal Stiffness of a Self-Steered Radial Truck with Heumann Wheels Negotiating 2.5°, 5°, 10°, and 20° Curves	165
3.25	Work at Flanging Wheel vs. Interaxle Bending Stiffness of a Forced-Steered Radial Truck, FSR I, with New Wheels Negotiating 2.5°, 5°, 10°, and 20° Curves	171

FIGURE NUMBER	TITLE	PAGE
3.26	Work at Flanging Wheel vs. Interaxle Bending Stiffness of a Forced-Steered Radial Truck, FSR II, with New Wheels Negotiating 2.5°, 5°, 10°, and 20° Curves	172
3.27	Work at Flanging Wheel vs. Interaxle Bending Stiffness of Self-Steered and Forced-Steered Radial Trucks with New Wheels Negotiating 10° Curves	174
3.28	Work at Flanging Wheel vs. Interaxle Bending Stiffness of a Forced-Steered Radial Truck, FSR I, with Heumann Wheels Negotiating 2.5°, 5°, 10°, and 20° Curves	176
3.29	Work at Flanging Wheel vs. Interaxle Bending Stiffness of a Forced-Steered Radial Truck, FSR II, with Heumann Wheels Negotiating 2.5°, 5°, 10°, and 20° Curves	177
3.30	Leading Wheelset Angle of Attack vs. Curvature Steering Gain for a Forced-Steered Radial Truck, FSR I, with New and Heumann Wheels Negotiating a 10° Curve	182
3.31	Leading Wheelset Angle of Attack vs. Curvature Steering Gain for a Forced-Steered Radial Truck, FSR I, with New and Heumann Wheels Negotating a 20° Curve	183
4.1	Location of Conventional and Radial Trucks with New Wheels in the Truck Shear vs. Bending Stiffness Plane	194
4.2	Location of Conventional and Radial Trucks with Heumann Wheels in the Truck Shear vs. Bending Stiffness Plane	195
4.3	Curving Performance/Stability Tradeoff in Terms of Work at Flanging Wheel vs. Critical Speed of a Conventional Truck with New Wheels Negotiating 2.5°, 5°, 10°, and 20° Curves	197
4.4	Curving Performance/Stability Tradeoff in Terms of Work at Flanging Wheel vs. Critical Speed of a Conventional Truck with Heumann Wheels Negotiating 2.5°, 5°, 10°, and 20° Curves	198

FIGURE NUMBER	TITLE	PAGE
4.5	Curving Performance/Stability Tradeoff in Terms of Work at Flanging Wheel vs. Critical Speed of a Self-Steered Radial Truck with New Wheels Negotiating 2.5°, 5°, 10°, and 20° Curves	200
4.6	Curving Performance/Stability Tradeoff in Terms of Work at Flanging Wheel vs. Critical Speed of a Self-Steered Radial Truck with Heumann Wheels Negotiating 2.5°, 5°, 10°, and 20° Curves	201
4.7	Curving Performance/Stability Tradeoff in Terms of Work at Flanging Wheel vs. Critical Speed of a Forced-Steered Radial Truck, FSR I, Negotiating 2.5°, 5°, 10°, and 20° Curves.	203
4.8	Curving Performance/Stability Tradeoff in Terms of Work at Flanging Wheel vs. Critical Speed of a Forced-Steered Radial Truck, FSR II, Negotiating 2.5°, 5°, 10° and 20° Curves.	204
4.9	Curving Performance/Stability Tradeoff in Terms of Work at Flanging Wheel vs. Critical Speed of a Forced-Steered Radial Truck, FSR I, with Heumann Wheels Negotiating 2.5°, 5°, 10° and 20° Curves	205
4.10	Curving Performance/Stability Tradeoff in Terms of Work at Flanging Wheel vs. Critical Speed of a Forced-Steered Radial Truck, FSR II, with Heumann Wheels Negotiating 2.5°, 5°, 10° and 20° Curves	206
4.11	Work at Flanging Wheel vs. Curvature for Baseline Truck Designs with New Wheels (Critical Speeds = 120 mph)	212
4.12	Leading Outer Wheel Lateral Force vs. Curvature for Baseline Truck Designs with New Wheels (Critical Speeds = 120 mph)	213
4.13	Work at Flanging Wheel vs. Curvature for Baseline Truck Designs with Heumann Wheels (Critical Speeds = 120 mph)	215
4.14	Leading Outer Wheel Lateral Force vs. Curvature for Baseline Truck Designs with Heumann Wheels (Critical Speeds = 120 mph)	216

FIGURE NUMBER	TITLE	PAGE
4.15	Total Work and Distribution of Work at Contact Patches for Baseline Trucks with New Wheels Negotiating 10° Curves	218
4.16	Total Work and Distribution of Work at Contact Patches for Baseline Trucks with Heumann Wheels Negotiation 10° Curves	219
5.1	History of Leading Wheelset Angle of Attack of a Conventional Vehicle Operating on Tangent Track at (a) 150 ft/sec, (b) 175 ft/sec, and (c) 200 ft/sec in Presence of Perturbation	226
5.2	History of (a) Wheelset Lateral Excursions and (b) Angles of Attack of a Baseline Conventional Vehicle with New Wheels Negotiating a 150 ft Curve Entry Spiral into a 10° Curve at a Balance Speed of 45 ft/sec	232
5.3	History of (a) Leading Outer (i.e., Flanging) Wheel Lateral Force and (b) Contact Work of a Baseline Conventional Vehicle with New Wheels Negotiating a 150 ft Curve Entry Spiral into a 10° Curve at a Balance Speed of 45 ft/sec	233
5.4	History of (a) Wheelset Lateral Excursions and (b) Angles of Attack of a Baseline Conventional Vehicle with New Wheels Negotiating a 150 ft Curve Entry Spiral into a 2.5° Curve at a Balance Speed of 90 ft/sec	237
5.5	History of (a) Leading Outer (i.e., Flanging) Wheel Lateral Force and (b) Contact Work for a Baseline Conventional Vehicle with New Wheels Negotiating a 150 ft Curve Entry Spiral into a 2.5° Curve at a Balance Speed of 90 ft/sec	238
5.6	History of (a) Wheelset Lateral Excursions and (b) Angles of Attack of a Baseline Conventional Vehicles with Heumann Wheels Negotiating a 150 ft Curve Entry Spiral into a 10° Curve at a Balance Speed of 45 ft/sec	244

FIGURE NUMBER	TITLE	PAGE
5.7	History of (a) Leading Outer (i.e., Flanging) Wheel Lateral Force and (b) Contact Work of a Baseline Conventional Vehicle with Heumann Wheels Negotiating a 150 ft Curve Entry Spiral into a 10° Curve at a Balance Speed of 45 ft/sec	245
5.8	Effect of Curve Entry Spiral Length on the Peak Lateral Wheel Force of a Baseline Conventional Vehicle with New Wheels Entering a 10° Curve at a Balance Speed of 45 ft/sec	248
5.9	History of (a) Wheelset Lateral Excursions and (b) Angles of Attack of a Self-Steered Radial Vehicle with New Wheels Negotiating a 150 ft Curve Entry Spiral into a 10° Curve at a Balance Speed of 45 ft/sec	249
5.10	History of (a) Leading Outer (i.e., Flanging) Wheel Lateral Force and (b) Contact Work of a Self-Steered Radial Vehicle with New Wheels Negotiating a 150 ft Curve Entry Spiral into a 10° Curve at a Balance Speed of 45 ft/sec	250
5.11	History of (a) Wheelset Lateral Excursions and (b) Angles of Attack of a Self-Steered Radial Vehicle with Heumann Wheels Negotiating a 150 ft Curve Entry Spiral into a 10° Curve at a Balance Speed of 45 ft/sec	254
5.12	History of (a) Leading Outer (i.e., Flanging) Wheel Lateral Force and (b) Contact Work of a Self-Steered Radial Vehicle with Heumann Wheels Negotiating a 150 ft Curve Entry Spiral into a 10° Curve at a Balance Speed of 45 ft/sec	255
5.13	History of (a) Wheelset Lateral Excursions and (b) Angles of Attack of a FSR I Forced-Steered Radial Vehicle with New Wheels Negotiating a 150 ft Curve Entry Spiral into a 10° Curve at a Balance Speed of 45 ft/sec	259
5.14	History of (a) Leading Outer (i.e., Flanging) Wheel Lateral Force and (b) Contact Work of a FSR I Forced-Steered Radial Vehicle with New Wheels Negotiating a 150 ft Curve Entry	

FIGURE NUMBER	TITLE	PAGE
	Spiral into a 10° Curve at a Balance Speed of 45 ft/sec	260
5.15	History of (a) Wheelset Lateral Excursions and (b) Angles of Attack of a FSR I Forced-Steered Radial Vehicle with Heumann Wheels Negotiating a 150 ft Curve Entry Spiral into a 10° Curve at a Balance Speed of 45 ft/sec	264
5.16	History of (a) Leading Outer (i.e., Flanging) Wheel Lateral Force and (b) Contact Work of a FSR I Forced-Steered Radial Vehicle with Heumann Wheels Negotiating a 150 ft Curve Entry Spiral into a 10° Curve at a Balance Speed of 45 ft/sec	265
A.1	Wheelset and Track Coordinate Systems	286
A.2	Definition of Wheelset and Track Coordinate System Orientations (Rotations Only)	287
A.3	Wheel/Rail Geometry and Normal Forces Assuming Single-Point Contact	294
A.4	Contact Patch Coordinate Systems	296
A.5	Contact Patch Creep Force vs. Creepage	301
A.6	Longitudinal Displacement of Contact Points Due to Wheelset Yaw	303
A.7	Lateral Track Model	307
A.8	Free-Body Diagram of Wheelset in Single-Point Contact	309
A.9	Left Wheel/Rail Contact	316
A.10	Wheel and Rail Forces for Two-Point Contact	318
A.11	Wheelset Dynamic Curving Analysis at One Time-Step	325
A.12	Wheel/Rail Force Calculation at One Time-Step	328
B.1	Rail Vehicle Model During Curving, Rear View.	332

FIGURE NUMBER	TITLE	PAGE
B.2	Rail Vehicle Model Coordinate System.....	333
B.3	Definition of Truck Frame Orientation (Rotation Only).....	335
B.4	Definition of Bolster Orientation (Rotation Only).....	336
B.5	Definition of Carbody Orientation (Rotation Only).....	337
B.6	Generic Truck Model.....	344
B.7	Suspension Forces and Moments Acting on Wheelset i.....	346
B.8	Lateral Suspension Forces and Yaw Suspension Moments Acting on Truck Frame.	354
B.9	Truck Frame/Bolster Yaw Suspension Characteristic.....	358
B.10	Yaw Suspension Moments Acting on Bolsters.....	359
B.11	Suspension Forces and Moments Acting on Carbody.....	361
B.12	Truck Frame/Bolster Yaw Suspension Characteristic.....	368
B.13	Wheel/Rail Contact Possibilities for Wheelsets of a Truck with New Wheels.....	378
B.14	Flowchart of Dynamic Curving Program.....	380
B.15	Layout of Equation Subroutines.....	381
C.1	Flexible Rail Model.....	386
C.2	Wheelset Free-Body Diagram: Single-Point Wheel/Rail Contact.....	388
C.3	Wheel and Rail Forces for Single-Point Contact.....	389
C.4	Wheel and Rail Forces for Two-Point Contact.....	393

FIGURE NUMBER	TITLE	PAGE
C.5	Overview of Wheelset Steady-State Curving Analysis	399
C.6	Flowchart for Wheelset Equilibrium with Rigid Rails: Single-Point Contact Model	402
C.7	Flowchart for Wheelset Equilibrium with Rigid Rails: Two-Point Contact Model	404
C.8	Primary Suspension Stiffnesses	408
C.9	Force-Displacement Characteristic for Primary Lateral Stiffness Model	409
C.10	Force-Displacement Characteristic for Primary Longitudinal Stiffness Model	409
C.11	Primary Suspension Arrangement with Auxiliary Suspension	411
C.12	Wheelset Misalignments	416
C.13	Forces Acting at Secondary Suspension of a Truck	424
C.14	Wheelset Free-Body Diagram	424
C.15	Vehicle Free-Body Diagram, Rear View	426
C.16	Schematic of One Iteration in SROOTS, from Rabinowitz [49]	429
C.17	Steady-State Curving Program SSCURV Layout	431

LIST OF TABLES

TABLE NUMBER	TITLE	PAGE
2.1	Proposed Wear Indices	47
2.2	Generic Truck Simplifications	93
2.3	Baseline Rail/Vehicle Parameters	106
3.1	Effects of Rail Flexibility on the Steady-State Curving of a Conventional Truck with New Wheels Negotiating a 10° Curve; $k_{px} = 5.0 \times 10^5$ lb/ft	157
3.2	The Effect of New and Heumann Wheel/Rail Profiles on the Work at the Flanging Wheel of a Conventional Truck with $k_{px} = 5.0 \times 10^5$ lb/ft Negotiating 2.5°, 5°, 10°, and 20° Curves	160
3.3	The Effect of New and Heumann Wheel/Rail Profiles on the Work at the Flanging Wheel of a Self Steered Radial Truck Negotiating 2.5°, 5°, 10°, and 20° Curves with Stiffnesses	166
3.4	Interaxle Bending Stiffnesses for Baseline Forced Steered Radial Truck Designs with Different Wheel/Rail Profiles All Having Critical Speeds of 120 mph	179
3.5	The Effect of New and Heumann Wheel/Rail Profiles on the Work at the Flanging Wheel of A Forced Steered Radial Truck, FSR I, Negotiating 2.5°, 5°, 10°, and 20° Curves with Stiffnesses	180
3.6	The Effect of New and Heumann Wheel/Rail Profiles on the Work at the Flanging Wheel of a Forced Steered Radial Truck, FSR II, Negotiating 2.5°, 5°, 10°, and 20° Curves with Stiffnesses	180
3.7	(a) Work at Flanging Wheel and (b) Wheel/Rail Force at Flanging Wheel vs. Misalignment Condition for Different Trucks Operating on 5° Curve	188

TABLE NUMBER	TITLE	PAGE
3.8	Wheelset Lateral Excursion and (b) Wheel/ Rail Force vs. Misalignment Condition for Baseline Trucks Operating on Tangent Track....	190
4.1	Stiffnesses vs. Critical Speed for Four Truck Designs with New Wheels.....	193
4.2	Stiffnesses vs. Critical Speed for Four Truck Designs with Heumann Wheels.....	193
4.3	Curving Performance/Stability Tradeoff in Terms of Work at Flanging Wheel vs. Critical Speed for Four Truck Designs with New Wheels Negotiating 2.5°, 5°, 10°, and 20° Curves.....	209
4.4	Curving Performance/Stability Tradeoff in Terms of Work at Flanging Wheel vs. Critical Speed for Four Truck Designs with Heumann Wheels Negotiating 2.5°, 5°, 10°, and 20° Curves.....	209
4.5	Comparison of Flanging Wheel Work, Total Work, and Power Requirements of Front and Rear Trucks for Baseline Designs with New Wheels Negotiating 10° Curves.....	220
5.1	Comparison of Steady-State and Dynamic Curving Results with Constant Secondary Yaw Breakaway Torques.....	224
5.2	Balanced Running Speeds Assuming 6 in Superelevation (i.e., ϕ_{SE} = 6.2°).....	228
5.3	Comparison of Steady-State and Dynamic Curving Results with and Without Secondary Yaw Breakaway Torques.....	230
5.4	Leading Outer Wheel Force and Work of a Baseline Conventional Vehicle with New Wheels Negotiating a 150 ft Curve Entry Spiral into a 2.5°, 5°, and 10° Curve.....	242
5.5	Dynamic Curve Entry Performance in Terms of Flanging Wheel Lateral Force and Contact Work for Baseline Vehicles with New Wheels Negotiating a 150 ft Spiral into a 10° Curve at a Balance Speed of 45 ft/sec.....	268

TABLE NUMBER	TITLE	PAGE
5.5	Dynamic Curve Entry Performance in Terms of Flanging Wheel Lateral Force and Contact Work for Baseline Vehicles with New Wheels Negotiating a 150 ft Spiral into a 10° Curve at a Balance Speed of 45 ft/sec.....	268
5.6	Dynamic Curve Entry Performance in Terms of Flanging Wheel Lateral Force and Contact Work for Baseline Vehicles with Heumann Wheels Negotiating a 150 ft Spiral into a 10° Curve at a Balance Speed of 45 ft/sec.....	268
B.1	Coordinate Systems.....	334
B.2	States of the Rail Vehicle Model.....	375
B.3	Subroutine Descriptions for Dynamic Curving Program.....	382

NOMENCLATURE

a	half of track gage
$\underline{}^{\beta}_{a}{}^{\alpha}$	acceleration of point α in reference system β
a_e	longitudinal semi-axis of contact patch ellipse
b	half of wheelbase
b_e	lateral semi-axis of contact patch ellipse
c_o	secondary yaw viscous damping
c_{px}	primary longitudinal damping
c_{py}	primary lateral damping
c_{pz}	primary vertical damping
c_r	effective lateral rail viscous damping
c_{sy}	secondary lateral damping
c_{sz}	secondary vertical damping
$C_{\beta/\alpha}$	coordinate transformation matrix from α to β
d_p	half of lateral spacing between primary longitudinal springs
d_s	half of lateral spacing between secondary vertical springs
D	degree curve
f^*_{ij}	nominal creep coefficients (ij = 11, 12, 22, 33)
f_{11}	lateral creep coefficient
f_{12}	lateral/spin creep coefficient
f_{22}	spin creep coefficient
f_{33}	longitudinal creep coefficient
$\bar{F}_{axle}$	vector of wheelset axle forces
F_{buff}	lateral buff load
$\bar{F}_c$	creep force vector (with components F_{CPX}, F_{CPY}, and M_{CP} in longitudinal, lateral, and normal contact patch directions, respectively)
F_{CPX}, F_{CPY}	creep force in longitudinal, lateral contact patch direction
F'_{CPX}, F'_{CPY}	unlimited creep force in longitudinal, lateral contact patch direction
F_{CXi}	longitudinal track component of creep force at i-th contact patch; i = L (left), R (right) for single-point; i = LT (left tread), LF (left flange), R (right) for two-point

F_f lateral flange force (i.e., leading outer wheel lateral force)

F_{lat} wheelset lateral force (in lateral track direction) provided by suspension and body forces

F_N normal force

F_N^* nominal normal force

F_{Ni} normal force at i-th contact patch; i = L (left), R (right) for single-point; i = LT (left tread), LF (left flange), R (right) for two-point

F_{NYi} lateral track component of normal force at i-th contact patch; i = L (left), R (right) for single-point, i = LT (left tread), LF (left flange), R (right) for two-point

F_{NZi} vertical track component of normal force at i-th contact patch; i = L (left), R (right) for single-point; i = LT (left tread), LF (left flange), R (right) for two-point

F_{rail_L}, F_{rail_R} lateral rail reaction force at left, right rail

F'_R unlimited resultant creep force

$\bar{F}_{susp}$ vector of suspension forces

F_t wheelset longitudinal thrust or drawbar force

F_y net lateral wheel force composed of creep and normal forces

g acceleration of gravity

g' actual rail gage

G track curvature steering gain

$G_{pr\ell}$ track curvature steering gain to follow pure rolling line

h_{cs} vertical distance from secondary suspension to carbody center of mass

h_{tp} vertical distance from primary suspension to truck center of mass

h_{ts} vertical distance from truck center of mass to secondary suspension

H cant deficiency steering gain

$\bar{H}^{\alpha/\beta}$ angular momentum of body α about point β

$\hat{i},\hat{j},\hat{k}$ unit vectors in longitudinal, lateral, vertical direction, respectively

I_{BZ} yaw principal mass moment of inertia of bolster

I_{CX} roll principal mass moment of inertia of carbody

I_{CZ} yaw principal mass moment of inertia of carbody

I_{FX} roll principal mass moment of inertia of truck frame

I_{FZ} yaw principal mass moment of inertia of truck frame

I_{WY} pitch principal mass moment of inertia of wheelset

I_{WZ} yaw principal mass moment of inertia of wheelset

k_b total bending stiffness of a truck

k_{b2} interaxle bending stiffness

k_{px} primary longitudinal suspension stiffness

k_{pxaux} auxiliary primary longitudinal suspension stiffness

k_{py} primary lateral suspension stiffness

k_{pz} primary vertical suspension stiffness

k_r effective lateral rail stiffness

k_s total shear stiffness of a truck

k_{sy} secondary lateral suspension stiffness

k_{sz} secondary vertical suspension stiffness

k_{s2} interaxle shear stiffness

$k_{s\psi}$ secondary yaw suspension stiffness

ℓ_s half of truck center pin spacing

(L/V) lateral to vertical wheel force ratio

m_r effective lateral rail mass

$\bar{M}^{\alpha}$ vector sum of all external moments acting about the center of mass of point α

$\bar{M}_{axle}$ vector of wheelset axle moments

M_{CP} creep moment normal to contact patch

M_{CYi} lateral track frame component of creep moment at i-th contact patch; i = L (left), R (right) for single-point; i = LT (left tread), LF (left flange), R (right) for two-point

M_{CZi} vertical track frame component of creep moment at i-th contact patch; i = L (left), R (right) for single-point; i = LT (left tread), LF (left flange), R (right) for two-point

$\bar{M}_{susp}$ vector of suspension moments

M_{yaw} wheelset yaw moment (in vertical wheelset frame direction) provided by suspension forces

P power dissipated at contact patch

P_{in}, P_{out} input, output power

$\bar{r}^{\beta/\alpha}$ position vector from point α to point β

r_i rolling radius measured from wheelset spin axis to i-th contact patch; i = L (left), R (right) for single-point, i = LT (Left tread), LF (left flange), R (right) for two-point

r_o rolling radius for centered wheelset; nominal rolling radius

R curve radius, often expressed in degree curve, D, where $D = \frac{360}{\pi}[\sin^{-1}(\frac{50}{R})] \simeq \frac{5730}{R}$ deg with R in ft

T_d wheelset drive/brake torque

T_o secondary yaw suspension breakaway torque

V vehicle speed

V_{cr} critical speed of the vehicle

V_L, V_R external vertical load acting on left, right wheel (in negative vertical track frame direction) provided by body and suspension forces

W contact patch work per unit distance (in force units) $W = \bar{F}_c \cdot \bar{\xi}$

W' contact patch work per unit distance (W) divided by contact patch area

W_B bolster weight

W_c carbody weight

W_F truck frame weight

W_V total vehicle weight

W_W wheelset weight

x longitudinal coordinate

$\bar{X}$ geometry state vector

$\bar{X}_m$ misaligned geometry state vector

y lateral coordinate

y_{fc} flange clearance

y_{rail_L}, y_{rail_R} lateral displacement of left, right rail

z vertical coordinate

β normalized unlimited resultant creep force

δ_i contact angle at i-th contact patch; i = L (left), R (right) for single-point; i = LT (left tread), LF (left flange), R (right) for two-point

Δx_i longitudinal displacement of i-th contact patch from vertically below wheelset axis

Δy track curvature steering offset

Δz vertical distance between points of flange and tread contact

$\Delta\psi$ cant deficiency steering offset

ϵ creep force saturation constant

$\dot{\theta}_w$ wheelset spin speed

λ wheel conicity

μ coefficient of friction

μ_f coefficient of flange friction

$\bar{\xi}$ creepage vector (with components ξ_{Xi}, ξ_{Yi}, and ξ_{SPi} in longitudinal, lateral, and normal contact patch directions, respectively)

ξ_R resultant creepage

ξ_{SPi} spin creepage in normal contact patch direction at i-th contact patch

ξ_{Xi} longitudinal creepage at i-th contact patch

ξ_{Yi} lateral creepage at i-th contact patch

ϕ_d cant deficiency (lateral unbalance load)

$$\phi_d = \frac{V^2}{Rg} - \phi_{SE}$$

ϕ_{SE} track superelevation (or bank) angle

ϕ_w wheelset roll angle with respect to track plane

ψ yaw angle

ψ_w wheelset angle of attack, or yaw angle with respect to radial alignment

$\overline{\omega}^{\beta\,\alpha}$ angular velocity of system α relative to system β

1.0 INTRODUCTION

1.1 Background

Rail passenger vehicles are often required to negotiate tight curves, especially in urban transit systems. During curve negotiation, vehicle performance is generally degraded in comparison to straight track operation. The rate of wear at the wheels and rails is accelerated, the fuel consumption is increased, the potential danger of derailment is enhanced, and objectionable screeching noise is often generated. Several urban transit systems have reported problems of high rates of wheel and rail wear [1,2]. Excessive wear necessitates frequent wheel reprofiling and rail renewal, increasing maintenance costs. In the last decade, with the renewed interest in rail transportation and the growing concern for energy efficient operation, interest has focused on improving rail vehicle curving performance.

During curve negotiation, the wheelsets of conventional vehicles generally misalign radially with the track. Stiff suspension systems traditionally designed for dynamic stability prevent the wheelsets from proper tracking and, as a result, large wheel/rail contact forces develop. These forces have been linked with the increased wear, fuel consumption, risk of derailment, and noise generation. To alleviate these problems several suggestions have been proposed, including the use of alternate wheel profiles and modified suspension designs.

The wheel/rail profile geometry has a strong influence on vehicle curving performance and stability. The standard wheel profile

used nearly exclusively in the U.S., called the new AAR* 1 in 20 wheel profile, has a 1 in 20 taper tread and a steep flange. The new wheel profile develops two-point tread and flange contact in most curving situations which accentuates wear [3,4]. To minimize wear, wheel profiles that achieve a more conformal mating to the rail head have been designed. Heumann [5] adopted this design approach and proposed a profile characterized by a smooth transition from tread to flange which maintains single-point wheel/rail contact even in curves. The Heumann wheel profile is typically used by European and Japanese rail authorities [4].

Modifications to the vehicle suspension system have been proposed to control wheelset angles and wheel/rail forces during curve negotiation and thus improve performance. One suggestion is to soften the suspension stiffnesses in conventional vehicles. However, a design tradeoff exists since softening the suspension system reduces the lateral stability of the vehicle on straight track. To achieve wheelset radial alignment during curve negotiation without degrading dynamic stability, vehicles with innovative suspension designs have been proposed. Examples include vehicles with self-steered trucks which employ direct interconnections between the wheelsets and vehicles with forced-steered trucks which employ both direct interconnections and passive linkages between the carbody and wheelsets. Despite their increased complexity, these vehicles have received much attention in recent years due to their potential for improving vehicle curving performance without sacrificing dynamic stability.

*Association of American Railroads.

The appropriate vehicle modifications depend strongly on the system route characteristics, particularly, the prevalence and distribution of sharp curves. In systems with few sharp curves, the performance of conventional vehicles with standard wheels may be acceptable. On the other hand, in systems with many sharp curves such as urban transit systems, self or forced-steered vehicles with alternate wheel profiles may be desirable despite initial modification costs and increased design complexity.

To evaluate the curving performance of rail vehicles with the suggested modifications, analytical prediction methods, design data, and field test data are required. This thesis is directed to providing analytical evaluation methods and curving performance data for rail passenger vehicles of conventional and innovative design.

1.2 Literature Review

Steady-State Curving Analytical models of rail vehicle curve negotiation were reported by Eksergian [6] and Porter [7] over fifty years ago. These early works assume rigid frame vehicles negotiating constant radius curves. They lack an appropriate treatment of the frictional behavior that arises between a rail and wheel which is rolling with slip, known as creep. It took thirty years before any significant theoretical progress was made in developing the relationships between the slip rates or creepages and the resulting creep forces (by Vermuelen and Johnson [8] and Kalker [9]). Kalker provided comprehensive mathematical models of wheel/rail interaction in the presence of slip assuming elastic deformation and ellipitical contact zones.

Newland [10] and Boocock [11] each described simple linear models to study steady-state curving. Conical wheels, flexible primary suspensions, and wheel/rail interaction effects due to creep and wheel/rail geometry are assumed. By linearizing the analysis, each developed efficient computational tools to predict slip and flange contact boundaries that define regions of "good" curving performance as functions of curve radius and lateral force unbalance. However, because of the imposed linearization, the results are applicable only for steady curving situations involving large radius curves.

Bell, Horak, and Hedrick [12,13] exercised simple linear models to understand the mechanics of steady-state curving and stability of rail vehicles. They investigated the influence of the shear and bending stiffnesses of a rail truck on curving performance and stability, demonstrating a basic design conflict. Ideally, low bending stiffness (achieved by employing soft longitudinal suspension) and highly profiled wheels (i.e., wheels of high conicity) provide superior curving performance during curve traversal. However, these two requirements lower the critical speed for the onset of wheelset/truck lateral instability on tangent track. Using low order, predominantly linear models Bell, Horak, and Hedrick investigated the stability versus curving tradeoff of conventional and self-steered radial trucks. They showed that the self-steered truck allows improved wheelset alignment in curves without degrading the dynamic performance on tangent track. Bell and Hedrick [14] reported that potentially the curve negotiation capability of forced-steered trucks is significantly improved over conventional and self-steered trucks.

Nonlinear steady-state curving models were developed by Elkins and Gostling [15]. They incorporated large wheel/rail contact angles and Kalker's nonlinear creep theory while retaining linear suspension elements. Law and Cooperrider [16] and Hedrick, et al. [17] explored the effects of nonlinear suspension components. In doctoral research, Bell [18] developed a detailed nonlinear steady-state curving model to study the effects of nonlinear suspension and wheel/rail profile on conventional, self-steered, and forced-steered truck performance. His results emphasized the importance of suspension design on vehicle curving performance, and suggested that for negotiation of sharp curves significant benefits are possible by forced-steering the wheelsets.

The majority of previous steady-state curving studies have assumed that each wheel of the vehicle contacts the rails at a single point. This is an acceptable approximation of tread contact, but for some profiles this represents a simplistic view of flange contact. Two-point tread and flange contact can occur for profiles with steep flanges, such as the new AAR 1 in 20 wheel profile. The vehicle curving studies of Marcotte, et al. [19] accounted for the possibility of two-point wheel/rail contact by using a wheel profile composed of a tread and flange segment of constant (but different) conicity. Using experimental data, Elkins and Weinstock [20] showed that significant errors result in predicting curving behavior based on analyses assuming single-point wheel/rail contact when in fact two-point contact occurs.

Dynamic Curving An early investigator of dynamic curving was Mueller [21] who used the friction center method to study the performance of a rail truck during transition from tangent to curved track. The friction center method assumes that the wheel profiles are cylindrical, the primary suspension elements are rigid, and that one or more wheels are in flange contact. Despite the limitations of his model, Mueller predicted that the magnitude of the impact force on the flange can become significant in comparison to the steady-state curving force.

During the last few years nonlinear dynamic analyses have been possible, relying heavily on large-scale computer systems. Smith [22] formulated a dynamic curving analysis which considers nonlinear suspension, damping, and creep forces. The analysis is limited in that it assumes conical wheels and a carbody which does not yaw with respect to the local tangent to the track centerline. The study does not consider track superelevation (banking), irregularities, or flexibility. However, Smith was able to show that the shorter the spiral of the transition track (between tangent and constant radius track), the more violent the response during curve entry.

Law and Cooperrider [16,23] developed comprehensive steady-state and dynamic curving models that include nonlinear suspension elements, creep forces, and wheel/rail geometry but do not directly account for rail flexibility. System inputs are track curvature, superelevation angle, and irregularities. Results of their models indicate that dynamic wheel/rail forces dominate in large radius curves, at balance speed (corresponding to zero lateral unbalance), and in situations

where flange contact is not severe. A reduction in dynamic flange forces is demonstrated using self-steered radial trucks.

Clark, et al. [24] introduced a nonlinear dynamic curving analysis that predicts the transient response of two-axle vehicles. The analysis accounts for lateral track flexibility and irregularities. Predictions made for a vehicle traversing a section of misaligned track agreed well with an experimental derailment.

Duffek and Jaschinski [25] formulated a detailed model of wheel/rail interaction to be used for dynamic curving studies. The model includes nonlinear creep force laws and accounts for the influence of wheelset yaw angle on wheel/rail contact geometry. Single-point wheel/rail contact is assumed.

Krolewski [26] developed a model for freight car dynamic curving simulations that includes nonlinear wheel/rail geometry, coulomb friction elements, and creep force saturation. With the model, dynamic wheel/rail forces exceeding steady-state values have been predicted.

A thorough search of the literature indicates the absence of dynamic curving studies that account for two-point wheel/rail contact.

1.3 Study Objectives and Methods

The purpose of this research is to gain a fundamental understanding of rail vehicle curving dynamics via appropriate analytical treatment and computer simulation. To gain this understanding, analytical methods and computational tools are developed and exercised to investigate the curving performance of rail passenger vehicles. A principal objective of this research is to establish the effects of suspension

design and wheel/rail interaction, particularly two-point contact, on vehicle curving performance.

Studies are based upon a generalized rail vehicle model that represents conventional and innovative suspension designs, including self-steered and forced-steered vehicles. The curving analysis accounts for nonlinear wheel/rail profile geometry, wheel/rail friction force saturation, and nonlinear suspension components. The analysis considers the important case of two-point wheel/rail contact which occurs with many common wheel profiles during curving.

In the development of this thesis, much use is made of a steady-state curving analysis. The steady-state analysis assumes that the vehicle is in steady-state force and moment equilibrium as it negotiates smooth, constant radius curved track. The analysis has proven to be a very useful tool for gaining a fundamental understanding of vehicle curving behavior and for parametric design studies. The steady-state analysis is computationally efficient and simple enough to allow tractable parametric design studies and the results are rich with the fundamental properties of curve negotiation.

A dynamic curving analysis is used to assess the predictive capabilities of the steady-state analysis and to evaluate transient behavior during curve negotiation. The dynamic analysis is a computationally time-consuming and expensive design tool. However, the analysis is important since it predicts the dynamic behavior during curve entry and exit during which steady-state conditions are not achieved.

Due to limited experimental data available in the literature, model validation studies have not been conducted. However, the basic trends predicted by the curving analyses are consistent with available data and field experience. The influence of suspension stiffness, wheel profile, and curve radius on conventional vehicle performance reported for tests conducted at WMATA* [1,27] correspond directly with the effects predicted by the curving analyses. Specifically, the observations from the WMATA tests that wheel/rail forces are reduced as the stiffness is softened and as single-point contact wheel profiles are employed correspond directly with the results described in this thesis. Furthermore, the curving studies predict dynamic wheel/rail forces which exceed those generated in steady curving situations, which agrees with the results of field measurements [28].

1.4 Organization of Thesis

This thesis is organized as follows. Chapter 2 describes analytical methods that characterize the curving performance and stability of rail passenger vehicles. These methods include the establishment of performance criteria and the development of rail and vehicle models and associated computational tools. In Chapters 3, 4, and 5 these tools are used to study the performance of conventional and advanced design rail vehicles. Chapter 3 presents the results of extensive parametric studies of steady-state curving performance. The results demonstrate that the principal parameters influencing steady-state

*Washington Metropolitan Area Transit Authority.

curving performance are suspension design and wheel/rail profile. Chapter 4 combines curving performance and stability results to identify inherent vehicle design tradeoffs. Vehicles with innovative suspension configurations such as forced-steered vehicle designs are shown to offer significant improvements in curving performance and stability in comparison to conventional vehicles. In addition, the results indicate that improved performance can be obtained by employing wheel profiles characterized by single-point contact rather than two-point contact. Chapter 5 focuses on rail vehicle dynamic curving performance. Preliminary studies of curve entry behavior indicate that transient characteristics, although limited, are most evident for forced-steered vehicles with single-point contact wheels. Conclusions and recommendations for future work are discussed in Chapter 6.

The appendices contain a detailed description of the model development and associated equation derivation. Appendix A derives the equations to predict the dynamic behavior of a wheelset during negotiation of flexible, curved track. The formulation accounts for both single-point and two-point wheel/rail contact. The wheelset model represents the most important element in any total vehicle model and thus merits such a detailed discussion. Appendix B formulates the dynamic curving equations of motion of a rail vehicle model and describes a numerical solution procedure. The vehicle model incorporates the nonlinear wheelset model developed in Appendix A and includes nonlinear suspension effects. Appendix C addresses

analytical and computational methods that characterize rail vehicle steady-state curving behavior. The steady-state curving conditions represent a special case of the dynamic curving equations developed in Appendices A and B.

2.0 STUDY METHODOLOGY

2.1 Introduction

This chapter describes analytical methods that characterize the curving performance and stability of rail passenger vehicles. These methods include the establishment of performance criteria, the formulation of rail and vehicle models, and the development of computational tools. In subsequent chapters, these methods are used to study the performance of conventional and advanced design rail vehicles.

The curve negotiation and stability capabilities of rail vehicles are evaluated in terms of performance criteria or indices. In this thesis, the principal curving performance index is the contact work due to friction which is related to wheel and rail wear [29]. The stability index is the maximum speed for stable operation, called the critical speed.

A rail passenger vehicle consists of a carbody supported at the front and rear by a bolster. As shown in Figure 2.1, each bolster rests on a truck frame which is connected to two wheelsets. The wheelsets represent the basic elements of the rail vehicle steering and support system. The curving performance and stability of the vehicle is directly related to the ability of its wheelsets to negotiate the track.

In this thesis, a simple model of the track is adopted in which the track curvature and bank angle are assumed to be known functions

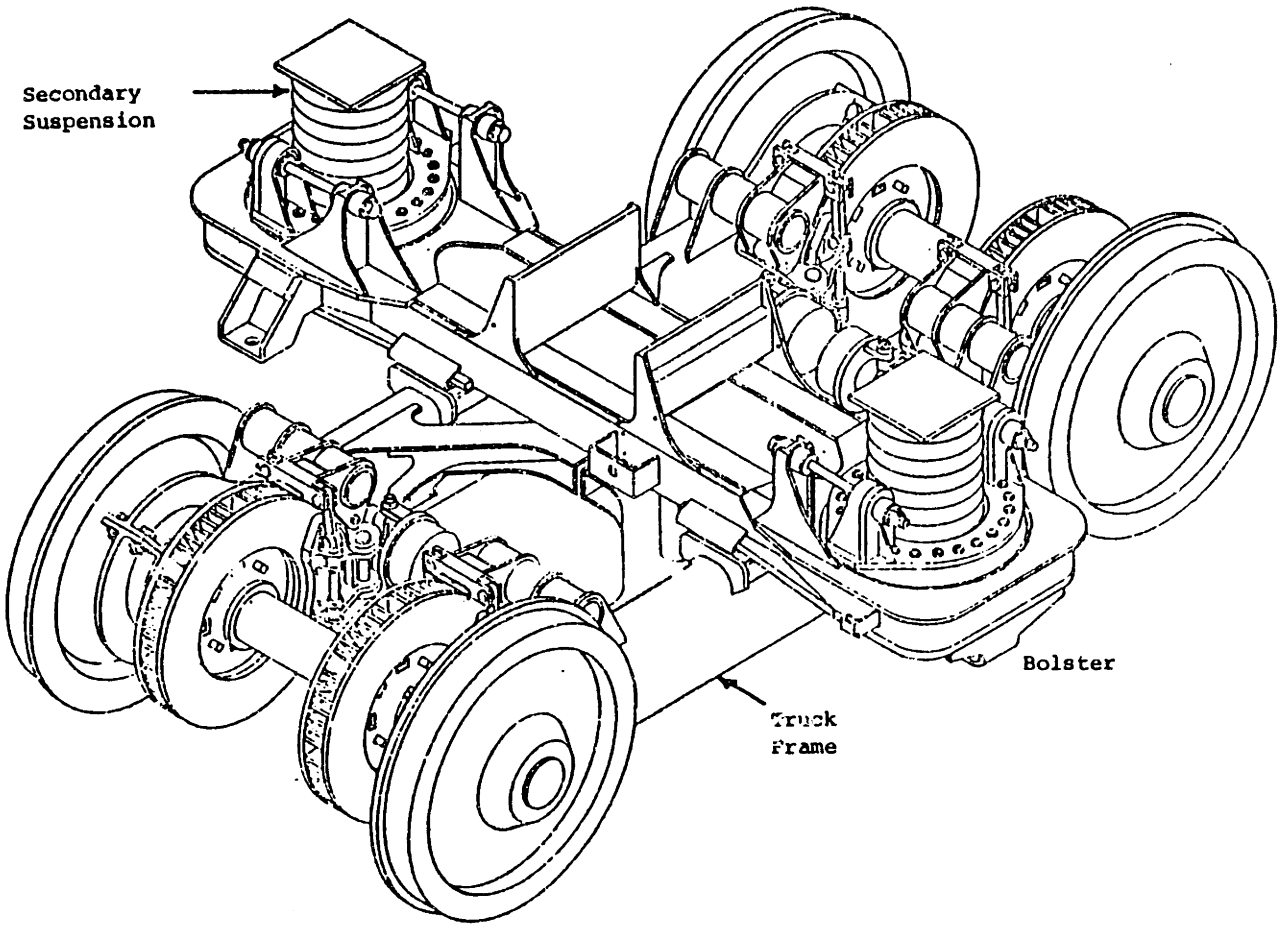

Figure 2.1 Truck Arrangement [18]

of the distance along the track. In addition, the rails are assumed to have lateral flexibility.

A model of the wheelset is developed that accounts for nonlinear wheel/rail profile geometry and friction force saturation. The profile geometry is a principal parameter influencing the performance of the vehicle. Some profiles have smooth geometries and are characterized by a single "point" of wheel/rail contact. Other profiles have sharper geometries and encounter multiple points of contact. For profiles with steep flanges including many U.S. profiles, two points of contact can occur simultaneously at the flanging wheel.

The nonlinear wheelset model is incorporated into a vehicle model. The vehicle model includes nonlinear suspension components and a generic truck model that can represent conventional as well as advanced design suspension configurations.

The performance of the rail vehicle model is investigated by analytical and computational tools. To predict dynamic behavior during negotiation of curved track, a dynamic curving analysis has been developed. In this analysis, the coupled, nonlinear, differential equations of motion are solved numerically using a fourth order Runge-Kutta integration scheme. A specialized analysis has been developed to predict steady-state curving behavior. The steady-state equilibrium conditions represent a set of coupled, nonlinear, algebraic equations of motion which are solved using a combined steepest descent and Newton-Raphson method. A stability analysis has been developed to determine

the linear critical speed. The eigenvalues of a linearized model are calculated and the lowest forward speed associated with zero damping represents the critical speed.

Baseline rail and vehicle parameters are used in the performance studies. The vehicle parameters have been selected to represent typical conventional and advanced-design urban transit vehicles. Two wheel profiles have been identified to represent profiles characterized by single-point and two-point wheel/rail contact.

The analytical methods developed in this chapter are used to investigate the curving performance and stability of rail transit vehicles. Vehicles with conventional and advanced suspension designs are studied. A primary motivation for considering innovative designs is the potential for improved curving performance by reducing wheel/rail wear and forces. In general, improved curving performance is achieved at the expense of decreased stability. The relationship between rail vehicle curving perforamance and stability is addressed in subsequent chapters.

2.2 Performance Critieria

The curve negotiation and stability capabilities of a rail vehicle are measured in terms of performance criteria or indices. This section presents different available criteria which are used to characterize vehicle performance.

2.2.1 Curve Negotiation

Several criteria have been developed to represent the curving performance of a rail vehicle. During curve negotiation, different performance objectives can be identified, including perfect steering, prevention of derailment, minimum wheel/rail forces, and minimum wheel/rail wear.

Perfect steering, or optimal curve negotiation, occurs if each wheelset in a vehicle adopts a radial position and displaces laterally so that it rolls without slip around the curve. As such, the wheelset angle of attack or radial misalignment and the wheelset lateral excursion are natural performance indices. The wheelset angle of attack is the yaw angle of the wheelset measured with respect to radial alignment. The lateral excursion is usually measured from the track centerline. In this thesis, ψ_w represents the wheelset angle of attack and y_w denotes the wheelset lateral excursion with respect to the track centerline. These displacements are defined in Figure 2.2. An undesirable situation exists when these indices become large in magnitude.

The derailing tendencies of a vehicle are associated with the ratio of lateral flange force to vertical wheel load. When this ratio exceeds a critical value, a situation conducive to a flange-climbing type derailment occurs [30, 31].

Much of the wear suffered by the wheel profile and rail head occurs during curve negotiation. Several indices have been proposed

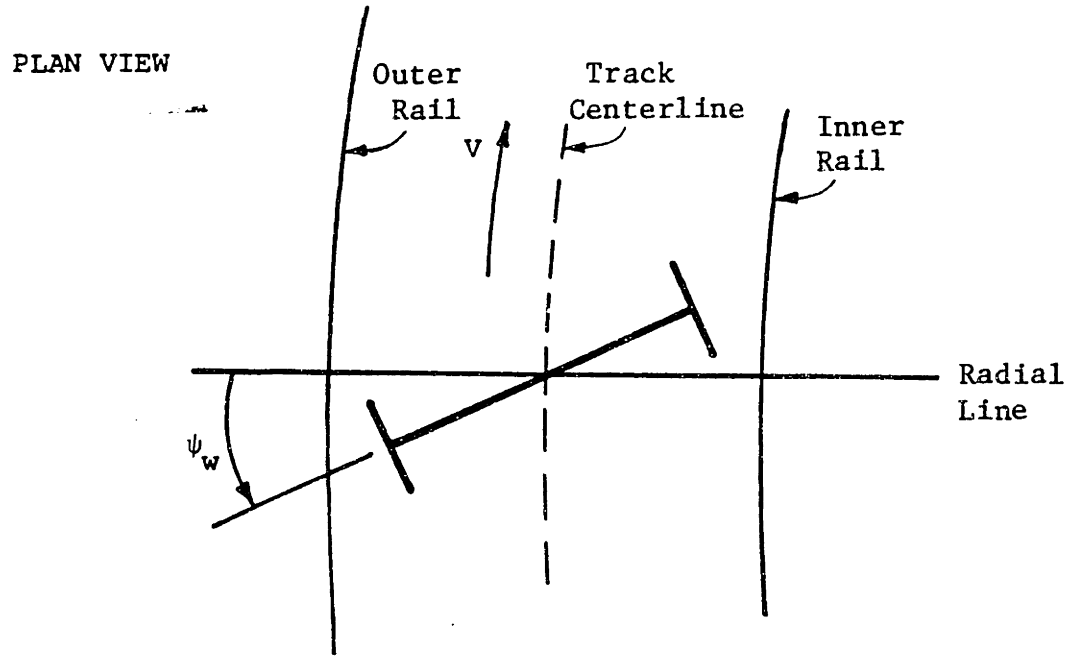

a) Angle of Attack

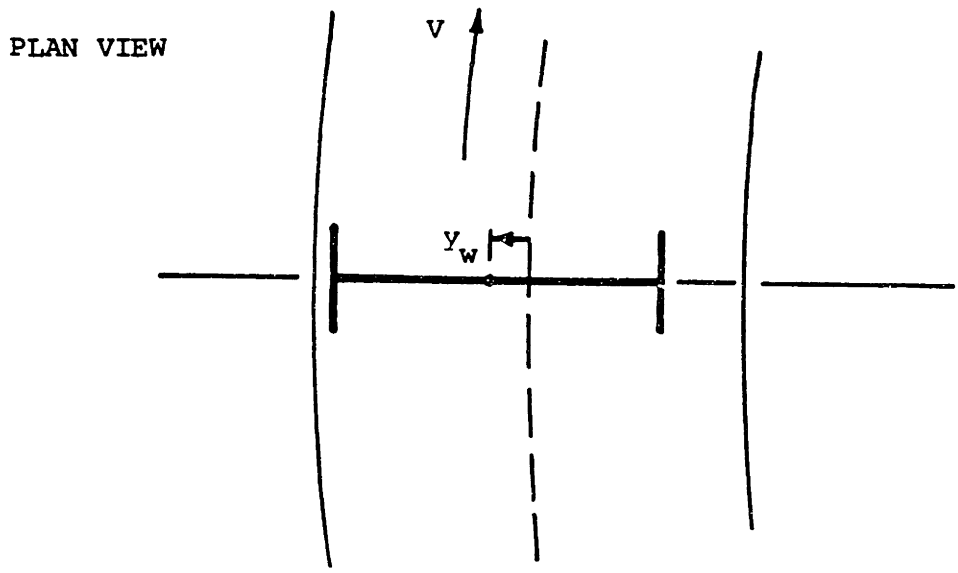

b) Lateral Wheelset Excursion

Figure 2.2 Definition of Angle of Attack and Lateral Wheelset Excursion

to predict wear rates at the wheel/rail interface. Due to the complex nature of wear, these indices are intended to indicate relative levels of wear, rather than to accurately predict actual wear rates. A list of proposed wear indices appears in Table 2.1. The wheelset angle of attack, ψ_w, the creepages (or normalized rates of slippage), ξ_i, and the lateral flange force (for a flanging wheel), F_f, are related to the the wear rate [10, 11]. Larger ψ_w, ξ_i, and/or F_f result in more wear at the wheel/rail interface.

Heumann proposed using the product of flange force and angle of attack, $F_f\psi_w$, as a wear index [19]. This flange wear index, as well as Marcotte's two-point contact flange wear index [19], are related to the energy dissipated at the wheel flange and rail. As a measure of the wear between the wheel tread and the top of the rail head, Doyle introduced a tread wear index, defined as the product of the vertical wheel load and the resultant total creepage, $V_i\xi_R$ [32].

A wear index which more completely represents the work expended at the wheel/rail contact interface has been recommended by British Rail [29]. Their index is the contact patch work, W, defined as the dot product of the resultant creep force and creepage vectors. When summed over all contact patches, this index represents the additional work per unit distance along the track required for the vehicle to negotiate the curve. This index has units of work per distance, or force.

Energy consumption is an important curving performance index,

TABLE 2.1 PROPOSED WEAR INDICES*

WEAR INDEX		UNITS	SOURCE
ψ_w	Angle of Attack	(rad)	[10, 11]
ξ_i	Creepage	(-)	
F_f	Flange Force	(lb)	
$F_f\psi_w$	Flange Wear Index	(lb)	[19]
$\mu_f F_f \sqrt{(\Delta z/r_{LT})^2+(\psi_w \tan\delta_{LF})^2}$	Two-point Flange Wear Index	(lb)	[19]
$V_i\xi_R$	Tread Wear Index	(lb)	[32]
$W=\bar{F}_c \cdot \bar{\xi}$	Contact Patch Work	(ft-lb/ft)	[29]
$W' = \frac{W}{\pi a_e b_e}$	Contact Patch Work/Area	(lb/ft^2)	[33]
$P = VW$	Contact Patch Power	(ft-lb/sec)	

*Variables in Table 2.1 are defined in the nomenclature.

and is related to wheel/rail wear. A useful energy index is the product of vehicle speed and contact patch work, VW, which represents the power dissipated due to friction.

No comprehensive verification of the proposed wear indices has been conducted. Limited tests by British Rail [33] and I.I.T. [34] has shown potentially useful trends, including a positive relation between contact patch work (W) and experimentally-induced wear. Dry wear laboratory tests by British Rail [29] have suggested that the wear rate can be expressed in terms of creep force, creepage, and Hertzian contact area. Wide-scale experimental validation of wear models need to be undertaken to identify indices related directly to wear.

In this thesis, the contact patch work, W, has been selected as the principal index of curving performance. The contact patch work is a comprehensive measure of the work expended (i.e., energy dissipated) due to friction at the wheel/rail interface. The work index includes the effect of wheel/rail creepage and, in particular, wheelset angle of attack. In addition, preliminary experimental evidence suggests that the work index is positively correlated with wheel/rail wear rates [35].

Experience shows that the flanging wheel is responsible for the majority of wheel and track wear [36]. For a vehicle negotiating a curve, flanging usually occurs at the leading outer wheel. Significant wear occurs on the wheel flange and on the gage face of

the outer rail. Therefore, the principal curving performance index used in this thesis is the contact work at the flanging wheel.

2.2.2 Lateral Stability

A useful index of vehicle stability is the critical speed. At the critical speed, the vehicle exhibits sustained oscillatory behavior called hunting, involving coupled lateral and yaw motions of the wheelsets, truck frames, and carbody. In general, the wheelset oscillations tend to diverge until they are limited by the wheel flanges. The wheelsets slam back and forth between the rails resulting in large dynamic wheel/rail forces which potentially may damage the wheels and track and lead to derailment. To avoid this behavior, a vehicle should be designed to achieve a critical speed significantly greater than the operating speed.

In this thesis, the linear critical speed is selected as the stability performance index. The linear critical speed is the lowest forward speed associated with zero damping, determined by computing the eigenvalues of a linearized model as a function of vehicle speed. The linear stability analysis is discussed in Section 2.7.3.

2.3 Track Model

The track is characterized by its curvature, superelevation, and irregularities. The track curvature is defined as 1/R, where R is the curve radius. It is often expressed in terms of degree curve, D, corresponding to the degrees of arc subtended by a 100 ft

chord at the track centerline. Mathematically,

$$D = \frac{360}{\pi} \sin^{-1} \left(\frac{50}{R}\right) \tag{2-1}$$

with R in ft. The track superelevation or bank angle, ϕ_{SE}, is the angle between the track and the horizon. It is usually expressed in degrees. Degree curve and superelevation are shown in Figure 2.3.

It is convenient to combine the track curvature, the superelevation angle, and the vehicle forward speed, V, into a parameter of net lateral unbalance called the cant deficiency, ϕ_d. Cant deficiency is defined by

$$\phi_d = \frac{V^2}{Rg} - \phi_{SE} \tag{2-2}$$

and represents an angular measure of lateral unbalance between centrifugal and gravitational forces. When $\phi_d = 0$, a condition of "balanced running" is achieved for which the components of centrifugal force and weight parallel to the rail plane cancel each other. For comfort and safety, the cant deficiency is limited in the U.S. to 6° of inboard unbalance and 3° of outboard unbalance [18].

The superelevation angle and cant deficiency are often expressed in terms of equivalent inches of elevation of the outer rail. Because the standard rail gage is approximately 2a = 57 in, the numerical value of superelevation or cant deficiency expressed in inches

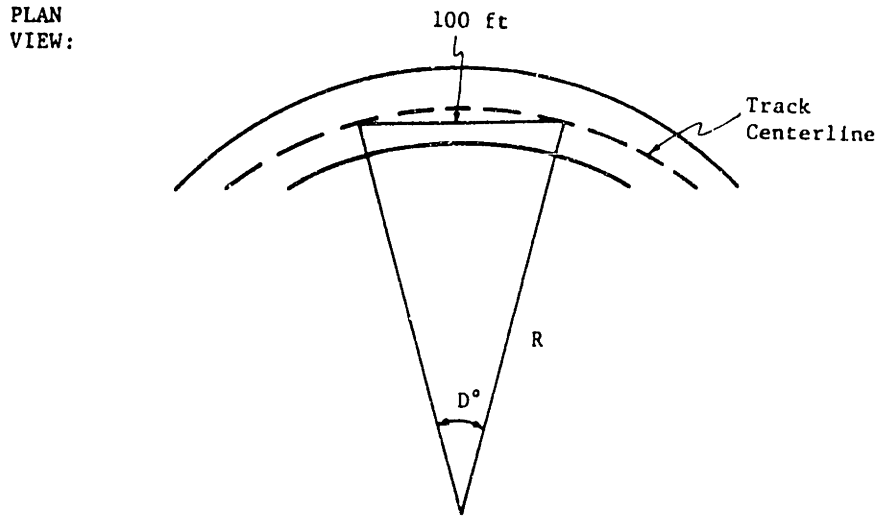

(a) Degree Curve, D

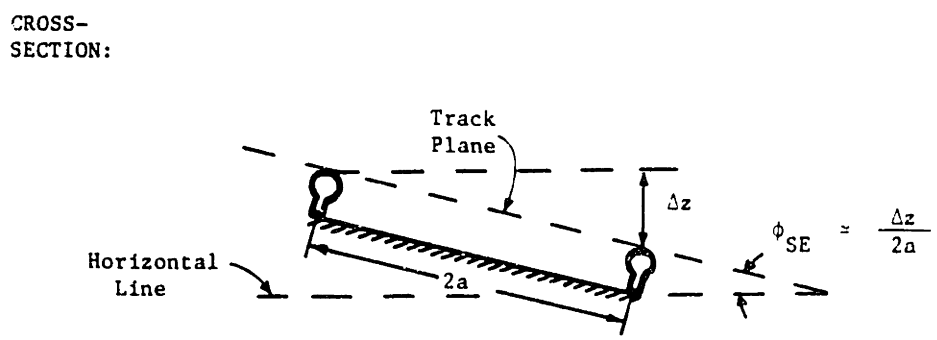

(b) Superelevation Angle, ϕ_{SE}

Figure 2.3 Definition of (a) Degree Curve and (b) Superelevation Angle

is very close to that of the corresponding angle expressed in degrees.

Track irregularities are due to a combination of installation error and gradual degradation. In the literature, four types of irregularities are defined: gage, cross-level, alignment, and vertical. Gage is the horizontal distance between two rails; cross-level is the difference between the elevations of the rails, alignment is the average of two rail lateral positions; and, vertical is the average of the two rail elevations.

In this thesis, track irregularities are neglected and the track is assumed to be smooth. Implementation of cross-level and alignment irregularities is possible by the addition of a random disturbance to the superelevation angle and the rail lateral excursion, respectively.

In general, the track consists of sections of tangent (or straight), transition spiral, and constant radius curve track. The different track sections are shown in Figure 2.4. Transition spiral track couples tangent and constant radius curve track. Depending on the direction of vehicle travel, transition track represents curve entry or curve exit sections.

In this thesis, a simple model of track curve geometry is adopted [37]. In tangent track, the track curvature and superelevation angle are zero. In constant radius curve track, the curvature and superelevation angle are constants (and maximum). In transition spiral sections, the track curvature and superelevation

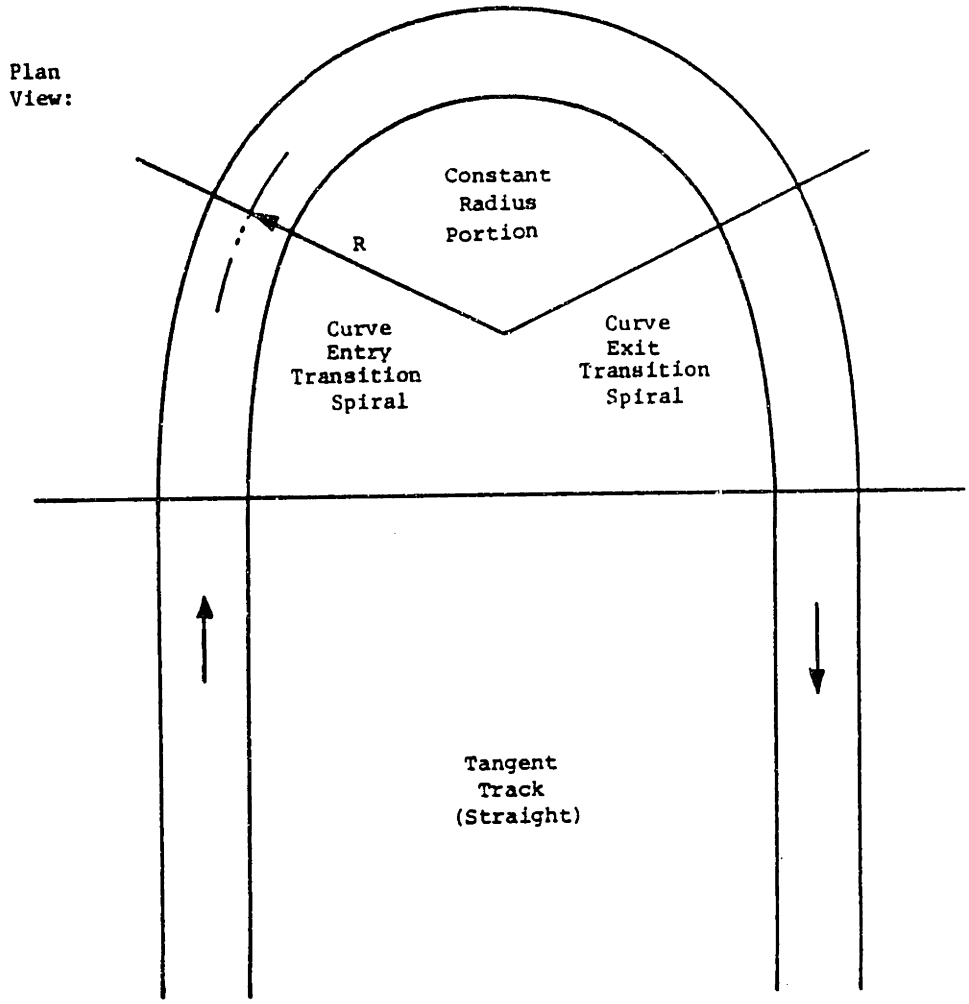

Figure 2.4 Curved Track Definitions

angle vary quadratically, as shown in Figure 2.5. The track curvature and superelevation angle of a spiral section are approximated by second order polynomial functions fitted between tangent and constant radius curve track sections.

2.3.1 Flexible Rail Model

A simple model of track flexibility is adopted in which each rail is assumed to have lateral freedom only. In this model, rail rollover or overturning motion is neglected.* The mass-spring-damper model of the rail is shown in Figure 2.6. The rail is assumed to have effective lateral mass, viscous damping, and linear stiffness, m_r, c_r, and k_r, respectively. The rail lateral displacement, y_{rail}, is related to the net lateral wheel force by the rail equation of motion presented in Appendix A.

Typical values of effective lateral stiffness are 1.0×10^5 lb/ft for soft rail and 1.0×10^7 lb/ft for stiff rail [38]. A representative value of effective lateral damping is 1.0×10^4 lb-sec/ft. In the curving performance studies, the effect of lateral mass, m_r, is neglected.

2.4 Wheelset Model

The wheelset represents the basic element of the rail vehicle steering and support system. Each wheelset consists of two steel wheels rigidly mounted to a solid axle. A typical wheelset cross-

*If rail rollover occurs, the wheel/rail profile data which assumes fixed gage must be modified. The implications of gage changes due to rail flexibility are discussed in Section 2.4.2.

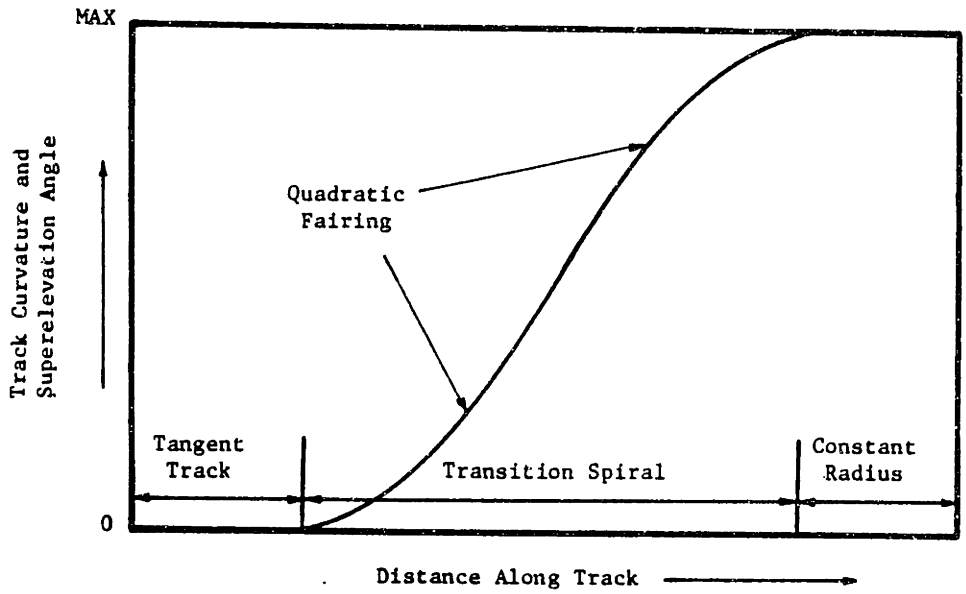

Figure 2.5 Track Curvature and Superelevation as a Function of Distance

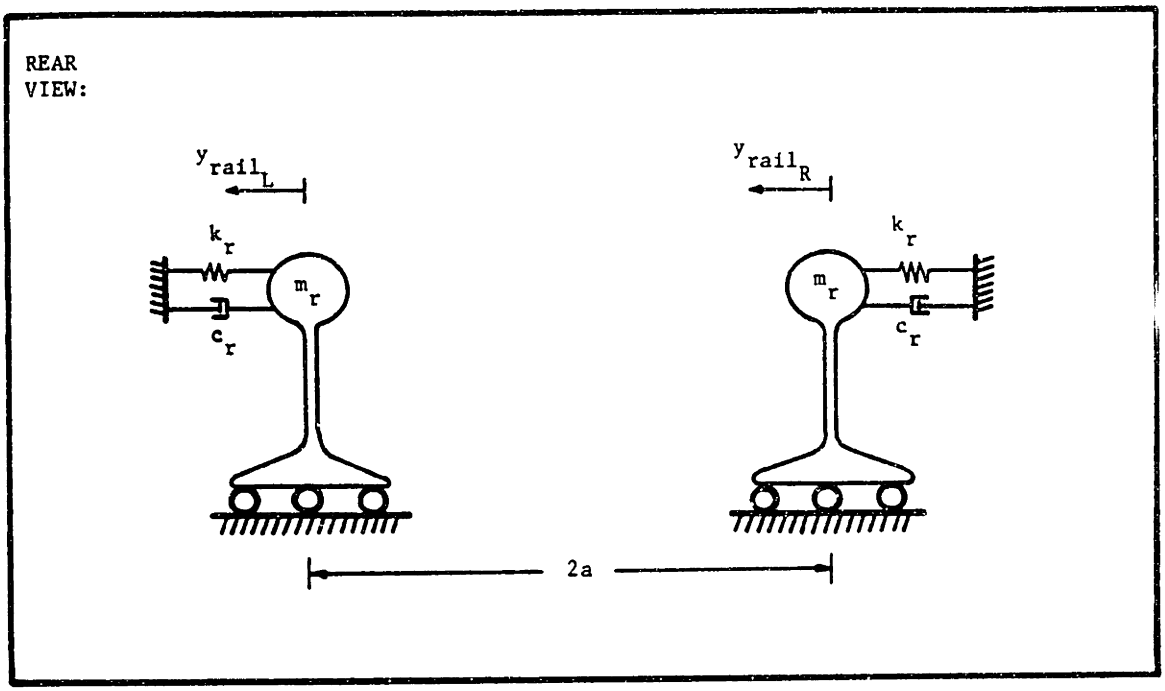

Figure 2.6 Lateral Track Model

section is shown in Figure 2.7. Each wheel profile has a steep taper section at the inner edge known as the flange and a shallow taper (or sometimes cylindrical) section from the flange to the outer edge known as the tread. A variety of wheel profile shapes are used by the transit industry. Two representative profiles are discussed in Section 2.3.2.

The contact and friction mechanisms which develop at the wheel/rail interfaces have a dominant effect on vehicle curving behavior. Modelling the wheel/rail contact forces is a difficult problem since the wheelsets of a vehicle generally roll with slip. A nonlinear model of the wheel/rail contact forces is adopted in this thesis and is described in Section 2.4.3.

A model has been developed to characterize wheelset dynamic curving behavior. The model accounts for nonlinear wheel/rail profile geometry and contact forces, and represents single-point and two-point contact at the flanging wheel. The following three sections discuss wheelset and track coordinate systems, wheel/rail geometric constraints, and wheel/rail contact forces. The development of the dynamic curving equations of motion of the wheelset model are presented in Appendix A.

2.4.1 Coordinate Systems

A free wheelset negotiating smooth, curved track is exposed to track curvature and inertial force inputs, including cant deficiency. The track curvature and cant deficiency are defined in Section 2.3 The

REAR VIEW:

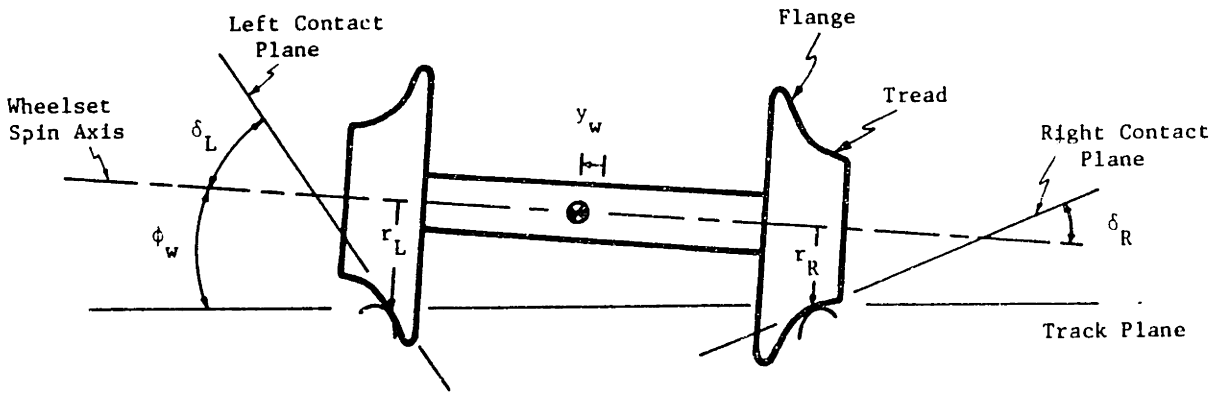

Figure 2.7 Typical Wheelset Cross-Section

inertial force inputs are due to dynamic effects, and are discussed in detail in Appendix A.

Assuming continuous wheel/rail contact, a wheelset negotiating curved track at constant speed is described by 5 states: lateral displacement, y_W, and velocity, $\dot{y}_W$; yaw angle, ψ_W, and rate, $\dot{\psi}_W$; and spin speed, $\dot{\theta}_W$. The convention for positive y_W and ψ_W displacements is shown in Figure 2.2. For a wheelset traversing right-handed curved track, positive lateral displacements, y_W, are associated with excursions toward the left rail (i.e., the outer or high rail). Thus, as the wheelset displaces laterally in the positive sense, flange contact occurs at the left wheel. In general, the spin speed, $\dot{\theta}_W$, differs from the pure rolling angular speed due to slippage (i.e., creepage) at the wheels. For steady-state curving, the wheelset is described by two independent states: y_W and ψ_W. The lateral velocity and yaw angle rate vanish due to steady-state conditions. The spin speed, $\dot{\theta}_W$, still can differ from the pure rolling spin speed but is a known constant since the slippage is a function of y_W and ψ_W.

Wheelset (W) and track (T) coordinate systems are introduced in Figure 2.8. The relation between the wheelset and track coordinate systems is

$$\begin{Bmatrix} x_W \\ y_W \\ z_W \end{Bmatrix} = \begin{bmatrix} 1 & \psi_W & 0 \\ -\psi_W & 1 & \phi_W \\ 0 & -\phi_W & 1 \end{bmatrix} \begin{Bmatrix} x_T \\ y_T \\ z_T \end{Bmatrix} \qquad (2\text{-}3)$$

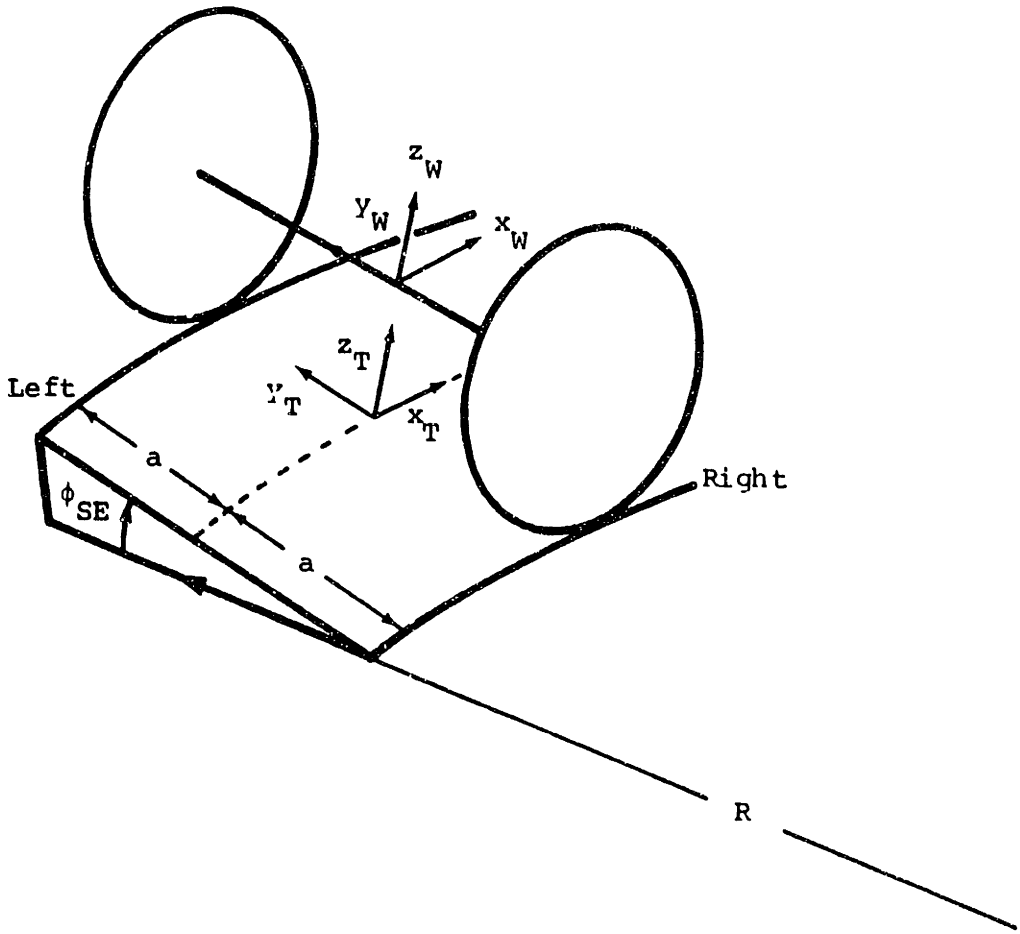

Figure 2.8 Track and Wheelset Coordinate Systems

where small yaw (ψ_W) and roll (ϕ_W) angles are assumed and pitch (θ_W) is neglected. Coordinate system transformation relations are derived in Appendix A (Section A.2).

2.4.2 Wheel/Rail Geometric Constraints

The following wheel/rail contact geometry parameters are defined:

δ_L, δ_R left, right contact angle; i.e., angle of contact patch plane with respect to wheelset spin axis

r_L, r_R left, right rolling radius, i.e., radial distance from wheelset spin axis to contact "point"

ϕ_W wheelset roll angle relative to track plane.

The contact angles, rolling radii, and wheelset roll angle are shown in Figure 2.7 for a wheelset in single-point contact at the left and right wheels.

For a wheelset which never loses contact with the rails, the rolling radii, contact angles, and wheelset roll angle are functions of the net wheelset-rail lateral excursion for a given wheel/rail profile. These functions are shown in Figures 2.9a, 2.10a, and 2.11a for a Heumann wheel on worn rail profile and in Figures 2.9b, 2.10b, and 2.11b for a new AAR 1 in 20 wheel on worn rail [39]. The data for both profiles assume standard gage rails. In this thesis, the new AAR wheel profile is referred to as "new wheel". For the new wheel profile, the flange clearance is 0.32 in. The flange clearance is the wheelset excursion which distinguishes between tread and flange contact. When the wheelset excursion relative to the rail is less than the flange clearance, tread contact occurs. When the net

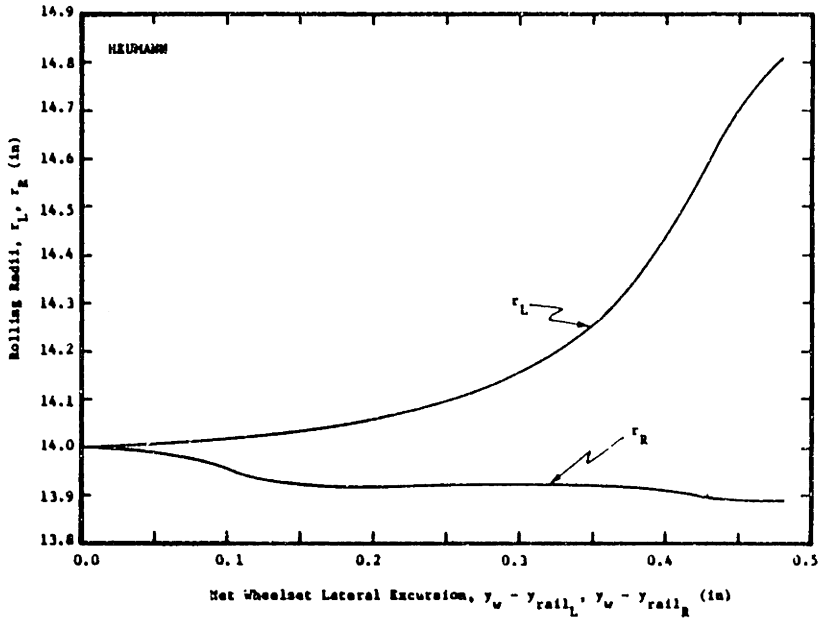

(a)

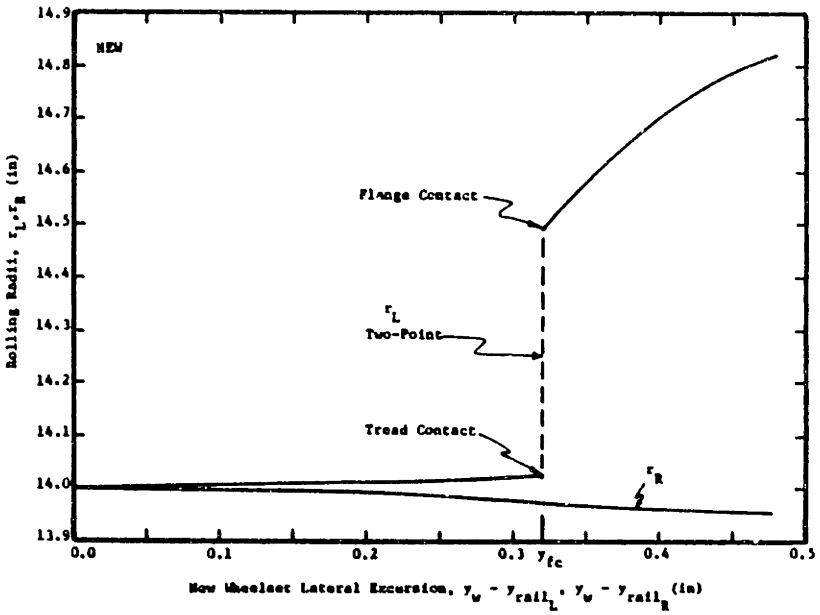

(b)

Figure 2.9 Rolling Radii vs. Net Wheelset Lateral Excursion for (a) Heumann Wheel and (b) New Wheel on Worn Rails

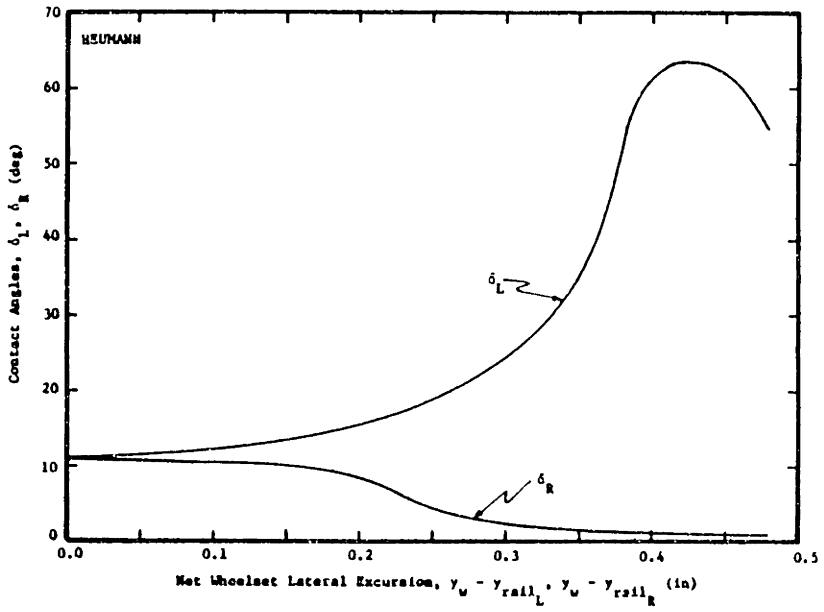

(a)

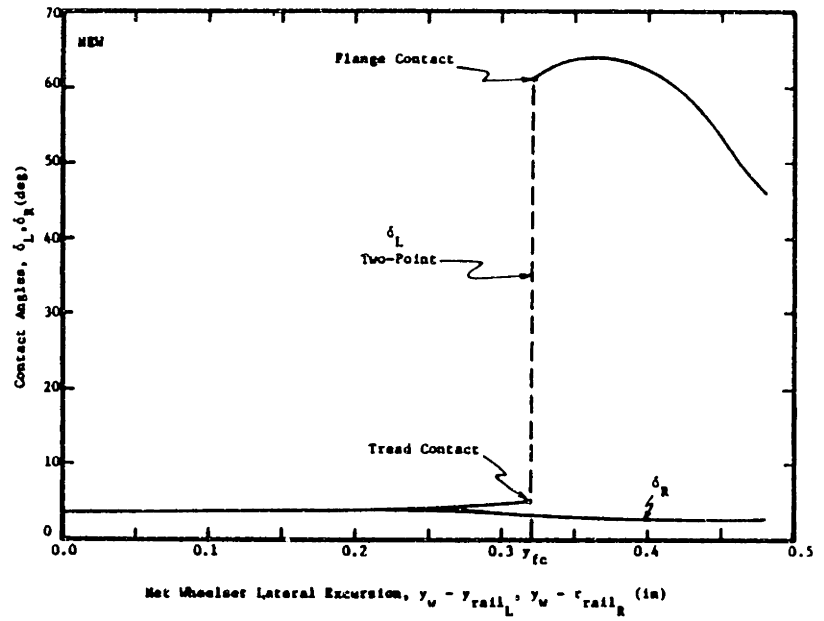

(b)

Figure 2.10 Contact Angles vs. Net Wheelset Lateral Excursion for (a) Heumann Wheel and (b) New Wheel on Worn Rails

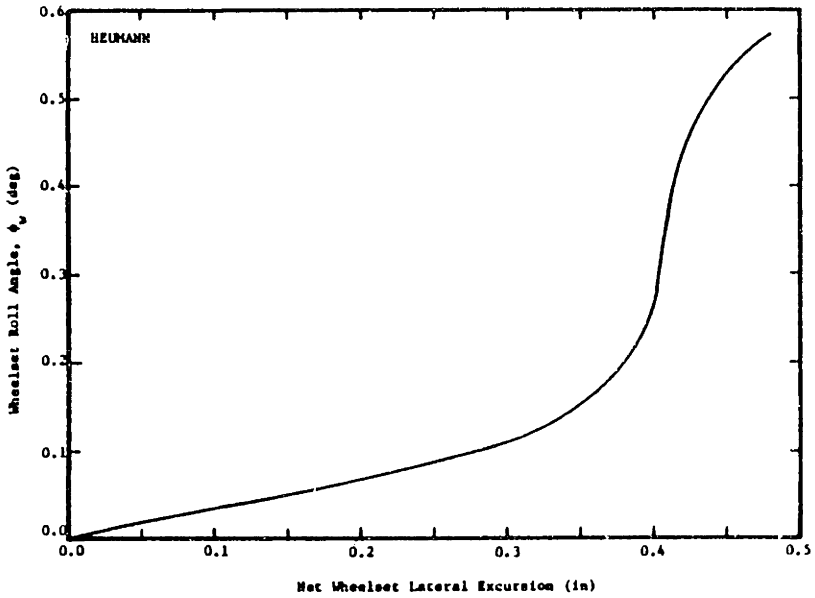

(a)

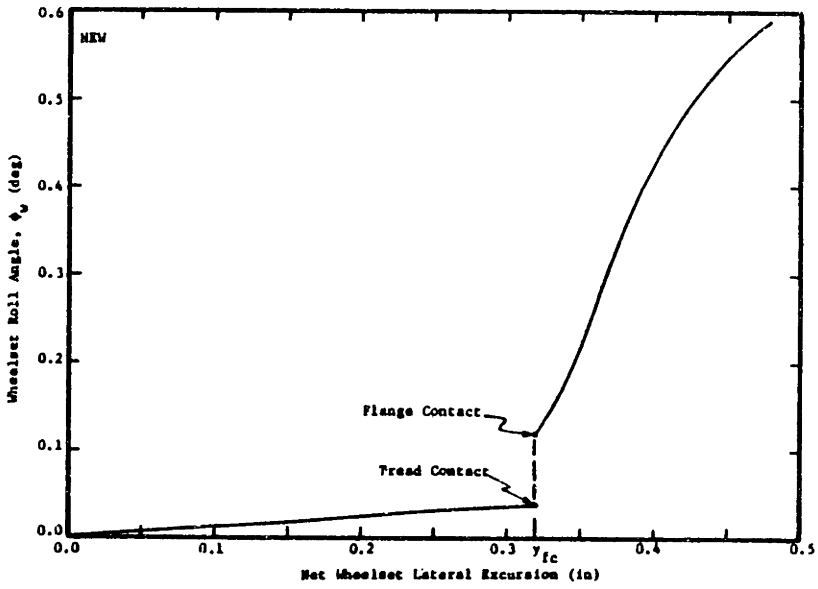

(b)

Figure 2.11 Wheelset Roll Angle vs. Net Wheelset Lateral Excursion for (a) Heumann and (b) New Wheel on Worn Rails

wheelset excursion equals or exceeds the flange clearance, flanging occurs. From Figure 2.10, the contact angle approaches 65° for severe flanging.

The rolling radii, contact angles, and roll angle are wheel/rail geometric constraint variables since they are functions of the net wheelset rail lateral displacement. These variables indicate the nature of wheel/rail contact as the wheelset displaces laterally. If the rolling radii and contact angles are single-valued functions of the lateral excursion, single-point contact occurs at both wheels for all displacements. Continuous single-point contact occurs for the Heumann wheel profile. As the wheelset displaces laterally, the outer wheel shifts smoothly from tread to flange contact, while the inner wheel maintains tread contact. For other profiles with steep flanges, such as the new wheel profile, the outer wheel rolling radius and contact angle functions have discontinuous jumps at net lateral excursions equal to the flange clearance. The discontinuous jumps indicate that multiple points of contact can develop at the flanging wheel. As before, single-point tread contact occurs at both the inner and outer wheels for a net wheelset excursion less than the flange clearance. Two-point contact occurs at the flanging wheel and single-point contact occurs at the inner wheel for a wheelset excursion (relative to the flanging wheel rail) equal to the flange clearance. Single-point flange contact occurs at the flanging wheel for net excursions greater than the flange clearance.

For a wheelset negotiating right-handed curved track, the left wheel represents the outer or flanging wheel. Figure 2.12 shows the contact condition at the left wheel as the wheelset displaces laterally. Single-point tread contact (Figure 2.12a) and single-point flange contact (Figure 2.12c) occur for net excursions less than and greater than the flange clearance, respectively. Two-point contact occurs for a wheelset excursion (with respect to the left rail) equal to the flange clearance. Two-point contact is depicted in Figure 2.12b where the rail head is shown to contact simultaneously both the tread and flange of the left wheel.

For a wheelset in two-point contact,* the displacement relative to the left rail is fixed at the flange clearance. Mathematically,

$$y_W - y_{rail_L} = y_{fc} \tag{2-4}$$

where y_W and y_{rail_L} are the lateral displacements of the wheelset and left rail, respectively, and y_{fc} is the flange clearance. Equation (2-4) represents a constraint relation between the wheelset and left rail lateral excursions for two-point contact. The constraint relation determines the contact geometry of the tread and flange contact points at the left wheel.

The contact geometry (rolling radius, contact angle) at each wheel is specified by the net lateral excursion according to the

*The terminology assumes that the two points of contact occur at the flanging wheel. "A wheelset in two-point contact" actually has three points of wheel/rail contact, two at the flanging or outer wheel and one at the inner wheel.

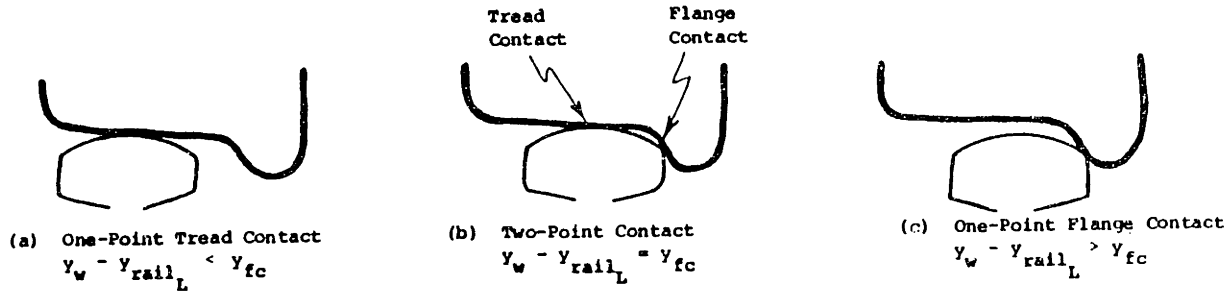

Figure 2.12 Left Wheel/Rail Contact

geometric constraint functions shown in Figures 2.9 and 2.10. These profile functions apply for a fixed standard rail gage. Due to rail flexibility, the actual gage is not constant. The gage, g', is given by

$$g' = 2a + y_{rail_L} - y_{rail_R} \qquad (2\text{-}5)$$

and differs only slightly from 2a. Since gage changes occur, use of the fixed-gage wheel/rail profile data represents an approximation. In this work, it is assumed that (1) the flanging wheel contact geometry is correct, and (2) the nonflanging wheel contact geometry is in error but the error is small since the tread contact geometry is relatively constant.

In addition to rail flexibility, rail rollover alters the wheel/rail profile data. The effect of rail rollover, which changes the rail cant angle, is not addressed in this thesis and represents future work.

In summary, some wheel/rail profiles, notably many European profiles including the Heumann wheel profile of Figures 2.9a, 2.10a and 2.11a, achieve single-point contact at all realistic displacements. Many new wheel profiles, including the standard AAR 1 in 20 profile used commonly in the U.S. and shown in Figures 2.9b, 2.10b, and 2.11b, contact the rails at multiple points during normal use.

2.4.3 Wheel/Rail Contact Forces

For a wheelset negotiating a curve, slip or creepage may develop

at the rails. Normal loads acting on the slipping wheelset result in the generation of friction-type forces known as creep forces. In general, the wheel/rail contact forces are separated into normal forces acting perpendicular to the contact plane and creep forces acting in the plane.

Each point of wheel/rail contact is actually a "patch" of finite area. At each patch, a state between pure-roll and pure-slip exists. During the last ten years there has been a significant improvement in the understanding of the friction mechanism which develops at the contact patch. Kalker [40] has developed linear, simplified nonlinear, and exact nonlinear theories and computational programs to predict contact patch creep forces. In this thesis, a heuristic nonlinear creep force model is used which is computationally fast and reasonably accurate. This model predicts a resultant creep force which agrees with Linear Kalker Theory for small creepages and which saturates at the adhesion limit for larger creepages, as shown in Figure 2.13. In Appendix A, the creep force model is described in detail and expressions for the creepages are derived.

2.5 Truck Model

Rail passenger vehicles incorporate two wheelsets into an undercarriage called the truck or truck frame (or bogie in European usage). This section describes models of conventional and innovative truck configurations. All of the physical configurations discussed in Section 2.5.1 through 2.5.3 represent special cases of the generic

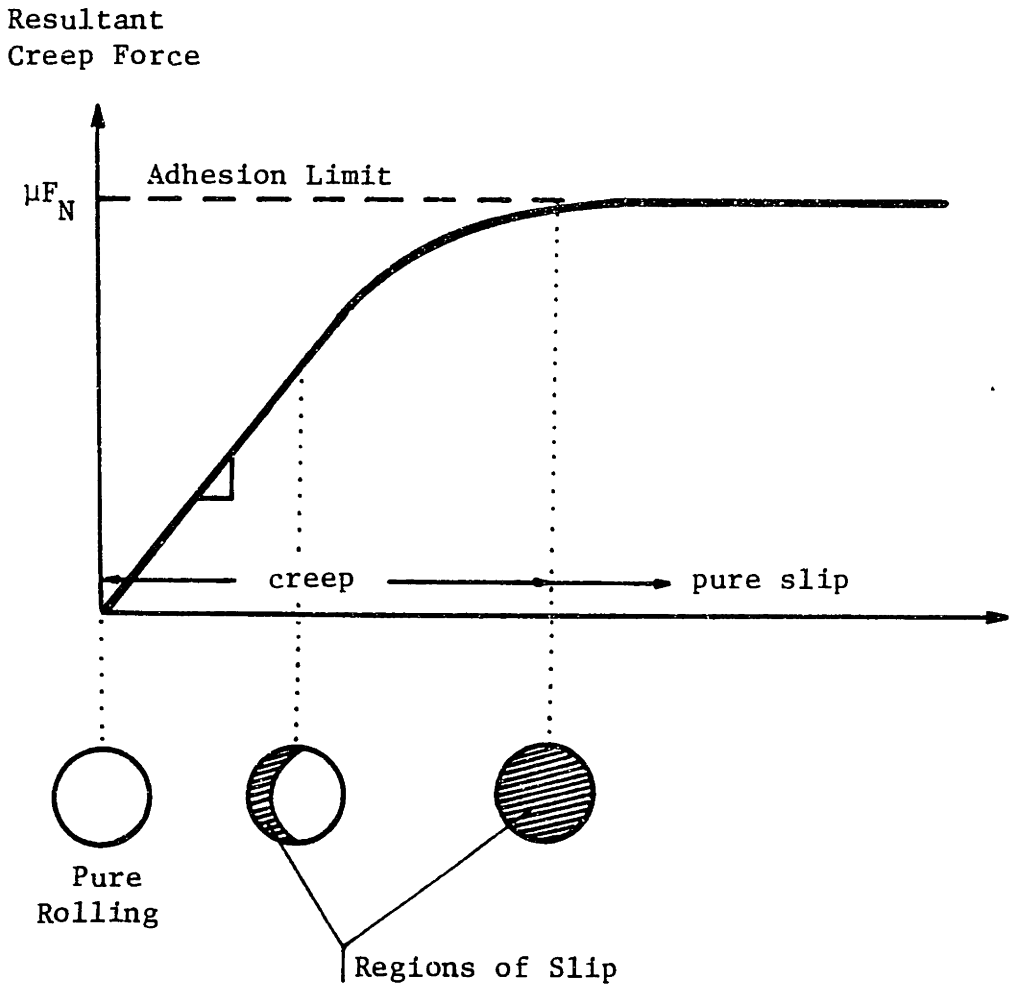

Figure 2.13 Contact Patch Creep Force vs. Creepage Relation

model presented in Section 2.5.4.

2.5.1 Conventional Truck

In a conventional truck, the wheelsets are connected to the truck frame by primary suspension elements. Typically, the primary suspension elements consist of coiled springs, rubber chevrons or rubber bushings between the bearing adapter and the truck frame. A conventional truck is shown schematically in Figure 2.14. The following notation is used: k_{px} is the primary longitudinal stiffness, k_{py} is the primary lateral stiffness, $2d_p$ is the distance between the longitudinal springs, and 2b is the truck wheelbase.

2.5.2 Self-Steered Radial Truck

A self-steered radial truck is a conventional truck with an additional direct connection between the two wheelsets by means of passive springs or structural members in shear and bending. A schematic representation of a self-steered truck is shown in Figure 2.15.

A self-steered truck has two additional stiffness parameters which connect the two wheelsets directly. These are defined as the direct interaxle bending stiffnes, k_{b2}, and the direct interaxle shear stiffness, k_{s2}. The stiffnesses k_{b2} and k_{s2} are sufficient to model any direct elastic connection between the two wheelsets. Most often this connection takes the form of steering arms [41], cross-braces [42], or similar linkages. Figure 2.16 illustrates two physical implementations; a cross-braced truck is shown in Figure 2.16a and a steering arm truck in Figure 2.16b.

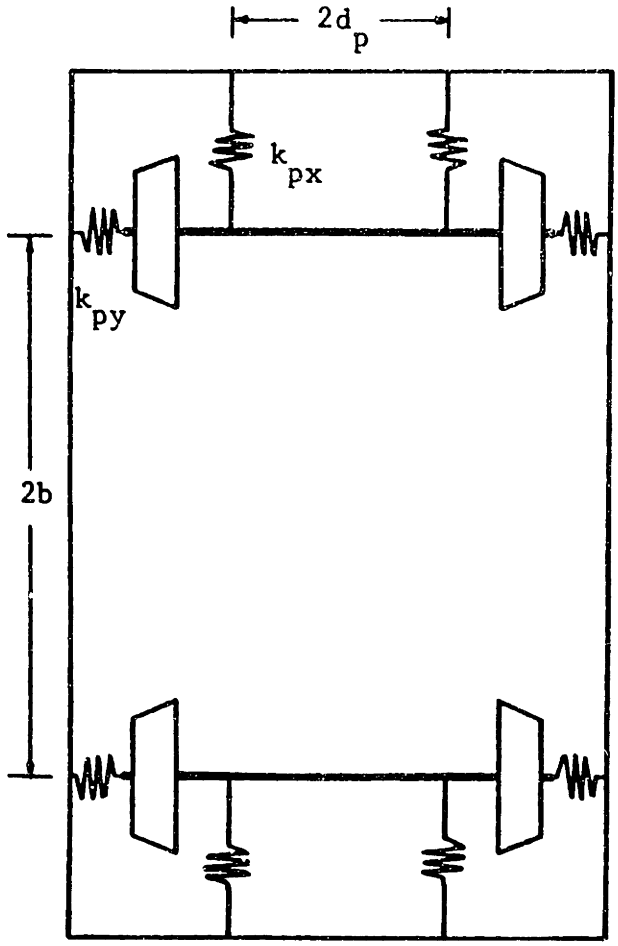

Figure 2.14 Schematic of Conventional Truck

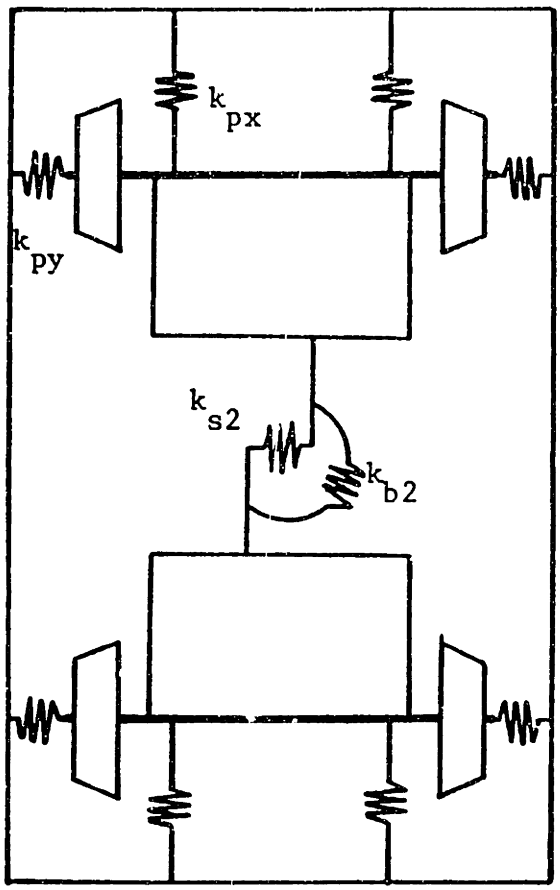

Figure 2.15 Schematic of Self-Steering Radial Truck

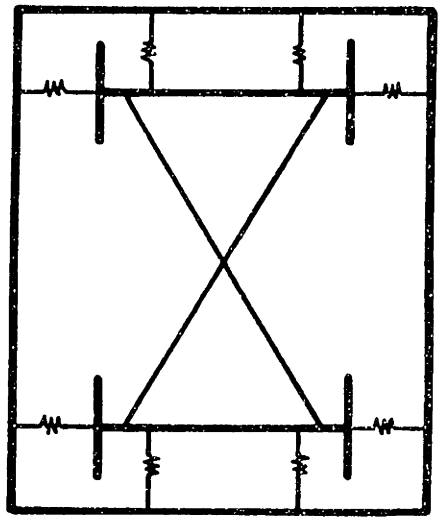

(a)

Cross-Braced

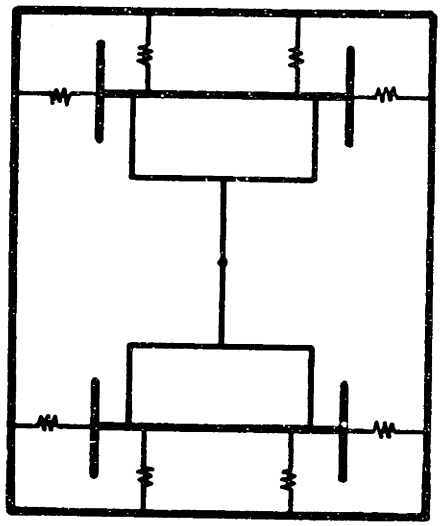

(b)

Steering Arm

Figure 2.16 Alternative Self-Steering Radial Truck Configurations

The term self-steered radial truck describes the steering action produced by direct interwheelset connections when the stiffness k_{b2} is low. With soft k_{b2}, a yaw motion of one wheelset causes the other wheelset to yaw in the opposite direction helping to align the wheelsets radially in a curve. The self-steered radial design has two essential differences from the conventional design. First, forces are transmitted directly between the wheelsets, and second, the total truck shear stiffness is not limited as it is in the conventional design. The first property allows for a more stable design since the truck frame can become dynamically decoupled from hunting wheelsets [13]. The second property helps the truck reduce wheelset angles of attack during curve negotiation after flanging has occurred.

The dynamics of a flexible truck are strongly influenced by the forces transmitted between the wheelsets. For a conventional truck, these interwheelset forces occur due to interaction through the truck frame. For a self-steered radial truck, additional forces occur through the interconnection elements. It is convenient to characterize the total truck stiffness by defining the following two parameters: k_s and k_b, the total truck static shear and bending stiffnesses, respectively. These are defined in Figure 2.17.

Shear Stiffness:

$$k_s = \left. \frac{\text{lateral force on leading wheelset due to lateral displacement of trailing wheelset}}{\text{lateral displacement of trailing wheelset}} \right|_{\Delta\psi = 0}$$

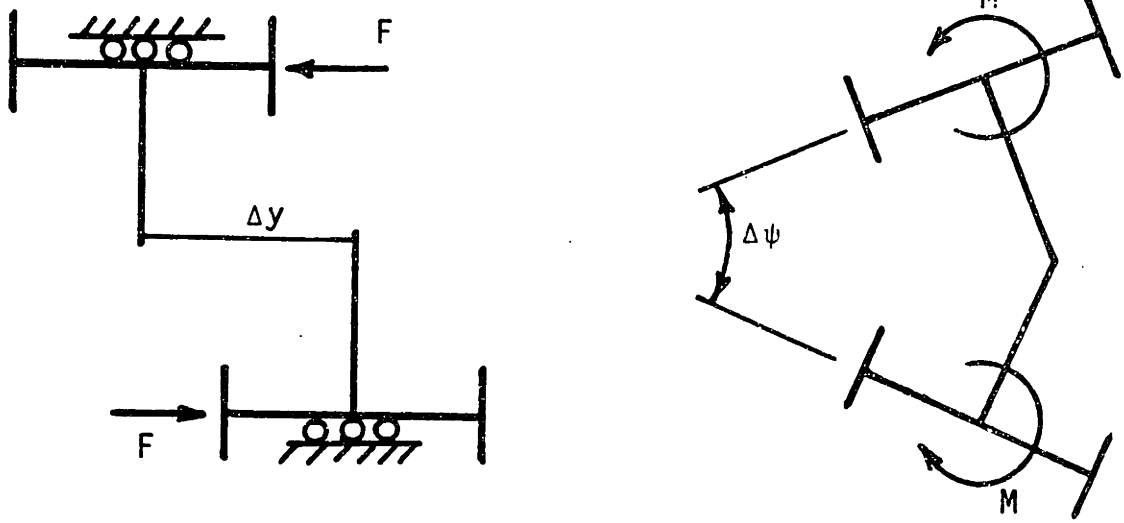

$$k_s = \frac{F}{\Delta y}$$

Shear Stiffness

$$k_b = \frac{M}{\Delta \psi}$$

Bending Stiffness

Figure 2.17 Shear and Bending Stiffness Definitions

Bending Stiffness:

$$k_b = \left.\frac{\text{yaw moment on leading wheelset due to yaw displacement of trailing wheelset}}{\text{yaw displacement of trailing wheelset}}\right|_{\Delta y = 0}$$

These generalized stiffness parameters were suggested by Wickens [43]. For a free truck (not connected to a carbody) with two wheelsets, the expressions for k_b and k_s are:

Conventional Truck:

$$k_b = d_p^2 k_{px} \tag{2-6}$$

$$k_s = \frac{d_p^2 k_{px} k_{py}}{d_p^2 k_{px} + b^2 k_{py}} \tag{2-7}$$

Self-Steering Radial Truck:

$$k_b = d_p^2 k_{px} + k_{b2} \tag{2-8}$$

$$k_s = \frac{d_p^2 k_{px} k_{py}}{d_p^2 k_{px} + b^2 k_{py}} + k_{s2} \tag{2-9}$$

These stiffnesses are useful in identifying the design region of different types of trucks in the k_s - k_b plane. Equations (2-6)

and (2-7) imply that conventional trucks must satisfy the relation $k_s < \frac{k_b}{b^2}$. The limiting value is obtained by setting the primary lateral stiffness to infinity in equation (2-7). Thus, conventional truck designs lie below the line $k_s = \frac{k_b}{b^2}$ on the $k_s - k_b$ plane, shown in Figure 2.18. The self-steered designs can be anywhere in the $k_s - k_b$ plane by virtue of the interaxle bending and shear stiffnesses.

A drawback of the $k_s - k_b$ plane is that a particular design point in the plane can be obtained with different combinations of primary and interaxle stiffnesses. Trucks with identical k_s and k_b do not possess the same curving and stability properties due to differences in the distribution of truck frame mass (for instance, due to steering arms). Changes in the mass distribution influence curving by altering the inertial forces and affect stability by changing the kinematic modes of the truck [13]. Thus, the k_s and k_b designation does not uniquely define the curving and stability characteristics of a truck.

2.5.3 Forced-Steered Radial Truck

A forced-steered truck utilizes linkages between the carbody and the truck frame to force the wheelsets into near radial alignment when traversing curves. The essential motivation is to take advantage of the relative truck/carbody orientation that develops as a vehicle negotiates a curve. In particular, the yaw angle that develops between the carbody and the truck is related to the curve

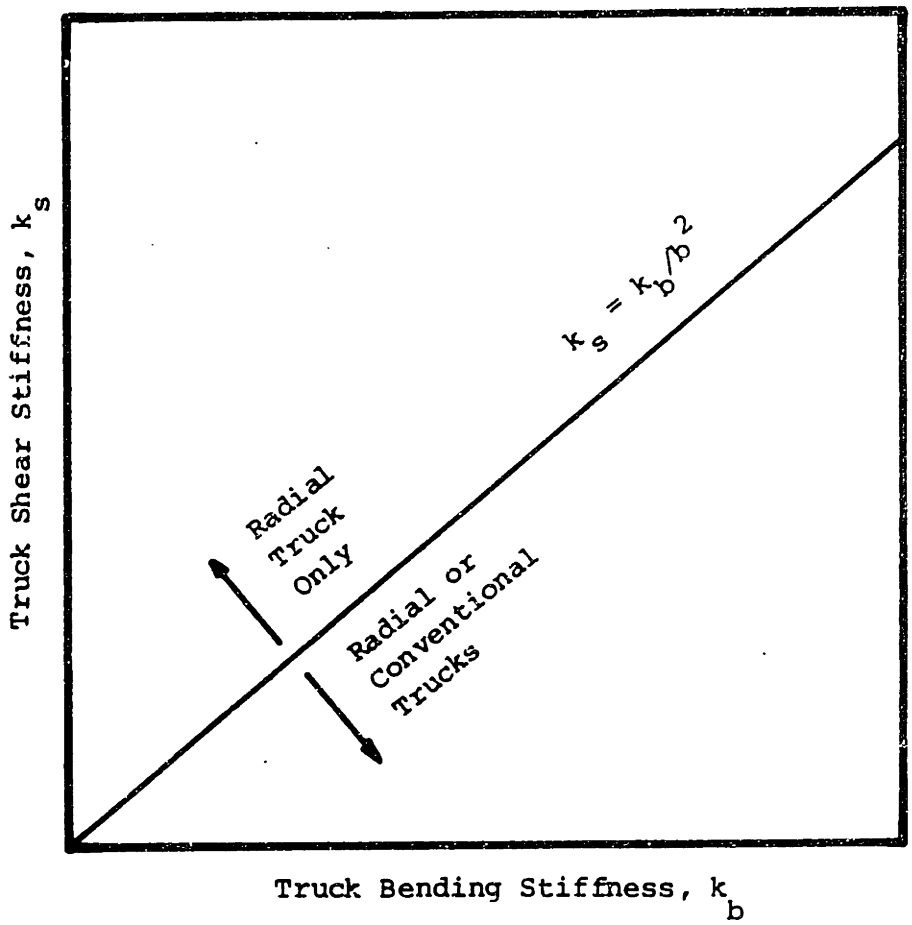

Figure 2.18 Design Region for Conventional and Radial Trucks in the Truck Shear vs. Truck Bending Stiffness Plane.

radius, and linkages between the carbody and the wheelsets can be used to force the wheelsets into a more radial alignment. Similarly, the lateral displacement between the carbody and truck is related to the cant deficiency, and linkages can be designed to produce forces on the wheelsets as a function of the cant deficiency. Thus, a forced-steered radial truck is a self-steered radial truck with additional linkages which impose forces on the wheelsets as a function of the relative yaw and lateral displacements between the carbody and truck.*

Several forced-steered truck configurations have been proposed with different linkage arrangements. The schematics of three configurations that have forced steering action are shown in Figures 2.19, 2.20, and 2.21. In this study they are designated the S, L, and U trucks because configurationally they are similar to the Scales [44], List [41], and UTDC** [45] designs, respectively.

The bending and shear stiffnesses due to forced-steering linkages are equivalent to "effective" truck interaxle bending and shear stiffnesses, respectively. Typically, the L truck has high effective interaxle shear stiffness and the U truck has zero interaxle shear

---

*Typically, the forced-steering linkages are connected to the bolsters, rather than the carbody directly. However, since the bolsters are stiffly connected to the carbody, they essentially execute the same motions. Thus, in this discussion, the forced-steering linkages are assumed to be connected to the carbody. This differs from the development in Appendix B, which assumes that the linkages are connected to the bolster (in yaw).

**Urban Transportation Development Corporation Ltd., Ontario, Canada.

"S" Truck

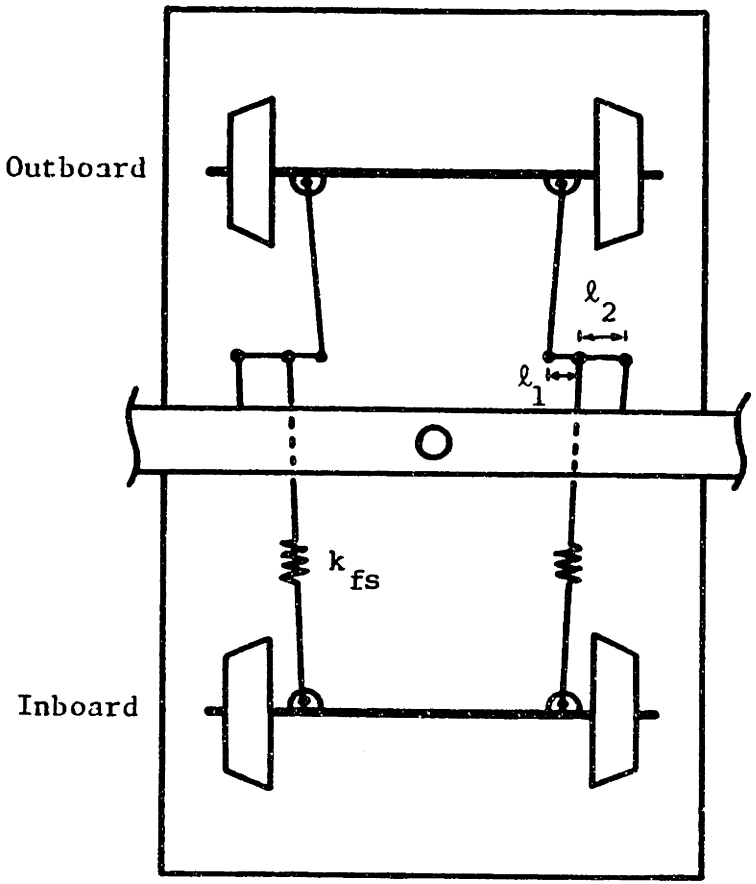

$$k_b = k_{b1} + k_{b2}$$

$$k_{b1} = d_p^2 k_{px}$$

$$k_{b2} = \frac{1}{2} d_p^2 k_{fs} \left(1 + \frac{\ell_2}{\ell_1+\ell_2}\right)^2$$

$$k_s = k_{s1} + k_{s2}$$

$$k_{s1} = \frac{d_p^2 k_{px} k_{py}}{d_p^2 k_{px} + b^2 k_{py}}$$

$$\Delta\psi_1 = \pm 2G\left(\frac{\psi_{w1} + \psi_{w2}}{2} - \psi_c\right)$$

$$\Delta\psi_2 = 0$$

$$G = \frac{1}{\ell_1+2\ell_2}$$

Figure 2.19 Schematic Diagram of "S" Forced-Steered Truck
(Primary Suspension System Not Shown)

"L" Truck

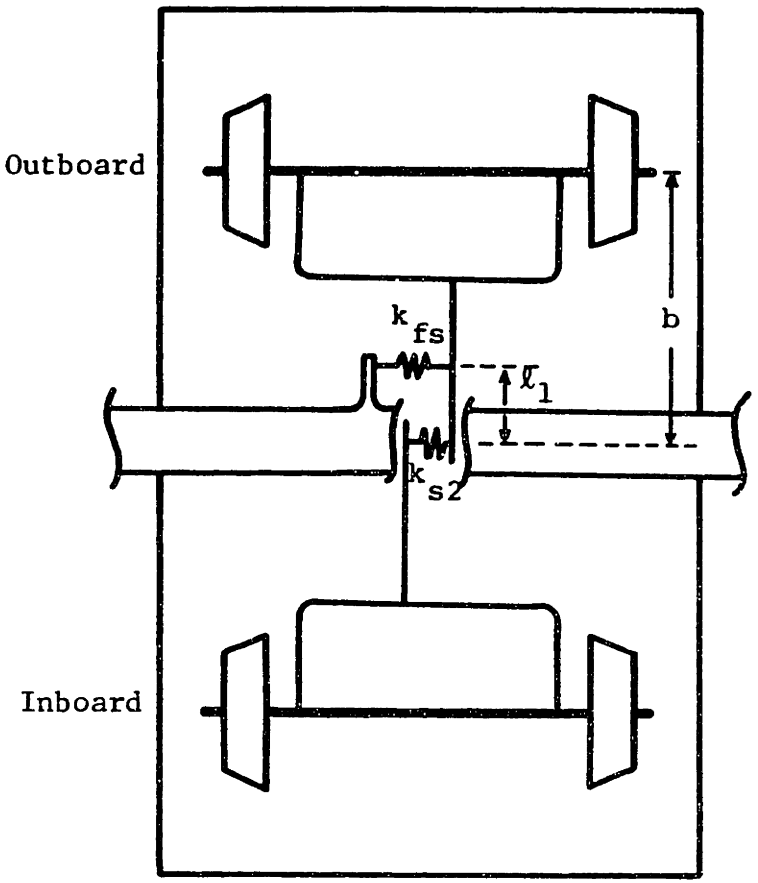

$$k_b = k_{b1} + k_{b2}$$

$$k_{b1} = d_p^2 k_{px}$$

$$k_{b2} = \frac{(b-\ell_1)^2 k_{fs} k_{py}}{(4k_{py} + k_{fs})} \quad *$$

$$k_s = k_{s1} + k_{s2} + \left(\frac{G_2}{b}\right)^2 k_{b2} \quad \text{very small}$$

$$k_{s1} = \frac{d_p^2 k_{px} k_{py}}{d_p^2 k_{px} + b^2 k_{py}}$$

$$\Delta\psi_1 = \pm 2G\left(\frac{y_{w1} - y_{w2}}{2b}\right) - \psi_c)$$

$$+ 2\left(\frac{G+1}{b}\right)\left(\frac{y_{w1} + y_{w2}}{2} - y_F\right)$$

$$\Delta\psi_2 = 0$$

$$G = \frac{\ell_1}{b-\ell_1}$$

*Assumes stiff k_{s2} (for symmetry).

Figure 2.20 Schematic Diagram of "L" Forced-Steered Truck (Primary Suspension System Not Shown)

"U" Truck

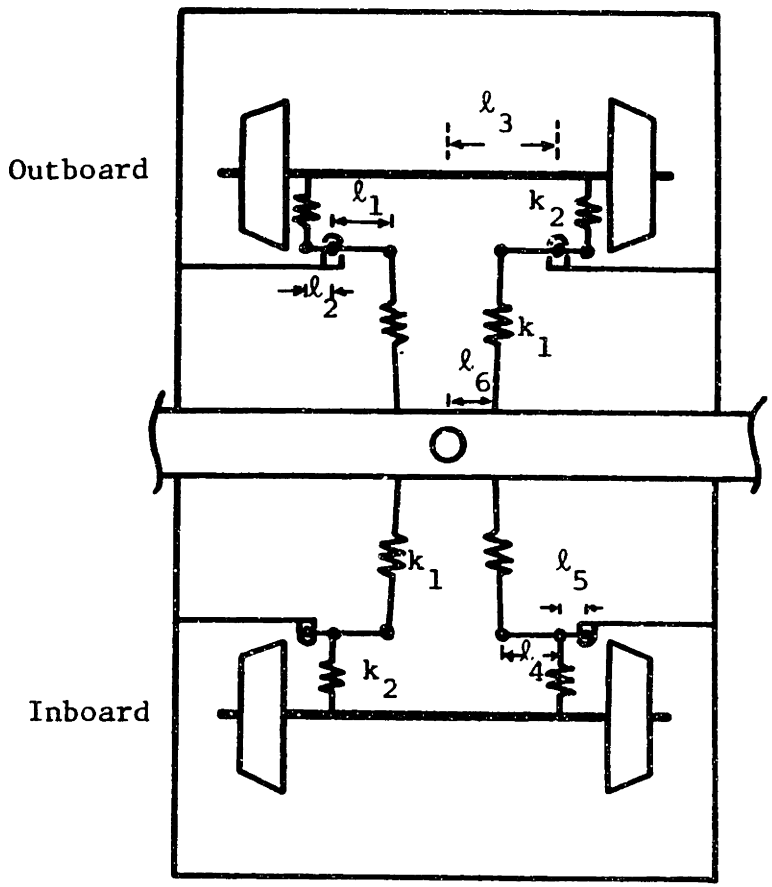

$$k_b = k_{b1} + k_{b3}$$

$$k_{b1} = d_p^2 k_{px}$$

$$k_{b3} = \frac{k_1 k_2 \ell_3^2 \ell_R^2}{(\ell_R^2 k_1 + k_2)}$$

$$\ell_R = \frac{\ell_1}{\ell_2} \quad \text{Outboard}$$

$$\ell_R = \frac{\ell_4 + \ell_5}{\ell_5} \quad \text{Inboard}$$

$$k_s = k_{s1}^* + k_{s3}$$

$$k_{s1}^* = \frac{(d_p^2 k_{px} + k_{b3})\, k_{py}}{d_p^2 k_{px} + k_{b3} + b^2 k_{py}}$$

$$\Delta\psi_1 = 0$$

$$\Delta\psi_2 = \pm 2G(\psi_F - \psi_C)$$

$$G = \frac{\ell_6}{\ell_R \ell_3} \quad **$$

*Assumes stiff k_{s2}.

**Linearized.

Figure 2.21 Schematic Diagram of "U" Forced-Steered Truck (Primary Suspension System Not Shown)

stiffness. The S truck has properties similar to the three piece freight truck because of its high interaxle bending stiffness and relatively low interaxle shear stiffness. For each prototype, expressions for the effective stiffnesses and the steering gains in terms of linkage stiffness and dimensions are included in Figures 2.19, 2.20, and 2.21; detailed derivations appear in [46].

The actuation of the forced-steering linkages can be represented by a geometric offset in series with a linkage bending and/or shear stiffness. The lateral and yaw offsets, Δy and $\Delta\psi$, as well as the linkage stiffnesses, k_{s2} and k_{b2}, are shown in Figure 2.22. The forced-steering forces and moments are:

$$\Delta F = k_{s2}\Delta y \tag{2-10}$$

$$\Delta M = k_{b2}\Delta\psi \tag{2-11}$$

The geometric offsets Δy and $\Delta\psi$ are controlled by the linkage design and can differ in alternative truck designs. In general, though, they are related to the relative lateral and yaw displacements between the truck frame and carbody, i.e.

$$\Delta y = 2H(y_F - y_c) \tag{2-12}$$

$$\Delta\psi = \pm 2G(\psi_F - \psi_c) \tag{2-13}$$

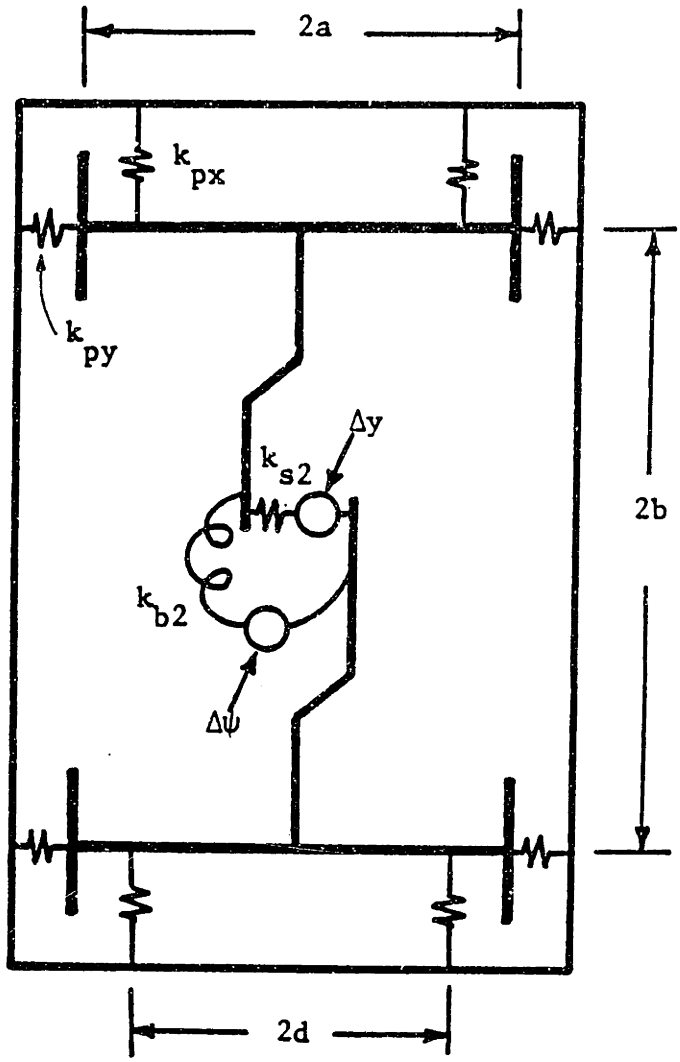

Figure 2.22 Forced-Steering Truck Model

where y_F, y_C and ψ_F, ψ_C are the lateral excursions and yaw angles of the truck frame, carbody, respectively. The $\pm$ sign in equation (2-13) indicates that a (+) counter-clockwise moment acts on the front truck and a (-) clockwise moment acts on the rear truck. It has been shown in [14] that ΔF can be used to control cant deficiency loads and ΔM can be used to compensate for track curvature effects. Thus, H is called the cant deficiency steering gain and G is called the curvature steering gain. These gains are kinematically related to the physical dimensions of the steering linkages. Figure 2.23 illustrates a possible forced-steering configuration that uses a cant deficiency steering law.

The curving performance of a forced-steered truck is a function of the steering gain G. The gain is regulated by the dimensions of the forced-steering linkages. The gain can be set by appropriate selection of linkage dimensions such that kinematically (i.e., with the assumption of rigid steering linkages and no flange forces) the wheelsets track the pure rolling line,* the track centerline or any line parallel to the track centerline. Theoretically, the gain which makes the wheelsets track the pure rolling line ensures perfect radial alignment (i.e., neutral steering) of the wheelsets.

*The lateral displacement that produces pure kinematic rolling of a single wheelset.

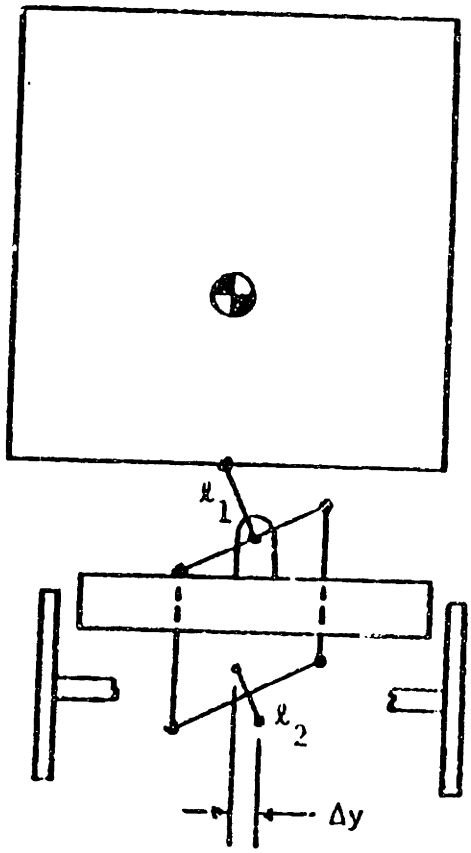

$$\Delta y = 2H\left(\frac{y_{W1} + y_{W2}}{2} - y_C\right)$$

$$H = \frac{\ell_2}{\ell_1}$$

FIGURE 2.23 SCHEMATIC DIAGRAM OF A FORCED STEERING TRUCK MODEL WITH CANT DEFICIENCY STEERING ACTION

The steering gain which results in both wheelsets tracking the pure rolling line is:

$$G_{pr\ell} = \frac{b}{\ell_s} \tag{2-14}$$

where $G_{pr\ell}$ is the pure rolling line steering gain and ℓ_s is half the distance between the truck centers. The above kinematic result is derived in [47] and assumes no flange forces, balanced running (no cant deficiency), and small secondary yaw and primary longitudinal stiffnesses. With the additional assumption of stiff interaxle shear stiffness, the cant deficiency gain for equal wheelset excursions is:

$$H = \frac{bk_{sy}}{2f_{11}} \tag{2-15}$$

where f_{11} is the lateral creep coefficient and k_{sy} is the secondary lateral suspension stiffness [47].

In general, the pure rolling line gain is appropriate before flange contact occurs since it correctly aligns the wheelsets radially. However, after flange contact occurs the assumptions implicit in the derivation of the pure rolling line gain are violated and as a result $G_{pr\ell}$ may not align the wheelsets appropriately. Other gains may have relative advantages. The pure rolling line gain is typically used in practice in prototype vehicles [48].

2.5.4 Generic Truck Model

A generic truck model that represents the different forced-

steered truck prototypes as well as the conventional and self-steered radial trucks is shown in Figure 2.24. The generic truck model represents the suspension system of the conventional truck consisting of bearing connections between the wheelsets and truck frame. These primary suspension elements are modelled as parallel combinations of linear springs and viscous dampers between the wheelsets and truck frame in the longitudinal and lateral directions. In addition, the generic truck model includes the effect of steering linkages between the wheelsets to represent self-steered trucks and steering linakges between the wheelsets, trucks, and carbody to represent a variety of forced-steered truck designs. The steering linkages of self and forced-steered trucks are also modelled as parallel linear spring/viscous damper combinations.

In Figure 2.24, the effects of linkages between the carbody, the truck and the wheelsets are represented by geometric offsets, according to the following steering laws:

$$\Delta\psi_1 = \Delta\psi_2 = \pm 2G_1 \left(\frac{\psi_{W1} + \psi_{W2}}{2} - \psi_C\right) \pm 2G_2 \left(\frac{y_{W1} - y_{W2}}{2b} - \psi_C\right)$$

$$+2G_3 \left(\frac{y_{W1} + y_{W2}}{2} - y_F\right) \pm 2G_4 \left(\psi_F - \psi_C\right)$$

$$\pm 2G_5 \left(\frac{\psi_{W1} + \psi_{W2}}{2} - \psi_F\right) \pm 2G_6 \left(\frac{y_{W1} - y_{W2}}{2b} - \psi_F\right) \quad (2\text{-}16)$$

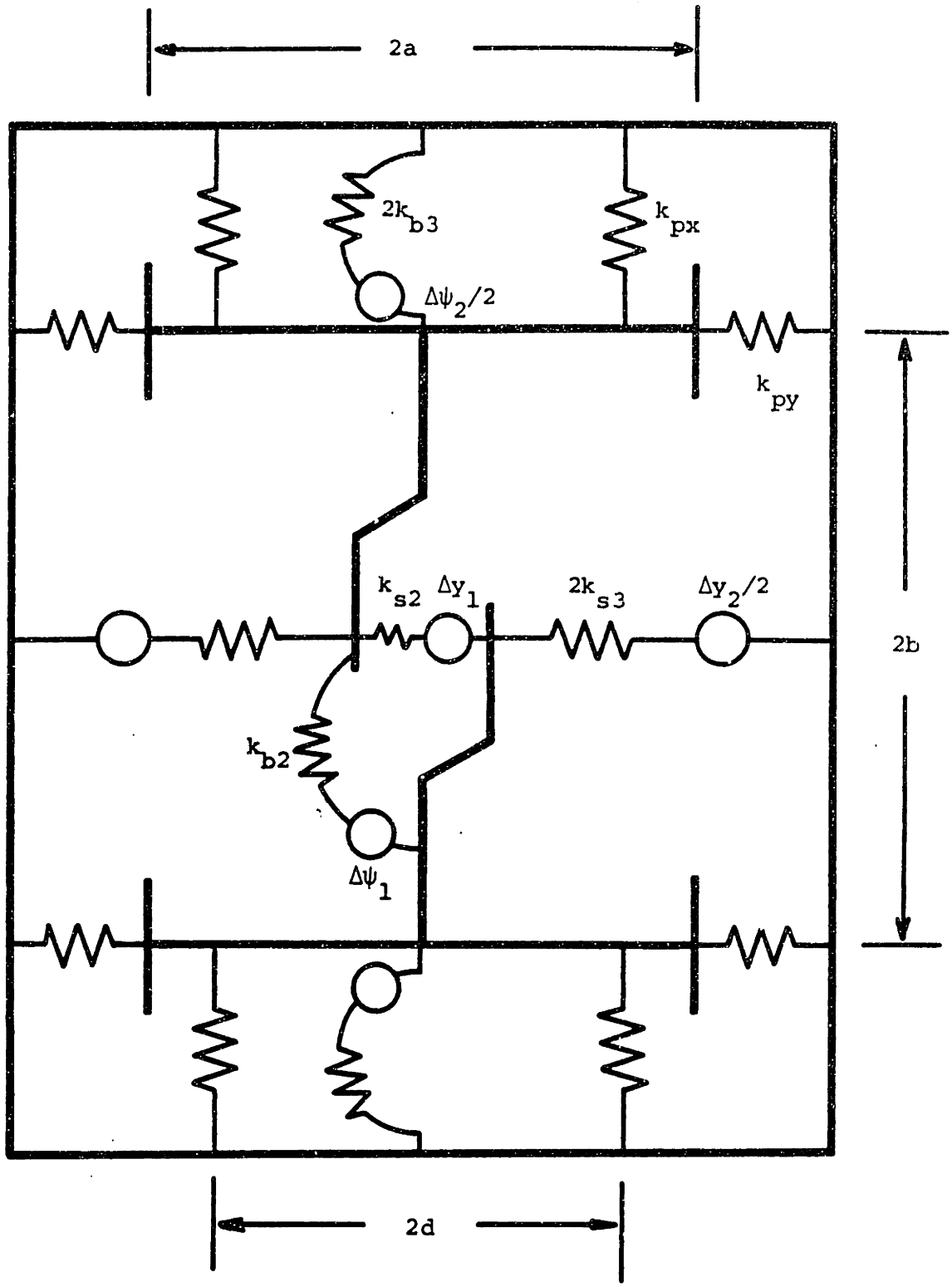

Figure 2.24 Generic Truck Model

$$\Delta y_1 = \Delta y_2 = 2H_1\left(\frac{y_{w1} + y_{w2}}{2} - y_C\right) + 2H_2(y_F - y_C) + 2H_3\left(\frac{y_{w1} + y_{w2}}{2} - y_F\right) \tag{2-17}$$

where the G_1's and the H_1's are the steering gains; y_{w1}, y_{w2} are the lateral displacements of the leading, trailing wheelsets of the truck; and, ψ_{w1}, ψ_{w2} are the yaw angles of the leading, trailing wheelsets, respectively. The differences in yaw displacement between the wheelset pair, the truck, and the carbody have an opposite effect on the rear truck than on the front truck because the two trucks yaw in opposite directions in curves and is illustrated by the $\pm$ sign change in equation (2-16). The $\pm$ notation implies + for the front truck and - for the rear truck. When a term has only one sign, the same expression is used for both trucks.

The steering laws are relatively general. They represent a linear combination of the differences in yaw displacement between the wheelset pair, the truck and the carbody, and the differences in the lateral displacement between the wheelset pair and the truck to sense track curvature and activate $\Delta\psi_1$ and $\Delta\psi_2$. Similarly, a linear combination of the differences in the lateral displacement between the wheelset pair, the truck and the carbody is used to sense cant deficiency and actuate Δy_1 and Δy_2.

The term forced-steering usually implies direct carbody connections to the wheelsets to steer the wheelsets into radial alignment. For the sake of generality and to represent physically realizable trucks, terms that represent wheelset-truck interconnections have

been included in the steering laws. These are the terms with the G_3, G_5 and G_6 gains in equation (2-16), and the term with the H_3 gain in equation (2-17). For most practical parameter values, however, the contributions of these terms to the geometric offset $\Delta\psi$ or Δy are negligible as shown below:

- stiff k_{py} implies $y_F \simeq \frac{y_{w1}+y_{w2}}{2} \longrightarrow 2G_3(\frac{y_{w1}+y_{w2}}{2} - y_F)$

  is negligible

  $\longrightarrow 2H_3(\frac{y_{w1}+y_{w2}}{2} - y_F)$

  is negligible

- stiff k_{px} implies $\psi_F \simeq \frac{\psi_{w1}+\psi_{w2}}{2} \longrightarrow 2G_5(\frac{\psi_{w1}+\psi_{w2}}{2} - \psi_F)$

  is negligible

- stiff k_{py} also implies $\psi_F \simeq \frac{y_{w1}-y_{w2}}{2b} \longrightarrow 2G_6(\frac{y_{w1}-y_{w2}}{2b} - \psi_F)$

  is negligible

The generic truck model is reduced to particular truck configurations by appropriate assignment of stiffnesses and steering gain values. Truck simplifications are given in Table 2.2.

The forced-steered truck studies in this thesis are based primarily on the L design. The L design has the inherent features of forced-steered trucks making it suitable for parametric study.

(Important design parameters for forced-steered trucks include shear and bending stiffnesses and the steering gains.) In addition, the L truck was selected as one which has potential application to transit systems. Relative performance, design, and manufacturing benefits of specific forced-steered truck configurations are not addressed in this thesis. Detailed studies of alternate configurations represent an area of future research.

TABLE 2.2 - GENERIC TRUCK SIMPLIFICATIONS

TRUCK TYPE*	k_{b2}	k_{b3}	k_{s2}	G_1	G_2	G_3	G_4
Conventional	0	0	0	0	0	0	0
Self Steering	k_{b2}	0	k_{s2}	0	0	0	0
S Prototype	k_{b2}	0	0	G	0	0	0
L Prototype	k_{b2}	0	k_{s2}	0	G	$\frac{G+1}{b}$	0
U Prototype	0	k_{b3}	0	0	0	0	G

*For these trucks G_5, G_6, H_1, H_2, H_3, k_{s3} = 0.

2.6 Vehicle Model

A rail passenger vehicle consists of a carbody supported by four wheelsets, two truck frames, and two bolsters. The wheelsets are connected to the truck frame via primary suspension elements. Each bolster rests on a truck frame and is attached to the carbody via secondary suspension elements.

As a rail vehicle negotiates a curve, internal and external forces and moments act on the wheelsets, trucks, bolsters, and carbody. The internal forces and moments are due to the suspension components. The external forces and moments are due to (1) inertial forces, including weight and cant deficiency forces, (2) wheel/rail contact forces, and (3) drawbar or buff loads.

This section presents the rail vehicle model, shown schematically in Figures 2.25 and 2.26. The vehicle model incorporates the generic truck model described in the previous section. The dynamic curving equations of motion of the rail vehicle model are developed in Appendix B.

2.6.1 Carbody/Bolster Model

The bolster is the structural member which rests on the truck and carries the load of the carbody from the secondary springs to the centerplate of the truck frame. During curve negotiation, the truck frame yaws relative to the bolster against the frictional resistance due to pads at the centerplate. The physical arrangement and the model of the yaw suspension are shown in Figures 2.27 and 2.28,

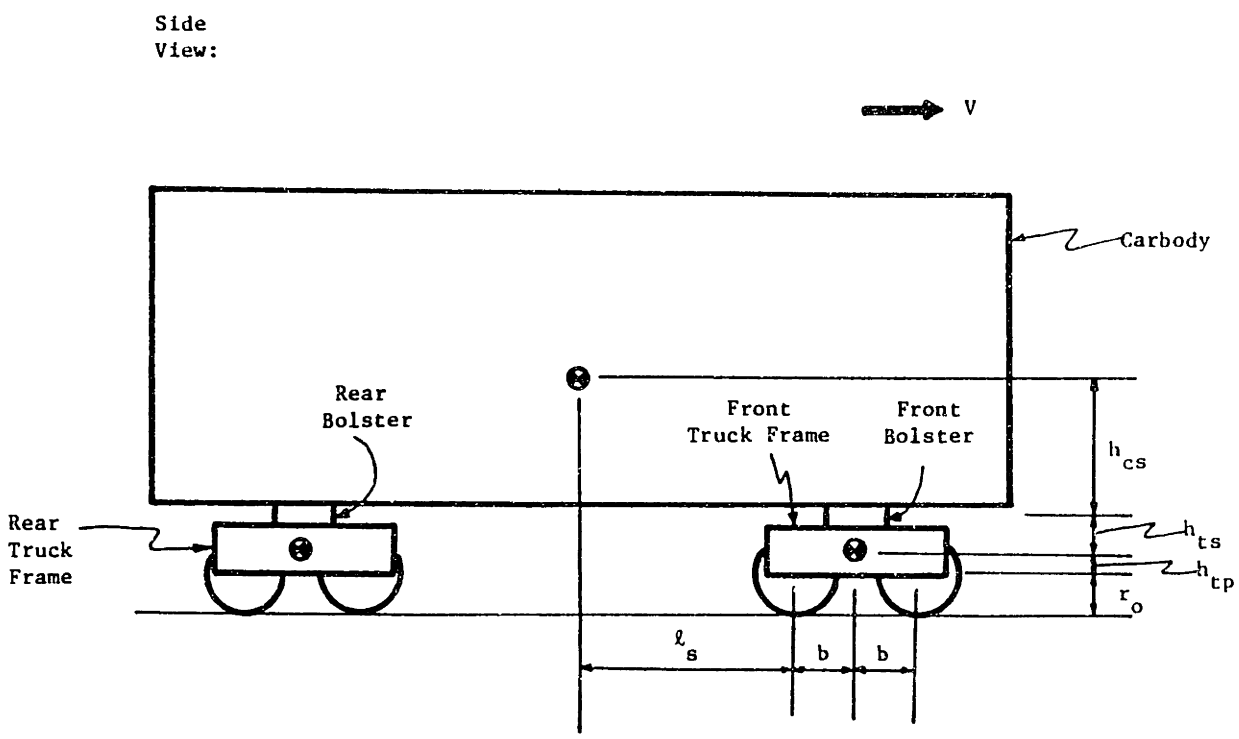

Figure 2.25 Rail Vehicle Model, Side View

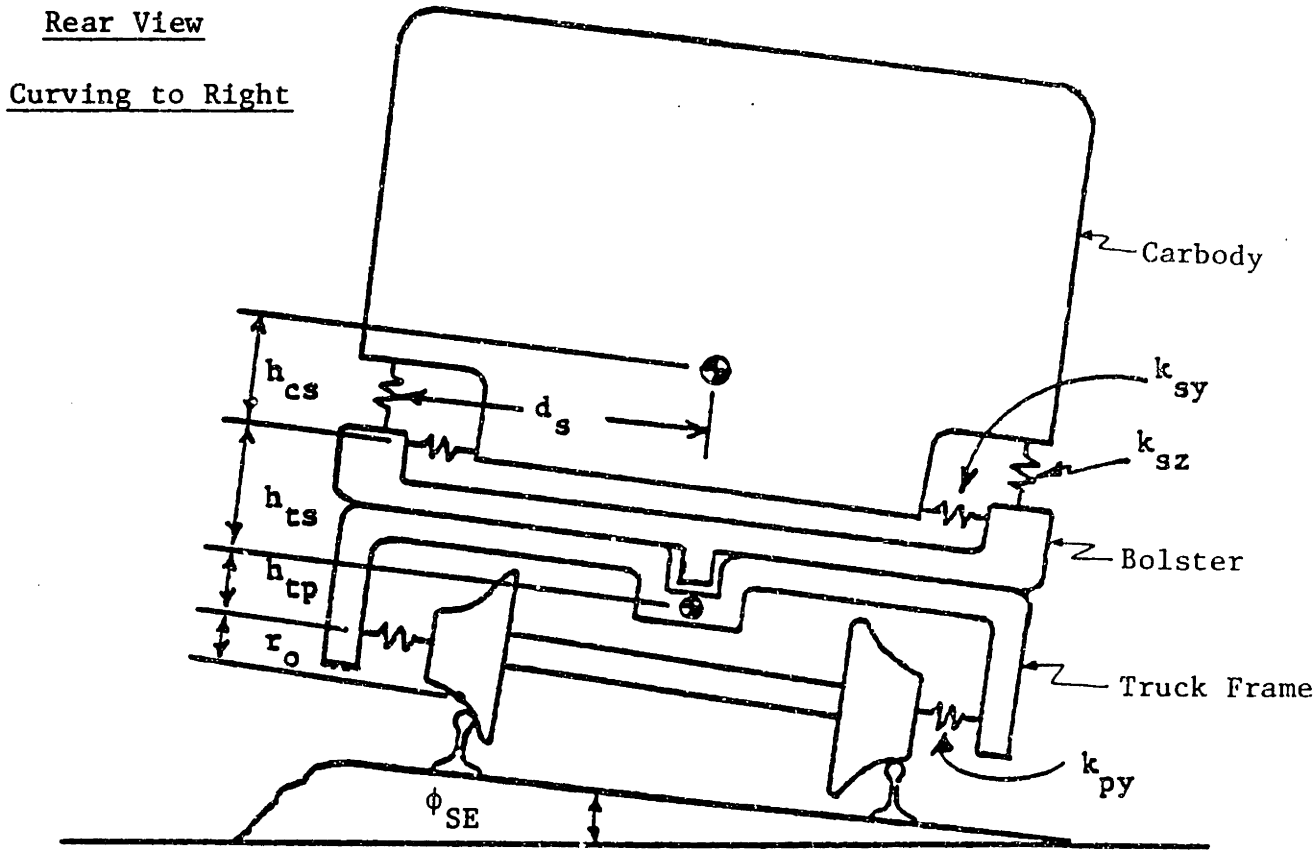

Figure 2.26 Rail Vehicle Model During Curving, Rear View

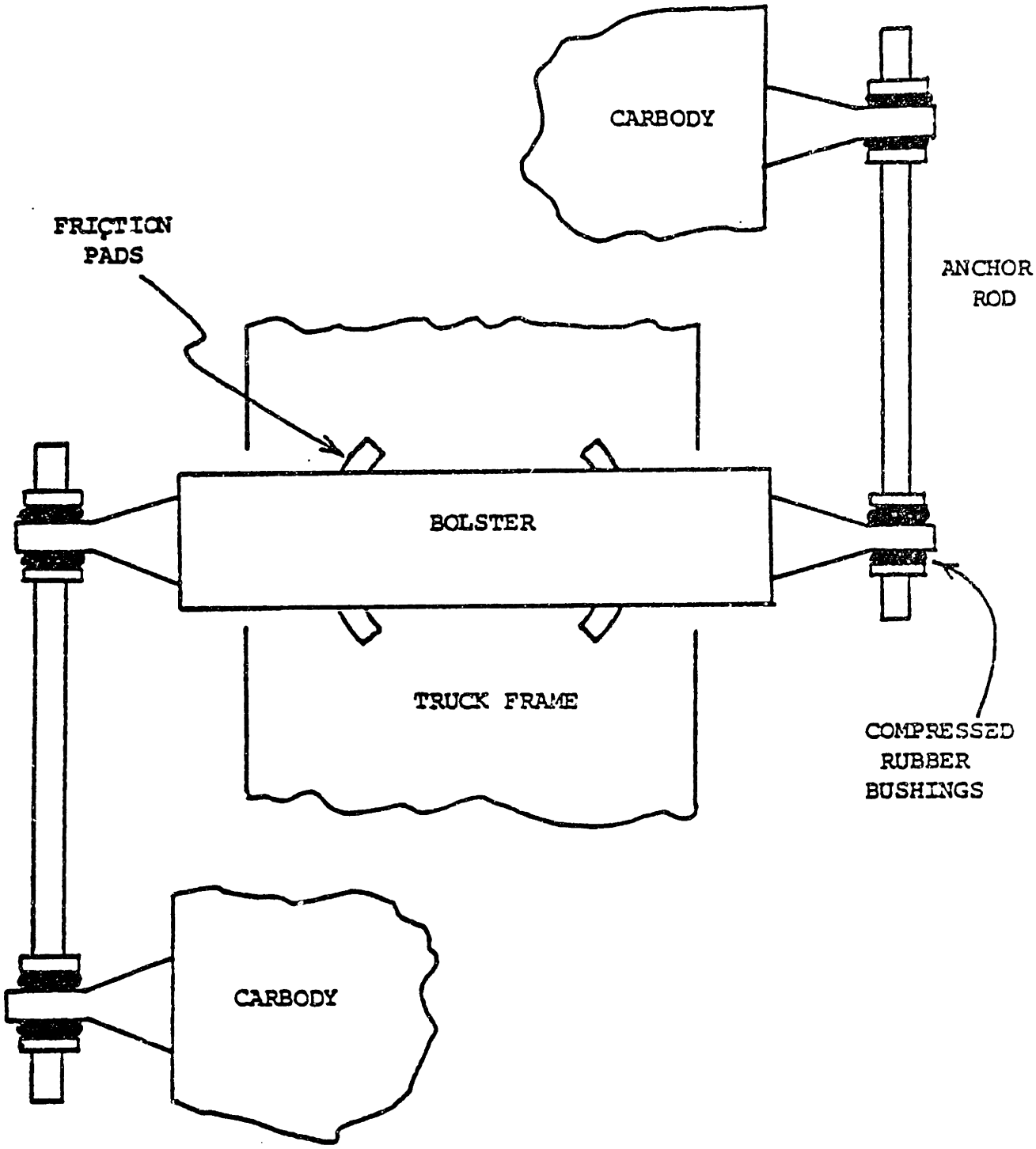

Figure 2.27 Physical Arrangement of the Secondary Yaw Suspension

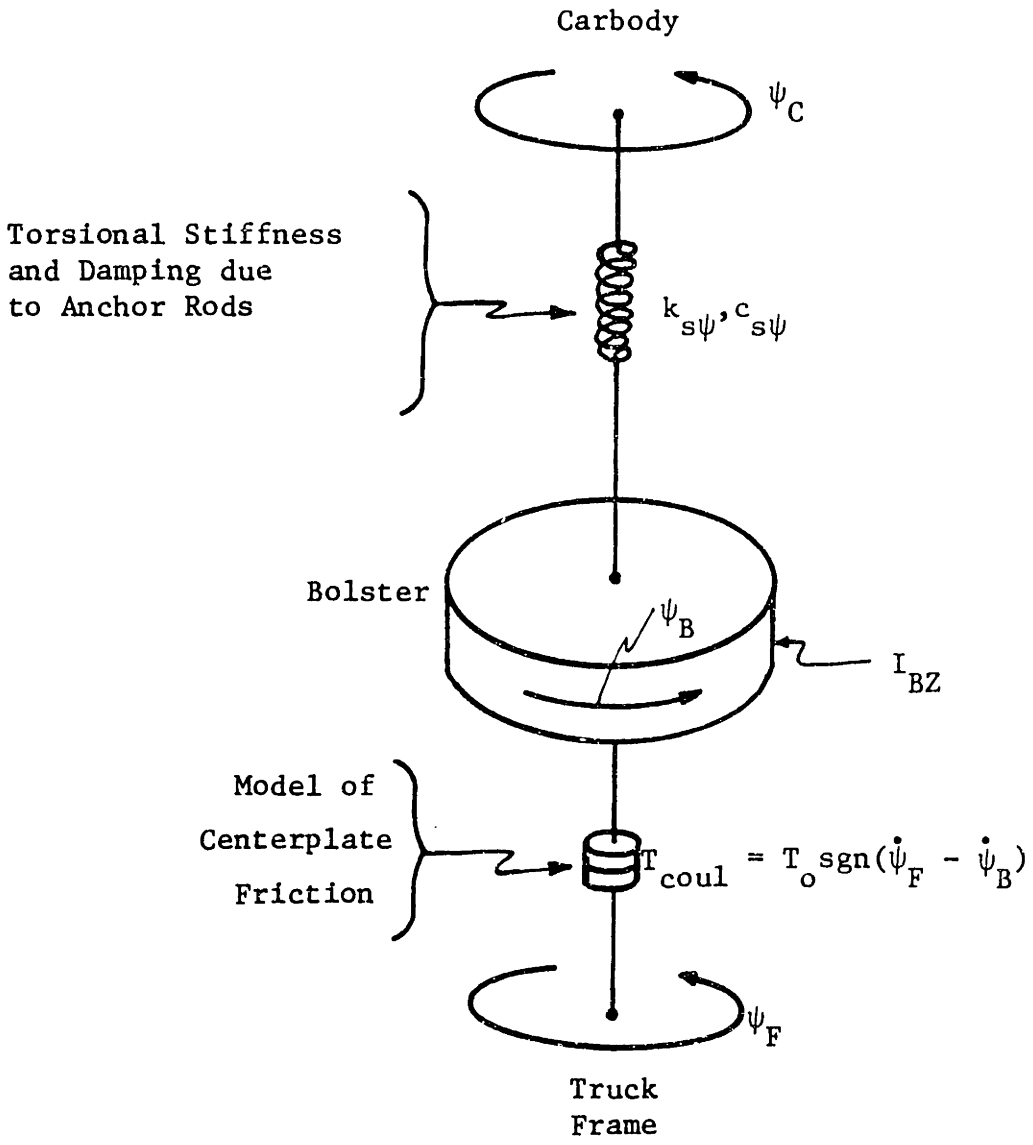

Figure 2.28 Model of Secondary Yaw Suspension

respectively. The bolster is connected to the carbody by anchor rods which provide torsional stiffness and damping. Typically the torsional stiffness is quite high (i.e., $k_{s\psi} > 5.0 \times 10^6$ ft-lb/rad).

The secondary suspension system acting between the truck, bolster, and carbody is modelled as follows. The carbody is coupled to the bolster via (1) parallel spring/viscous friction elements in the lateral and vertical directions, as shown in Figure 2.25, and (2) a torsional spring/viscous damper combination in the yaw direction. The bolster is connected to the truck frame by a torsional coulomb damper which saturates at a breakaway torque. For computational reasons, the model of the coulomb damper is modified to include a linear viscous band at the origin, as shown in Figure 2.29.

In the performance studies, it is assumed that the anchor rods are rigid, i.e., $k_{s\psi} = \infty$. Thus, each bolster follows the carbody motion in yaw and the truck motion in the lateral direction.

2.7 Numerical Methods

The performance of the rail vehicle model is evaluated using appropriate analytical and computational tools. This section describes the methods used to study dynamic curving, steady-state curving, and linear stability.

2.7.1 Dynamic Curving Analysis

A dynamic curving analysis has been developed to predict dynamic behavior of the rail vehicle model during curve negotiation. The behavior is described by coupled, nonlinear, differential equations

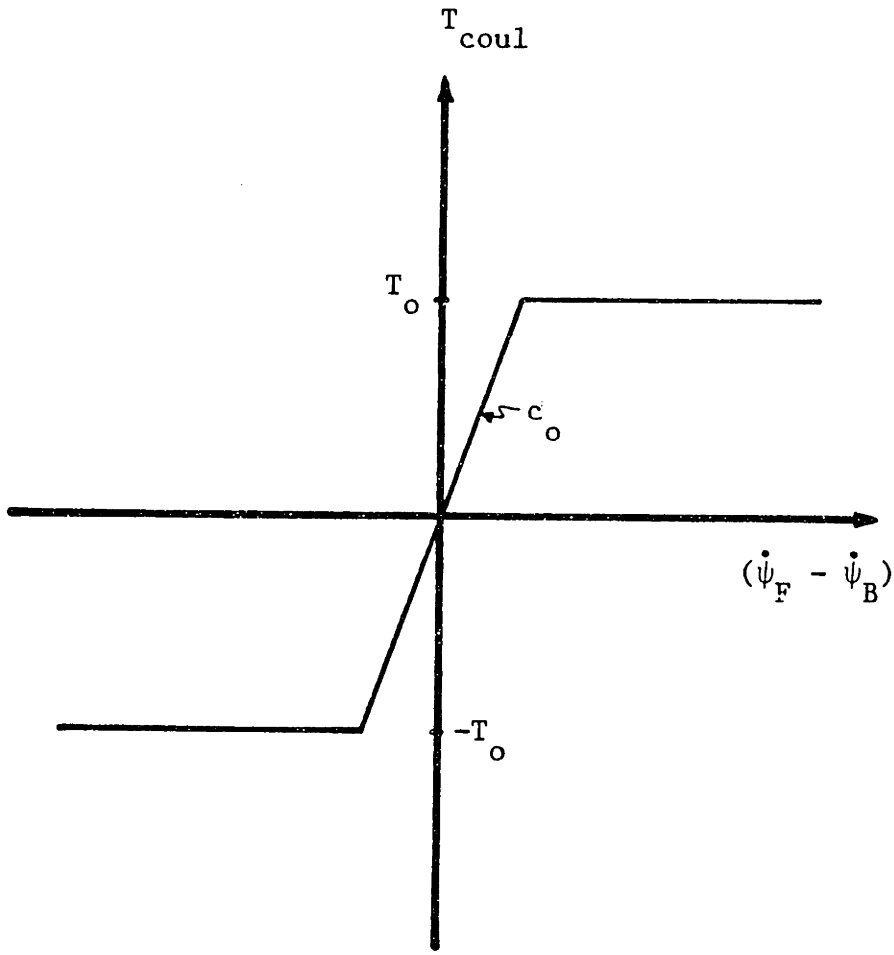

Figure 2.29: Truck Frame/Bolster Yaw Suspension Characteristic

of motion, which are developed in detail in Appendix B.

A total of 42 states (or 21 degrees of freedom) are used to characterize the full vehicle model: 20 states for the 4 wheelsets, 8 states for the 2 trucks, 6 states for the carbody, and 8 states for the rails. Each wheelset has a degree of freedom (i.e., 2 states) to describe its lateral and yaw motions, as well as a state to describe its spin speed. Each truck has a degree of freedom to describe its lateral and yaw motions. The carbody is characterized by lateral, yaw, and roll degrees of freedom. In addition, a simple model of the track is adopted in which the rail at each wheel has a state to describe its lateral motion.

In matrix notation, the dynamic curving equations of motion are written as:

$$[M]\ \{\ddot{\bar{X}}\} + [C(\bar{X}, \dot{\bar{X}})]\ \{\dot{\bar{X}}\} + [K(\bar{X}, \dot{\bar{X}})]\ \{\bar{X}\} = \{\bar{B}(\bar{X}, \dot{\bar{X}})\} \quad (2\text{-}18)$$

where [M], [C], and [K] are mass, damping and stiffness matrices, {B} is a forcing function vector due to track curvature and cant deficiency, and {X} is a displacement state vector. The damping and stiffness matrices are functions of displacements and velocities due to nonlinear suspension components.

Mathematically, equation (2-18) represents a set of coupled, nonlinear differential equations. The equations are solved by digital integration using a variable time-step, fourth-order Runge-Kutta scheme, which requires that the equations be in first-order

form. The transformation is obtained by letting

$$\dot{\{\bar{X}\}} = \{\bar{U}\} \tag{2-19}$$

where $\{\bar{U}\}$ is a velocity state vector. Substituting into equation (2-18) gives

$$\dot{\{\bar{U}\}} = [M]^{-1}(\{B(\bar{X}, \dot{\bar{X}})\} - [K(\bar{X}, \dot{\bar{X}})]\{\bar{X}\} - [C(\bar{X}, \dot{\bar{X}})]\{\bar{U}\}) \tag{2-20}$$

Equations (2-19) and (2-20) are numerically integrated to provide time histories of (1) all the state variables, i.e., $\{\bar{X}\}$ and $\{\bar{U}\}$, (2) the wheel/rail contact forces, and (3) the contact patch work.

The dynamic curving analysis is coded in a FORTRAN program, entitled DYCURV (DYnamic CURVing). A flowchart of the program appears in Appendix B. The program automatically accounts for the possibility of two-point contact at any wheel of the vehicle. Figure 2.30 shows the possible wheel/rail contact conditions for the leading and trailing wheelsets of a truck with new wheels. Two-point contact can develop at the outer or inner wheels of any of the wheelsets, especially during violent curve entry and exit, during negotiation of reverse curves, and during hunting.

Program DYCURV has been used to simulate the dynamic response of the rail vehicle model as it enters and negotiates curved track. The dynamic curving results are discussed in Chapter 5. In general, the program requires a very small time-step of digital integration ($\sim$ 0.0005 sec) for numerical stability, making it computationally time-consuming (and expensive) to use. For extensive parametric

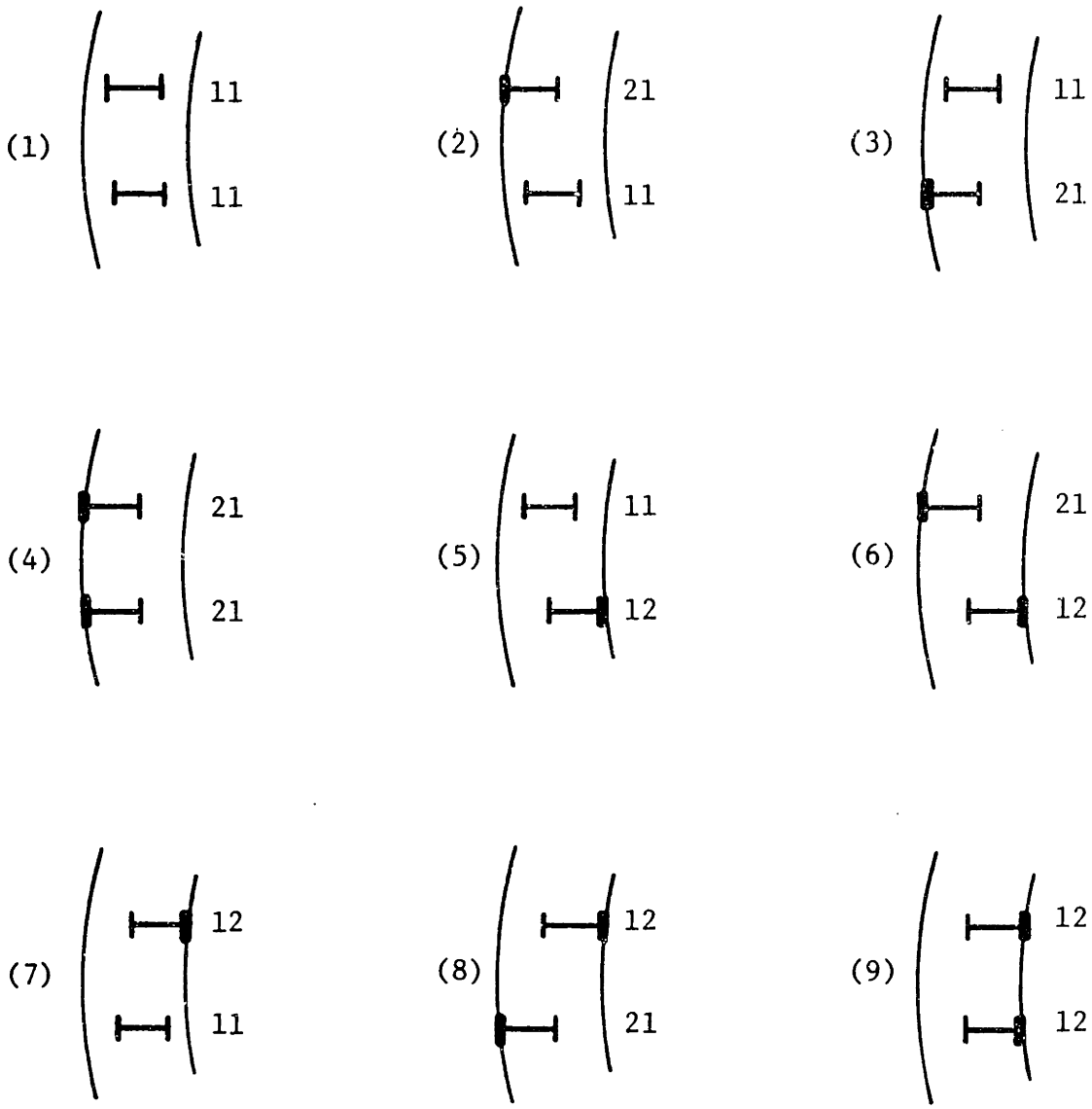

Key:

11 Single-Point Contact Outer and Inner Wheels.

21 Two-Point Contact Outer Wheel; Single-Point Contact Inner Wheel.

12 Single-Point Contact Outer Wheel; Two-Point Contact Inner Wheel.

Figure 2.30 Wheel/Rail Contact Possibilities for Wheelsets of a Truck with New Wheels.

studies a specialized steady-state analysis which is computationally efficient has been used.

2.7.2 Steady-State Curving Analysis

A steady-state curving analysis has been developed to predict the steady-state behavior of a vehicle negotiating constant radius curved track. The steady-state curving equations of motion are obtained by equating the displacement rate vectors, $\{\dot{\bar{X}}\}$ and $\{\ddot{\bar{X}}\}$, in equation (2-18) to zero, yielding

$$[K(\bar{X})]\{\bar{X}\} = \{\bar{B}(\bar{X})\} \qquad (2\text{-}21)$$

Equation (2-21) represents the steady-state equilibrium conditions, which are presented in detail in Appendix C.

In steady-state conditions, the front and rear trucks are essentially decoupled (for typical secondary suspension parameters). Thus, in order to reduce numerical computations, the equations for a single-truck/half-carbody model are solved. The following 9 states are identified: lateral displacement and yaw angle of the leading and trailing wheelsets, the truck, and half-carbody, as well as the roll angle of the carbody.

Equation (2-21) represents a set of coupled, nonlinear, algebraic equations, which are solved interatively using a combined steepest descent and Newton-Raphson algorithm [49]. The steady-state curving analysis is coded in a FORTRAN program called SSCURV (Steady-State CURVing), which is discussed in Appendix C. Program SSCURV is efficient and inexpensive to run and has been used to conduct

extensive parametric studies which are discussed in Chapter 3.

2.7.3 Linear Stability Analysis

A linear stability analysis has been developed to determine the linear critical speed. This analysis is conducted by evaluating the eigenvalues of

$$[M]\{\ddot{\bar{X}}\} + [C]\{\dot{\bar{X}}\} + [K]\{\bar{X}\} = \{\bar{0}\} \qquad (2\text{-}22)$$

which represents the homogeneous part of a linearized equation (2-18). To calculate the critical speed, the forward speed is increased until the damping in the least damped eigenvalue vanishes.

The stability analyses of two models have been conducted. The first model represents a full vehicle with 15 degrees of freedom; the second model represents a single truck (attached to an inertial reference) with 6 degrees of freedom. A complete description of the stability analyses as well as the results of extensive parametric stability studies appear in [46].

2.8 Baseline Rail and Vehicle Parameters

The baseline parameters used in the rail and vehicle models are listed in Table 2.3. They were selected to represent typical conventional and steered urban transit vehicles.

Two wheel/rail profiles were used in the studies: a new AAR wheel and a Heumann wheel both on worn rail of standard gage. Both profiles were obtained from tables in [39], smoothed, and modified to account for a centered rolling radius of 14.0 in. Geometric

TABLE 2.3 - BASELINE RAIL/VEHICLE PARAMETERS

WHEEL/RAIL	New Wheel	Heumann Wheel
f_{11T} [lb]*	1.09E6**	1.01E6
f_{12T} [ft-lb]	8615.	9620.
f_{22T} (ft^2-lb]	82.	14.
f_{33T} [lb]	1.18E6	9.805E6
f_{11F} [lb]	7.34E5	5.755E5
f_{12F} [ft-lb]	6820.	4735.
f_{22F} [ft^2-lb]	2.	1.
f_{33F} [lb]	6.71E5	5.26E5
λ	0.05	0.20
μ	0.30	0.30

GEOMETRY

r_o [ft]	1.167	h_{ts} [ft]	1.48
a [ft]	2.32	h_{tp} [ft]	0.52
b [ft]	3.75	h_c [ft]	2.375
d_p [ft]	1.92	ℓ_s [ft]	23.75
h_{cs} [ft]	2.90	d_s [ft]	3.71

*Creep coefficients are half-Kalker values with a nominal contact patch normal load of 15,000 lb.

**E represents to the power of 10, e.g., 1.0E6 = 1.0×10^6

COMPONENT WEIGHTS AND MOMENTS OF INERTIA

WHEELSET	Conventional Truck	Radial Trucks
W_W [lb]	4054.	4854.
I_{WY} [slug-ft^2]	28.	28.
I_{WZ} [slug-ft^2]	547.	946.
TRUCK		
W_F [lb]	4697.	4697.
I_{FX} [slug-ft^2]	1166.	1166.
I_{FZ} [slug-ft^2]	1251.	1251.
CARBODY		
W_C [lb]	70,190.	
I_{CX} [slug-ft^2]	4.40E4	
I_{CZ} [slug- t^2]	8.96E5	

VEHICLE WEIGHT	CONVENTIONAL	RADIAL
W_V [lb]	95,800	99,000

BASELINE STIFFNESSES AND DAMPING

PRIMARY SUSPENSION

	New Wheel		Heumann Wheel	
	Conventional	Radial	Conventional	Radial
k_{px} [lb/ft]	1.35E5	1.20E5	6.50E5	5.00E5
C_{px} [lb-sec/ft]	574.	756.	2760.	3150.

k_{py} [lb/ft]	7.50E5	k_{pz} [lb/ft]	1.0E6
C_{py} [lb-sec/ft]	620.	C_{pz} [lb-sec/ft]	600.

INTERWHEELSET STIFFNESSES

	Conventional	Radial
k_{b2} [ft-lb/rad]	0.0	1.0E3
k_{s2} [lb/ft]	0.0	1.0E6

SECONDARY SUSPENSION

k_{sy} [lb/ft]	19,500.	k_{sz} [lb/ft]	20,400.
C_{sy} [lb-sec/ft]	1420.	C_{sz} [lb-sec/ft]	1630.
C_o [ft-lb-sec/rad]	1.E7	T_o [ft-lb]	7500.

FORCED STEERING PARAMETERS

$G_{pr\ell} = 0.1579$ $\quad$ $H = 0.0$

constraint functions for these two symmetric profiles are described in Section 2.4.2. The new AAR wheel represents a wheel with a 1/20 tread taper and a steep flange. Single-point contact occurs in the tread region. However, due to the steep flange of this profile, two-point tread and flange contact occurs at wheelset lateral excursions equal to the flange clearance. In this thesis, the new AAR wheel profile is designated as "new wheel". The Heumann wheel profile was designed with the intention of maintaining single-point contact at all wheelset excursions to obtain a profile that would mtaintain its shape as it wears [50]. The new and Heumann wheel profiles are representative two-point contact and single-point contact profiles, respectively.

Linear profile coefficients were computed by linearization of the profile functions about the centered wheelset position. The nominal conicity in the tread of the Heumann wheel profile is 0.20, compared with a conicity of 0.05 for the new wheel profile.

Linear creep coefficients typical of the tread and flange of the two wheel profiles were calculated using Hertzian contact theory. Rail and wheel radii of curvature were obtained from [39]. Flange creep coefficients are less than tread coefficients* (by about 30 percent for longitudinal and lateral coefficients). This decrease in flange creep coefficients is expected since the contact patch

*The contact patch ellipse (a/b) ratio for the flange patch is limited to 10. This agrees with calculations by British Rail which show that the (a/b) ratio rarely exceeds 10 [51].

area decreases in the flange, and its effect outweighs the opposite effect of increased ellipticity.

The vehicle dimensions and weights are representative of urban transit trucks. Specifically, the geometry, weights and inertias are based on those reported for the existing and modified PATCO* Pioneer III trucks used by Budd [48]. The weight and inertia parameters reflect the fact that in yaw and roll the contribution of the traction motor must be included. In addition, for radial trucks the contribution of the steering arms is added. The weight and roll and pitch inertias of the truck include the side frames, braking equipment, and bolster. The bolster does not influence the truck yaw inertia.

The baseline primary, secondary, and interaxle suspension stiffnesses and damping are typical of urban truck designs. The primary longitudinal stiffnesses were chosen to yield vehicles with the same stability characteristics, i.e., critical speeds of 120 mph. The interaxle bending stiffness is quite low for the self-steered radial truck (k_{b2} = 1.0 x 10^3 ft-lb/rad) and is typically quite high for forced-steered trucks as a result of the stiffnesses of the carbody to wheelset linkages, as discussed in Chapter 3.

The baseline track curvature steering gain used in the performance studies of the forced-steered truck designs is the pure rolling line gain, $G_{pr\ell}$. The pure rolling line gain is the wheelbase

*Port Authority Transit Corporation

divided by the truck centerpin spacing, according to equation (2-14). A limited study of alternate curvature steering gains was conducted and the results, presented in Chapter 3, suggest that $G_{pr\ell}$ results in slight understeering of the wheelsets during flanging. As suggested in Chapter 3, gains slightly larger than $G_{pr\ell}$ may be appropriate during flanging. However, the selection of an optimal track curvature steering gain represents an area of future research. Thus, for the forced-steering studies of this thesis, the track curvature steering gain is $G_{pr\ell}$. The cant deficiency steering gain, H, is set to zero in the forced-steered studies since the curvature effects are in general much more important.

3.0 STEADY-STATE CURVING STUDIES

3.1 Introduction

The steady-state curving performance of conventional rail vehicles is influenced strongly by the stiffness of suspension elements, the wheel/rail profile geometry, and the track curvature. As suspension elements are stiffened for stability, they prevent radial alignment of the wheelsets and increase the lateral flange forces, especially on tight curves. Advanced vehicle designs with innovative suspension configurations are intended to improve the curving performance while providing adequate stability.

The wheel/rail profile is a dominant parameter influencing the vehicle curving performance. The profile determines the nature of the wheel/rail contact at the flanging wheel as the wheelset displaces laterally. As discussed in Chapter 2, some profiles, such as the Heumann wheel profile, are characterized by a smooth transition from tread to flange and maintain single-point contact at all lateral excursions. Other profiles, such as the new AAR 1 in 20 wheel profile, have steep flanges and two-point contact can occur simultaneously at the flanging wheel. In this thesis, the new AAR wheel profile is referred to as "new wheel".

The track curvature constitutes an input to the wheelsets and represents a principal parameter influencing the vehicle curving

performance. Many urban transit systems include sections of track with steep curvatures. Some systems have curves as high as 30°, although common transit curves are less than 7.5°. In general, yard curves are greater than 7.5°, and most often restraining rails are present. In the curving performance studies, four track curvatures have been selected: 2.5°, 5°, 10°, and 20° curves. The 2.5° and 5° curves represent shallow curves of 2290 ft and 1150 ft radius, the 10° curve represents a moderate curve of 575 ft radius, and the 20° curve represents a steep curve of 288 ft radius. In this work, the 10° curve is assumed to be a representative transit curve which typically may be encountered.

In curved track, the distance which must be traversed along the outer rail is greater than the distance along the inner rail. For a curve of large radius, the difference in distance is small and a wheelset can roll without slip around the curve by displacing outwards slightly. The wheelset displaces laterally, increasing the rolling radius of the outer wheel and decreasing the rolling radius of the inner wheel such that the wheel and rail path lengths are identical. In steady-state curving, this fundamental property is known as the lateral shift of the "zero longitudinal creepage" or "pure rolling line" toward the outer rail. For a free wheelset centered over the pure rolling line, the longitudinal component of creepage (slippage) between each wheel and rail is zero. The wheelset is in steady-state

equilibrium in the yaw direction.*

For shallow curves, the lateral shift of the pure rolling line is less than the available flange clearance. A free wheelset displaces to the pure rolling line and steers itself perfectly around the curve. As the curvature increases, the pure rolling line moves out. When the lateral shift of the pure rolling line exceeds the flange clearance, sustained flange contact occurs. The wheelset is forced to remain inside the pure rolling line resulting in longitudinal creepage at the wheels. To satisfy equilibrium, the wheelset adopts a positive yaw angle of attack.

Theoretically, the wheelsets of a rigid truck are locked together by an infinitely stiff primary suspension preventing any relative lateral or yaw displacement. As a rigid truck negotiates a curve, it is impossible for both wheelsets to align radially and thus perfect steering cannot be achieved.

A realistic truck possesses some bending and shear flexibility and its wheelsets assume a steady-state geometry in between the free wheelset and rigid truck configurations. For a truck with soft shear and bending stiffnesses, the wheelsets behave like free wheelsets. For a truck with stiff shear and bending stiffnesses, the behavior is closer to that of a rigid truck. Figure 3.1 shows pictorially the equilibrium wheelset geometry of a truck with intermediate shear and bending stiffnesses negotiating a tight curve. Shear and bending

*This neglects the effects of spin components of creepage.

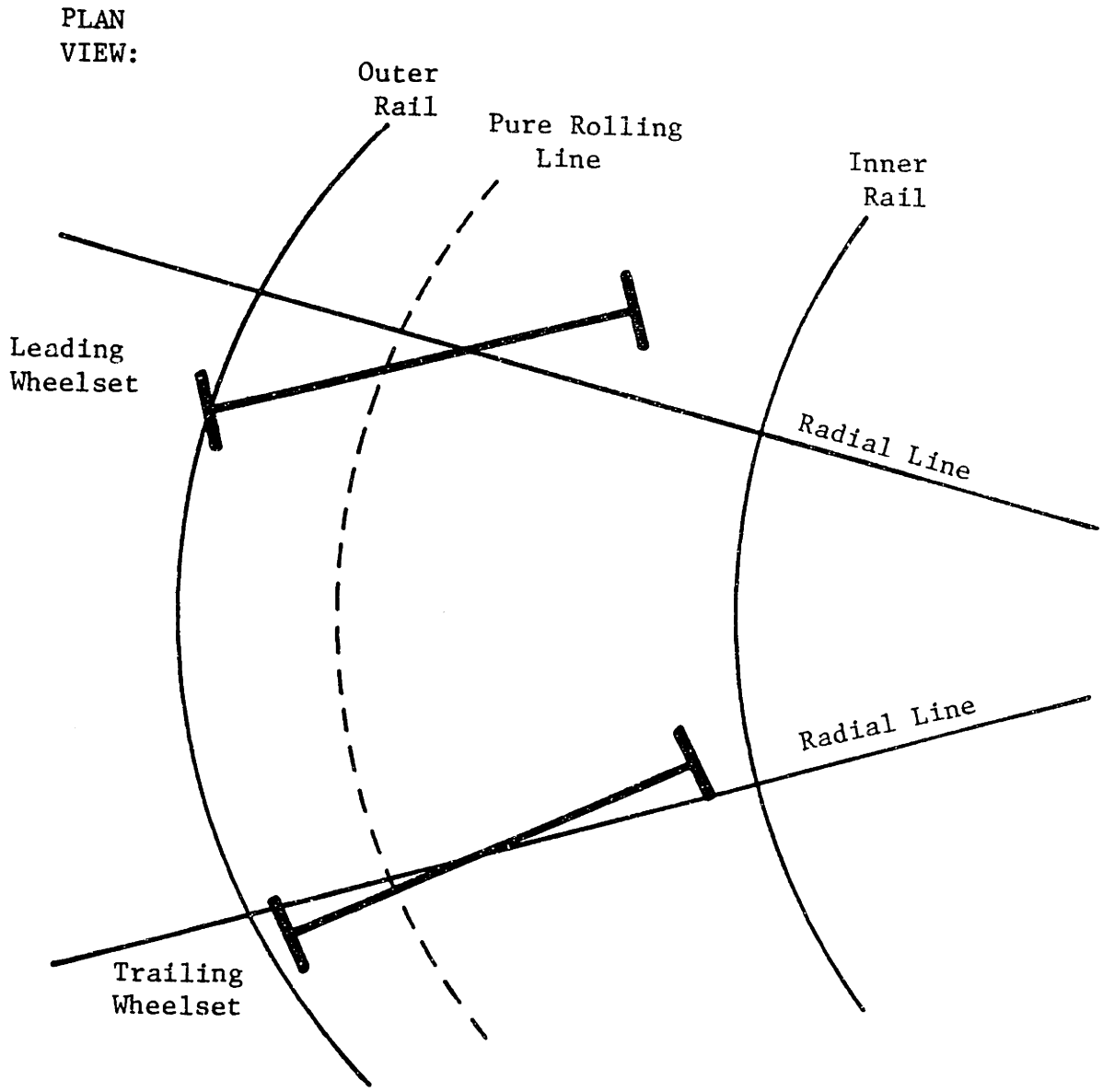

Figure 3.1 Steady-State Equilibrium Configuration for the Wheelsets of a Flexible Truck

deflections occur resulting in a leading wheelset angle of attack and flange force smaller than those which occur for the rigid truck configuration. For equilibrium, the rear wheelset of the flexible truck swings toward the outer rail and approaches radial alignment helping to reduce the leading wheelset angle of attack.

In this chapter, the results of parametric studies that investigate the steady-state curving performance of rail vehicles are reported. The principal parameters influencing curving performance are suspension design, wheel/rail profile, and track curvature. The steady-state curving performance of a single wheelset is investigated and the results underscore the importance of wheel/rail profile. Extensive parametric studies of a conventional truck are described. The results indicate that suspension stiffness, wheel/rail profile, and track curvature are the dominant parameters influencing the curving performance of a conventional truck. The steady-state curving performance of self-steered and forced-steered trucks are studied. The results suggest that trucks with innovative suspension designs potentially offer significant improvements in curving performance in comparison to conventional truck performance.

3.2 Curving Performance of a Single Wheelset

The curving performance of a vehicle is intimately related to the ability of its wheelsets to negotiate a curve. In this section, the steady-state curving performance of a single wheelset is investigated using the detailed nonlinear wheelset analysis described in Appendix C.

The behavior of a wheelset in steady-state curving is determined by the equilibrium values of net lateral force and yaw moment acting on the wheelset. The wheelset lateral force, F_{lat}, and yaw moment, M_{yaw}, are shown in Figure 3.2. The lateral force equilibrates the lateral components of creep and normal forces at the left and right wheels. The yaw moment equilibrates the moment provided principally by the longitudinal creep forces at the left and right wheels. In a vehicle, suspension and body forces produce the lateral force and yaw moment acting on the wheelset.

The wheelset lateral force and yaw moment are functions of the wheelset lateral excursion, angle of attack, axle drive torque, and vertical loads at the left and right wheels. In the following, the vertical load at each wheel is assumed to be 12,500 lb, corresponding to the nominal wheel load of a 100,000 lb vehicle. The wheelset is assumed to be unpowered, and thus no external drive torque is applied. In addition, the rails are assumed to be rigid. Figures 3.3 and 3.4 show families of the force-displacement and moment-displacement functions for a wheelset with Heumann wheels on worn rails negotiating a 10° curve. For each wheelset lateral excursion and angle of attack, Figure 3.3 shows the lateral force needed to obtain lateral equilibrium and Figure 3.4 shows the yaw moment needed for yaw equilibrium.

The effects of creep force saturation and the influence of vertical creep force components on the wheelset lateral force are exhibited in Figure 3.3. For small lateral excursions corresponding to tread

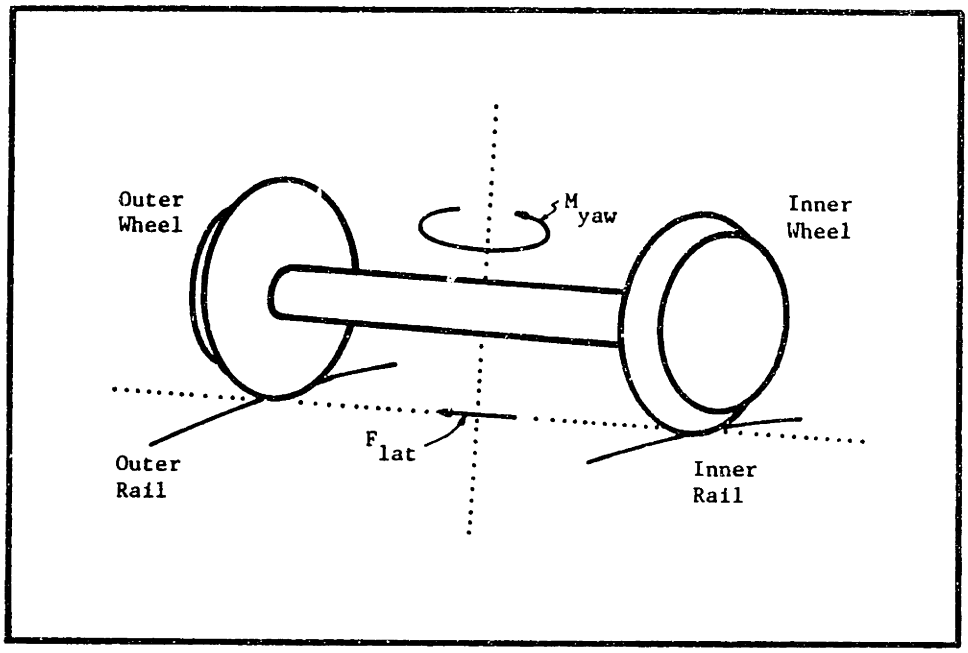

Figure 3.2 Wheelset Lateral Force and Yaw Moment

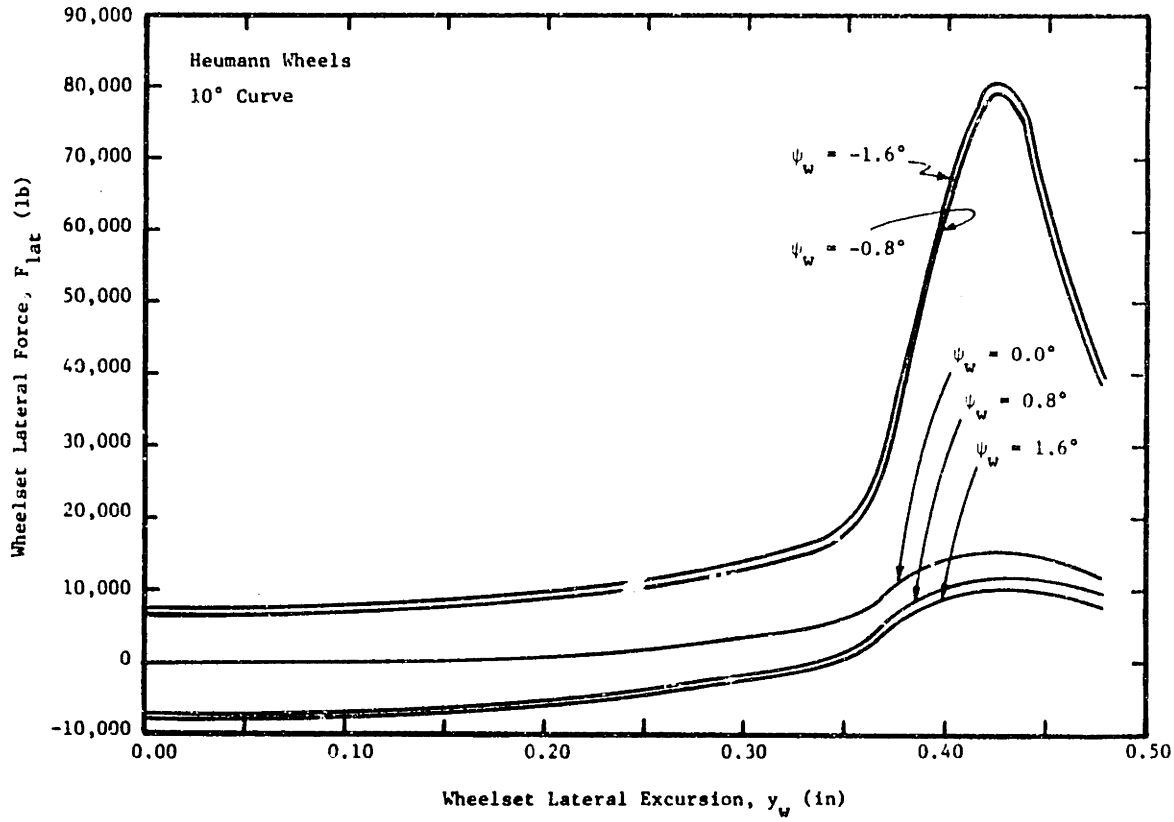

Figure 3.3: Wheelset Lateral Force as a Function of Lateral Excursion and Angle of Attack for a Wheelset with Heumann Wheels on Worn Rails Negotiating a 10° Curve (Axle Load = 25,000 lb; Rigid Rails)

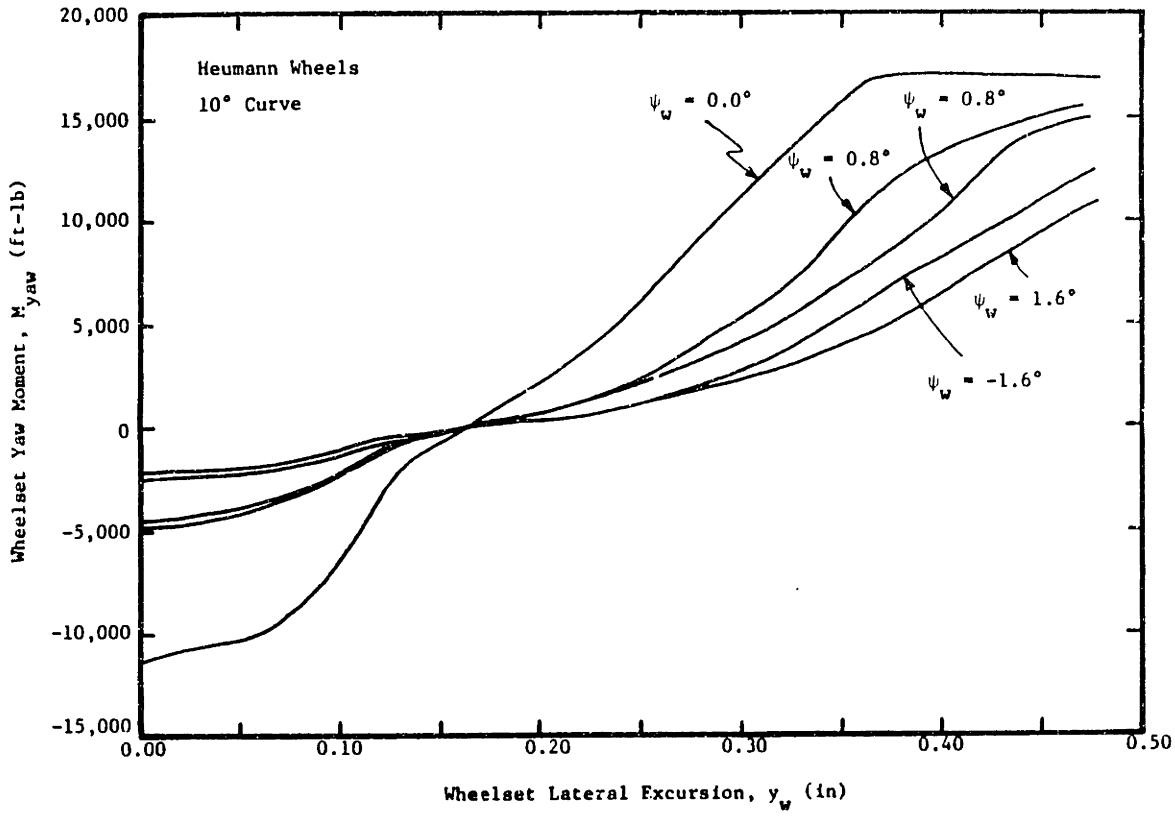

Figure 3.4: Wheelset Yaw Moment as a Function of Lateral Excursion and Angle of Attack for a Wheelset with Heumann Wheels on Worn Rails Negotiating a 10° Curve (Axle Load = 25,000 lb; Rigid Rails)

contact, the wheelset lateral force saturates at the adhesion limit (μ x Axle Load) for large positive and large negative angles of attack. For small excursions and zero angle of attack, the wheelset lateral force is negligible since the lateral creepages vanish and the spin creepages are small. For large lateral excursions corresponding to flange contact, the vertical components of creep force help the outer wheel climb the flange for positive angles of attack. The contributions of the lateral and spin creepages tend to lift the wheel off the rail. For negative angles of attack, the vertical creep forces (due to lateral creepages) change direction and tend to press the wheel down harder against the rail allowing the wheelset to support a much larger lateral force before derailment occurs.

Figure 3.4 shows the equilibrium wheelset yaw moment as a function of lateral excursion and angle of attack. The yaw moment counteracts the moment created primarily by the longitudinal creep forces at the wheels. For small lateral excursions (< 0.16 in), a negative yaw moment develops for all angles of attack which helps to steer the wheelset around the curve. The negative yaw moment is opposed principally by longitudinal creep forces which occur since the wheelset excursion is too small. The wheelset cannot develop a sufficient rolling radius difference to roll without slip around the curve. For larger lateral excursions (> 0.16 in), a positive or anti-curving wheelset yaw moment develops. The positive yaw moment is opposed by longitudinal creep forces in the opposite directions which occur since the wheelset develops too large a rolling radius difference.

In Figure 3.4, the longitudinal creep forces and thus the wheelset yaw moment vanish at a lateral excursion of 0.16 in. This excursion is the "pure rolling line" excursion for a wheelset with Heumann wheels negotiating a 10° curve. A wheelset which operates at the pure rolling line does not develop longitudinal components of creepage. The pure rolling line excursion is a function of track curvature. For tangent track (i.e., 0° curve), the pure rolling line coincides with the track centerline, and thus the wheelset yaw moment vanishes at zero lateral excursion. Figure 3.5 shows the wheelset yaw moment versus displacement function for a wheelset with Heumann wheels negotiating tangent track.

The maximum wheelset yaw moment occurs at zero angle of attack for all excursions. As the wheelset contacts the flange (i.e., at excursions > 0.35 in), the longitudinal creep forces saturate at the adhesion limit due to the very large rolling radius difference and large flange contact angle. As the angle of attack increases in either the positive or negative direction, the wheelset yaw moment decreases, illustrating the coupling between the lateral and longitudinal creep forces. For a given creepage in a particular direction, the creep force in that direction is always a maximum when the creep forces in the other directions are zero.

The maximum lateral-to-vertical force ratio at the flanging wheel (denoted L/V) as a function of wheelset angle of attack is shown in Figure 3.6. This graph is indicative of the derailment tendencies of the wheelset. For negative angles of attack, the peak

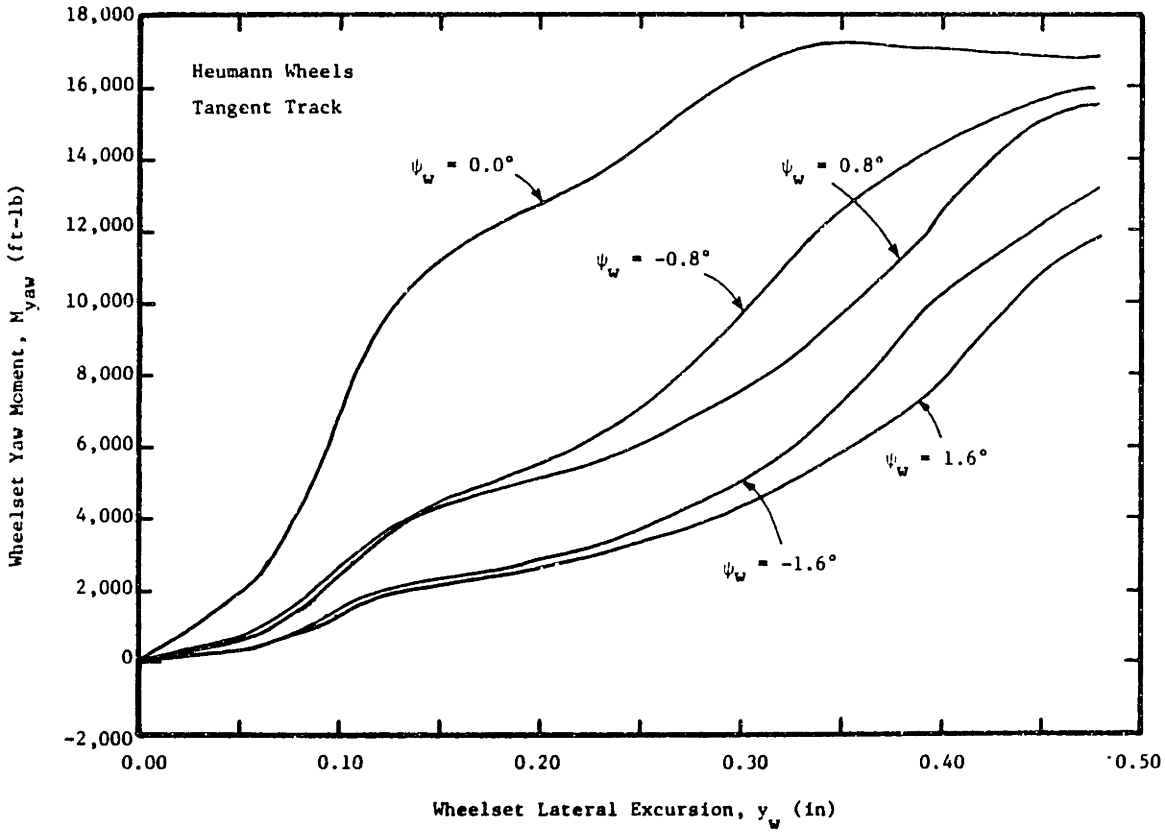

Figure 3.5: Wheelset Yaw Moment as a Function of Lateral Excursion and Angle of Attack for a Wheelset with Heumann Wheels on Worn Rails Negotiating Tangent Track (Axle Load = 25,000 lb; Rigid Rails)

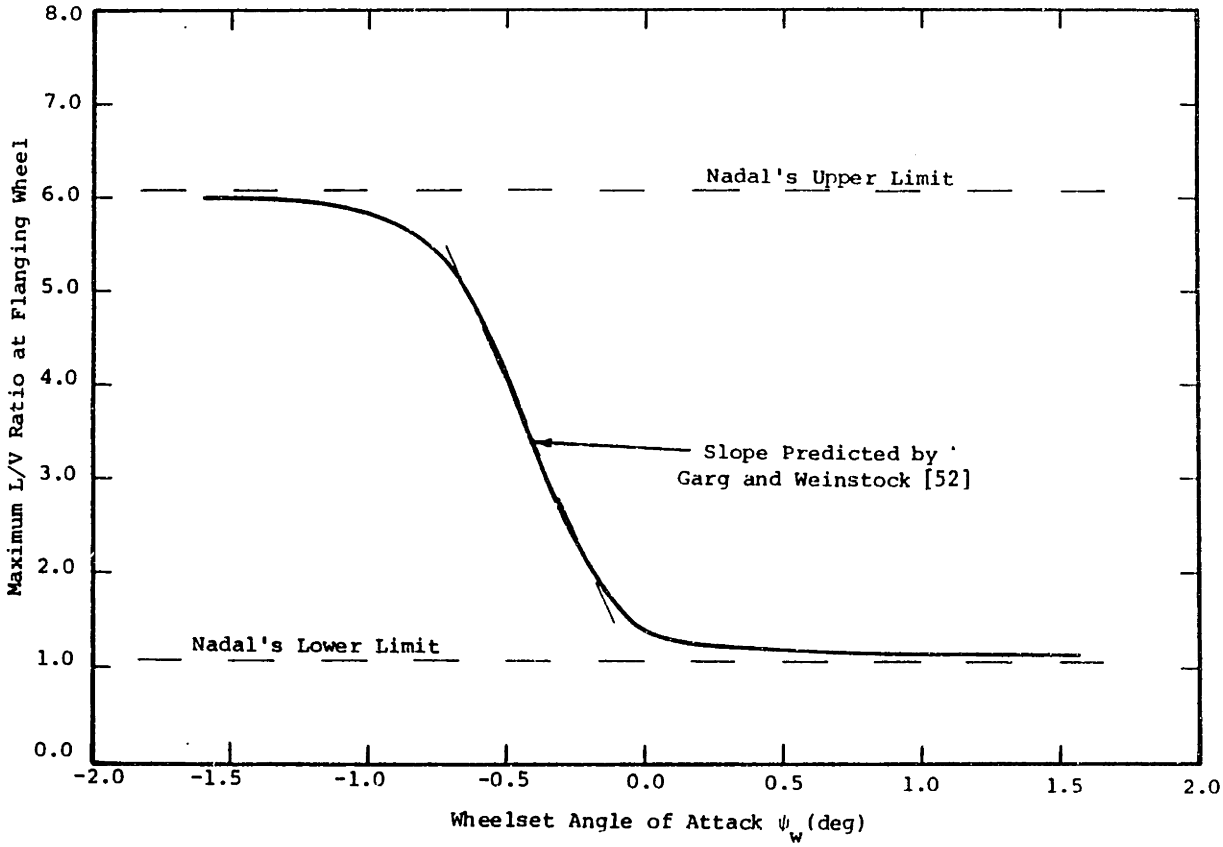

Figure 3.6: Maximum L/V Ratio at Flanging Wheel vs. Wheelset Angle of Attack (Axle Load = 25,000 lb; Rigid Rails).

L/V ratio increases significantly and saturates to Nadal's upper limit [30], given by

$$\left(\frac{L}{V}\right)_{upper} = \frac{\tan \delta_i + \mu}{1 - \mu \tan \delta_i} \tag{3-1}$$

where $\left(\frac{L}{V}\right)_{upper}$ is the maximum possible value of the lateral-to-vertical force at the flanging wheel and δ_i is the flange contact angle. Similarly, for large positive yaw angles, the maximum L/V ratio saturates to Nadal's lower limit,

$$\left(\frac{L}{V}\right)_{lower} = \frac{\tan \delta_i - \mu}{1 + \mu \tan \delta_i} \tag{3-2}$$

where $\left(\frac{L}{V}\right)_{lower}$ is the minimum value possible. For a coefficient of friction of 0.3 and a flange contact angle of 64°, Nadal's limits predict: $\left(\frac{L}{V}\right)_{upper} = 6.11$ and $\left(\frac{L}{V}\right)_{lower} = 1.08$. These boundaries are marked in Figure 3.6. Garg and Weinstock [52] showed that the slope of the curve between Nadal's limits at intermediate yaw displacements is approximated by:

$$\text{slope} = -\frac{f_{11}}{V_i}\left(\tan^2 \delta_i + 2\right) \tag{3-3}$$

where f_{11} is the lateral creep coefficient and V_i is the vertical load at the flanging wheel. Equation (3-3) predicts a slope of -6.36/deg which agrees with the slope in Figure 3.6.

3.2.1 Effect of Wheel/Rail Profile on Curving Performance of a Single Wheelset

The steady-state curving performance of a single wheelset is influenced significantly by the wheel/rail profile. The forces and moments acting on the wheelset are markedly different if two-point contact rather than single-point contact occurs at the flanging wheel. If two-point contact occurs, large longitudinal creep forces develop in opposite directions at the tread and flange contact patches of the flanging wheel which partially cancel one another. With single-point contact, a longitudinal creep force develops at the flanging wheel which is larger than the net longitudinal creep force with two-point contact. The larger longitudinal creep force with single-point contact produces a larger yaw restoring moment which helps to position the wheelset radially. Thus, a wheelset with single-point contact Heumann wheels develops a larger restoring moment (at the same lateral force) than a wheelset with two-point contact new wheels.

Figure 3.7 shows the yaw moment versus lateral force function for wheelsets with new and Heumann wheels negotiating a 10° curve at zero angle of attack. For the wheelset with Heumann wheels the outer (flanging) wheel is in tread contact and a small longitudinal creep force develops at small wheelset lateral forces. At larger lateral forces the wheelset with Heumann wheels displaces laterally. The outer wheel begins flanging and the longitudinal creep force at the single contact patch grows large, significantly increasing the wheelset yaw moment. For wheelset lateral forces greater than 8,000 lb,

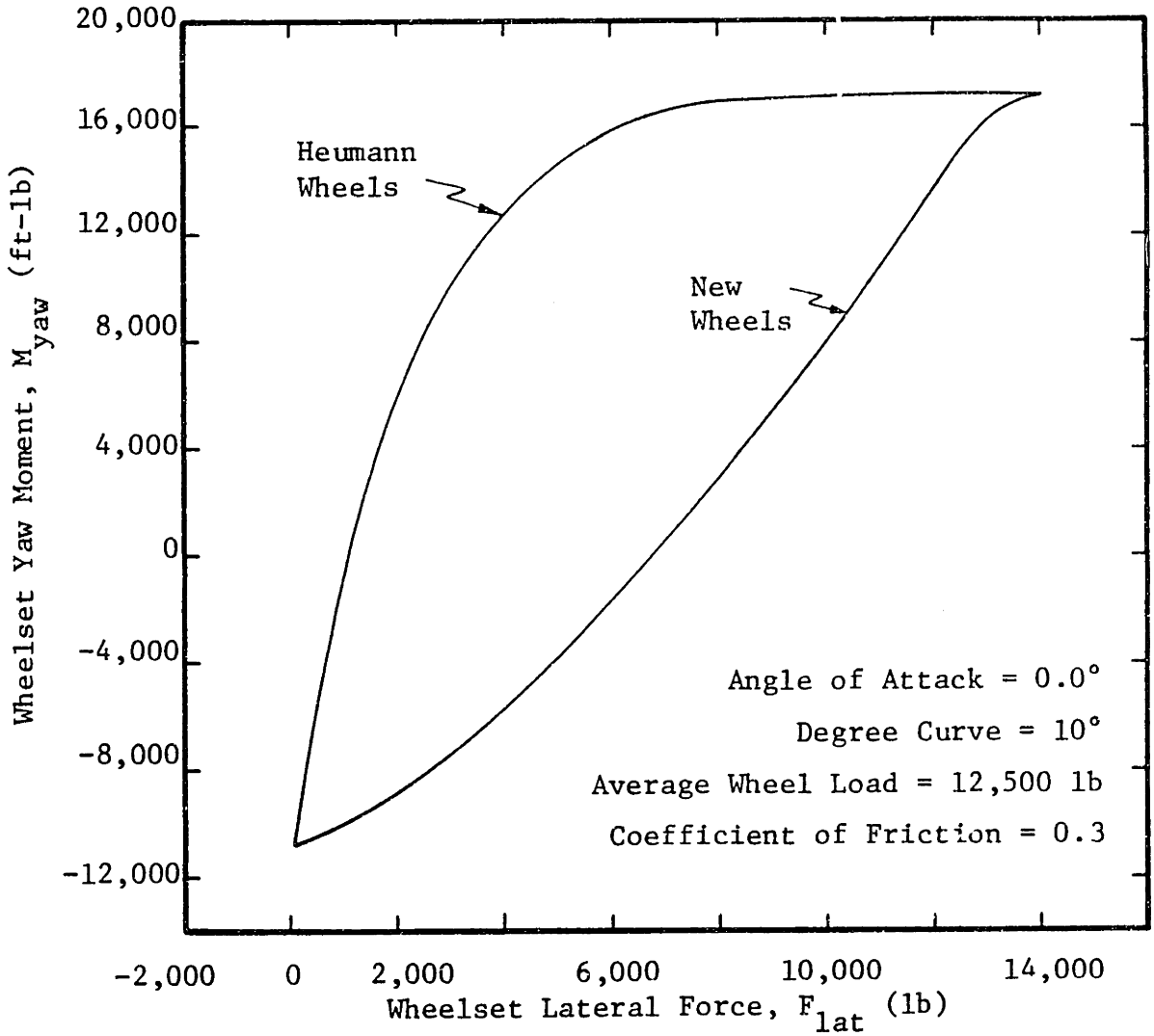

Figure 3.7 Wheelset Yaw Moment vs. Wheelset Lateral Force for New and Heumann Wheels.

the creep forces saturate as the outer wheel rides high up on the flange and a maximum wheelset yaw moment develops.

For the wheelset with new wheels, the lateral excursion equals the flange clearance and the outer wheel is in two-point tread and flange contact for the range of lateral forces plotted in Figure 3.7. The longitudinal creep forces at the flange and tread contact patches act in opposite directions. For small lateral forces, the longitudinal creep force at the flange contact patch is less than at the tread contact patch, while for higher lateral forces the longitudinal creep force at the flange contact patch is larger. With increasing lateral force, the net longitudinal creep force at the flanging wheel changes direction and thus the yaw moment changes from negative to positive. The creep forces at the flange contact patch do not saturate until the lateral force exceeds 14,000 lb. Results of further study show that the difference between the yaw moments for wheelsets with new and Heumann wheels diminishes with increasing track curvature since the creep forces saturate earlier. In summary, the results of Figure 3.7 show that for negotiation of a 10° curve, a larger restoring moment develops for a wheelset with Heumann wheels than for a wheelset with new wheels, suggesting that the Heumann wheel profile is advantageous for curve negotiation.

The improved steady-state curving performance of a wheelset with Heumann wheels in comparison to a wheelset with new wheels is borne out by considering the work at the flanging wheel. Figure 3.8 is a plot of the work versus lateral-to-vertical (L/V) force ratio at the

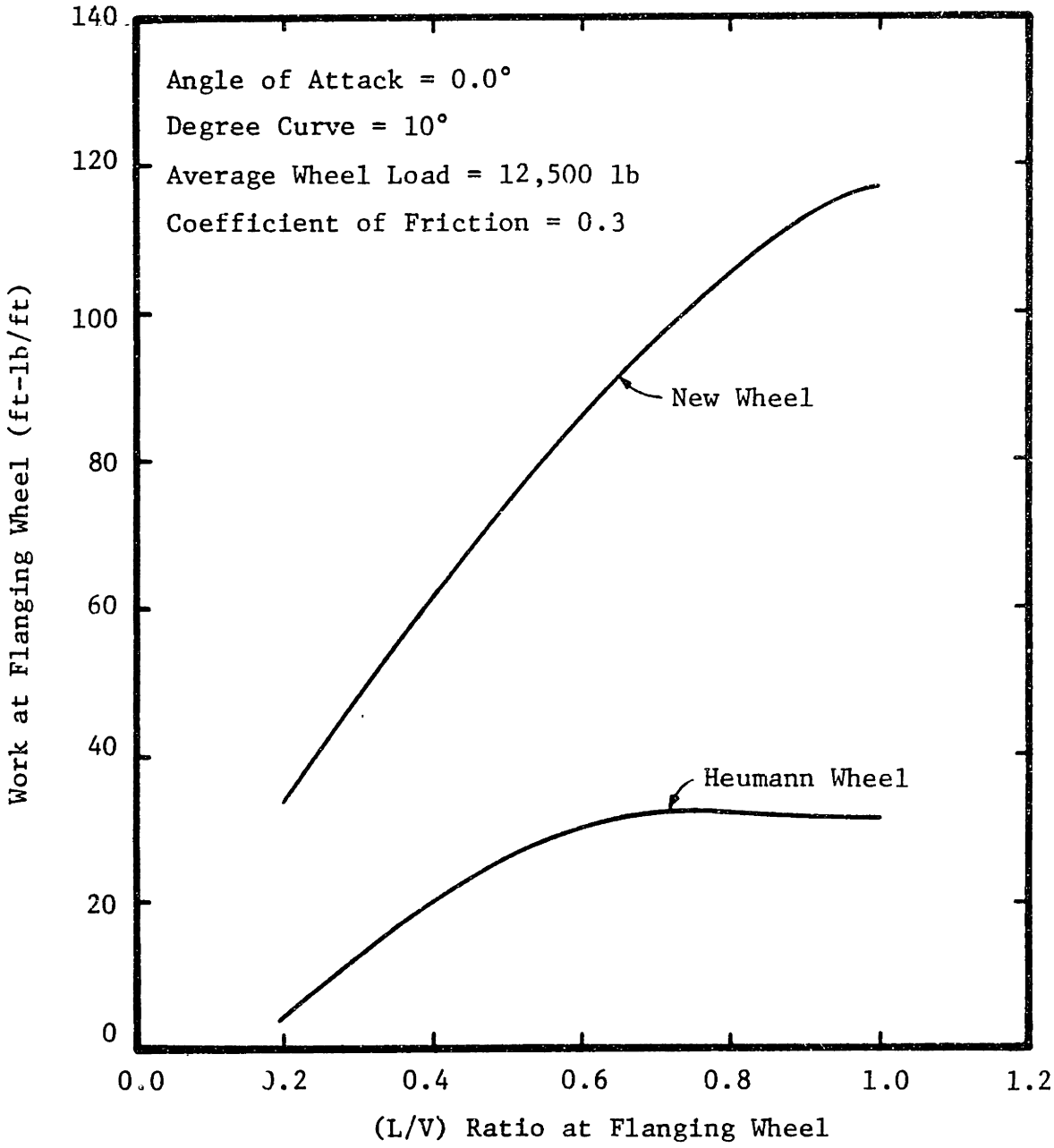

Figure 3.8 Flanging Wheel Work vs. (L/V) Ratio for New and Heumann Wheels.

flanging wheel for wheelsets with new and Heumann wheels negotiating a 10° curve at zero angle of attack. Less work is expended for the wheelset with Heumann wheels than for the wheelset with new wheels at the same L/V ratio since single-point contact always occurs at Heumann wheels. With increasing L/V, the work for both wheelsets increases as the creep forces and creepages grow. For the wheelset with Heumann wheels, the work reaches a maximum of 32 ft-lb/ft at L/V $\simeq$ 0.7 (equivalent to a wheelset lateral force of $\simeq$ 9,000 lb). Further increases in L/V result in constant work since the creep forces are fully saturated.

For the wheelset with new wheels, two-point contact occurs. The work at the flanging wheel is the sum of the work at the tread and flange contact patches. The work at the flange contact patch increases significantly while the work at the tread contact patch diminishes with increasing L/V ratio as the distribution of forces shifts from the tread to flange patches. The creep forces at the flange do not saturate until L/V > 1.2 (equivalent to a wheelset lateral force > 14,000 lb), which is out of the range of values plotted in Figure 3.3. The work at the flanging wheel approaches 120 ft-lb/ft, four times the work expended by the Heumann wheel at saturation. Again, as the track curvature increases, the flanging wheel work for a wheelset with new wheels approaches the work for a wheelset with Heumann wheels due to the earlier onset of creep force saturation.

This section has focused on the steady-state curving performance of a single wheelset and has emphasized the importance of wheel/rail profile. The remainder of this chapter discusses the curving performance of conventional and advanced truck designs.

3.3 Curving Performance of Conventional Trucks

The dominant parameters influencing the steady-state curving performance of conventional trucks are the primary longitudinal stiffness, the wheel/rail profile, and the track curvature. The primary longitudinal stiffness, k_{px}, is equivalent to the total truck bending stiffness: $k_b = d_p^2 k_{px}$. For soft truck bending stiffness (i.e., soft k_{px}) the wheelsets have minimum yaw bending resistance, which is beneficial for curving performance. The wheelsets can adopt yaw displacements which are decoupled from the truck orientation.

Suspension elements in a truck change their properties with time and wear due to general deterioration. These changes may lower the critical speed. In order to maintain a safety margin, vehicle suspension design should be based on a critical speed above the intended maximum operating speed. In this thesis, baseline suspension parameters are selected such that the vehicles have critical speeds of 120 mph.* (Typical transit operating speeds are 60 mph.) To achieve a 120 mph critical speed, the primary longitudinal stiffness of a conventional truck with new wheels is $k_{px} = 1.35 \times 10^5$ lb/ft;

*The critical speeds were determined by a linear stability analysis. The stability results are presented in detail in [46].

the stiffness of a conventional truck with Heumann wheels is $k_{px} = 6.50 \times 10^5$ lb/ft. The truck with Heumann wheels requires a stiffer primary longitudinal stiffness to achieve the same critical speed as the truck with new wheels due to the higher conicity of the Heumann wheel. The primary longitudinal stiffnesses of the baseline conventional trucks are within the range of typical stiffnesses: 1.0×10^5 lb/ft $< k_{px} < 5.0 \times 10^6$ lb/ft. For instance, the primary spring of UTDC's existing CTA 2400 rapid transit truck has a relatively soft longitudinal stiffness of 2.0×10^5 lb/ft [45]. The standard Rockwell truck used by WMATA has a moderately stiff primary longitudinal stiffness of 1.38×10^6 lb/ft, while the Budd Pioneer III truck has a very stiff primary longitudinal stiffness of 3.5×10^6 lb/ft [27, 2]. Attempts have been made to reduce the longitudinal stiffness through redesign of the primary bushing/shear pad assembly. The proposed primary springs must fit in the space available in the existing trucks. A modified bonded rubber bushing built for the Rockwell truck was designed to achieve a minimum longitudinal stiffness of approximately 3.0×10^5 lb/ft [27]. Metalastick Canada has designed a new primary spring consisting of flat rubber shear pads for the CTA 2400 rapid transit truck with a longitudinal stiffness of 5.0×10^4 lb/ft [2].

3.3.1 Effect of Primary Suspension Stiffness on Curving Performance of Conventional Trucks

This section discusses the influence of primary longitudinal stiffness, k_{px}, and primary lateral stiffness, k_{py}, on the curving

behavior of a conventional truck with new wheels. The effect of k_{px} on the work at the flanging wheel is shown in Figure 3.9 for 2.5°, 5°, 10°, and 20° curves. For shallow and moderate (i.e., 2.5°, 5°, and 10°) curves, the work increases as k_{px} stiffens; for tight (i.e., 20°) curves the work rises sharply and then approaches a constant as k_{px} increases.

At low stiffnesses, i.e., soft k_{px}, the wheelsets are loosely restrained in yaw and can adopt yaw displacements independent of the truck yaw position. Lateral creep forces develop balancing forces from the primary lateral stiffness. At high stiffnesses, equivalent to a rigid wheelset-truck configuration, the work approaches a constant. The increased bending stiffness yaws the wheelsets away from radial alignment. The wheelsets develop longitudinal creep forces to partially counteract the increase in yaw stiffness, and these forces help the wheelsets to yaw toward radial alignment. At very high stiffnesses, the creep forces saturate at the adhesion limit and the work at the flanging wheel reaches a constant. Further increases in k_{px} have negligible effect.

The creep forces are a function of track curvature as well as stiffness. At very small curvatures, the track is essentially tangent and the pure rolling line coincides with, or is just slightly outside of, the track centerline. As the curvature increases, the pure rolling line moves farther out. The leading wheelset attempts to follow it by displacing laterally until it reaches the flange clearance. Two-point tread and flange contact occurs at the outer

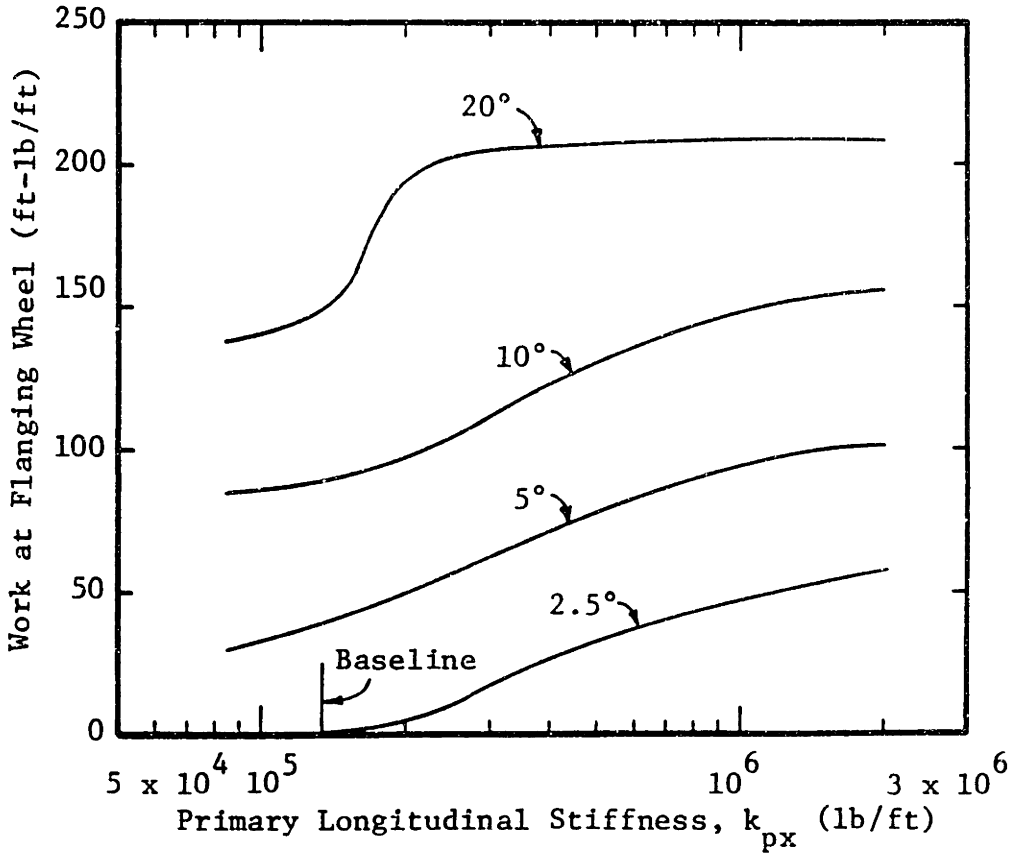

Figure 3.9 Work at Flanging Wheel vs. Primary Longitudinal Stiffness of a Conventional Truck with New Wheels Negotiating 2.5°, 5°, 10°, and 20° Curves.

wheel, with forces at the tread patch dominating. With still tighter curvatures, the leading wheelset lateral excursion remains fixed at the flange clearance. At the outer wheel the forces decrease at the tread contact patch and grow at the flange patch until they saturate at the adhesion limit. In Figure 3.9, the work reaches a constant at the lowest k_{px} for the tight 20° curve since the creep forces saturate faster with increased curvature.

The behavior of the trailing wheelset is also a function of k_{px} (and curvature). In general, with increasing k_{px} the trailing wheelset displaces laterally inward and the angle of attack decreases slightly, as shown schematically in Figure 3.10. The truck stiffens and the wheelsets and truck assume a more rigid configuration. For a tight curve, the trailing wheelset moves from flange contact at the outer wheel for a truck with very soft k_{px} to flange contact at the inner wheel for a rigid truck with stiff k_{px}. Thus, for a conventional truck with new wheels and very soft k_{px} negotiating a tight curve, two-point contact occurs at the leading and trailing outer wheels. For a truck with very stiff k_{px}, two-point contact occurs at the outer wheel of the leading wheelset and the inner wheel of the trailing wheelset. For a shallow curve, the trailing wheelset of a truck with very soft k_{px} does not displace to the flange clearance at the outer wheel. The trailing wheelset displaces inward only slightly as the truck stiffens. Thus, single-point contact occurs at all wheels of a soft truck with new wheels traversing a shallow curve, whereas two-point contact develops at the leading outer wheel of a stiff truck.

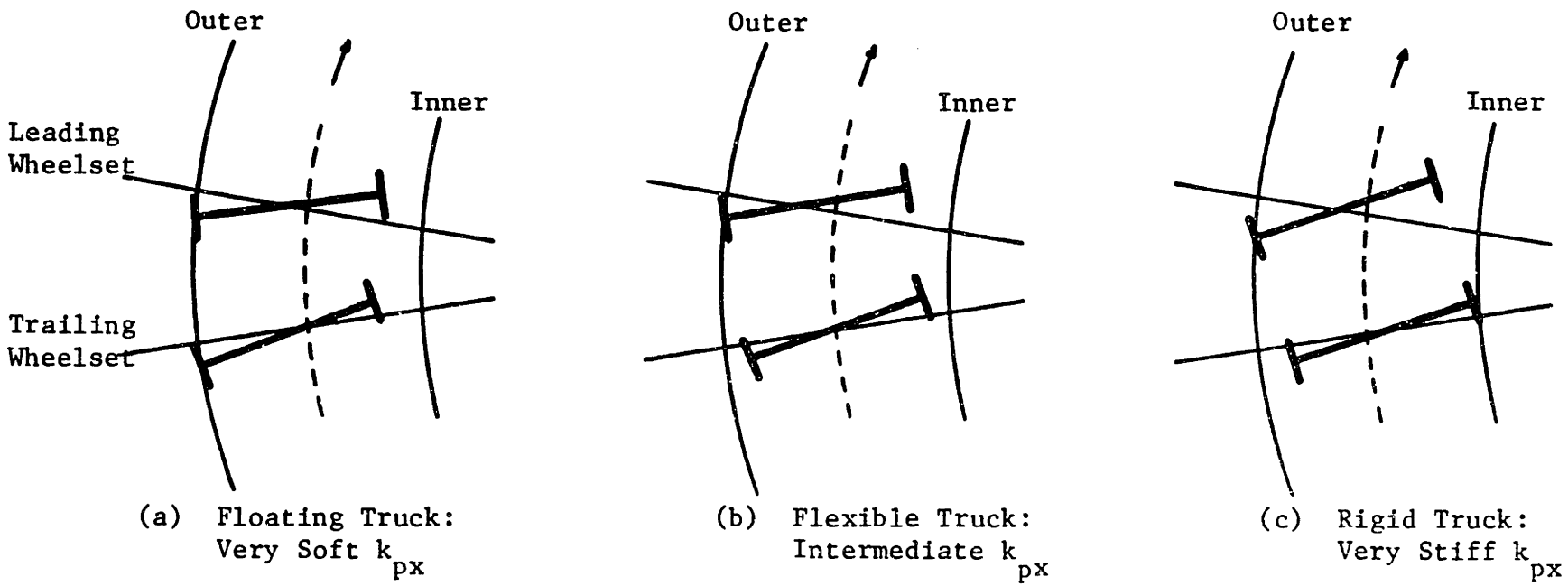

Figure 3.10 Effect of Increasing Primary Longitudinal Stiffness on the Curving Behavior of a Conventional Truck Negotiating a Tight Curve.

The leading wheelset angle of attack of a conventional truck with new wheels as a function of primary longitudinal stiffness and curvature is shown in Figure 3.11. This figure is very similar to Figure 3.9 which shows flanging wheel work. The angle of attack of the leading wheelset increases as k_{px} increases for shallow and moderate degree curves (2.5°, 5°, and 10°); the angle of attack increases sharply and then approaches a constant as k_{px} increases for sharp curves (20°). For very soft k_{px}, the wheelsets are essentially "free" to adopt angles of attack independent of the truck yaw. The predominate creep forces are the lateral creep forces, which are a function of wheelset angle of attack. For positive angles of attack, positive lateral creep forces develop which push the wheelset toward the outer rail. For negative angles of attack, negative lateral creep forces develop which restrain the wheelset from displacing out. A conventional truck with soft k_{px} traversing moderate and tight curves (5°, 10°, and 20° curves) has a positive leading wheelset angle of attack. Thus, the leading wheelset develops positive lateral creep forces which are needed for equilibrium. A truck with soft k_{px} negotiating a shallow (2.5°) curve develops a slightly negative leading wheelset angle of attack. Lateral creep forces develop in the opposite direction to balance the lateral components of primary suspension and normal forces. For stiff k_{px}, the wheelsets are almost rigidly coupled to the truck and follow it in yaw due to the high yaw bending stiffness. Longitudinal creep forces develop which create wheelset yaw moments to help balance

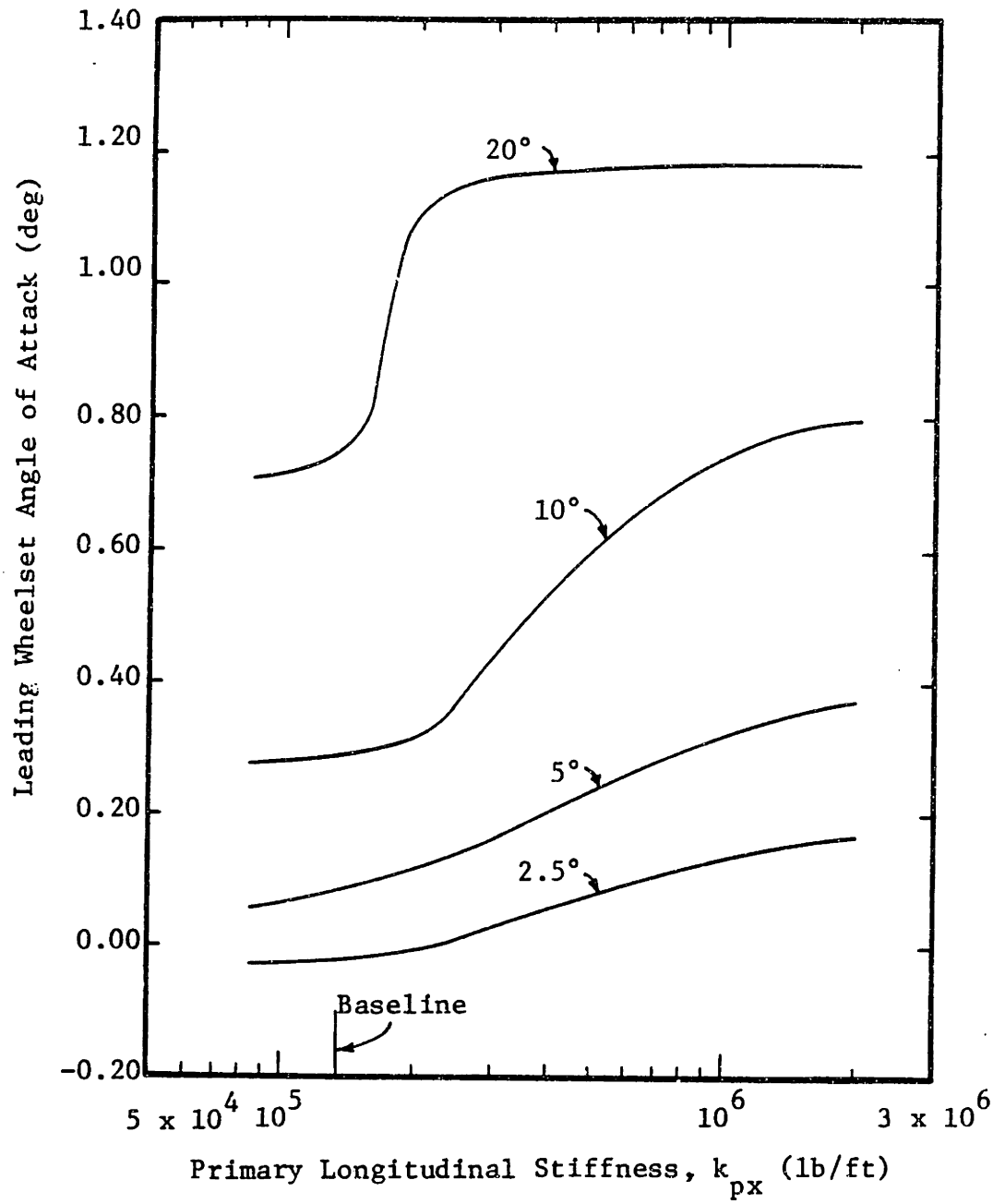

Figure 3.11 Leading Wheelset Angle of Attack vs. Primary Longitudinal Stiffness of a Conventional Truck with New Wheels Negotiating 2.5°, 5°, 10°, and 20° Curves.

the large yaw bending moment from k_{px}. As k_{px} stiffens still further, the longitudinal creep forces grow until the resultant creep force at each contact patch saturates at the adhesion limit. Eventually, the wheelset-truck configuration becomes fully rigid and the wheelset angles of attack approach a constant.

A suspension yaw moment acts on the leading wheelset due to k_{px} and is balanced by a yaw moment provided predominantly by the longitudinal creep forces. As mentioned, for a truck with soft k_{px} the longitudinal creep forces are small (in comparison to the lateral creep forces which are large) corresponding to a small wheelset yaw moment. For a truck with very stiff k_{px} negotiating shallow curves, large longitudinal creep forces develop and thus a large wheelset yaw moment occurs. As this almost-rigid truck negotiates tighter curves, severe flanging at the leading outer wheel occurs and the creep forces at the flange contact patch saturate. Larger lateral creep forces are needed for equilibrium (to balance the larger lateral normal forces) and thus the angle of attack grows. As a result of the creep force saturation and the requirement for larger lateral creep forces, smaller longitudinal creep forces are available and thus the wheelset yaw moment decreases. This information is summarized in Figure 3.12 which shows the effect of primary longitudinal stiffness, curvature, and leading wheelset angle of attack on the leading wheelset yaw moment of a conventional truck with new wheels. The leading wheelset of a truck with soft k_{px} negotiating shallow curves develops small negative angles of attack which correspond to

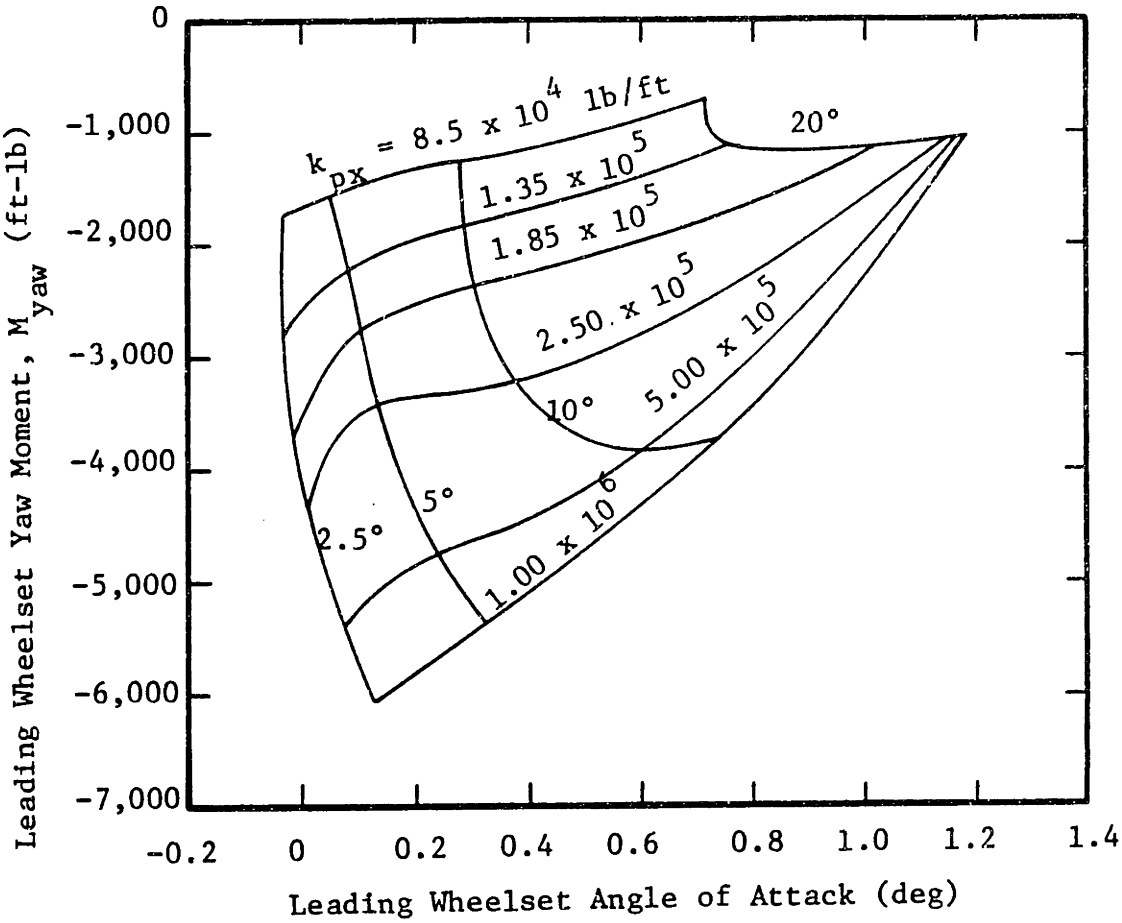

Figure 3.12 Effect of Curvature and Primary Longitudinal Stiffness on the Leading Wheelset Angle of Attack and Yaw Moment of a Conventional Truck with New Wheels.

negative lateral creep forces needed for equilibrium.

The effect of primary longitudinal stiffness and curvature on the leading outer wheel lateral force of a conventional truck with new wheels is shown in Figure 3.13. The leading outer or flanging wheel lateral force is the sum of the lateral components of the creep and normal forces which act at the contact patches of the flanging wheel. As with the work and angle of attack versus stiffness functions (Figures 3.9 and 3.11, respectively), the lateral force (1) increases and then approaches a constant as k_{px} increases, and (2) increases as tighter curves are negotiated. At stiff k_{px}, the creep forces saturate at the adhesion limit and the normal forces approach a constant since the truck assumes a rigid configuration. The leading outer wheel lateral force remains constant with further increases in k_{px}.

Lateral equilibrium of the wheelsets represents a balance of lateral normal forces, lateral creep forces, and primary lateral suspension forces. The latter suspension forces are determined by the primary lateral stiffness and the relative truck-wheelset lateral strokes. These strokes are influenced by the secondary suspension yaw moments exerted on the trucks by the carbody. The moments are normally similar in magnitude, but opposite in directions on the two trucks as shown in Figure 3.14. A positive moment acts on the front truck, which hinders curving by turning the truck toward the outside rail. A negative moment acts on the rear truck, which tends to help curving by steering the truck toward the inside rail. (If secondary

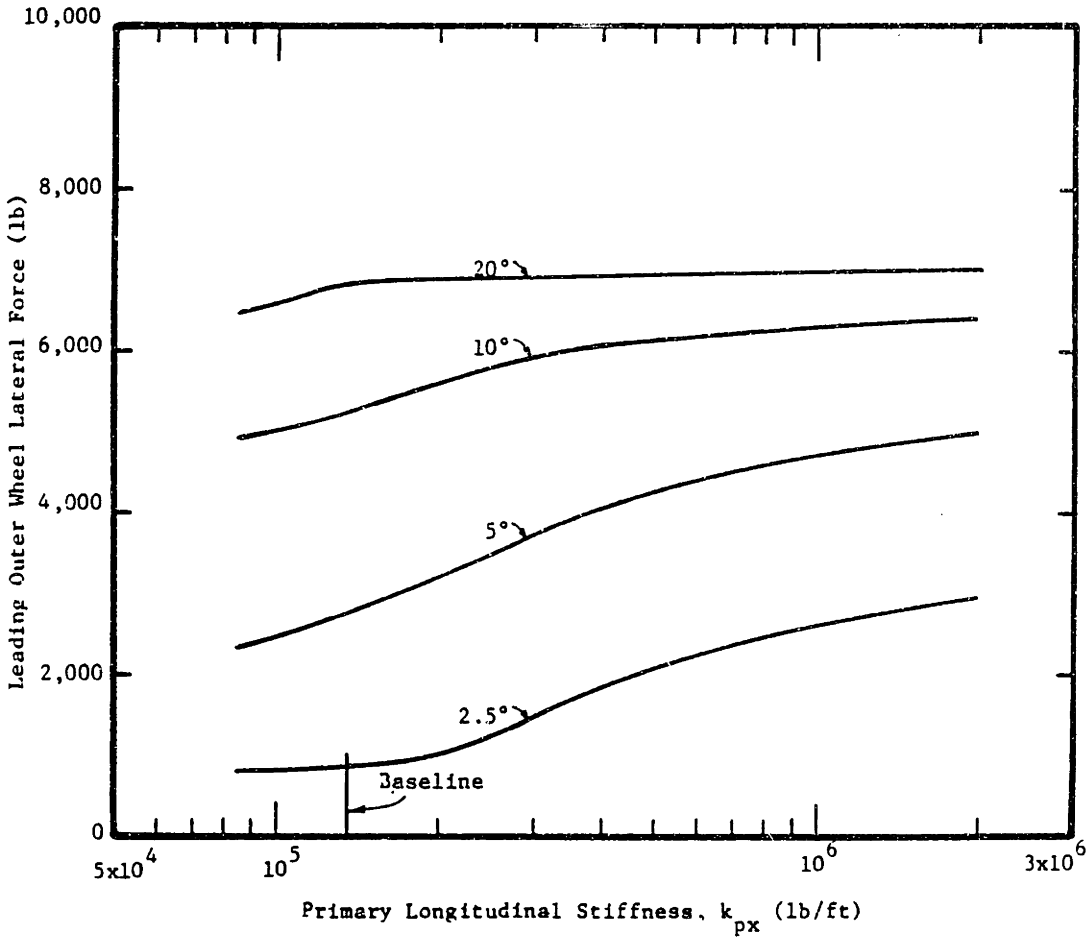

Figure 3.13 Leading Outer Wheel Lateral Force vs. Primary Longitudinal Stiffness of a Conventional Truck with New Wheels Negotiating 2.5°, 5°, 10°, and 20° Curves.

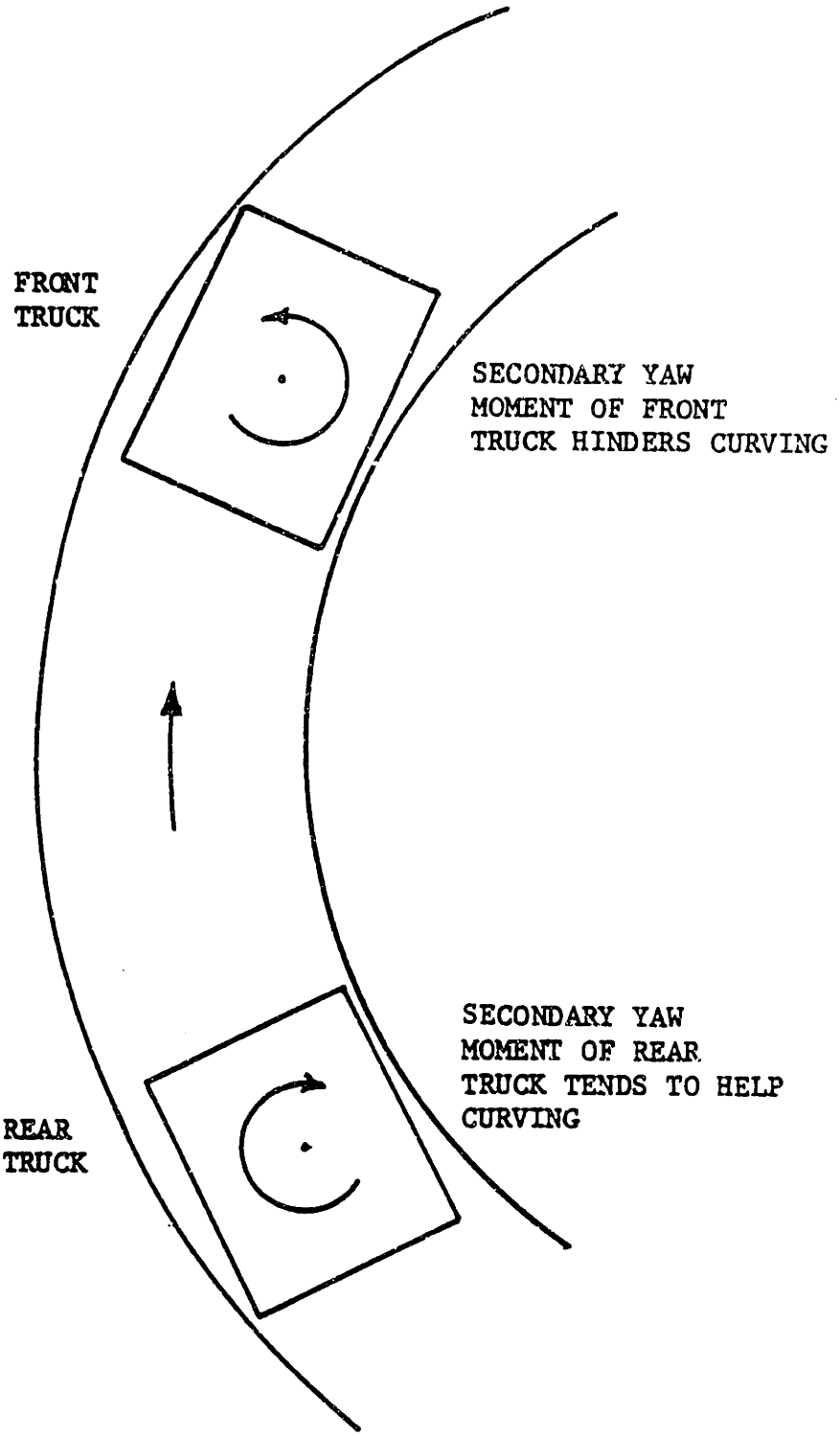

Figure 3.14 Direction of Secondary Yaw Moment on Front and Rear Trucks During Curve Negotiation.

yaw breakaway has already occurred, however, the above moments change direction in the curve exit spiral. This reversal is not considered here.) In summary, the primary lateral suspension forces included in the lateral force equilibrium of a wheelset depend on the yaw moment from the secondary suspension. The secondary suspension yaw moment acting on the front truck degrades curving performance by pushing the leading outer wheel of the front truck into the flange (assuming a moderate or stiff value of primary lateral stiffness, k_{py}). This wheel experiences the most severe flanging of all the wheels of the full vehicle. The effect of secondary yaw breakaway torque on the work at the leading outer wheel is discussed in the next section.

The effect of primary lateral stiffness, k_{py}, on the work at the flanging wheel of a conventional truck with new wheels negotiating a 10° curve is shown in Figure 3.15. As k_{py} increases, the work decreases slightly and approaches a constant. For soft k_{py}, the wheelsets are loosely restrained laterally relative to the truck frame. The leading wheelset displaces laterally to the flange clearance, and two-point wheel/rail contact occurs at the outer wheel. For stiff k_{py}, the lateral displacements of the wheelsets are coupled to the truck position resulting in a laterally rigid configuration. The leading wheelset is still fixed at the flange clearance and two-point contact occurs at the outer wheel. However, the laterally stiffer truck somewhat restrains the wheelset and thus smaller creep forces and work develop.

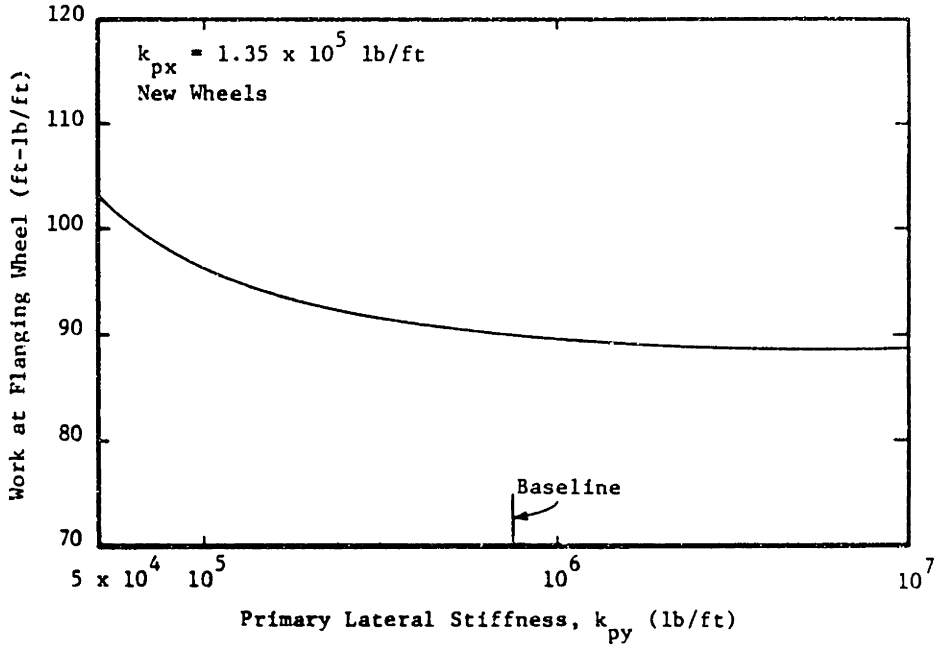

Figure 3.15 Work at Flanging Wheel vs. Primary Lateral Stiffness of a Conventional Truck with New Wheels Negotiating a 10° Curve.

3.3.2 Effect of Secondary Yaw Breakaway on Curving Performance of Conventional Trucks

The interaction of the bolster and truck at the centerplate connection is modelled as a torsional coulomb friction element which saturates at the secondary yaw breakaway torque. Figure 3.16 illustrates the effect of the secondary yaw breakaway torque on the curving performance of a conventional truck with new wheels operating on a 10° curve. As the breakaway torque increases, the work at the leading outer wheel of the front truck increases and the work at the leading outer wheel of the rear truck decreases. This is consistent with the behavior predicted by considering the directions of the yaw breakaway torques on the two trucks, shown in Figure 3.14. On the front truck, the torque acts to steer the truck toward the outer rail. (The lateral and longitudinal creep forces acting on the wheelsets also turn the truck toward the outer rail.) This creates larger forces at the leading outer wheel as well as a larger leading wheelset angle of attack, both of which increase the work. On the rear truck, the torque acts in the opposite direction and relieves the forces at the leading outer wheel and the work decreases. In this thesis, the baseline breakaway torque is 7500 ft-lb, which is a typical transit value [18], and the performance is based on the work at the front truck. Furthermore, it is assumed that secondary yaw breakaway has occurred, which is true for trucks negotiating curves greater than 1°.

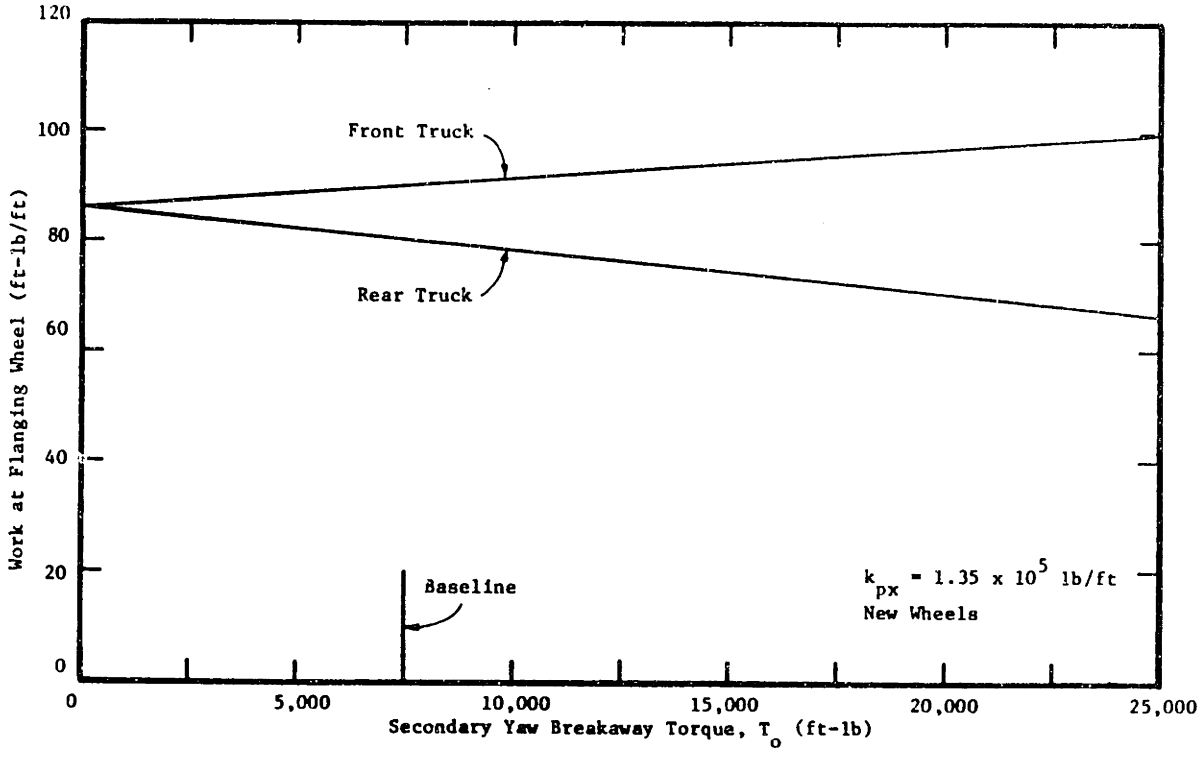

Figure 3.16 Effect of Secondary Yaw Breakaway Torque on the Work at the Flanging Wheel of a Conventional Truck with New Wheels Negotiating a 10° Curve

3.3.3 Effect of Track Curvature and Cant Deficiency on Curving Performance of Conventional Trucks

A conventional truck negotiating a constant radius curve in steady-state conditions is exposed to track curvature and lateral force unbalance inputs. Figures 3.17 and 3.18 show the influence of these two curving inputs on the work at the flanging wheel of a conventional truck with new wheels. In Figure 3.17 the track curvature is varied from 0° for tangent track to 20° for a tight curve of 288 ft radius. For shallow curves (less than 2.5°), the leading wheelset lateral excursion is less than the flange clearance and thus single-point contact occurs. Very little work (less than 1 ft-lb/ft) is expended at the flanging wheel. As the curvature increases (i.e., 2.5° curves and greater), the leading wheelset displaces to the flange clearance and two-point contact occurs at the outer wheel. Significant increases in work occur: at 5°, 10°, and 20° the work is 39, 90, and 149 ft-lb/ft, respectively. The majority of transit curves are less than 7.5°, although some systems have curves as high as 30°.

In Figure 3.18 the work at the flanging wheel of a conventional truck with new wheels negotiating a 10° curve is shown as the cant deficiency is varied from $\phi_d = 0$ for balanced running to $\phi_d = 0.1$ g (corresponding to $\phi_d = 5.7°$). The curving performance is a weak function of cant deficiency. The work increases slightly with increasing cant deficiency. Larger forces develop at the flange contact patch to counteract the increased lateral force on the wheel-

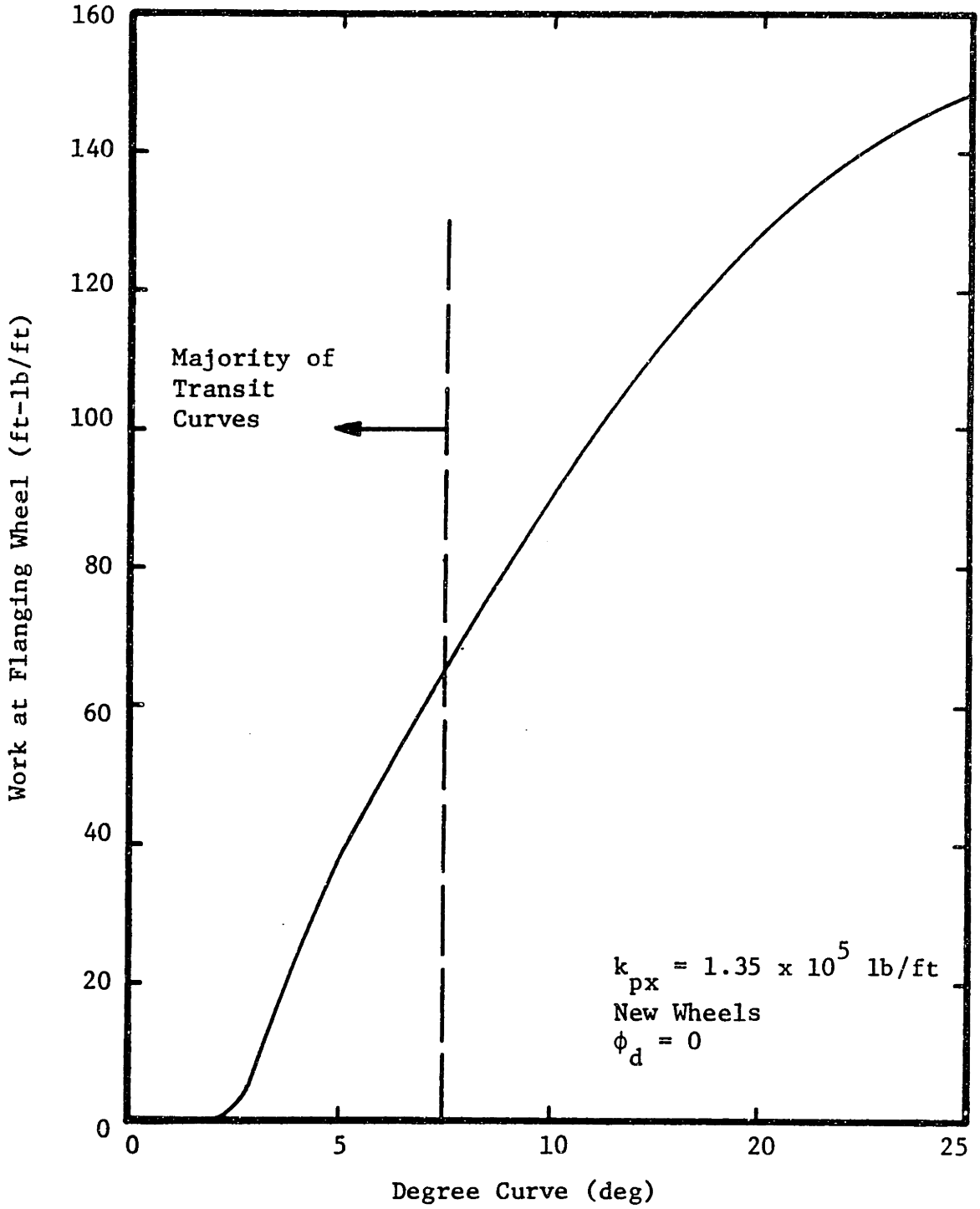

Figure 3.17 Effect of Curvature on the Work at the Flanging Wheel of a Conventional Truck with New Wheels at Balanced Running.

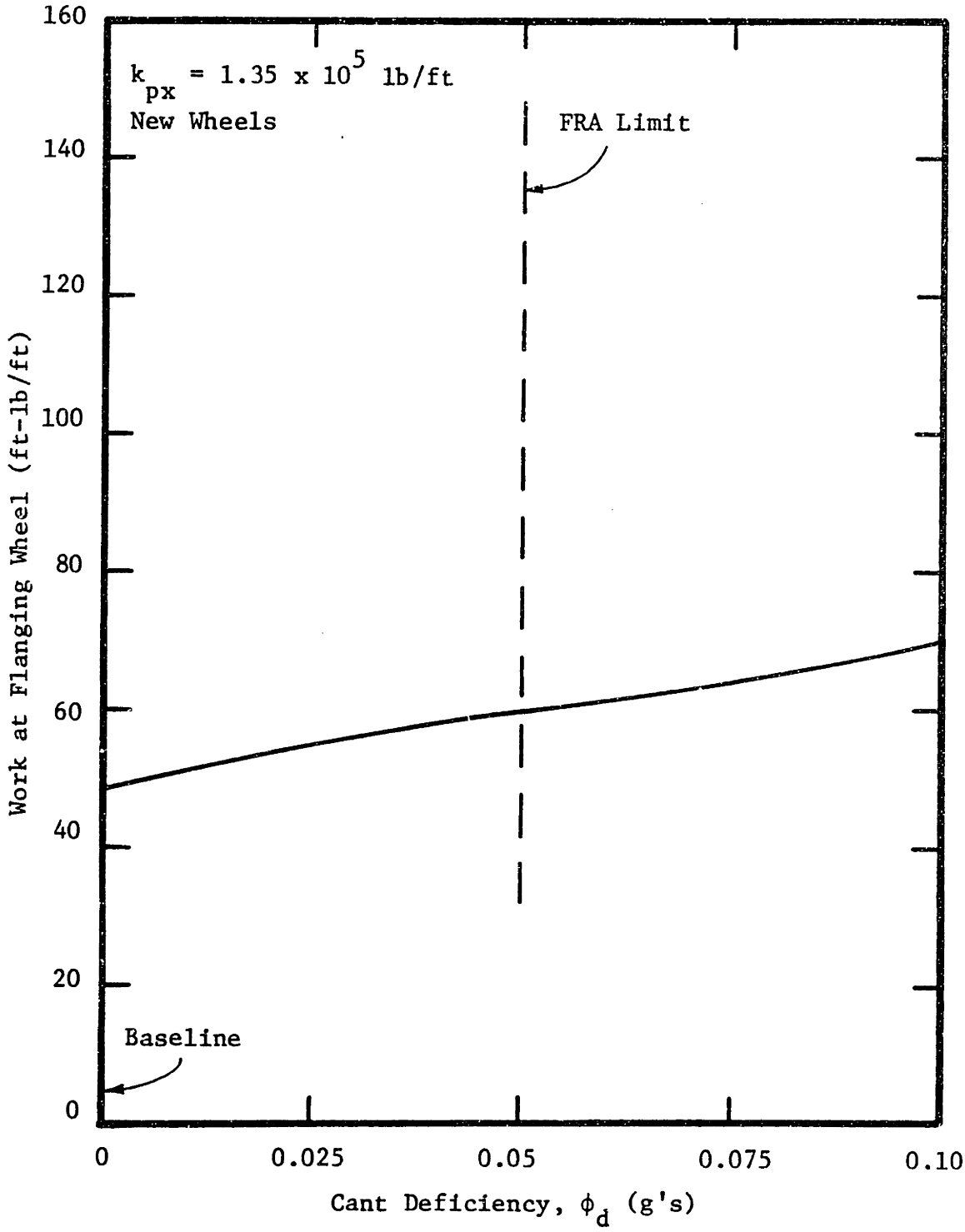

Figure 3.18 Effect of Cant Deficiency on the Work at the Flanging Wheel of a Conventional Truck with New Wheels Negotiating a 10° Curve.

set and, as a result, the work at the flanging wheel increases. Wheel lift at the inner wheel occurs for large cant deficiency, for instance $\phi_d > 0.5$ g which is equivalent to negotiating a 20° curve with a superelevation of 6 in at V > 75 ft/sec. Cant deficiency is the less important of the two curving inputs, especially since it is limited by the Federal Railway Administration to $\phi_d < 0.05$ g [18]. In the steady-state curving studies, it is assumed that the trucks operate at balanced running, i.e., $\phi_d = 0$.

3.3.4 Effect of Creep Coefficients and Coefficient of Friction on Curving Performance of Conventional Trucks

The friction mechanism at each point of wheel/rail contact is modelled by a heuristic nonlinear creep force representation which is described in Appendix A. The creep forces are initially computed using the Kalker Linear Theory [40], but are limited using a cubic saturation scheme to prevent the resultant creep force from exceeding the amount of available adhesion. Studies have shown that the heuristic model provides quite accurate predictions of the creep forces in comparison to more complicated nonlinear analyses [53].

The heuristic method requires as input: (1) linear Kalker creep coefficients, and (2) the wheel/rail coefficient of friction. Figure 3.19 shows the work at the flanging wheel as a function of creep coefficients for a conventional truck negotiating a 10° curve. The creep coefficients are varied from zero to 100 percent of the values predicted by Kalker's Linear theory of creep [40]. With zero creep coefficients, no creep forces develop and thus the work is zero. With

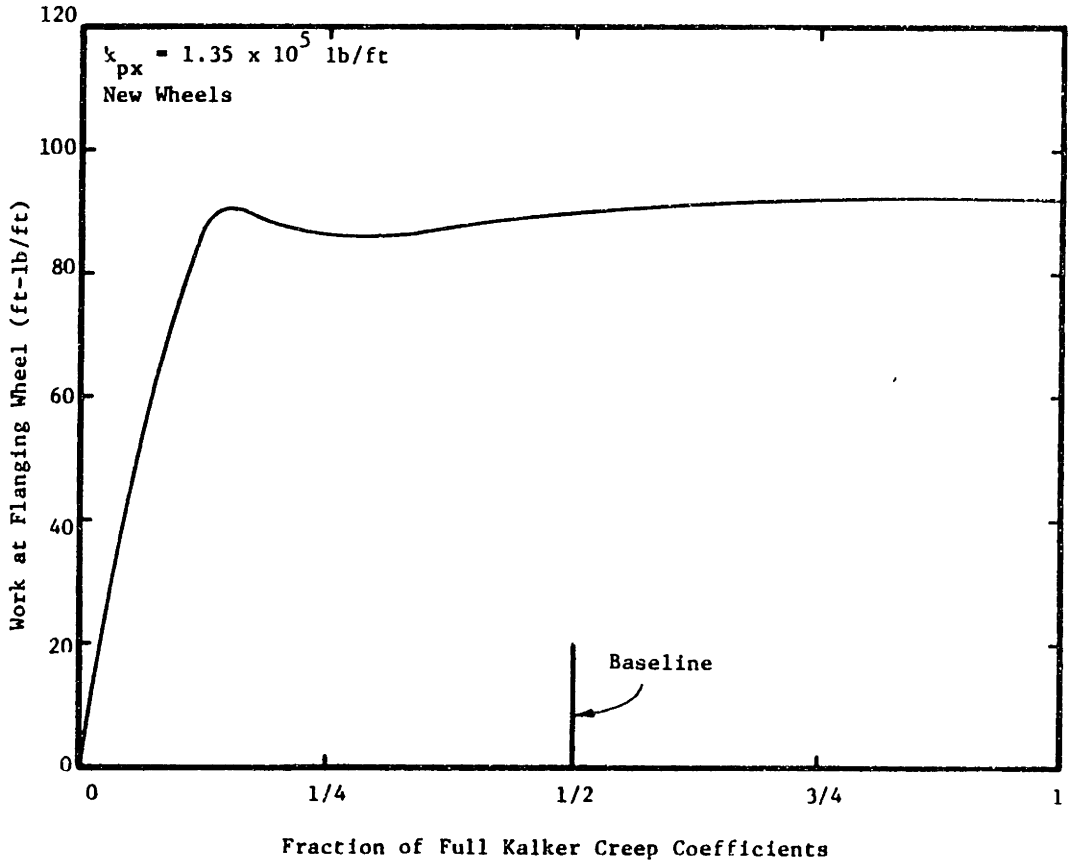

Figure 3.19 Work at Flanging Wheel vs. Fraction of Full Kalker Creep Coefficients for a Conventional Truck with New Wheels Negotiating a 10° Curve

increasing fractions of full Kalker coefficients, the creep forces grow until saturation occurs. Creep forces at the flange contact patch saturate fully for fractions greater than about 1/8. The work is constant with further increases in creep coefficients. Since the curving performance is insensitive to variations in the creep coefficients over a wide range, the use of more sophisticated creep force models would not change the results of the curving analysis.

The magnitude of the resultant creep force is dictated by the coefficient of friction. The influence of the coefficient of friction on the work at the flanging wheel of a conventional truck is shown in Figure 3.20. The performance is virtually linear with the friction coefficient for $\mu < 0.4$. For higher coefficients of friction, $\mu > 0.4$, severe flanging occurs leading to wheel climb and eventually derailment may occur. Field experiments show that the coefficient of friction between wheel and rail varies over a wide range, from $\mu = 0.1$ for wet surfaces to $\mu = 0.6$ for very clean dry surfaces [36]. A baseline value of 0.3 is used in this thesis.

3.3.5 Effect of Axle Drive Torque on Curving Performance of Conventional Trucks

In a conventional transit vehicle, each axle is powered by a drive or traction motor. The traction motor exerts a torque about the spin axis of each wheelset. The influence of the axle drive torque on the work at the flanging wheel of a conventional truck with new wheels negotiating a 10° curve is shown in Figure 3.21. The work remains relatively constant, increasing slightly with drive torque

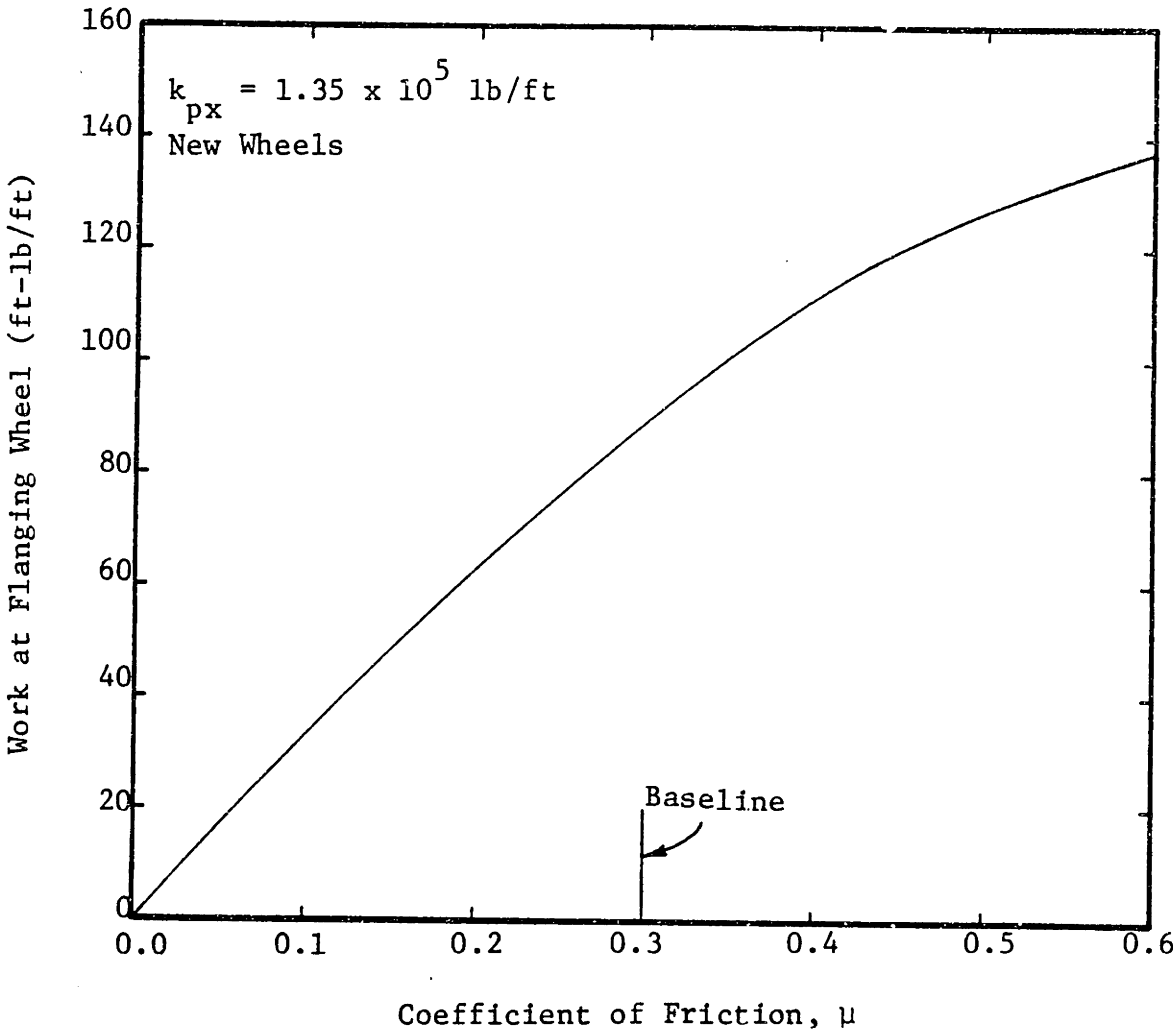

Figure 3.20 Effect of Coefficient of Friction on the Work at the Flanging Wheel of a Conventional Truck With New Wheels Negotiating a 10° Curve.

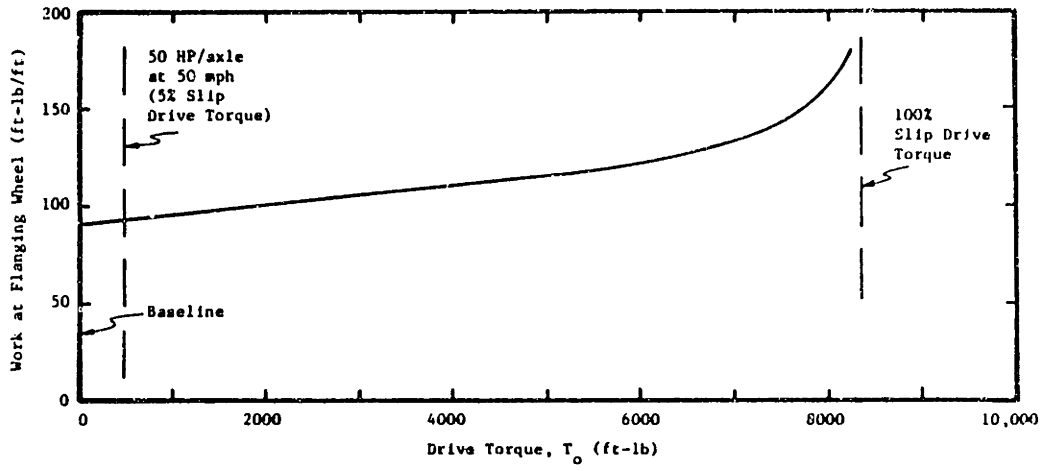

Figure 3.21 Effect of Axle Drive Torque on the Work at the Flanging Wheel of a Conventional Truck with New Wheels Negotiating a 10° Curve

due to longitudinal creepage. As the drive torque increases, it approaches the maximum torque the wheelset can support since the longitudinal creep forces saturate at the wheel/rail friction limit. Significant longitudinal creepage occurs and thus the work index rises sharply.

For a typical transit vehicle with traction motors which provide 50 HP per axle operating at 50 mph, the axle drive torque is 5% of the maximum or slip drive torque. From Figure 3.21, this torque corresponds to the portion of the graph with slightly increasing work. Thus, the drive torque has little influence on steady-state curving performance.

3.3.6 Effect of Rail Flexibility on Curving Performance of Conventional Trucks

A simple model of lateral rail flexibility, discussed in Chapter 2, was used to study the effect of lateral rail stiffness on the steady-state curving performance. In this model the rails deflect laterally due to lateral wheel loads. Table 3.1 compares the influence of flexible and rigid rails on the curving performance of a conventional truck with new wheels negotiating a 10° curve. With flexibility, the high rail deflects out increasing the leading wheelset lateral excursion. However, the wheel/rail forces and work are practically insensitive to rail flexibility.

In the steady-state curving studies, rail flexibility is neglected and the rails are assumed rigid. The rigid rail approximation is

TABLE 3.1

EFFECTS OF RAIL FLEXIBILITY ON THE STEADY-STATE CURVING OF A CONVENTIONAL TRUCK WITH NEW WHEELS NEGOTIATINC A 10° CURVE; $k_{px} = 5.0 \times 10^5$ lb/ft

	Rigid Rail ($k_{flex}=1.0\times10^{10}$ lb/ft)	Flexible Rail ($k_{flex}=5.0\times10^{6}$ lb/ft)
Lead Wheelset Lateral Displacement, y_{w1} (in)	0.3200*	0.3357
Lead Wheelset Angle of Attack, (deg)	0.6000	0.5993
Trailing Wheelset Lateral Displacement, y_{w2} (in)	-0.0922	-0.0763
Trailing Wheelset Angle of Attack (deg)	0.1028	0.1012
Lead Left Rail Lateral Displacement (in)	0.0000	0.0147
Lead Right Rail Lateral Displacement (in)	0.0000	-0.0011
Lead Left Wheel Lateral Force (lb)	-6140.	-6135.
Lead Right Wheel Lateral Force (lb)	3998.	3999.
Work at Lead Left Wheel (ft-lb/ft)	130.	130.
Total Work = Work at all Wheels (ft-lb/ft)	196.	195.

*Flange Clearance

acceptable since the curving performance is measured principally in terms of flanging wheel work.

3.3.7 Effect of Wheel/Rail Profile on Curving Performance of Conventional Trucks

The curving performance of a conventional truck depends on the wheel/rail profile. Figure 3.22 shows the work at the flanging wheel of a conventional truck with Heumann wheels on worn rails as a function of k_{px} for 2.5°, 5°, 10°, and 20° curves. At all curvatures, the flanging wheel work increases and approaches a constant as k_{px} stiffens. Figure 3.22 is similar to Figure 3.9, the graph of flanging wheel work of a conventional truck with new wheels. For a conventional truck with Heumann wheels the baseline value of k_{px} is 6.50×10^5 lb/ft; at this stiffness the critical speed is 120 mph.

For soft k_{px}, the wheelsets are loosely restrained in yaw and the dominant frictional forces are the lateral creep forces. The flanging wheel work is small: less than 5 ft-lb/ft for 2.5°, 5°, and 10° curves, and less than 50 ft-lb/ft for the tight 20° curve. For stiff k_{px}, the wheelsets are locked to the truck frame in yaw. Longitudinal creep forces develop providing a wheelset yaw moment to counteract the large suspension bending stiffness due to the stiff k_{px}. For very stiff k_{px}, the creep forces saturate at the adhesion limit and work becomes a constant. In Figure 3.22, the work approaches a constant for the 20° curve at the lowest k_{px}. In general, creep force saturation occurs at the lowest k_{px} for tighter curves due to larger lateral creep forces which develop for equilibrium.

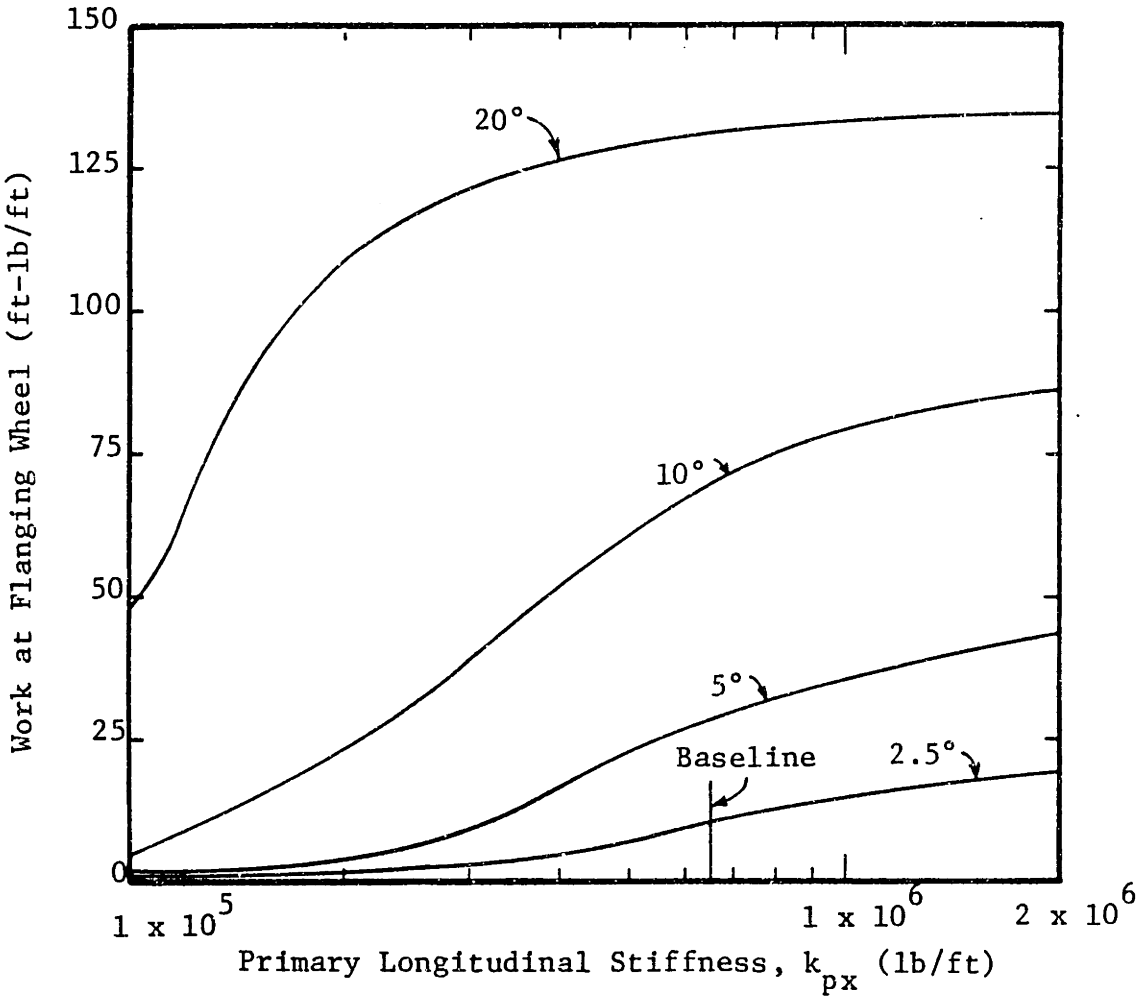

Figure 3.22 Work at Flanging Wheel vs. Primary Longitudinal Stiffness of a Conventional Truck with Heumann Wheels Negotiating 2.5°, 5°, 10°, and 20° Curves.

The wheel/rail profile strongly influences the curving behavior of a conventional truck in terms of flanging wheel work. Table 3.2 shows that for trucks of identical stiffness substantially less work is expended for a conventional truck with Heumann wheels than for a truck with new wheels at all degree curves. The Heumann wheel profile maintains single-point wheel/rail contact at all lateral excursions. For a conventional truck with Heumann wheels, a larger restoring moment is available to help align the wheelsets radially leading to improved curving performance.

TABLE 3.2

THE EFFECT OF NEW AND HEUMANN WHEEL/RAIL PROFILES ON THE WORK AT THE FLANGING WHEEL OF A CONVENTIONAL TRUCK WITH $k_{px} = 5.0 \times 10^5$ lb/ft NEGOTIATING 2.5°, 5°, 10°, and 20° CURVES

Work at Flanging Wheel (ft-lb/ft) / Wheel/Rail Profile	Degree Curve			
	2.5°	5°	10°	20°
New	33	80	130	206
Heumann	8	24	62	130

Table 3.2 shows that the advantage of employing Heumann wheels is greatest at low degree curves. More than a four-fold decrease in flanging wheel work is obtained at 2.5° curves (33 ft-lb/ft for new wheels versus 8 ft-lb/ft for Heumann wheels), whereas less than a two-fold decrease is obtained at 20° curves (206 ft-lb/ft versus 130 ft-lb/ft). The differences in curving behavior decrease with increasing curvature due to the earlier onset of creep force saturation.

3.4 Curving Performance of Self-Steered Radial Trucks

The curving performance of a self-steered radial truck is governed principally by the primary longitudinal suspension stiffness, k_{px}, the interaxle bending stiffness, k_{b2}, the wheel/rail profile, and the track curvature. The stiffness of the primary longitudinal suspension is related to the ability of the wheelsets to align radially. For soft k_{px}, the wheelsets and the truck frame are almost decoupled in yaw. For stiff k_{px}, the wheelsets and the truck frame are almost locked in a rigid configuration in yaw which prevents the wheelsets from independently adopting radial orientations.

In a self-steered radial truck, the interaxle bending stiffness, k_{b2}, provides direct communication between the wheelsets. Steering action results when k_{b2} is soft and the interaxle shear stiffness, k_{s2}, is stiff. The stiff shear spring increases the total truck shear stiffness of the self-steered truck above the value achievable

by the conventional truck, offering the possibility of improved curving (and stability) performance. A yaw motion of one wheelset causes the other wheelset to yaw in the opposite direction, helping the wheelsets to align radially in curves.

For a self-steered truck as for a conventional truck, the wheel/rail profile is important since it dictates the character of the wheel/rail contact. The profile geometry determines whether or not two-point contact can potentially occur at the flanging wheel.

3.4.1 Effect of Primary Longitudinal Suspension Stiffness on Curving Performance of Self-Steered Radial Trucks

As the primary longitudinal stiffness, k_{px}, of a self-steered radial truck increases, more contact work is expended and thus the curving performance is degraded. Figure 3.23 shows the work at the flanging wheel of a self-steered truck with low interaxle bending stiffness, $k_{b2} = 1.0 \times 10^3$ ft-lb/rad, and high interaxle shear stiffness, $k_{s2} = 1.0 \times 10^6$ lb/ft, as a function of k_{px} and track curvature. At all curvatures, the flanging wheel work rises with increasing k_{px} and approaches a constant. Similar behavior was observed for the conventional truck. However, for the self-steered radial truck, some steering action is provided due to the interaxle stiffnesses.

The higher total truck shear stiffness of the self-steered truck is advantageous for negotiation around tight curves. From Figures 3.9 and 3.23, less work is expended for the self-steered

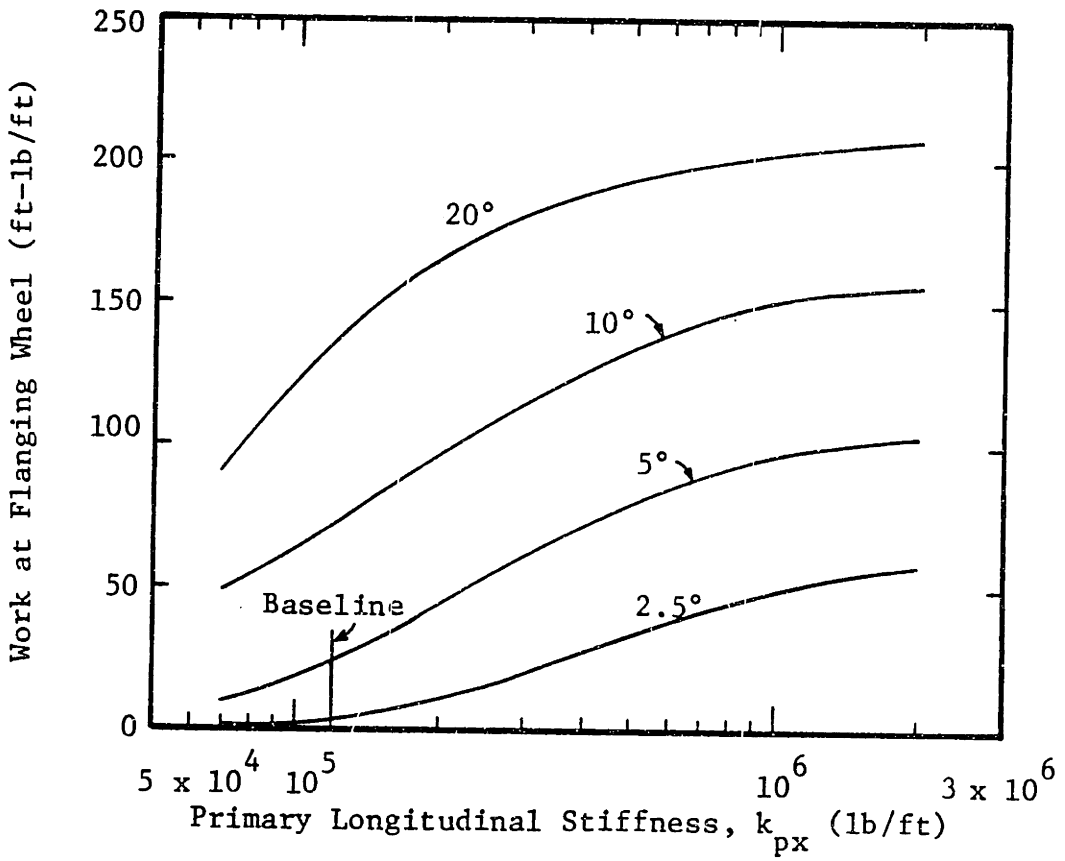

Figure 3.23 Work at Flanging Wheel vs. Primary Longitudinal Stiffness of a Self-Steered Radial Truck with New Wheels Negotiating 2.5°, 5°, 10°, and 20° Curves.

radial truck than for the conventional truck negotiating 20° curves. For shallow and moderate curves, insignificant differences in flanging wheel work occur between the conventional and self-steered radial trucks, especially at stiff k_{px}. For low degree curves, the conventional truck is desirable since its low total truck shear stiffness helps to minimize wheelset lateral excursions and angles of attack. In contrast, the high total truck shear stiffness of the self-steered truck can keep the leading wheelset at the flange clearance resulting in more work at the outer wheel, as will be discussed later.

3.4.2 Effect of Wheel/Rail Profile on Curving Performance of Self-Steered Radial Trucks

The steady-state curving performance of a self-steered radial truck is influenced strongly by the wheel/rail profile. In Figure 3.24, the work at the flanging wheel of a self-steered radial truck with Heumann wheels on worn rails is shown as a function of k_{px}. The figure demonstrates the characteristic behavior of increasing flanging wheel work with increasing k_{px}. However, in comparison to the work of a self-steered truck with new wheels shown in Figure 3.23, less work is expended at the same stiffness for all degree curves. Results are summarized in Table 3.3 for a stiffness of $k_{px} = 5.0 \times 10^5$ lb/ft. The single-point contact Heumann wheel profile is responsible for the improvement in curving performance. As with the conventional truck, the advantage of employing Heumann wheels in comparison to new wheels decreases with tighter curves.

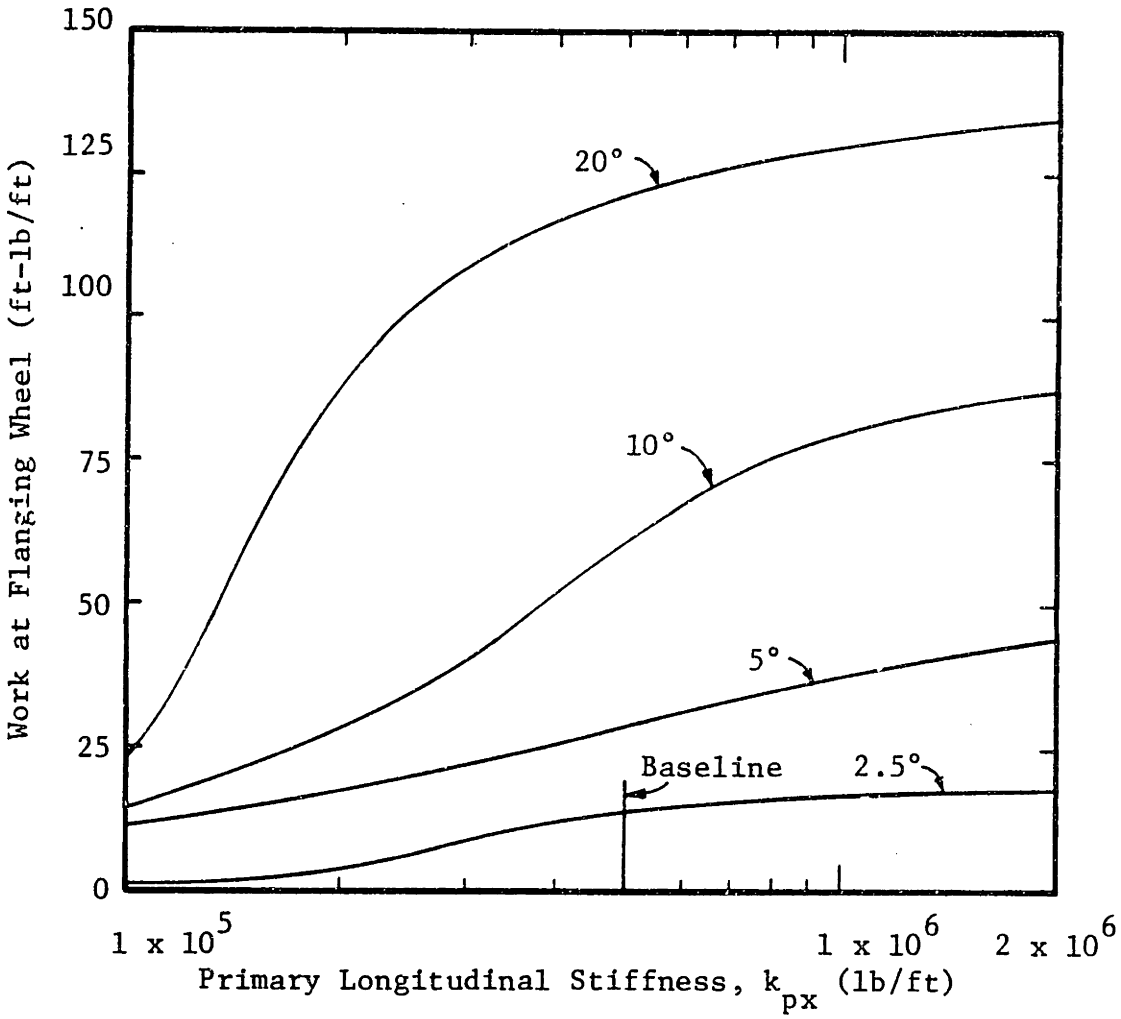

Figure 3.24 Work at Flanging Wheel vs. Primary Longitudinal Stiffness of a Self-Steered Radial Truck with Heumann Wheels Negotiating 2.5°, 5°, 10°, and 20° Curves.

TABLE 3.3

THE EFFECT OF NEW AND HEUMANN WHEEL/RAIL PROFILES ON THE WORK AT THE FLANGING WHEEL OF A SELF STEERED RADIAL TRUCK NEGOTIATING 2.5°, 5°, 10°, and 20° CURVES WITH STIFFNESSES: k_{px} = 5.0 x 10^5 lb/ft, k_{b2} = 1.0 x 10^3 ft-lb/rad, k_{s2} = 1.0 x 10^6 lb/ft.

Work at Flanging Wheel (ft-lb/ft) / Wheel/Rail Profile	Degree Curve			
	2.5°	5°	10°	20°
New	34	81	131	194
Heumann	14	29	61	122

For a shallow 2.5° curve, the work is 14 ft-lb/ft for Heumann wheels versus 3 ft-lb/ft for new wheels. For a tight 20° curve, the work is 122 ft-lb/ft for the Heumann wheels versus 194 ft-lb/ft for new wheels. The relative advantage of the truck with Heumann wheels decreases as track curvature increases due to creep forces which saturate earlier.

The trucks with new and Heumann wheels compared in Table 3.3 have the same stiffness but different stability properties. To obtain identical critical speeds, the truck with Heumann wheels

must be made stiffer than the truck with new wheels. The baseline value of k_{px} for a self-steered radial truck with new wheels is 1.20×10^5 lb/ft, and for a truck with Heumann wheels is 5.00×10^5 lb/ft. The baseline interaxle stiffnesses are: $k_{b2} = 1.0 \times 10^3$ ft-lb/rad and $k_{s2} = 1.0 \times 10^6$ lb/ft. At these values, the critical speeds are 120 mph.

The self-steered radial truck of Table 3.3 is obtained by adding interaxle stiffnesses to the conventional truck of Table 3.2. The resulting radial truck has a higher total shear stiffness (and a slightly higher bending stiffness) which is intended to improve the curving performance. The higher shear stiffness of the radial truck makes it slightly better for negotiating tight curves by helping to minimize the leading wheelset angle of attack and lateral force during flanging. For example, by adding interwheelset stiffnesses the work decreases from 206 to 194 ft-lb/ft for trucks with new wheels and from 130 to 122 ft-lb/ft for trucks with Heumann wheels negotiating 20° curves. However, the added shear stiffness increases the work for negotiation of shallow curves by forcing the leading wheelset into the flange and creating an increased angle of attack. For instance, by converting to the self-steered configuration the work rises from 33 to 34 ft-lb/ft for trucks with new wheels and from 8 to 14 ft-lb/ft for trucks with Heumann wheels negotiating 2.5° curves.

The work of the conventional and self-steered radial trucks with new wheels is essentially identical for negotiation of low

and moderate degree curves. For trucks with new wheels, two-point contact occurs at the leading outer wheels since the leading wheelset excursions equal the flange clearance. The added shear stiffness of the radial truck changes only slightly the distribution and magnitude of forces at the two contact patches of the flanging wheel. As a result, the work remains essentially constant. In contrast, more work is expended for the self-steered radial truck with Heumann wheels than for the conventional truck with Heumann wheels for negotiation of low and moderate degree curves. For trucks with Heumann wheels, single-point contact occurs at the flanging wheel. The lower truck shear stiffness of the conventional truck minimizes the leading wheelset excursion and angle of attack, and thus the work at the flanging wheel is less for the conventional truck than for the self-steered radial truck.

3.5 Curving Performance of Forced-Steered Radial Trucks

Vehicles with forced-steered radial trucks employ passive linkages between the wheelsets and carbody to sense track curvature and steer their wheelsets into radial alignment accordingly. The curving performance of these vehicles is a function of the primary longitudinal stiffness, the effective interaxle bending stiffness (due to forced-steering linkages), the steering action gain, the wheel/rail profile, and the track curvature. In these studies, an L-type forced-steered radial truck has been used with the curvature steering gain set to the pure rolling line gain, G_{prl}. The gain

G_{prl} is the appropriate gain required for the wheelsets to track the pure rolling line and achieve radial alignment, based on kinematic arguments which assume rigid steering linkages. Due to nonrigid linkages and the action of flange forces, however, the pure rolling line gain can result in imperfect steering of the wheelsets, as discussed later in this section.

The curving properties of a forced-steered truck are not unique since different combinations of primary longitudinal stiffness, k_{px}, and effective interaxle bending stiffness, k_{b2}, can result in the same total stiffness. The stability properties of a forced-steered truck are not unique since different combinations of k_{px} and k_{b2} can yield the same critical speed. For these reasons, two forced-steered truck designs are studied. Both designs represent trucks with soft k_{px}, which is advantageous for curving performance; the interwheelset and wheelset-carbody linkages provide the requisite stiffness for stability. The two designs are (1) FSR I with $k_{px} = 7.0 \times 10^4$ lb/ft, and (2) FSR II with $k_{px} = 1.0 \times 10^3$ lb/ft. In the curving performance studies of each truck, the primary longitudinal stiffness is assumed constant and the interaxle bending stiffness (or equivalently the linkage stiffness) is the design parameter.

The primary longitudinal stiffnesses of the two forced-steered truck designs are softer than those typically used in current transit trucks. There is, however, significant interest in designing trucks with reduced primary suspension stiffnesses. For instance, a primary spring has been designed for UTDC with a very soft longitudinal

stiffness of $k_{px} = 5.0 \times 10^4$ lb/ft [45]. The spring, consisting of an assembly of rubber shear pads, is for potential use on the CTA 2400 rapid transit truck. The soft primary suspensions of the two forced-steered truck designs have been selected to study the effect of reducing k_{px} on the curving performance of forced-steered trucks.

3.5.1 Effect of Effective Interaxle Bending Stiffness on Curving Performance of Forced-Steered Radial Trucks

The curving performance of forced-steered trucks is influenced by the stiffness of the forced-steering linkages or, equivalently, by the effective interaxle bending stiffness, k_{b2}. Figures 3.25 and 3.26 show the flanging wheel work as a function of k_{b2} for the two forced-steered truck designs, FSR I and FSR II, with new wheels. The curving performance is relatively insensitive to changes in k_{b2} for negotiation of low degree curves (2.5° for FSR I; 2.5° and 5° for FSR II). For soft k_{b2}, the wheelsets maintain almost radial orientations due to longitudinal creep forces which overcome the small yaw bending resistance and self-steered behavior is approached. For stiffer k_{b2}, the wheelsets are more restrained in yaw and the forced steering action is used to achieve radial alignment. For negotiation of higher degree curves, the flanging wheel work rises slightly with increasing k_{b2}. The pure rolling line gain, which was selected to kinematically align the wheelsets radially, slightly understeers the leading wheelset, as will be addressed later. With increasing k_{b2}, the leading wheelset adopts a slightly increasing positive angle of attack due to insufficient steering action and the

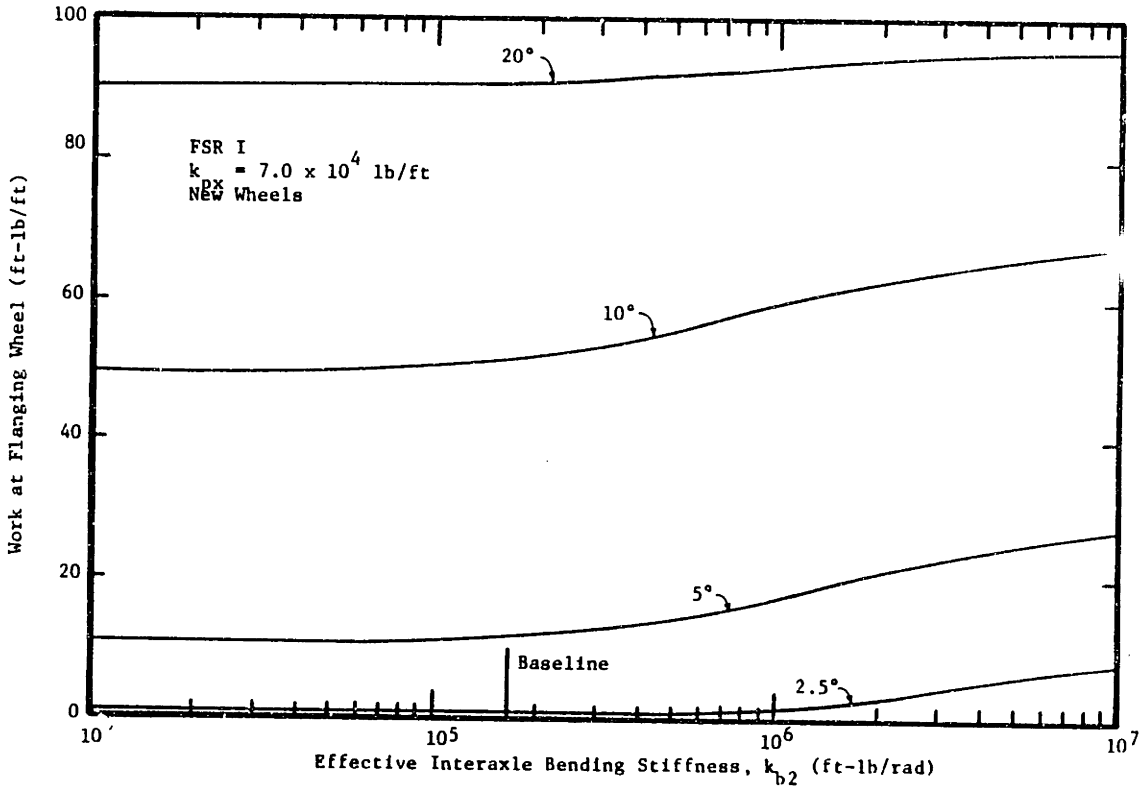

Figure 3.25: Work at Flanging Wheel vs. Interaxle Bending Stiffness of a Forced-Steered Radial Truck, FSR I, with New Wheels Negotiating 2.5°, 5°, 10°, and 20° Curves.

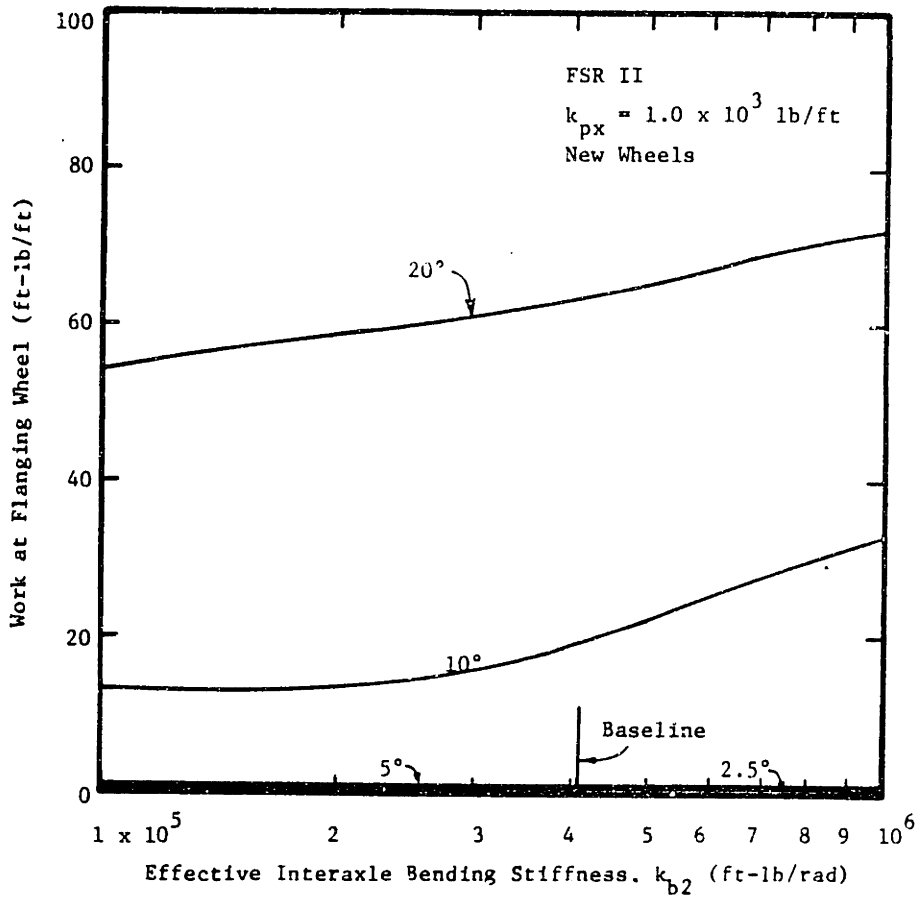

Figure 3.26 Work at Flanging Wheel vs. Interaxle Bending Stiffness of a Forced-Steered Radial Truck, FSR II, with New Wheels Negotiating 2.5°, 5°, 10°, and 20° Curves.

flanging wheel work increases slightly.

For forced-steered trucks negotiating moderate and tight curves, the flanging wheel work increases slightly with increasing k_{b2}. However, the increase in work is minimized by the action of forced-steering, as demonstrated in Figure 3.27. The flanging wheel work of a FSR I forced-steered radial truck with new wheels negotiating a 10° curve, reproduced from Figure 3.25, is compared to the work associated with a truck with no forced steering (G = 0), i.e., a self-steered radial truck. As k_{b2} increases, the creep forces are not sufficient to steer the wheelsets of the self-steered truck and the leading wheelset angle of attack increases. As a result, the flanging wheel work rises. For stiff k_{b2}, the wheelsets are rigidly connected. The creep forces at the flanging wheel saturate and the work reaches a constant. The work increases over 300% in the transition from very soft to very stiff interaxle bending stiffness. In comparison, for the forced-steered truck (with new wheels), the angle of attack increases slightly with increasing k_{b2} resulting in a 35% increase in the flanging wheel work. Figure 3.27 also demonstrates the importance of designing a self-steered radial truck with soft k_{b2} to permit the wheelsets to yaw due to action of the longitudinal creep forces.

A comparison of Figures 3.25 and 3.26 shows that the work for the FSR I forced-steered truck is greater than the work for the FSR II truck at all degree curves. The FSR I truck has a stiffer k_{px} and thus a larger yaw bending stiffness than the FSR II truck.

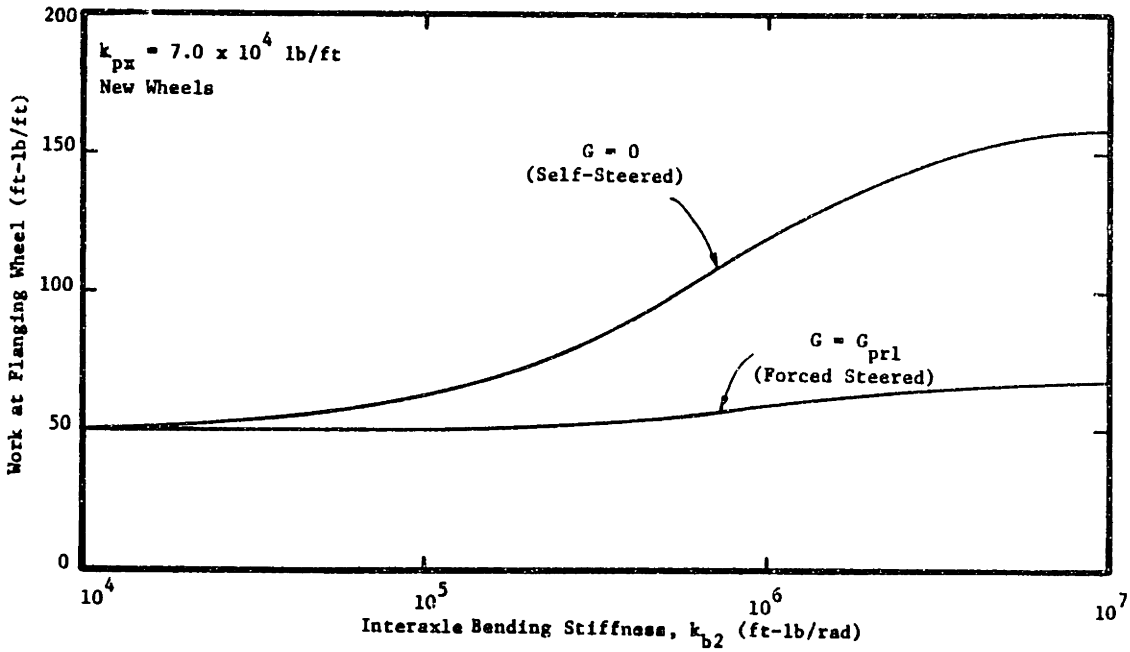

Figure 3.27 Work at Flanging Wheel vs. Interaxle Bending Stiffness of Self-Steered and Forced-Steered Radial Trucks with New Wheels Negotiating 10° Curves.

The forced steering action must overcome this additional bending resistance in the FSR I truck. As a result, the FSR I truck does not steer the wheelsets as successfully and the flanging wheel work is greater.

3.5.2 Effect of Wheel/Rail Profile on Curving Performance of Forced-Steered Radial Trucks

The curving performance of forced-steered trucks depends strongly on the choice of wheel/rail profile. Figures 3.28 and 3.29 show the work at the flanging wheel of the two forced-steered truck designs with Heumann wheels on worn rails. These figures demonstrate that the work for forced-steered trucks with Heumann wheels is substantially reduced in comparison to the work for trucks with new wheels shown in Figures 3.25 and 3.26. From Figure 3.28 for the FSR I truck with Heumann wheels, the work to negotiate shallow curves increases slightly with increasing k_{b2} but always is small (less than 2 ft-lb/ft for the 2.5° curve and less than 3 ft-lb/ft for the 5° curve). For the tighter (10° and 20°) curves, the work decreases slightly with increasing k_{b2}. For the 20° curve, more work is expended at the outer wheel of the trailing wheelset than the outer wheel of the leading wheelset, and thus the work at the trailing outer wheel is reported. For the FSR II truck with Heumann wheels shown in Figure 3.29, the work is essentially insensitive to changes in k_{b2}. For shallow curves, the work decreases insignificantly with increasing stiffness. The work associated with negotiation of the 2.5°, 5° and 10° curves is very small, less than 2.5 ft-lb/ft. Again,

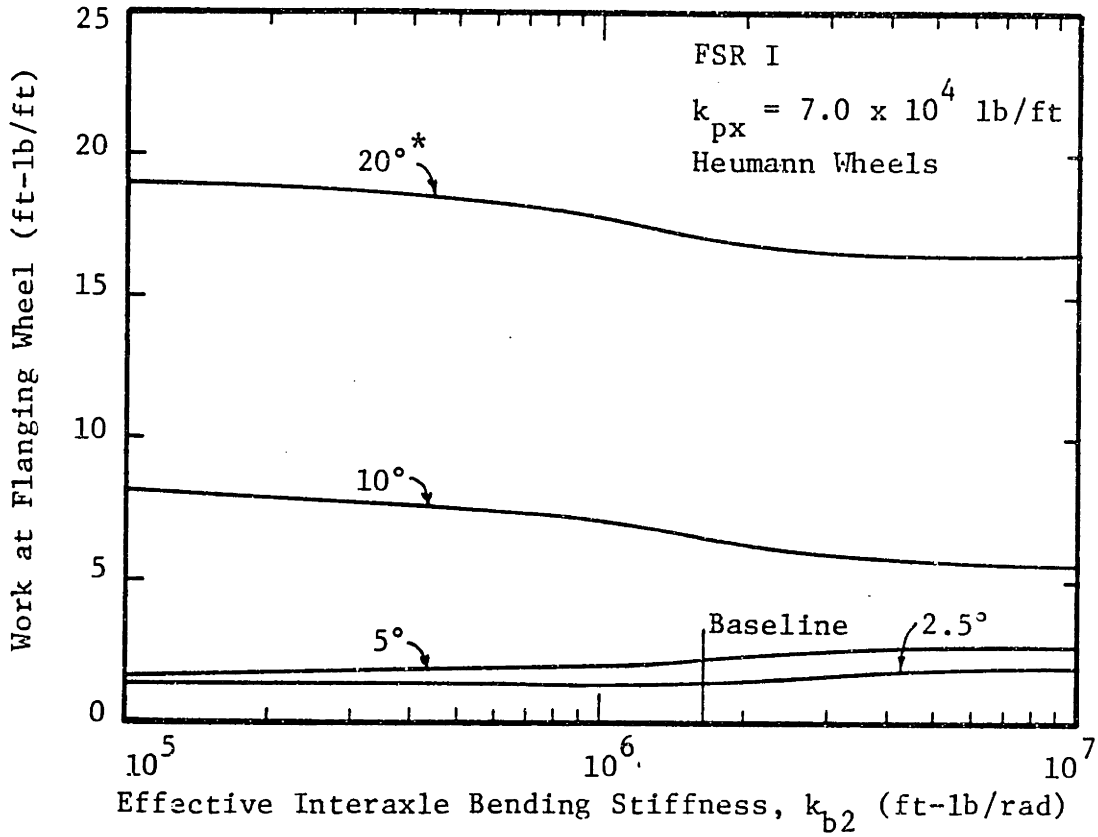

Figure 3.28 Work at Flanging Wheel vs. Interaxle Bending Stiffness of a Forced-Steered Radial Truck, FSR I, with Heumann Wheels Negotiating 2.5°, 5°, 10°, and 20° Curves. (*Work at Trailing Outer Wheel)

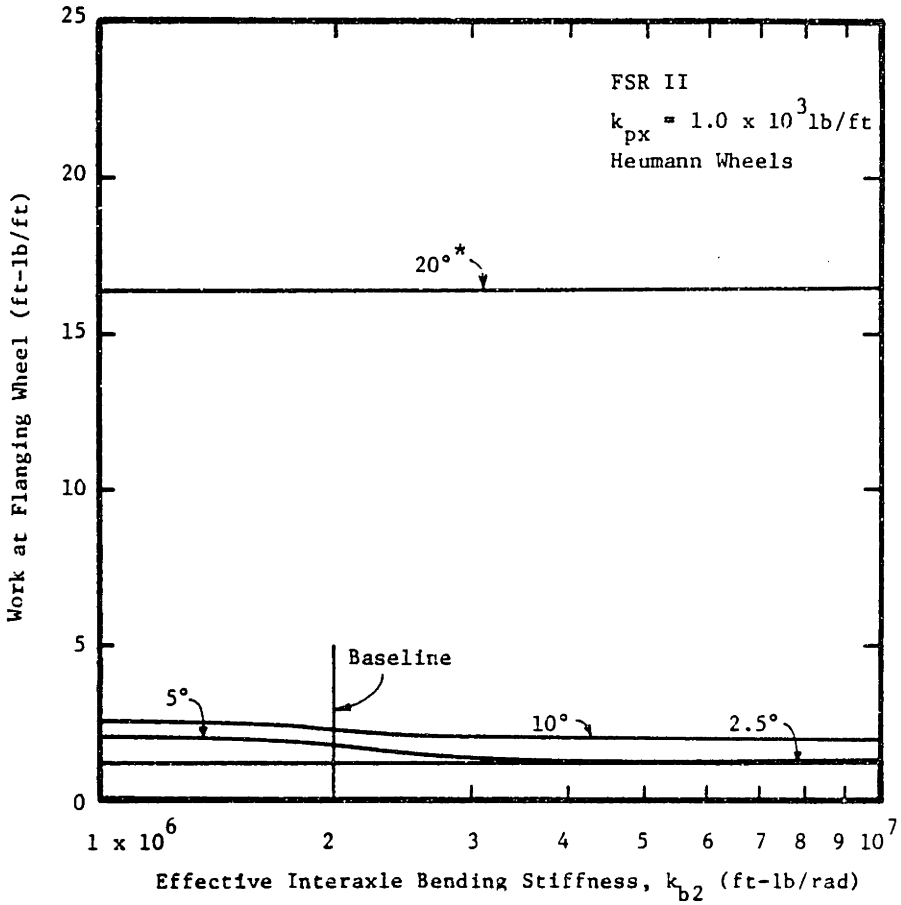

Figure 3.29 Work at Flanging Wheel vs. Interaxle Bending Stiffness of a Forced-Steered Radial, FSR II, with Heumann Wheels Negotiating 2.5°, 5°, 10°, and 20° Curves (*Work at Trailing Outer Wheel).

the work at the trailing outer wheel exceeds the work at the outer wheels for the 20° curve.

For forced-steered trucks with Heumann wheels the work decreases with increasing k_{b2} due to effective steering of the wheelsets. As k_{b2} stiffens, the steering linkages become more rigid and "force" the wheelsets into radial alignment. For the Heumann wheel, the pure rolling line steering gain results in almost perfect steering; actually, slight understeering occurs at high degree curves.

The stiffness of baseline forced-steered truck designs (i.e., designs with 120 mph critical speeds) are listed in Table 3.4 and are marked in Figures 3.25, 3.26, 3.28, and 3.29. The curving performances of the two forced-steered truck designs with new and Heumann wheels and identical interaxle stiffnesses are summarized in Tables 3.5 and 3.6 for the FSR I and FSR II trucks, respectively. These tables demonstrate the potential improvement in curving performance possible by using Heumann wheel profiles rather than new wheel profiles. The single-point contact Heumann profile develops less work and is advantageous for curving.

Tables 3.5 and 3.6 can be used to compare the two truck designs with the same wheel profile since the trucks have identical interaxle stiffnesses k_{b2} and k_{s2}. For the new and Heumann wheel profiles, less work develops for the FSR II design, with the lower k_{px}, than the FSR I design. With new wheels, the work to negotiate a 10° curve is 60 ft-lb/ft for the FSR I design versus 33 ft-lb/ft

for the FSR II design; with Heumann wheels, the work is 7 ft-lb/ft for the FSR I design versus 3 ft-lb/ft for the FSR II design. The FSR II design has minimal wheelset yaw bending resistance due to its very low primary stiffness, and thus the forced steering action can effectively align the wheelsets radially.

TABLE 3.4

INTERAXLE BENDING STIFFNESSES FOR BASELINE FORCED STEERED RADIAL TRUCK DESIGNS WITH DIFFERENT WHEEL/RAIL PROFILES ALL HAVING CRITICAL SPEEDS OF 120 MPH.

k_{b2} (ft-lb/rad) / Profile	FSR I $k_{px} = 7.0 \times 10^4$ lb/ft $k_{s2} = 1.0 \times 10^6$ lb/ft	FSR II $k_{px} = 1.0 \times 10^3$ lb/ft $k_{s2} = 1.0 \times 10^6$ lb/ft
New Wheel	1.68×10^5	4.10×10^5
Heumann Wheel	1.66×10^6	2.00×10^6

TABLE 3.5

The Effect of New and Heumann Wheel/Rail Profiles
On the Work at the Flanging Wheel of a Forced Steered
Radial Truck, FSR I, Negotiating 2.5°, 5°, 10°, and
20° Curves with Stiffnesses:
$k_{px} = 7.0 \times 10^4$ lb/ft, $k_{b2} = 1.0 \times 10^6$ ft-lb/rad, $k_{s2} = 1.0 \times 10^6$ lb/ft

Work at Flanging Wheel (ft-lb/ft) / Wheel/Rail Profile	Degree Curve			
	2.5°	5°	10°	20°
New	1	18	60	93
Heumann	1	2	7	19

TABLE 3.6

The Effect of New and Heumann Wheel Rail Profiles
On the Work at the Flanging Wheel of a Forced Steered
Radial Truck, FSR II, Negotiating 2.5°, 5°, 10°, and
20° Curves with Stiffnesses:
$k_{px} = 1.0 \times 10^3$ lb/ft, $k_{b2} = 1.0 \times 10^6$ ft-lb/rad, $k_{s2} = 1.0 \times 10^6$ lb/ft

Work at Flanging Wheel (ft-lb/ft) / Wheel/Rail Profile	Degree Curve			
	2.5°	5°	10°	20°
New	1	2	33	72
Heumann	1	2	3	16

3.5.3 Effect of Curvature Steering Gain on Curving Performance of Forced-Steered Radial Trucks

For a forced-steered truck with stiff k_{b2}, the steering gain determines the leading wheelset angle of attack, and thus strongly influences the work at the flanging wheel. The curvature steering gain used in these studies is the gain which kinematically aligns the wheelsets radially, called the pure rolling line steering gain, G_{prl}, derived in [47]. The pure rolling line gain positions the wheelsets radially assuming that no primary longitudinal and secondary yaw stiffnesses exist and no flange forces are present. These assumptions are violated for forced-steered trucks, and thus, the pure rolling line steering gain may result in yaw misalignment of the wheelsets.

Figures 3.30 and 3.31 show the effect of steering gain on the leading wheelset angle of attack of FSR I forced-steered radial trucks negotiating 10° and 20° curves, respectively. The trucks have stiff k_{b2} (1.0×10^7 ft-lb/rad) and are operating with new and Heumann wheel profiles. At G = 0, the forced-steered trucks behave like self-steered trucks (with stiff k_{b2}) since no forced-steering occurs. As the steering gain increases, the wheelsets are forced toward radial alignment. At a certain gain, the angle of attack vanishes and perfect steering is achieved. Further increases in steering gain result in oversteering of the wheelsets away from radial alignment.

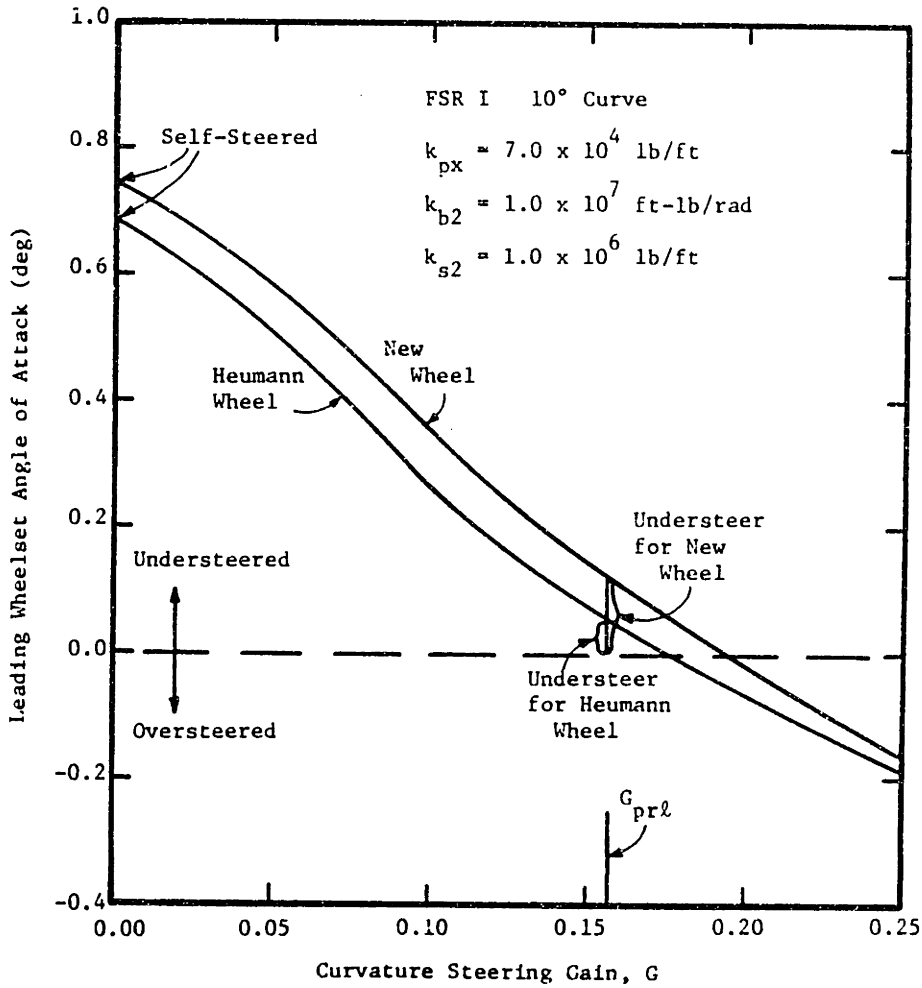

Figure 3.30: Leading Wheelset Angle of Attack vs. Curvature Steering Gain for a Forced-Steered Radial Truck, FSR I, with New and Heumann Wheels Negotiating a 10° Curve

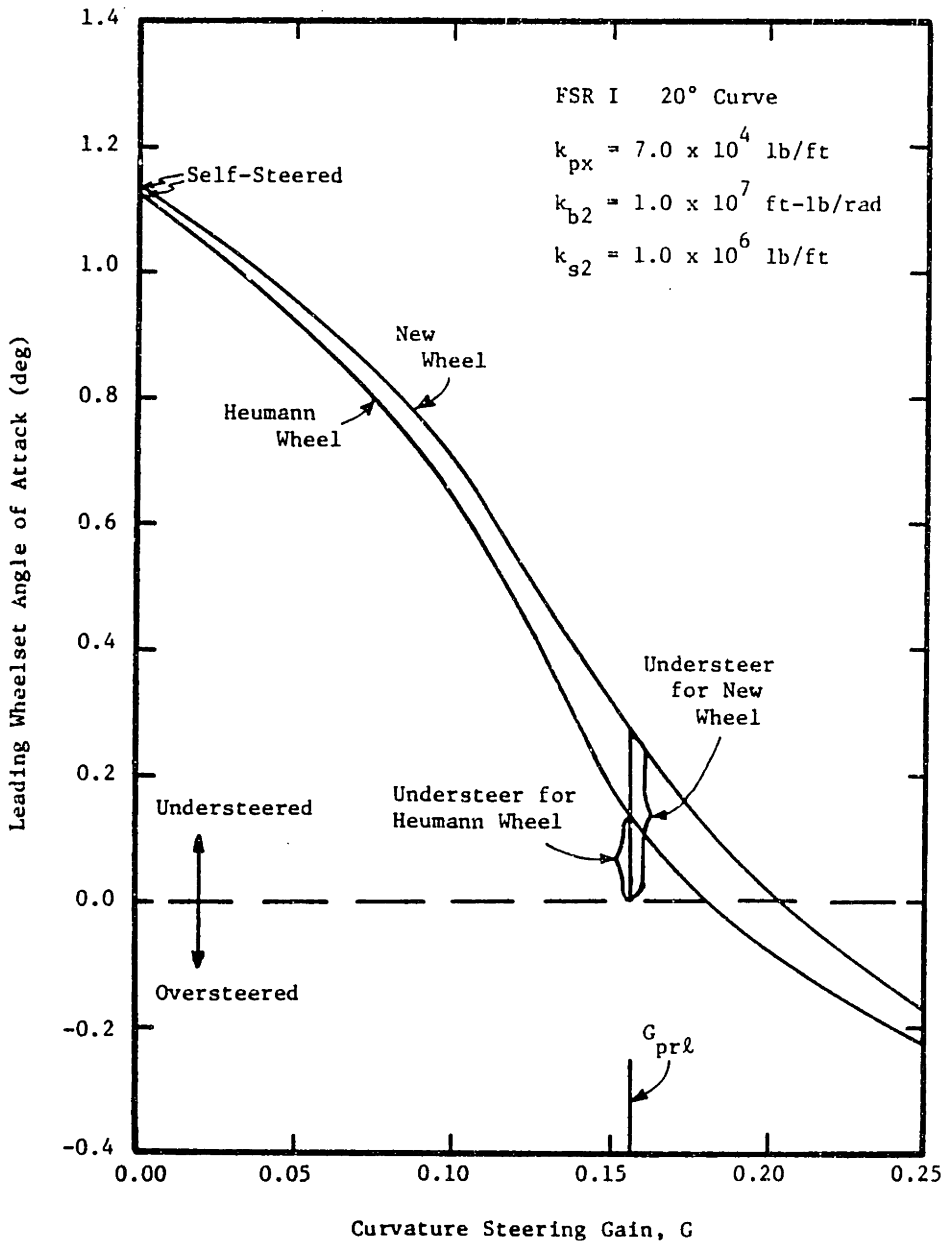

Figure 3.31: Leading Wheelset Angle of Attack vs. Curvature Steering Gain for a Forced-Steered Radial Truck, FSR I, with New and Heumann Wheels Negotiating a 20° Curve

From Figures 3.30 and 3.31, the steering gain associated with perfect radial alignment is higher than the pure rolling line gain (G_{prl} = 0.1579) for the trucks with new and Heumann wheels negotiating 10° and 20° curves. For negotiation of 10° curves, the gain for zero angle of attack is 0.195 for the truck with new wheels and 0.175 for the truck with Heumann wheels. For negotiation of 20° curves, the gain for perfect steering is 0.205 for the truck with new wheels and 0.180 for the truck with Heumann wheels. Lower gains are required for negotiation of the 10° curves (in comparison to the 20° curves) since the flange forces are smaller. The gain for perfect steering is closer to the pure rolling line gain for negotiation of 10° curves rather than 20° curves for trucks with both new and Heumann wheels. Thus, as shallower curves are traversed, the pure rolling line gain results in improved steering (i.e., decreased understeering).

At the pure rolling line gain, G_{prl}, a larger leading wheelset angle of attack occurs for the truck with new wheels than for the truck with Heumann wheels for negotiation of both the 10° and 20° curves. For the truck with new wheels, the gain G_{prl} results in comparatively more understeering of the leading wheelset. To eliminate wheelset misalignment, the steering gains must be increased only slightly for the truck with Heumann wheels and slightly more for the truck with new wheels.

The flanging wheel work of the forced-steered truck with new

wheels and steering gain G_{pr1}, shown in Figures 3.25 and 3.26, increases with stiffer k_{b2} because the leading wheelset is being forced to adopt a positive yaw misalignment. A larger gain is needed to eliminate the understeering, and would improve the curving performance as k_{b2} increases. Too large a steering gain would result in oversteering, which would also be detrimental to the curving performance. The selection of an optimal steering gain for a forced-steered truck is not addressed in this study, but represents an important area of future research.

In summary, forced-steered trucks adjust their geometry with track curvature to align their wheelsets in nominally radial positions. Because of the reduced wheelset misalignment in curves, the work expended at the flanging wheel decreases. In comparison to the performance of conventional and self-steered radial trucks, a significant improvement is possible by forced-steering the wheelsets.

3.6 Curving Performance of Trucks with Wheelset Misalignments

Wheelset misalignments may occur in transit trucks during construction or as a result of operation and maintenance practice. Misalignments position the wheelsets in offset or skewed initial positions and influence truck performance. In general, they hinder the tracking performance and contribute to asymmetric wear patterns on wheels.

Wheelset misalignments can be resolved into radial and lateral

components. With radial misalignment, the wheelsets have equal and opposite yaw angles with respect to the truck centerline, whereas with lateral misalignment the wheelsets are offset laterally with respect to one another. Previous analyses [27, 36] have indicated that the radial component of misalignment has the more detrimental influence on the curving behavior. The results of this study confirm that radial misalignment has a significant effect on curved as well as tangent track negotiation.

The effect of wheelset misalignments on truck curving performance is a function of both the magnitude and direction of the radial and lateral misalignment components. The ability of a truck to negotiate a curve is improved by misalignments which position the wheelsets more radially with the curve, and is hindered by misalignments in the opposite direction. For a vehicle which negotiates an equal number of right and left handed curves, the net effect of misalignments is negative. Any possible improvements gained in negotiating curves of a given direction are more than lost in negotiating curves of the opposite direction. In addition to direction, the magnitudes of the wheelset misalignment influence truck tracking ability. In the misalignment studies that follow, magnitudes of both lateral and radial misalignments are used which are consistent with observed values [36]. For lateral misalignment, the two wheelsets are each displaced 0.06 in (0.005 ft) in opposite directions relative to the truck centerline; for radial misalignment the two wheelsets are each yawed 0.0573° (0.001 rad) in opposite

directions from the perpendicular to the truck centerline. The directions of the misalignments are chosen to degrade the tracking performance.

The effects of wheelset misalignments on the work and lateral force at the flanging wheel are compared in Tables 3.7a and 3.7b, respectively, for conventional, self-steered, and forced-steered radial trucks negotiating 5° curves. Baseline and increased stiffness truck suspension designs are considered. For the conventional truck, radial misalignment has a stronger influence than the lateral misalignment, especially for the stiffer suspension design. For instance, for the stiff conventional truck, the flanging wheel work is 105 ft-lb/ft with lateral misalignment versus 119 ft-lb/ft with radial misalignment. For the baseline self-steered and forced-steered radial trucks, lateral misalignment increases the work and lateral force at the flanging wheel more than radial misalignment. The work at the flanging wheel of the baseline self-steered truck is 50 ft-lb/ft with lateral misalignment and 34 ft-lb/ft with radial misalignment. A reverse effect occurs for the self-steered and forced-steered radial trucks with stiff suspensions. Radial misalignment increases the work more than lateral misalignment. For the stiff self-steered (forced-steered) truck design, the work is 117 (36) ft-lb/ft with lateral misalignment and 123 (59) ft-lb/ft with radial misalignment. Thus, both radial and lateral misalignments increase the work to negotiate a curve. The influence of the radial component is most significant for baseline (i.e., decreased stiffness)

TABLE 3.7

(a) Work at Flanging Wheel and (b) Wheel/Rail Force at Flanging Wheel vs. Misalignment Condition for Different Trucks Operating on 5° Curve

	Baseline	Stiff
CONV	$k_{px} = 1.35 \times 10^5$	1.0×10^7 lb/ft
	$k_{py} = 7.5 \times 10^5$	7.5×10^6 lb/ft
SSR	$k_{px} = 1.20 \times 10^5$	1.0×10^7 lb/ft
	$k_{py} = 7.5 \times 10^5$	7.5×10^6 lb/ft
FSR	$k_{px} = 7.0 \times 10^4$	7.0×10^4 lb/ft
	$k_{b2} = 1.68 \times 10^5$	1.0×10^7 ft-lb/rad

Work at Flanging Wheel (ft-lb/ft) / Misalignment Condition	Conventional		Self-Steered Radial		Forced-Steered Radial (FSR I)	
	Baseline	Stiff	Baseline	Stiff	Baseline	Stiff
No Misalignment	39	105	24	108	12	27
Lateral Misalignment	47	105	50	117	45	36
Radial Misalignment	49	119	34	123	20	59

(a)

Lateral Force at Flanging Wheel (lb) / Misalignment Condition	Conventional		Self-Steered Radial		Forced-Steered Radial (FSR I)	
	Baseline	Stiff	Baseline	Stiff	Baseline	Stiff
No Misalignment	2700	5065	2260	5190	1720	2370
Lateral Misalignment	2910	5180*	2760	5840*	2490	2650*
Radial Misalignment	3100	5310	2660	5450	2090	3540

(b)

*Misalignment of Opposite Sign

self-steered and forced-steered truck designs.

To improve their ability to negotiate curved track, self and forced-steered trucks typically are designed with large total truck shear stiffness in comparison to conventional trucks. Due to the increased shear stiffness, the steady-state performance of steered trucks on tangent track is influenced more strongly by wheelset misalignments than the performance of conventional trucks. In Tables 3.8a and 3.8b the effects of wheelset misalignments on the tangent track performance of baseline conventional, self-steered, and forced-steered radial trucks are summarized in terms of wheelset lateral excursion and wheel/rail lateral force (at the leading wheelset and leading outer wheel, respectively, except where noted). The results show that radial misalignment has a more significant effect than lateral misalignment for tangent track negotiation, especially for the steered trucks. The self-steered and forced-steered radial trucks have large lateral excursions of 0.310 and 0.308 in, respectively, which indicate near flanging conditions at the leading outer wheels. The high shear properties of the steered trucks result in large excursions and increased lateral forces (1030 lb for both trucks) on tangent track. Tables 3.8 demonstrate that self-steered and forced-steered radial truck performance on tangent track is sensitive to wheelset misalignments. Thus, minimizing wheelset misalignments due to construction and tolerance errors is an important design consideration for steered trucks.

TABLE 3.8

(a) Wheelset Lateral Excursion and (b) Wheel/Rail Force vs. Misalignment Condition for Baseline Trucks Operating on Tangent Truck

Wheelset Lateral Excursion (in) / Misalignment Condition	Conventional	Self-Steered Radial	Forced-Steered Radial (FSR I)
No Misalignment	-0.001	-0.006	-0.004
Lateral Misalignment	-0.150*	-0.100*	-0.100*
Radial Misalignment	0.229	0.310	0.308

*Trailing Wheelset

(a)

Wheel/Rail Lateral Force (lb) / Misalignment Condition	Conventional	Self-Steered Radial	Forced-Steered Radial (FSR I)
No Misalignment	400	410	410
Lateral Misalignment	530*	440*	450*
Radial Misalignment	580	1030	1030

*Trailing Inner Wheel

(b)

4.0 CURVING PERFORMANCE/STABILITY TRADEOFF

4.1 Introduction

The ideal rail truck must simultaneously satisfy two design objectives. First, it must minimize wheel/rail forces and wheelset angles of attack during curving. Second, it must provide adequate vehicle stability to prevent the onset of hunting during which large forces develop. Large wheel/rail forces and wheelset angles induce wheel/rail wear, generate screeching noise, increase the potential danger of derailment due to wheel climb, and raise fuel consumption because of added resistance. The two design goals of improved curving and stability performance are usually represented as a tradeoff [43,12]. Designers of conventional rail trucks have traditionally achieved more stable designs by stiffening the primary suspension elements. However, the resulting improvement in stability is obtained at the expense of degraded curving performance. The conflicting design tradeoff between curving performance and stability creates special problems for urban transit applications in which many tight curves are encountered.

In this thesis, curving performance is represented by the work expended at the flanging wheel. Vehicle stability is characterized by the linear, tangent track critical speed. Increased flanging wheel work indicates a truck design with degraded curving ability; a higher critical speed implies a more stable truck design.

The stability properties of conventional, self-steered radial, and two forced-steered radial truck designs have been studied and are

reported in [46]. The results are summarized in Table 4.1 for trucks with new AAR wheels* and in Table 4.2 for trucks with Heumann wheels. At the same critical speed, the suspensions of the trucks with Heumann wheels are stiffer than the suspensions of the trucks with new wheels due to the effect of the higher conicity Heumann wheel.

The stiffnesses of Tables 4.1 and 4.2 have been used to determine the location of the different truck designs in the total truck shear versus bending stiffness plane. The locations are shown in Figure 4.1 for trucks with new wheels and in Figure 4.2 for trucks with Heumann wheels. With increasing critical speed, the self-steered and forced-steered trucks have increased total truck bending stiffnesses and approximately the same total shear stiffnesses. The conventional trucks have increased total bending and shear stiffnesses, but are restricted to stiffnesses below the line $k_s = k_b/b^2$. Due to this limitation, the total shear stiffnesses of the conventional trucks are significantly lower than the stiffnesses of the self and forced-steered trucks.

In Chapter 3, the results of parametric curving studies were presented. The functional relationship of truck suspension stiffness on flanging wheel work was established for conventional, self-steered radial, and forced-steered radial trucks with new and Heumann wheels. In this chapter, curving performance and stability results are combined to identify inherent design tradeoffs.

*New AAR wheels are referred to simply as "new wheels".

TABLE 4.1

STIFFNESSES VS. CRITICAL SPEED FOR FOUR TRUCK DESIGNS WITH NEW WHEELS

Vcr (mph)	CONV. k_{px} (lb/ft)	SSR k_{px} (lb/ft) (k_{b2}=10^3ft-lb/rad k_{s2}=10^6lb/ft)	FSR I k_{b2} (ft-lb/rad) (k_{px}=7.0x10^4lb/ft k_{s2}=10^6lb/ft)	FSR II k_{b2} (ft-lb/rad) (k_{px}=1.0x10^3lb/ft k_{s2}=10^6lb/ft)
100	8.5×10^4	7.0×10^4	1.0×10^4	2.4×10^5
110	1.08×10^5	9.5×10^4	9.0×10^4	3.3×10^5
120*	1.35×10^5	1.20×10^5	1.68×10^5	4.1×10^5
130	1.60×10^5	1.47×10^5	2.55×10^5	5.0×10^5
140	1.85×10^5	1.70×10^5	3.4×10^5	5.8×10^5

TABLE 4.2

STIFFNESSES VS. CRITICAL SPEED FOR FOUR TRUCK DESIGNS WITH HEUMANN WHEELS

Vcr (mph)	CONV k_{px} (lb/ft)	SSR k_{px} (lb/ft) (k_{b2}=10^3ft-lb/rad k_{s2}=10^6lb/ft)	FSR I k_{b2} (ft-lb/rad) (k_{px}=7.0x10^4lb/ft k_{s2}=10^6lb/ft)	FSR II k_{b2} (ft-lb/rad) (k_{px}=1.0x10^3lb/ft k_{s2}=10^6lb/ft)
90	3.45×10^5	3.10×10^5	9.5×10^5	1.25×10^6
100	4.25×10^5	3.70×10^5	1.18×10^6	1.50×10^6
110	5.25×10^5	4.32×10^5	1.42×10^6	1.75×10^6
120*	6.50×10^5	5.00×10^5	1.66×10^6	2.00×10^6
130	8.50×10^5	6.00×10^5	2.00×10^6	2.35×10^6

*Baseline

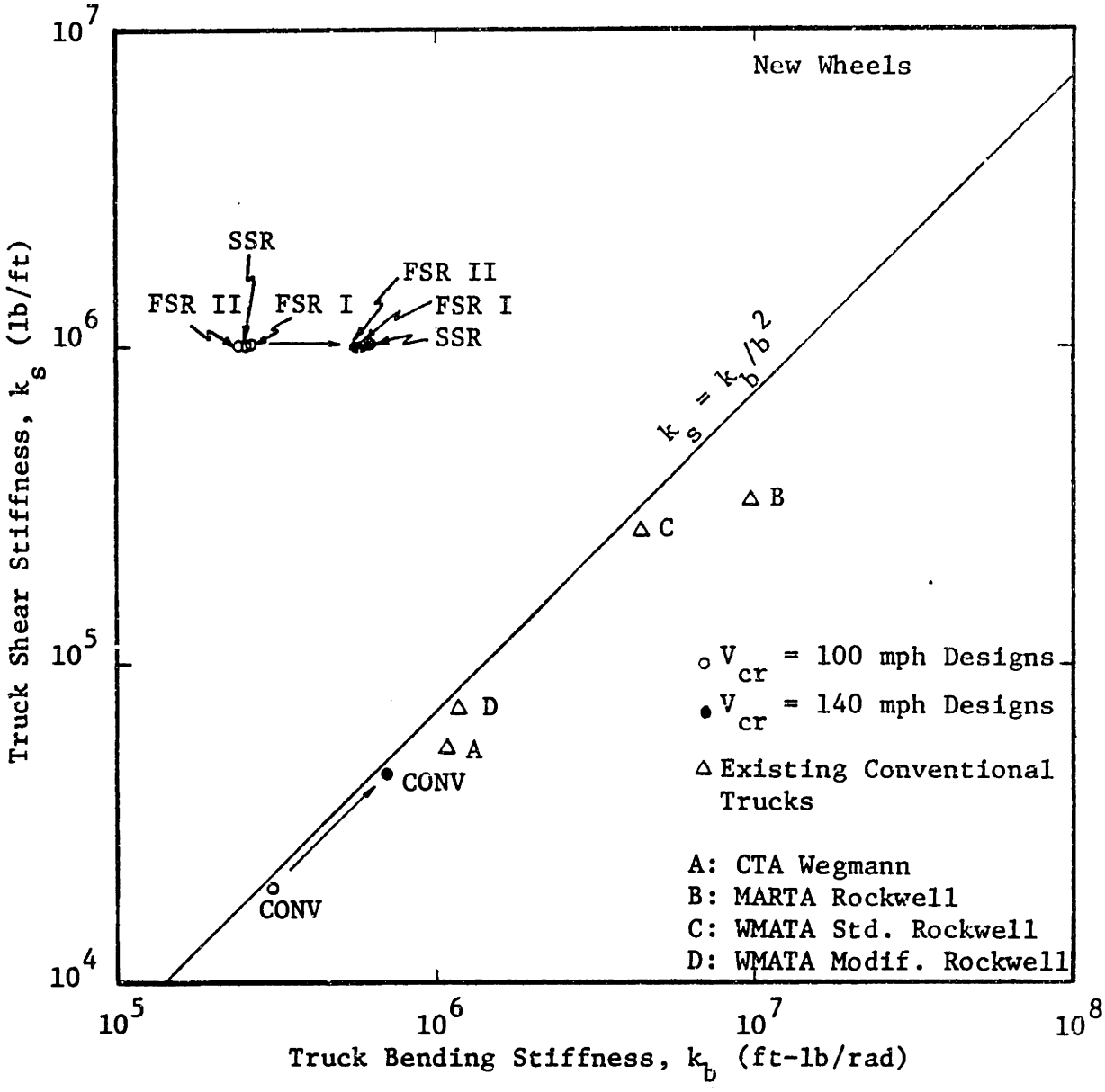

Figure 4.1 Location of Conventional and Radial Trucks with New Wheels in the Truck Shear vs. Bending Stiffness Plane.

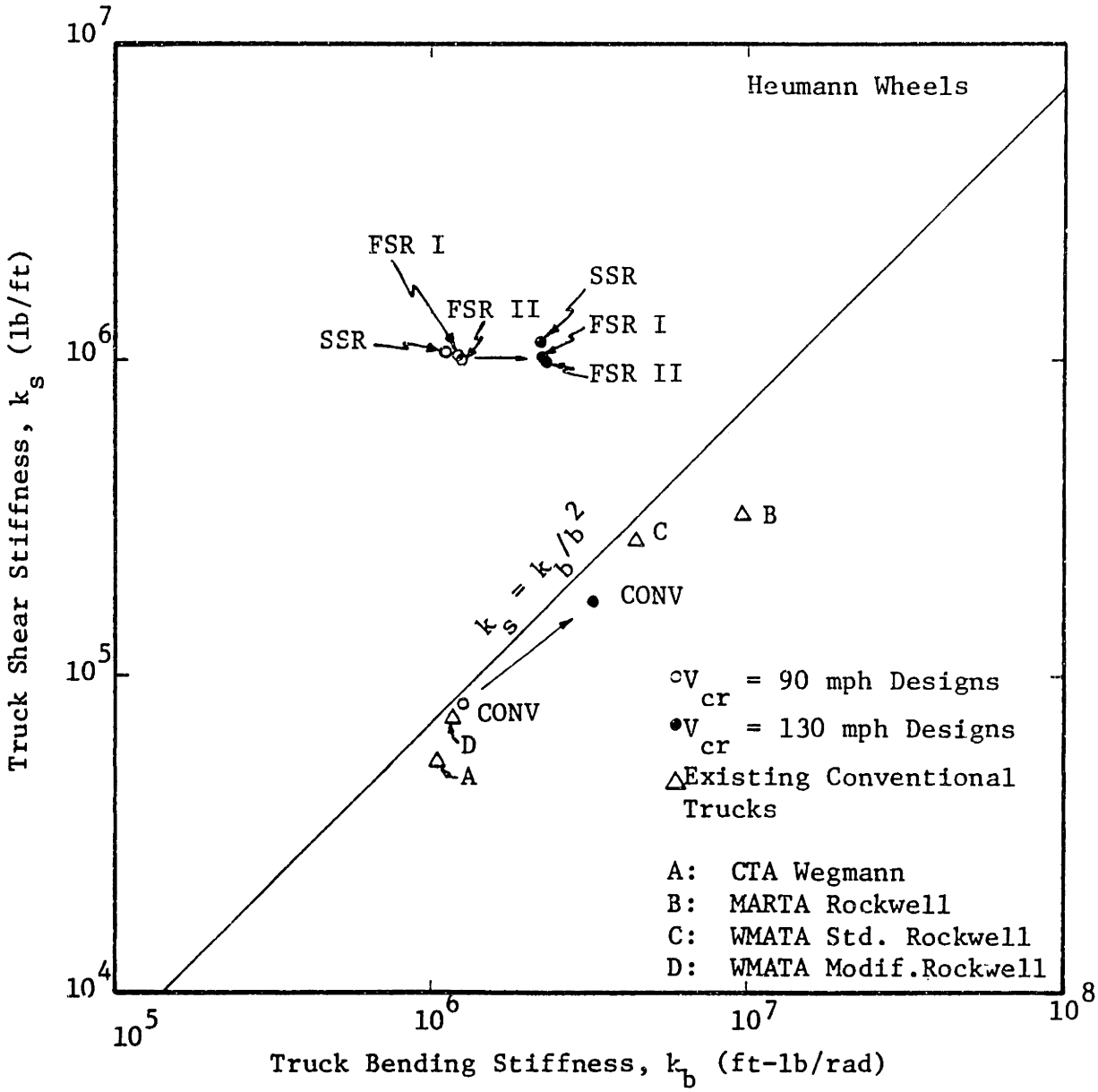

Figure 4.2 Location of Conventional and Radial Trucks with Heumann Wheels in the Truck Shear vs. Bending Stiffness Plane.

4.2 Curving Performance/Stability Tradeoff of Conventional Trucks

This section discusses the relationship between the curving performance and stability of conventional trucks. It is convenient to display this relationship by cross-plotting the work expended at the flanging wheel during curve negotiation and the tangent track critical speed, both as functions of primary longitudinal stiffness, k_{px}. The results for negotiation of 2.5°, 5°, 10°, and 20° curves are shown in Figure 4.3 for a conventional truck with new wheels and in Figure 4.4 for a truck with Heumann wheels. These figures demonstrate the inherent tradeoff between curving performance and stability. With stiffer k_{px}, the work and critical speed increase; with softer k_{px}, the work and critical speed decrease. For example, as k_{px} stiffens from 8.5×10^4 to 1.85×10^5 lb/ft, the work to negotiate a 20° curve increases from 139 to 189 ft-lb/ft and the critical speed increases from 100 to 140 mph. From Figure 4.3, the work to negotiate lower degree curves increases only slightly with increasing k_{px}. The work to negotiate a 2.5° curve is practically insensitive to changes in k_{px}. Thus, higher critical speeds can be achieved with minimal sacrifice in curving performance for negotiation of moderate and shallow curves.

Figure 4.4 shows the curving performance/stability tradeoff for a conventional truck with Heumann wheels. As k_{px} stiffens from 3.45×10^5 to 8.5×10^5 lb/ft, the critical speed increases from 90 to 130 mph and the work increases 6% for the 20° curve, 64% for the 10° curve, and 250% for the 2.5° curve.

In summary, for conventional trucks with new wheels, the curving

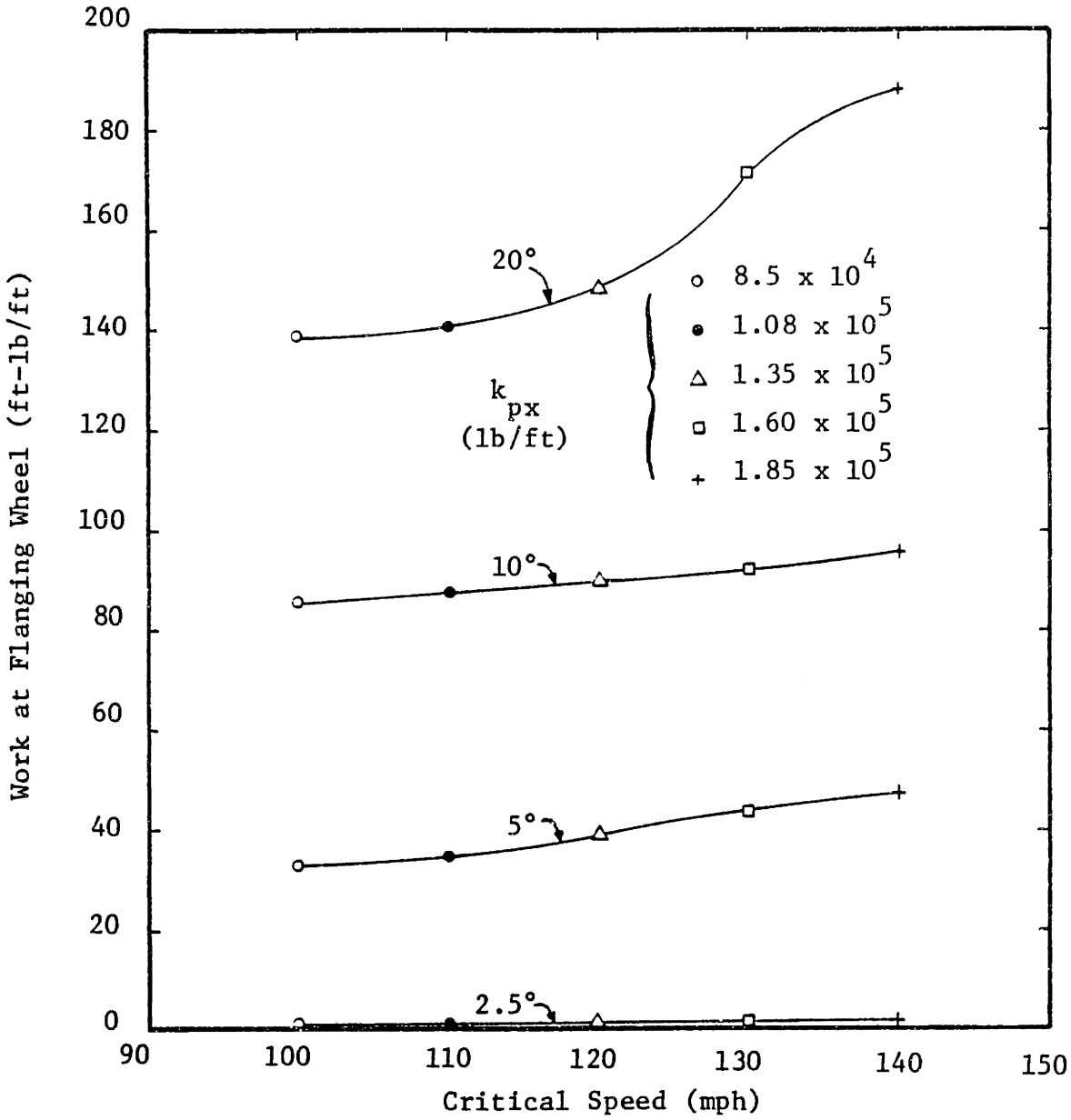

Figure 4.3 Curving Performance/Stability Tradeoff in Terms of Work at Flanging Wheel vs. Critical Speed of a Conventional Truck with New Wheels Negotiating 2.5°, 5°, 10°, and 20° Curves.

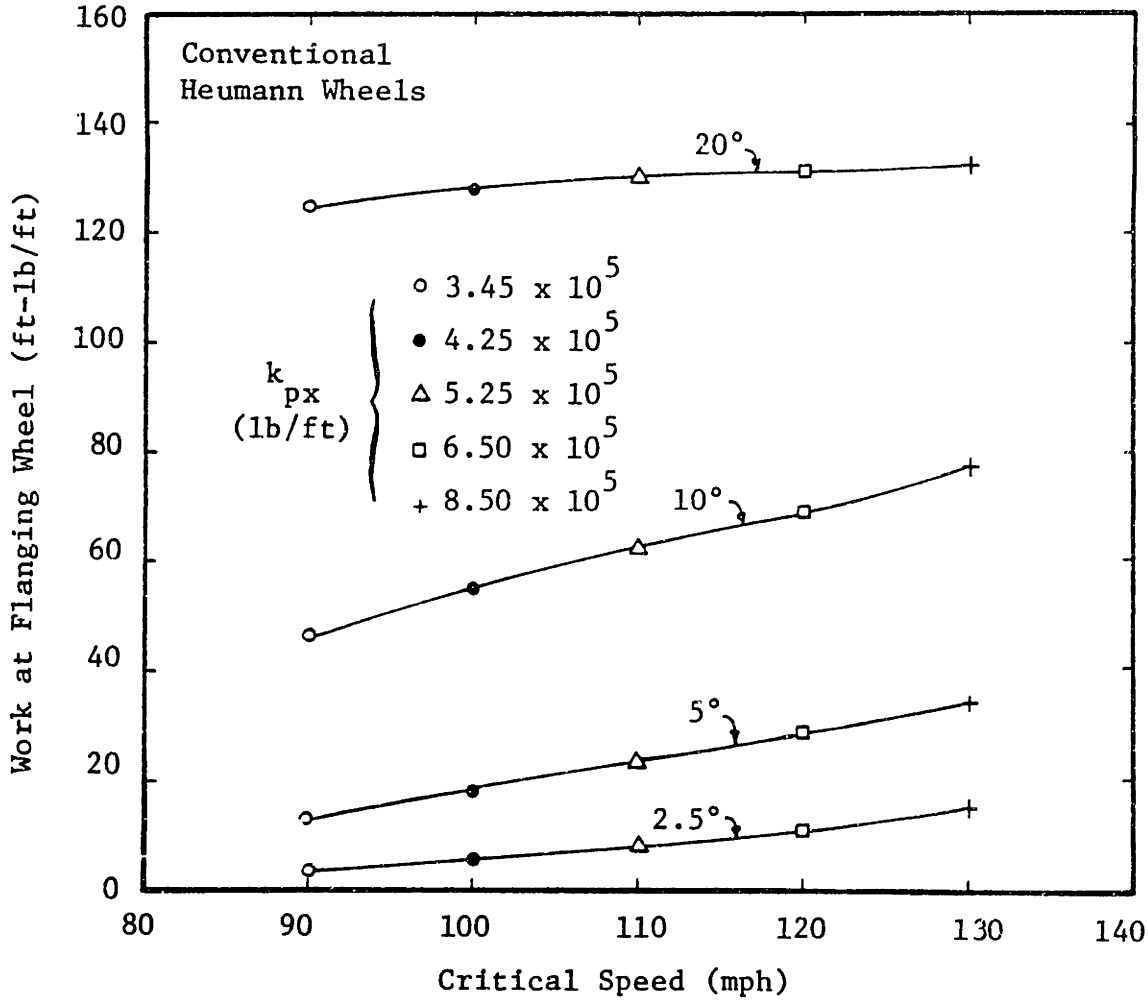

Figure 4.4 Curving Performance/Stability Tradeoff in Terms of Work at Flanging Wheel vs. Critical Speed of a Conventional Truck with Heumann Wheels Negotiating 2.5°, 5°, 10°, and 20° Curves.

performance/stability tradeoff is most significant for negotiation of tight curves. In contrast, for conventional trucks with Heumann wheels, the tradeoff is most important for negotiation of shallow curves.

4.3 Curving Performance/Stability Tradeoff of Self-Steered Radial Trucks

The curving performance versus stability relationship for a self-steered radial truck with new wheels is shown in Figure 4.5; the relationship for a self-steered radial truck with Heumann wheels is shown in Figure 4.6. The primary longitudinal stiffness, k_{px}, is the independent variable. These trucks have soft interaxle bending stiffness (k_{b2} = 1.0 x 10^3 ft-lb/rad) and stiff interaxle shear stiffness (k_{s2} = 1.0 x 10^6 lb/ft) to permit the wheelsets to yaw but not shear.

Figures 4.5 and 4.6 demonstrate that self-steered radial trucks with new and Heumann wheels are subject to the traditional design conflicts between improved curving performance and stability. For a self-steered radial truck with new wheels traversing 10° and 20° curves, the work increases approximately 75% as k_{px} increases from 7.0 x 10^4 to 1.70 x 10^5 lb/ft. For the same increase in k_{px}, the critical speed increases from 100 to 140 mph. In contrast, for a self-steered truck with Heumann wheels traversing 10° and 20° curves, the work increases 65% and 14%, respectively, and the critical speed increases from 90 to 130 mph as k_{px} increases from 3.10 x 10^5 to 6.00 x 10^5 lb/ft. Thus, for negotiation of tight curves, the work increases more for the truck with new wheels than for the truck with Heumann wheels.

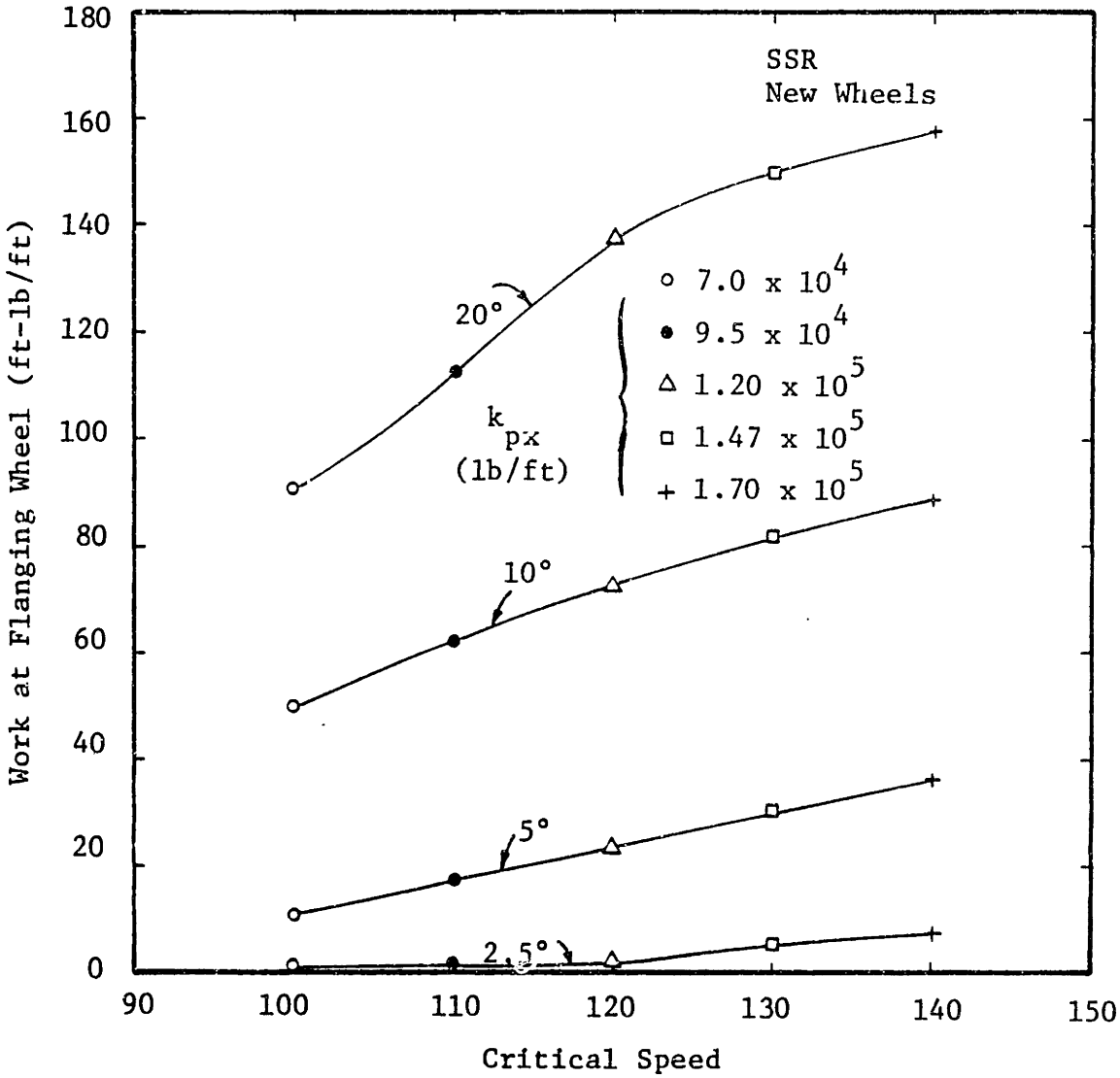

Figure 4.5 Curving Performance/Stability Tradeoff in Terms of Work at Flanging Wheel vs. Critical Speed of a Self-Steered Radial Truck with New Wheels Negotiating 2.5°, 5°, 10°, and 20° Curves.

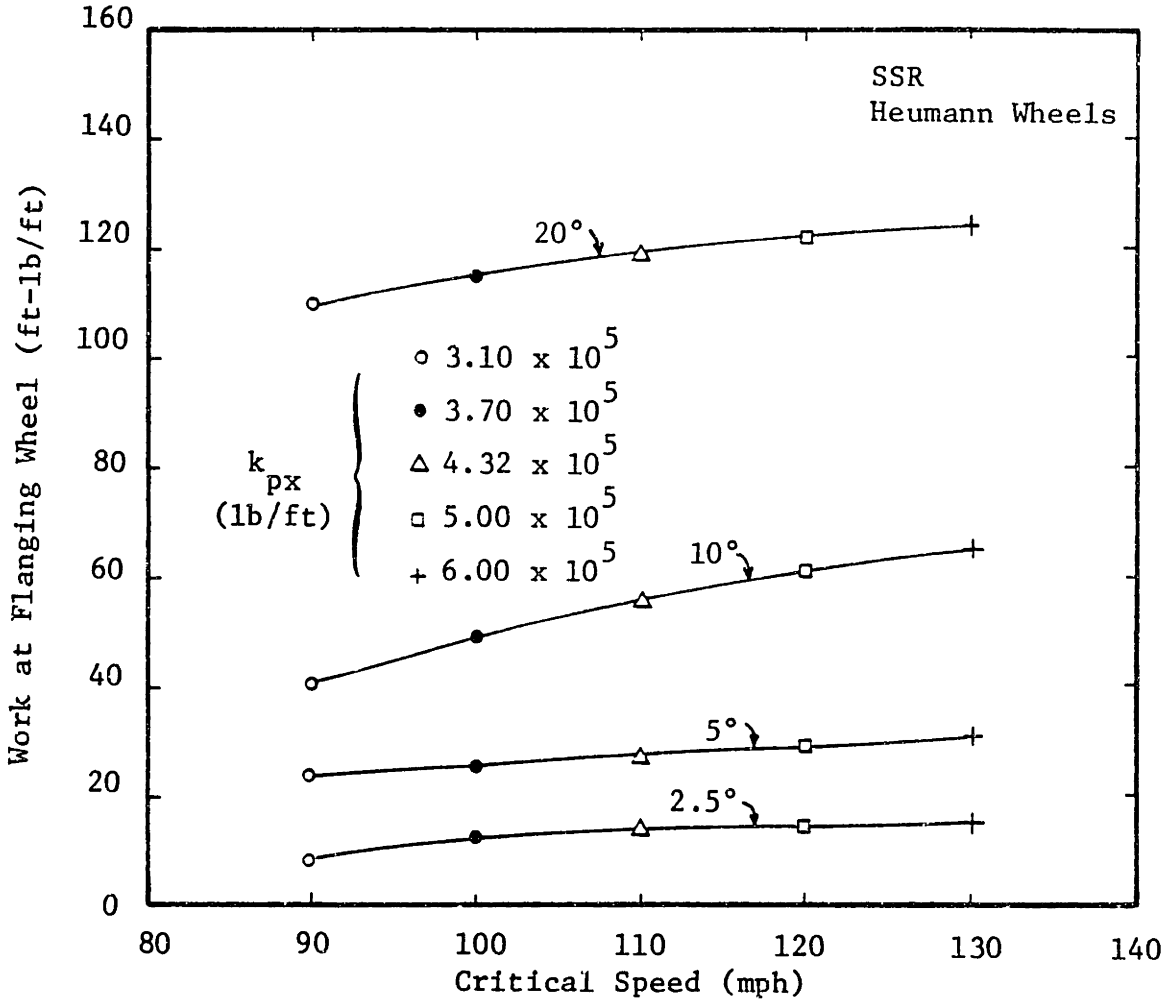

Figure 4.6 Curving Performance/Stability Tradeoff in Terms of Work at Flanging Wheel vs. Critical Speed of a Self-Steered Radial Truck with Heumann Wheels Negotiating 2.5°, 5°, 10°, and 20° Curves.

For negotiation of shallow curves, the work (in terms of percent) also increases more for the truck with new wheels. For a 2.5° curve, the work increases from 1 to 8 ft-lb/ft as the critical speed increases from 100 to 140 mph for the truck with new wheels; the work increases from 10 to 15 ft-lb/ft as the critical speed increases from 90 to 130 mph for the truck with Heumann wheels.

In summary, for self-steered radial trucks with new wheels, the curving performance/stability tradeoff is significant for negotiation of shallow, moderate, and tight curves. For self-steered trucks with Heumann wheels, the tradeoff exists but is not as pronounced for negotiation of shallow and tight curves.

4.4 Curving Performance/Stability Tradeoff of Forced-Steered Radial Trucks

Two forced-steered truck designs are considered in the tradeoff study. The first design, FSR I, has soft primary longitudinal stiffness (k_{px} = 7.0 x 10^4 lb/ft); the second design, FSR II, has practically negligible primary longitudinal stiffness (k_{px} = 1.0 x 10^3 lb/ft). For each design, the primary longitudinal stiffness is assumed constant. In the tradeoff study, the independent variable is the effective interaxle bending stiffness, k_{b2}, which is related to the stiffness of the forced-steering linkage. As k_{b2} stiffens, the forced-steering action increases.

The curving performance versus stability relationships for forced-steered trucks are shown in Figures 4.7 - 4.10. Figures 4.7 and 4.8 are graphs of flanging wheel work versus critical speed for the FSR I and FSR II designs with new wheels, respectively; Figures 4.9 and 4.10

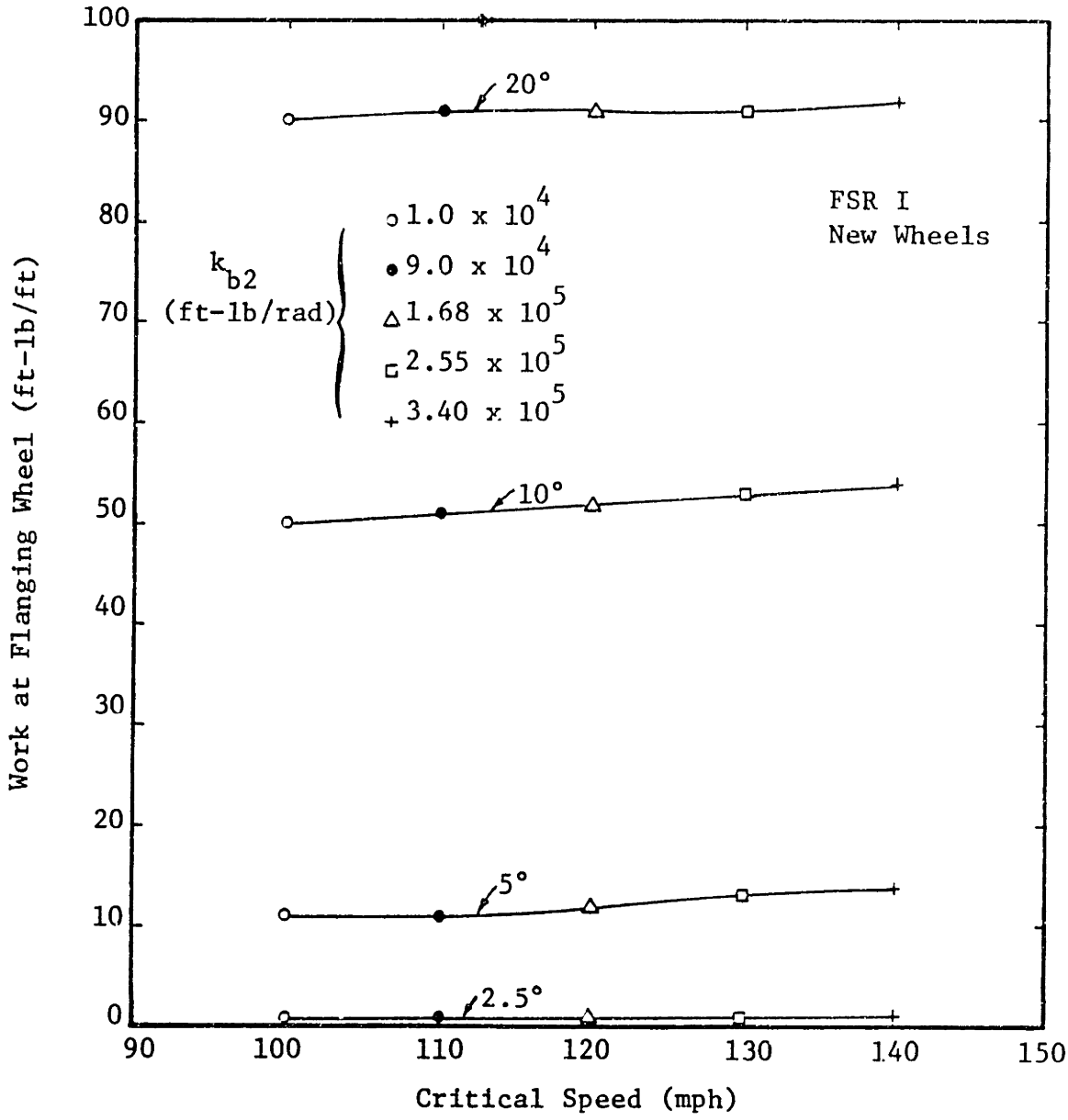

Figure 4.7 Curving Performance/Stability Tradeoff in Terms of Work at Flanging Wheel vs. Critical Speed of a Forced-Steered Radial Truck, FSR I, With New Wheels Negotiating 2.5°, 5°, 10°, and 20° Curves.

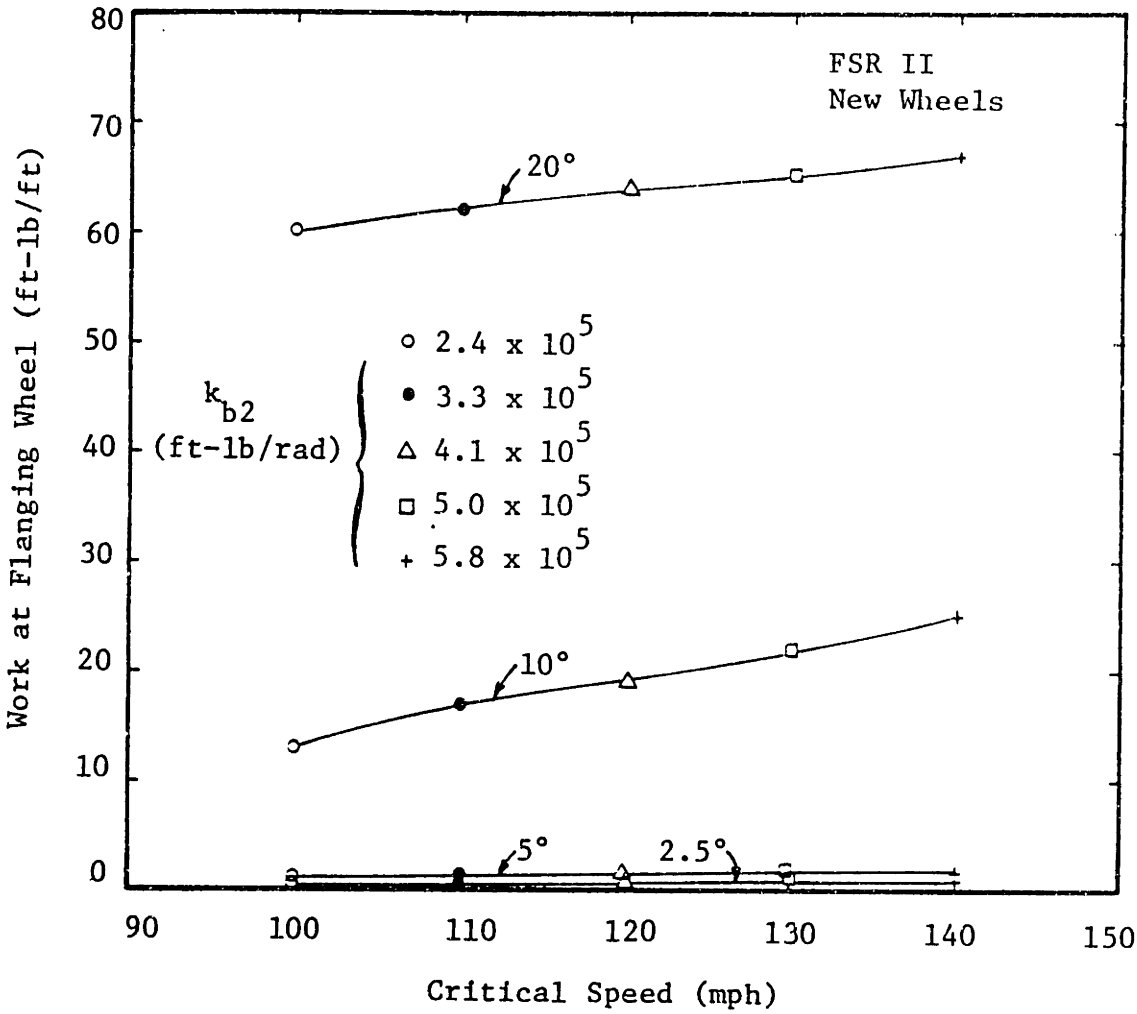

Figure 4.8 Curving Performance/Stability Tradeoff in Terms of Work at Flanging Wheel vs. Critical Speed of a Forced-Steered Radial Truck, FSR II, With New Wheels Negotiating 2.5°, 5°, 10°, and 20° Curves.

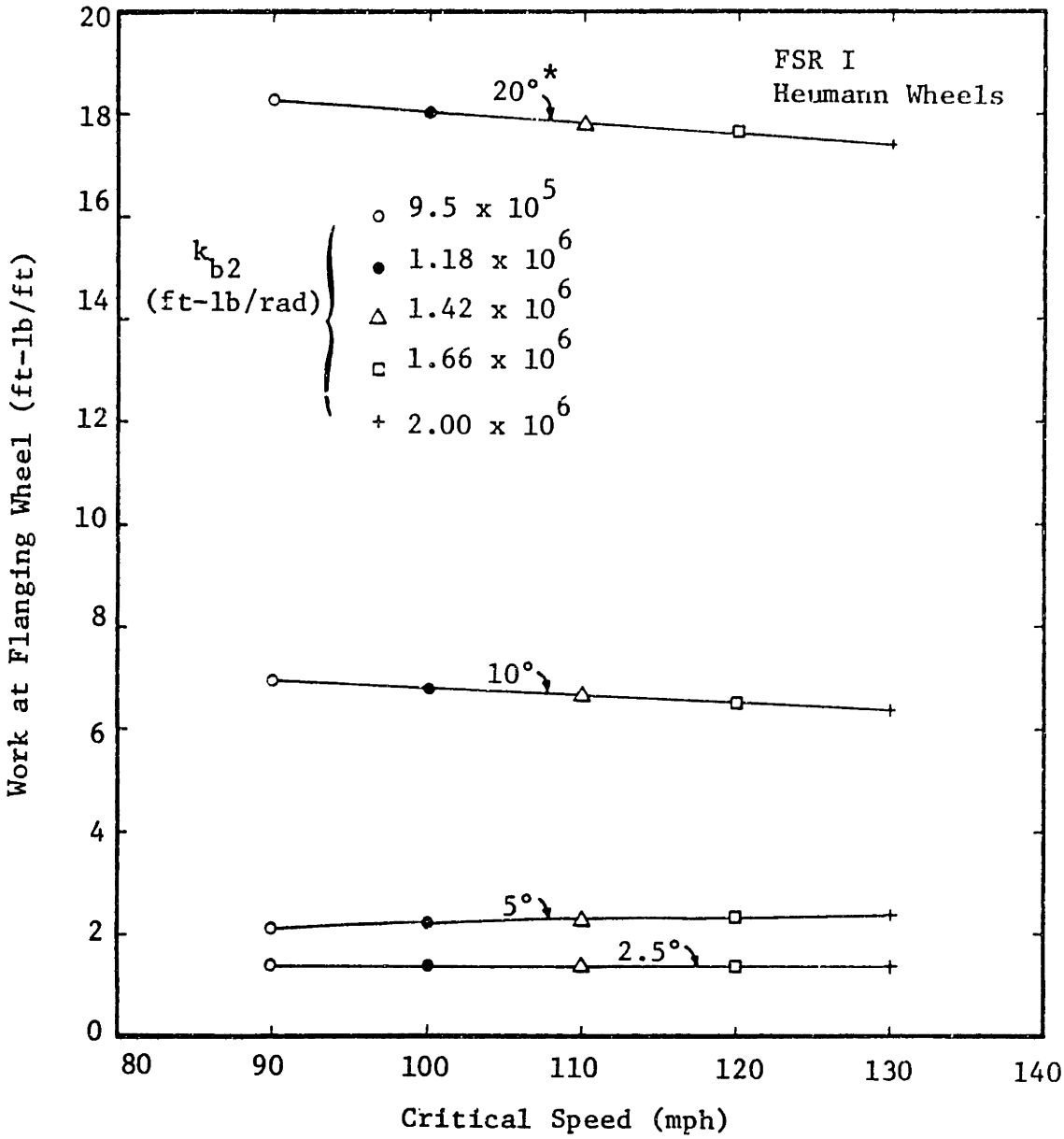

Figure 4.9 Curving Performance/Stability Tradeoff in Terms of Work at Flanging Wheel vs. Critical Speed of a Forced Steered Radial Truck, FSR I, With Heumann Wheels Negotiating 2.5°, 5°, 10°, and 20° Curves. (*Work at Trailing Outer Wheel).

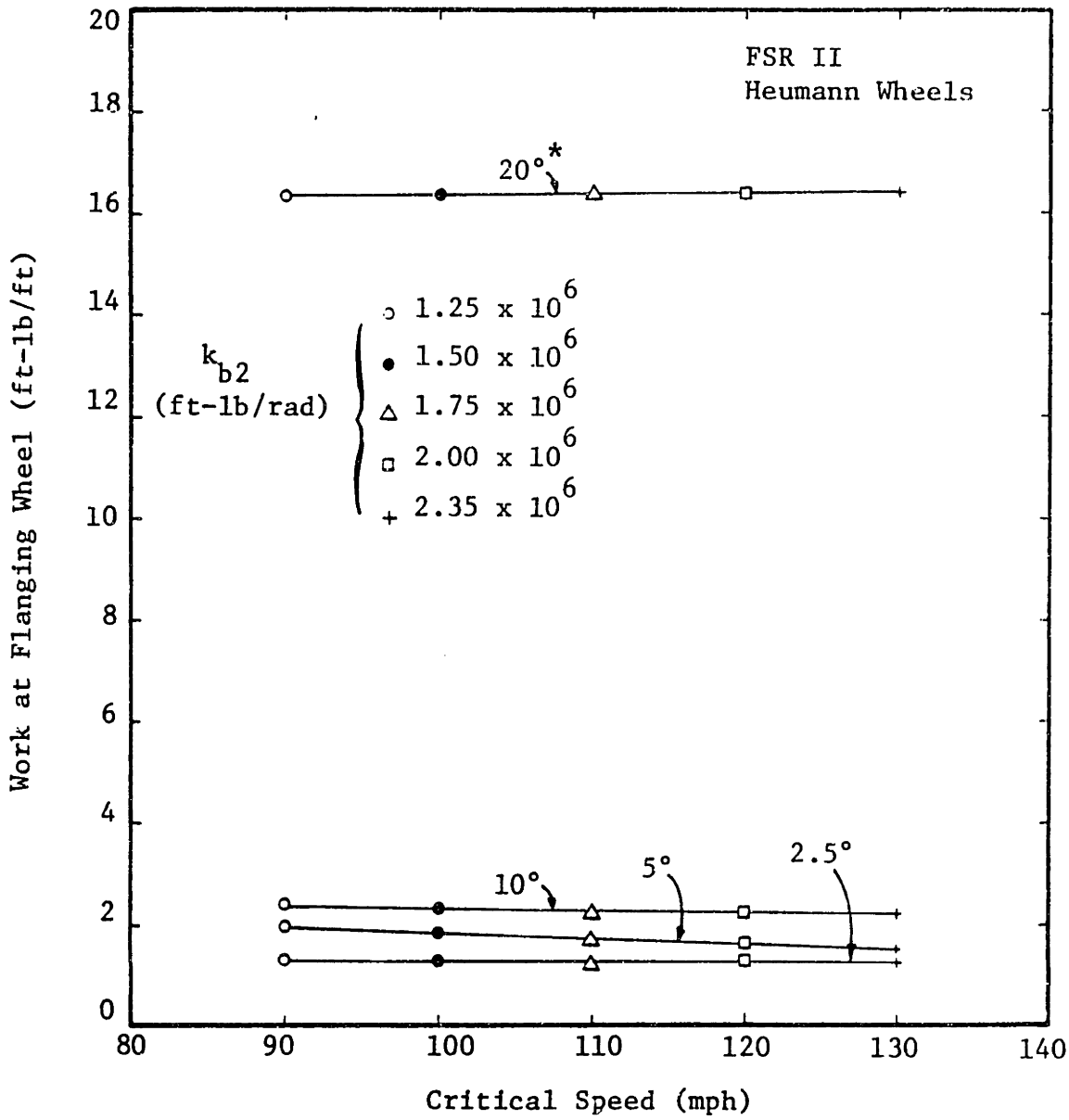

Figure 4.10 Curving Performance/Stability Tradeoff in Terms of Work at Flanging Wheel vs. Critical Speed of a Forced-Steered Radial Truck, FSR II, With Heumann Wheels Negotiating 2.5°, 5°, 10°, and 20° Curves. (*Work at Trailing Outer Wheel).

are graphs of work versus critical speed for the trucks with Heumann wheels. For both designs with new and Heumann wheels negotiating low degree curves, the work is small and almost insensitive to changes in k_{b2}. For instance, for all trucks traversing a 2.5° curve, the work is 1 ft-lb/ft for the range of k_{b2} values. Thus, for negotiation of low degree curves, it is advantageous to stiffen k_{b2} to maximize the critical speed since the work remains relatively constant (and small). For the two forced-steered truck designs with new wheels negotiating higher degree curves, the work increases slightly and the critical speed increases as k_{b2} stiffens. The work increases because of understeering of the leading wheelset which was shown to occur for forced-steered trucks with new wheels and pure rolling line steering gains. Despite the slight understeering, it is probably advantageous to stiffen k_{b2}, thereby increasing the critical speed and only slightly raising the work during curving. To avoid increases in work, a steering gain larger than the pure rolling line gain should be used.

For the forced-steered trucks with Heumann wheels negotiating moderate and tight curves, the curving performance is not degraded as stability increases. For the FSR I truck, the work at the flanging wheel decreases and the critical speed increases as k_{b2} stiffens. For the FSR II truck, the work remains essentially constant and the critical speed increases. For these forced-steered trucks with Heumann wheels, the pure rolling line steering gain provides effective steering of the wheelsets and thus the work decreases or stays constant as k_{b2} increases. In addition, as k_{b2} stiffens the critical speed grows. Thus, an ideal situation exists since no tradeoff occurs. A stiffer k_{b2} is desirable

since it yields a more stable truck with the same or improved curving properties.

4.5 Comparative Performance of Conventional, Self-Steered, and Forced-Steered Radial Trucks

The tradeoff plots of the previous section are summarized in Tables 4.3 and 4.4 for trucks with new and Heumann wheels, respectively. These tables list the work at the flanging wheel of a conventional, self-steered radial, and two forced-steered radial truck designs negotiating 2.5°, 5°, 10°, and 20° curves as a function of critical speed. Tables 4.3 and 4.4 are useful to compare the curving performances of the different trucks at the same critical speed.

The forced-steered radial truck designs exhibit superior performance, especially for designs with high critical speeds. For example, for trucks with new wheels and 140 mph critical speeds, the work to negotiate a 20° curve is 189, 158, 92, and 67 ft-lb/ft for the conventional, self-steered radial, forced-steered radial FSR I, and forced-steered radial FSR II truck, respectively. For the forced-steered radial trucks, higher critical speeds are obtained by increasing the effective interaxle bending stiffness, k_{b2}. This slightly increases the work for trucks with new wheels and actually decreases (or does not change) the work for trucks with Heumann wheels. On the other hand, for the conventional and self-steered radial trucks, higher critical speeds are achieved by increasing the primary longitudinal stiffness, k_{px}. This significantly degrades the curving performance by increasing the work.

TABLE 4.3

Curving Performance/Stability Tradeoff in terms of Work at Flanging Wheel vs. Critical Speed for Four Truck Designs with New Wheels Negotiating 2.5°, 5°, 10°, and 20° Curves.

Critical Speed (mph) \ Work at Flanging Wheel (ft-lb/ft)	Conventional				Self-Steered Radial				Forced Steered Radial FSR I				Forced Steered Radial FSR II			
	2.5°	5°	10°	20°	2.5°	5°	10°	20°	2.5°	5°	10°	20°	2.5°	5°	10°	20°
V_{cr} = 100	1	30	86	139	1	10	50	90	1	11	50	90	0	1	13	60
V_{cr} = 110	1	34	88	141	1	17	62	112	1	11	51	91	0	1	17	62
V_{cr} = 120*	1	39	90	149	2	24	72	138	1	12	52	91	0	1	19	64
V_{cr} = 130	1	44	92	171	5	31	82	150	1	13	53	91	1	1	22	65
V_{cr} = 140	1	48	95	189	8	37	89	158	1	14	54	92	1	1	25	67

TABLE 4.4

Curving Performance/Stability Tradeoff in terms of Work at Flanging Wheel vs. Critical Speed for Four Truck Designs with Heumann Wheels Negotiating 2.5°, 5°, 10°, and 20° Curves.

Critical Speed (mph) \ Work at Flanging Wheel (ft-lb/ft)	Conventional				Self-Steered Radial				Forced Steered Radial FSR I				Forced Steered Radial FSR II			
	2.5°	5°	10°	20°	2.5°	5°	10°	20°	2.5°	5°	10°	20°**	2.5°	5°	10°**	20°**
V_{cr} = 90	4	13	47	124	10	24	41	110	1	2	7	18	1	2	2	16
V_{cr} = 100	5	18	55	128	13	25	49	115	1	2	7	18	1	2	2	16
V_{cr} = 110	8	24	63	130	14	27	55	119	1	2	7	18	1	2	2	16
V_{cr} = 120*	11	29	69	131	15	29	61	122	1	2	7	18	1	2	2	16
V_{cr} = 130	14	34	77	132	15	31	68	125	1	2	6	17	1	2	2	16

*Baseline

**Work at Trailing Outer Wheel

The advantage of employing forced-steered radial trucks is most evident for negotiation of tight curves. In tight curves, forced-steered trucks use the large relative yaw angle between the truck and carbody to steer the wheelsets into radial alignment. Tables 4.3 and 4.4 show that the work of the forced-steered radial truck designs is appreciably lower than the work of the conventional or self-steered radial trucks for negotiation of 20° curves, except for the FSR I truck with new wheels at low critical speeds.

For trucks with new wheels and low critical speeds, Table 4.3 shows that the performance of the first forced-steered truck design, FSR I, and the self-steered radial truck is similar. For instance, for both trucks the work to negotiate a 20° curve is 90 ft-lb/ft at a critical speed of 100 mph. At low critical speeds, the FSR I truck does not possess sufficient steering action due to its soft interaxle bending stiffness, k_{b2}. At a critical speed of 100 mph, k_{b2} is 1.0×10^4 ft-lb/ft for the FSR I truck. (By comparison, $k_{b2} = 1.0 \times 10^3$ ft-lb/rad for the self-steered radial truck.) Thus, the FSR I and self-steered radial trucks with new wheels exhibit similar properties at low critical speeds. In contrast, the second forced-steered truck design, FSR II, offers superior curving performance due to its practical absence of primary longitudinal stiffness and due to its stiffer k_{b2}. For instance, at a critical speed of 100 mph, k_{b2} is 2.4×10^5 ft-lb/rad and the work to negotiate a 20° curve is 60 ft-lb/ft.

Conventional, self-steered, and forced-steered trucks with Heumann wheels are compared in Table 4.4. At all critical speeds, the self-

steered radial truck offers a slight improvement in curving performance in comparison to the conventional truck for negotiation of moderate and tight curves. In contrast, the conventional truck performs better than the self-steered truck for negotiation of shallow curves. The higher total shear stiffness of the radial truck causes its wheelsets to flange somewhat sooner than the wheelsets of the conventional truck. At all critical speeds, significant advantages are gained by employing forced-steering. Forced-steered trucks with Heumann wheels offer substantial improvements in curving performance for negotiation of shallow, moderate, and tight curves.

4.5.1 Comparative Performance of Baseline Trucks

In this thesis, baseline trucks signify trucks designed to achieve 120 mph critical speeds. Figure 4.11 shows the work at the flanging wheel as a function of track curvature for baseline trucks with new wheels. The figure demonstrates the improvement in curving performance gained by employing steered truck designs. Forced-steered trucks offer significant advantages, especially for negotiation of moderate and tight degree curves. The FSR II forced-steered truck offers over a factor of four (two) reduction in the work at the flanging wheel in comparison to conventional trucks operating on 10° (20°) curves.

The steady-state lateral force at the leading outer wheel as a function of curvature is compared in Figure 4.12 for baseline trucks with new wheels. Lower forces are predicted for the forced-steered truck designs than for the conventional and self-steered trucks. The self-steered truck has slightly lower forces in comparison to the con-

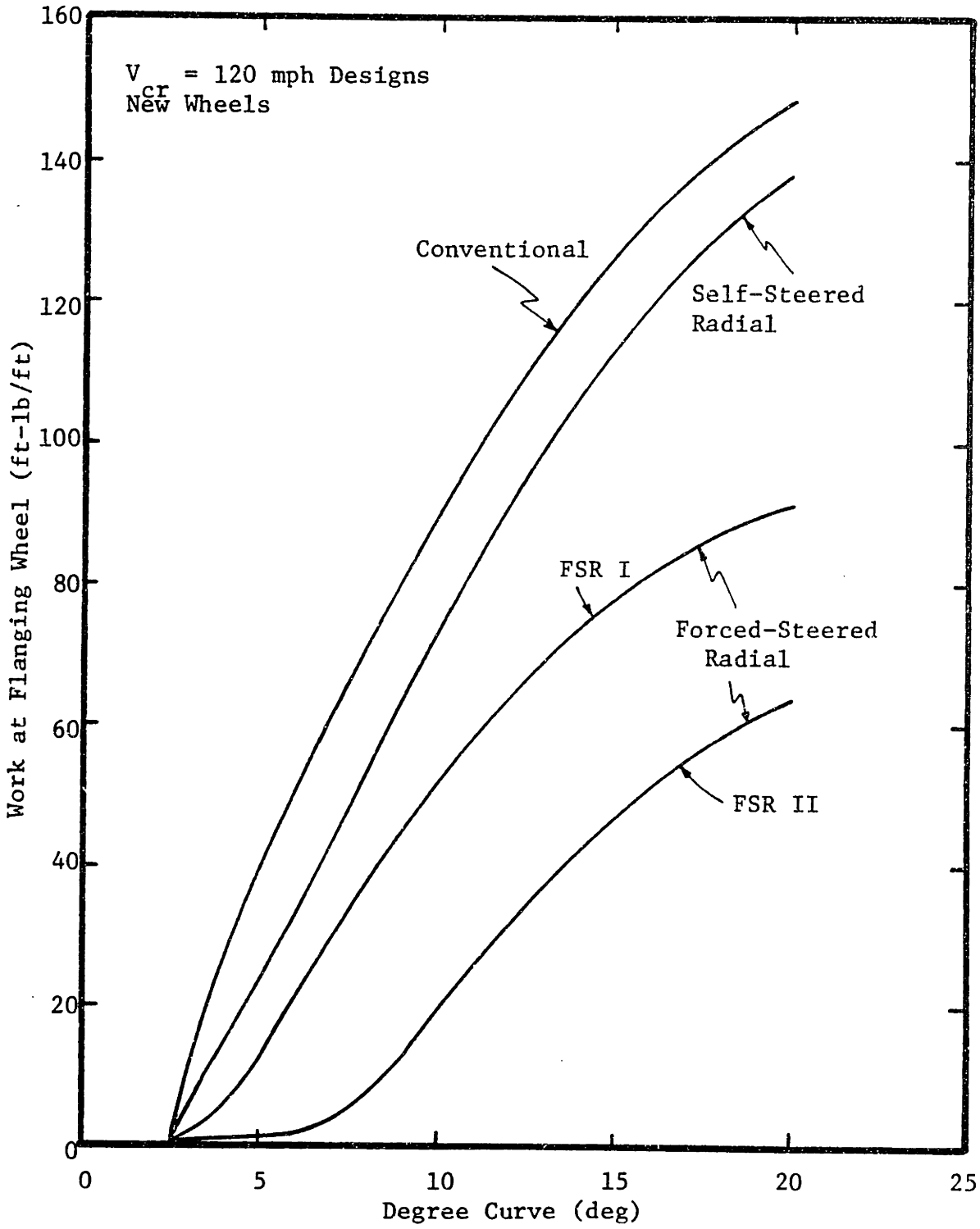

Figure 4.11 Work at Flanging Wheel vs. Curvature for Baseline Truck Designs with New Wheels (Critical Speeds = 120 mph).

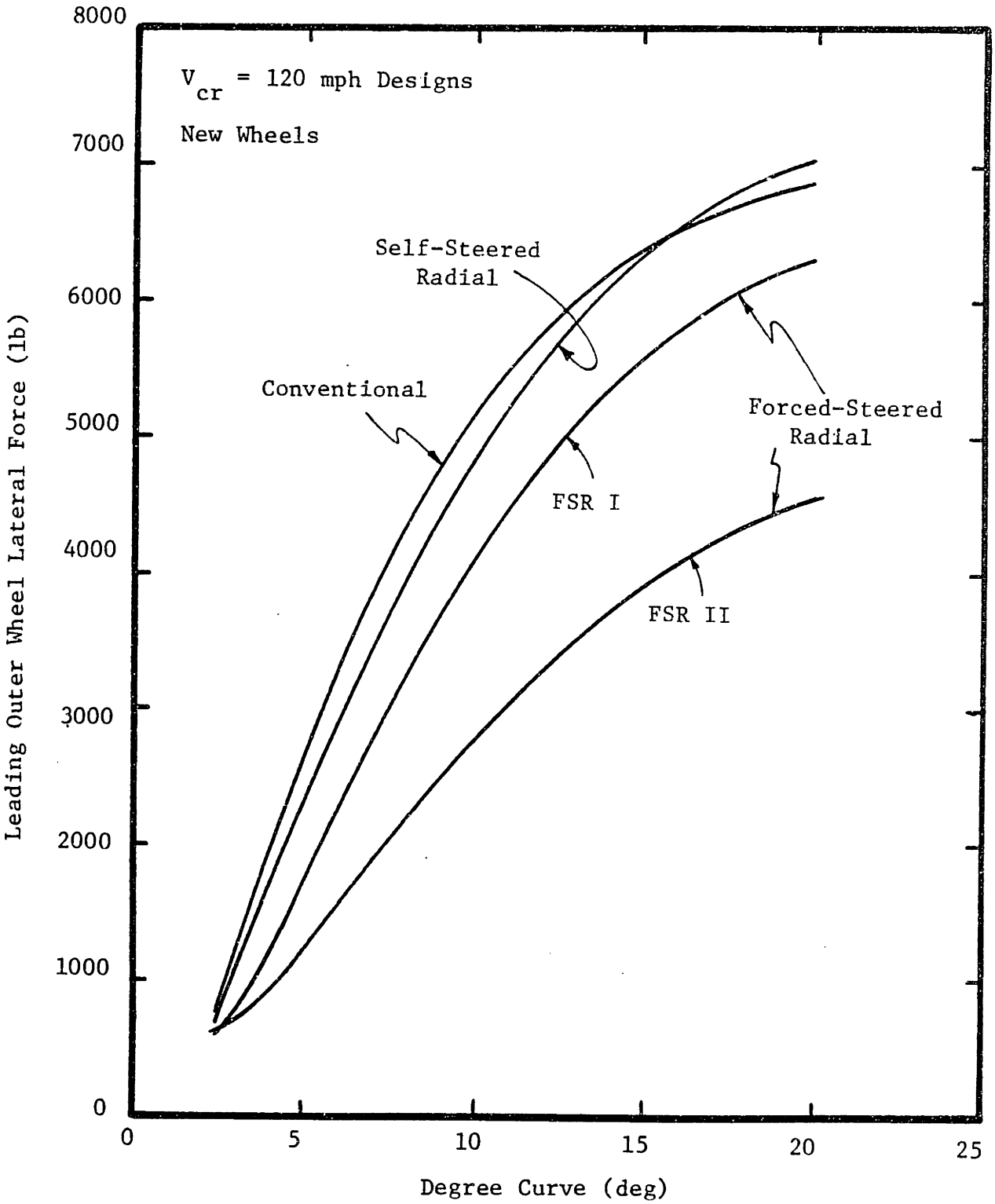

Figure 4.12 Leading Outer Wheel Lateral Force vs. Curvature for Baseline Truck Designs with New Wheels (Critical Speeds = 120 mph).

ventional truck, except at steep curvatures (> 15°). Around tight curves, the leading outer wheel lateral force of the self-steered truck is larger. Due to the added weight of the steering linkages, the self-steered truck has a higher normal load and thus a larger adhesion limit.

The flanging wheel work and lateral force as functions of track curvature are shown in Figures 4.13 and 4.14, respectively, for base-line truck designs with Heumann wheels. A significant improvement in curving performance is gained by using forced-steered trucks with Heumann wheels. For negotiation of 10° curves, the work at the flanging wheel of the forced-steered truck designs FSR I and FSR II is 7 and 2 ft-lb/ft, respectively, versus 61 ft-lb/ft for the self-steered truck and 69 ft-lb/ft for the conventional truck. At low degree curves, Figure 4.13 shows that the work of the conventional truck is slightly lower than the work of the self-steered radial truck. More work is expended for the self-steered truck since it has higher total shear stiffness causing its wheelsets to flange earlier. From Figure 4.14, the lateral force of the self-steered radial truck is slightly larger than the force of the conventional truck for curves greater than 10°. The added weight of the steering linkages of the radial truck results in a larger normal force and thus a larger adhesion limit at the leading outer wheel. In summary, Figures 4.13 and 4.14 demonstrate that substantial advantages are possible by employing forced-steered radial trucks with single-point contact Heumann wheels in comparison to conventional and self-steered trucks with Heumann wheels and in comparison to trucks with two-point contact new wheels.

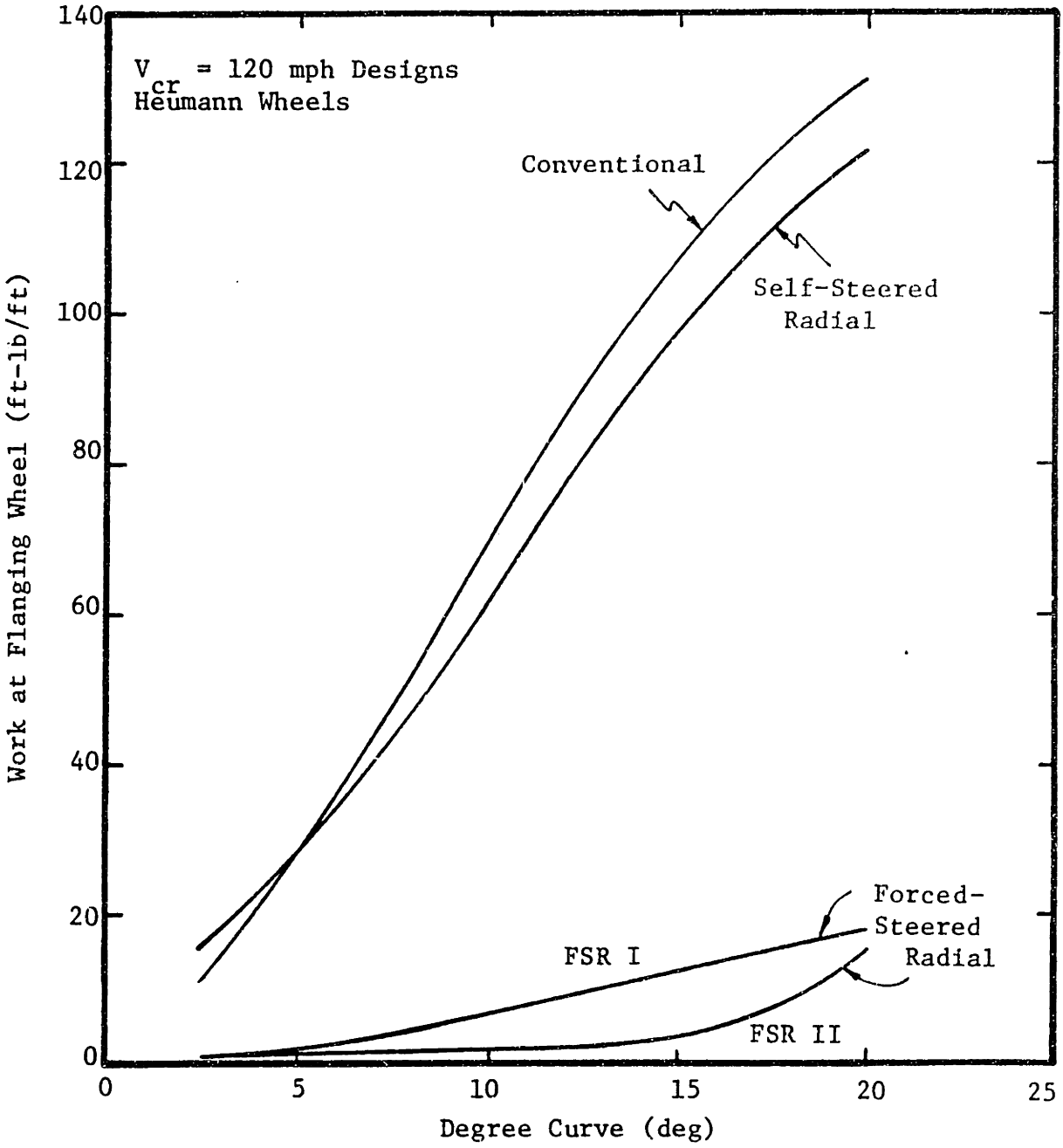

Figure 4.13 Work at Flanging Wheel vs. Curvature for Baseline Truck Designs with Heumann Wheels (Critical Speeds = 120 mph).

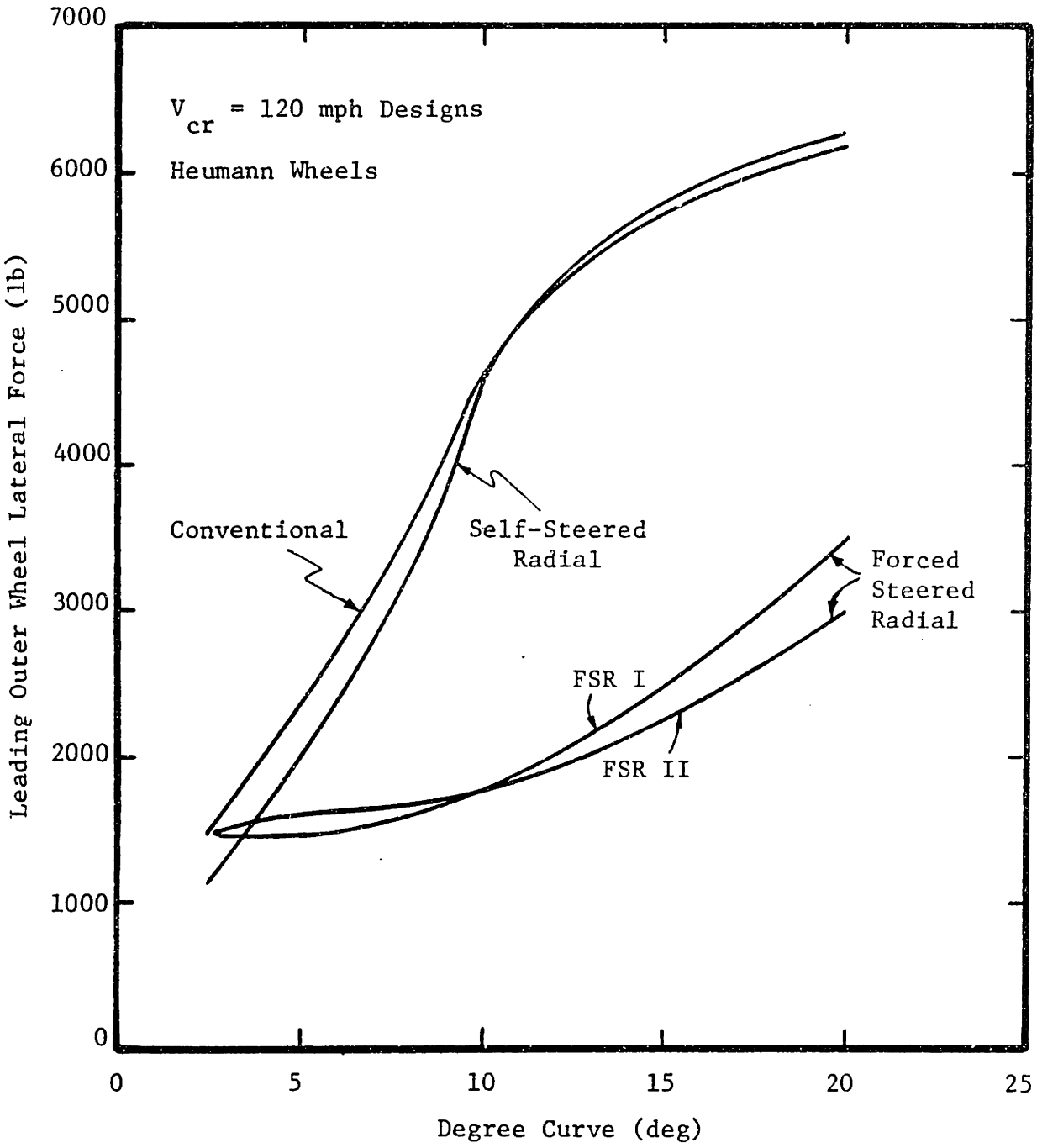

Figure 4.14 Leading Outer Wheel Lateral Force vs. Curvature for Baseline Truck Designs with Heumann Wheels (Critical Speeds = 120 mph).

Forced-steered truck designs are advantageous in comparison to conventional trucks since they reduce the work (and lateral force) at the flanging wheel. They also more equally distribute the work at the four wheels. The total work and distribution of work at the contact patches for the different trucks with new wheels are shown in Figure 4.15 and for trucks with Heumann wheels in Figure 4.16. In these figures, all trucks have critical speeds of 120 mph and are negotiating 10° curves. A reduction and equalization of work occurs for the forced-steered truck designs, especially designs with Heumann wheels.

In this thesis, the curving performance (and stability) studies have focused on the behavior of the front truck. In general, the front truck expends more work than the rear truck as a vehicle negotiates a curve. This is due to the directions of the secondary suspension yaw moments which act on the trucks, as shown in Figure 3.14. The yaw moment on the front truck hinders curving by pushing the leading outer wheel into the flange, whereas the moment on the rear truck helps curving by yawing the truck in the direction of the curve. In general, it is the leading outer wheel of the vehicle which experiences the majority of the contact patch work. Thus, in the steady-state curving performance studies the work expended at the leading outer or flanging wheel of the front truck is used as the principal curving performance index.

A comparison of the power dissipated by the different trucks during curve negotiation illustrates the potential improvements in performance possible with advanced designs. Table 4.5 summarizes the flanging wheel

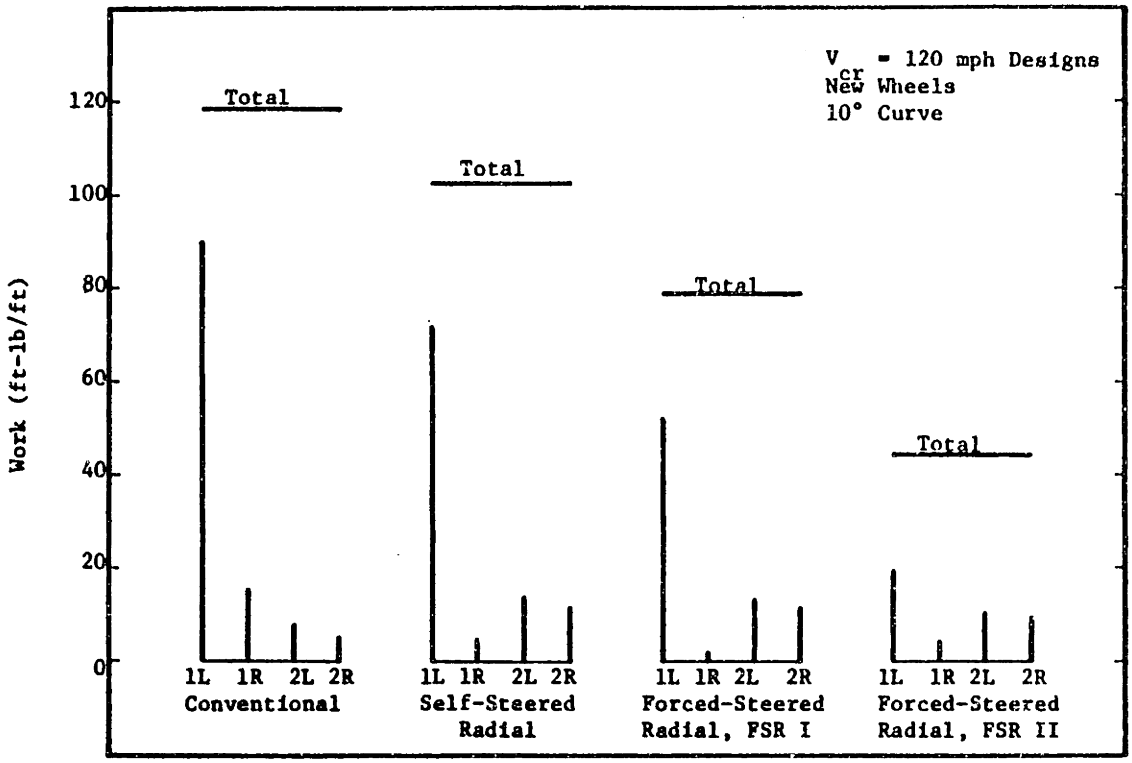

Figure 4.15 Total Work and Distribution of Work at Contact Patches for Baseline Trucks with New Wheels Negotiating 10° Curves (1L = Leading Left, 1R = Leading Right, 2L = Trailing Left, 2R = Trailing Right).

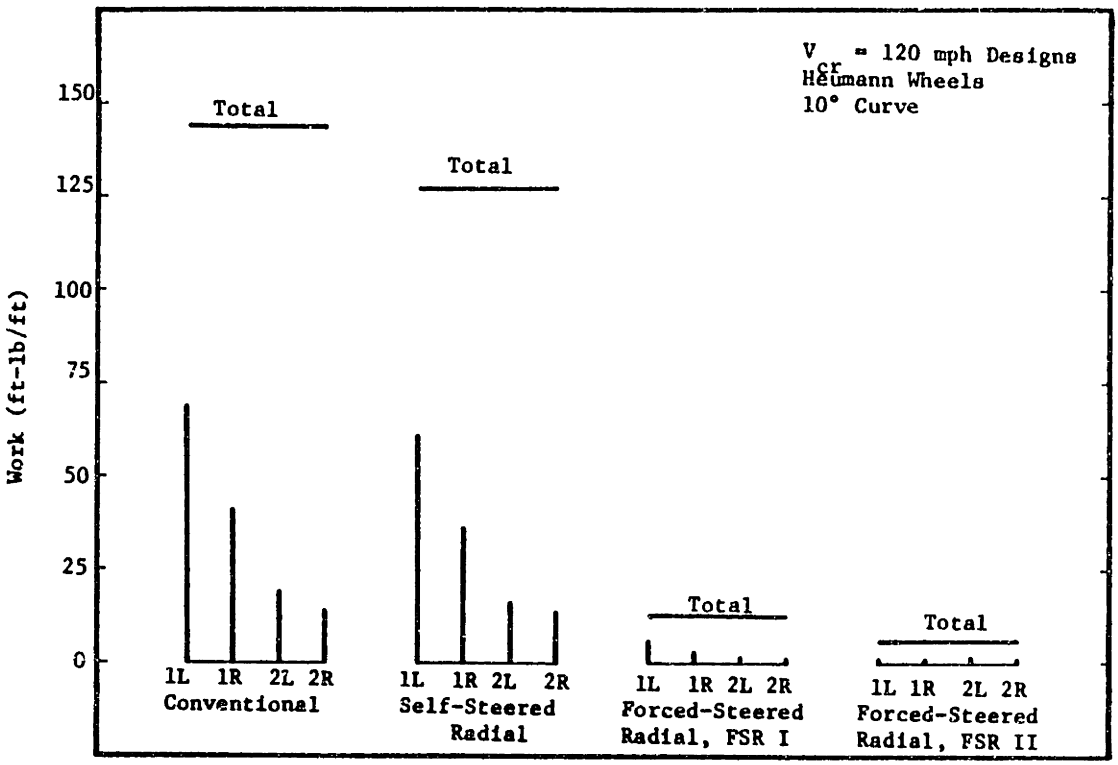

Figure 4.16 Total Work and Distribution of Work at Contact Patches for Baseline Trucks with Heumann Wheels Negotiating 10° Curves (1L = Leading Left, 1R = Leading Right, 2L = Trailing Left, 2R = Trailing Right).

TABLE 4.5

COMPARISON OF FLANGING WHEEL WORK, TOTAL WORK, AND POWER REQUIREMENTS OF FRONT AND REAR TRUCKS FOR BASELINE DESIGNS WITH NEW WHEELS NEGOTIATING 10° CURVES

		Conventional	Self-Steered Radial	Forced-Steered Radial	
				FSR I	FSR II
FRONT TRUCK	Flanging Wheel Work (ft-lb/ft)	90	72	52	19
	Truck Work (ft-lb/ft)	118	103	79	45
	Truck Power* (HP)	10.7	9.4	7.2	4.1
REAR TRUCK	Flanging Wheel Work (ft-lb/ft)	80	48	37	11
	Truck Work (ft-lb/ft)	118	84	57	25
	Truck Power* (HP)	10.7	7.6	5.2	2.3
Vehicle Total Power* (HP)		21.4	17.0	12.4	6.4

*@ 50 ft/sec (34 mph)

work, total work, and power requirements of baseline front and rear trucks with new wheels negotiating 10° curves. The table shows that more work is expended by the front truck than by the rear truck, especially for the steered truck designs which have additional moments helping to steer the rear truck around the curve. Furthermore, the table shows the front truck, rear truck, and total vehicle power for negotiation of the 10° curve at 50 ft/sec (34 mph) for the different truck designs. The significantly reduced dissipated power of the forced-steered vehicles, especially the FSR II design with 6.4 HP, in comparison to the conventional vehicle with 21.4 HP emphasizes the potential advantages of employing forced-steering to reduce fuel consumption.

In general, forced-steered truck designs offer significant advantages in comparison to conventional and self-steered trucks. This is especially true for trucks with Heumann wheels and for trucks negotiating tight curves.

CURVING PERFORMANCE OF RAIL PASSENGER VEHICLES

by

MARK L. NAGURKA

B.S.M.E., University of Pennsylvania, Philadelphia, Pennsylvania (1978)

M.S.E., University of Pennsylvania, Philadelphia, Pennsylvania (1979)

SUBMITTED IN PARTIAL FULFILLMENT
OF THE REQUIREMENTS OF THE DEGREE OF
DOCTOR OF PHILOSOPHY

at the

MASSACHUSETTS INSTITUTE OF TECHNOLOGY

Vol 2

May 1983

© Massachusetts Institute of Technology

Signature of Author Mark L. Nagurka
Department of Mechanical Engineering
May 1983

Certified by J. Karl Hedrick
Professor J. Karl Hedrick
Thesis Supervisor

Accepted by W M Rohsenow
Warren M. Rohsenow
Chairman, Departmental Graduate Committee

MASSACHUSETTS INSTITUTE
OF TECHNOLOGY
JUN 23 1983

LIBRARIES

5.0 DYNAMIC CURVING STUDIES

5.1 Introduction

The studies described in Chapters 3 and 4 have focused on the steady-state curving performance of rail vehicles. These studies have indicated the value of optimizing suspension design and wheel/rail profile to minimize wheelset angles and wheel/rail forces and thus reduce wheel and track wear, derailment proneness, and fuel costs. However, steady-state conditions rarely occur in actual operation. Most often dynamic effects occur due to deliberate and unintentional changes in track curvature and banking. Deliberate changes are imposed in sections of spiral transition track, such as curve entry and exit sections, whereas unintentional changes are introduced due to track irregularities.

The purpose of this chapter is to investigate the dynamic curving behavior of rail vehicles caused by deliberate changes in track curvature and banking. Studies of curve entry performance of conventional and innovative design vehicles are conducted using the dynamic curving analysis described in detail in Appendix C.

5.1.1 Dynamic Curving Model Evaluation

Preliminary evaluation studies have been conducted to compare the results of the dynamic curving analysis with the predictions of the steady-state curving and linear stability analyses. Excellent agreement has been obtained, as described in this section.

For comparison with the steady-state curving results, a dynamic curving simulation along constant radius track has been conducted.* In the study, the results of the steady-state analysis have been used as initial conditions. Baseline conventional vehicles with new** and Heumann wheels negotiating a 5° curve at a balanced running speed of 60 ft/sec have been simulated. For the vehicle with Heumann wheels, single-point contact occurs at all wheels, whereas for the vehicle with new wheels, two-point contact occurs at the leading outer wheel. In both cases, the dynamic curving analysis maintains the steady-state solution. Wheelset geometries, wheel/rail forces, and contact patch work are compared in Table 5.1. The table shows that for both Heumann and new wheels, for which single-point and two-point contact occurs, respectively, at the leading outer wheel, the results of the steady-state and dynamic curving analyses agree.

A study has been conducted to compare the results of the dynamic curving and linear stability analyses. In the study, nonlinearities in the dynamic curving analysis have been eliminated. Linear wheel/rail profile geometry data corresponding to constant 0.05 conicity wheels, as well as nonsaturating creep forces, have been assumed. The resulting "linearized" dynamic curving analysis has been used to

---

*Constant secondary yaw breakaway torques have been used. A positive (i.e., anti-curving) torque acts on the front truck and a negative torque acts on the rear truck.

**The new wheel profile represents the standard new AAR wheel with a 1 in 20 tread taper and a steep flange and is characterized by two-point wheel/rail contact during flanging.

TABLE 5.1

COMPARISON OF STEADY-STATE AND DYNAMIC CURVING RESULTS WITH CONSTANT SECONDARY YAW BREAKAWAY TORQUES

Baseline Conventional Vehicles Negotiating 5° Curve at Balance Speed of 60 ft/sec (45 mph); $k_{rail} = 1.0 \times 10^7$ lb/ft

HEUMANN WHEELS	Dynamic Curving Analysis in Steady-State	Steady-State Curving Analysis	Percent Difference
Leading Wheelset Lateral Excursion, y_{wl} (in)	0.2927	0.2925	0.1%
Leading Outer Rail Lateral Excursion, y_{rail_L} (in)	0.0027	0.0027	0%
Leading Wheelset Angle of Attack, ψ_{wl} (deg)	0.2007	0.1979	1.4%
Leading Outer Wheel Lateral Force, $F_{lat_{1L}}$ (lb)	2285	2295	0.4%
Leading Outer Wheel Work, W_{1L} (ft-lb/ft)	29	29	0%

NEW WHEELS	Dynamic Curving Analysis in Steady-State	Steady-State Curving Analysis	Percent Difference
y_{wl} (in)	0.3233	0.3233	0%
y_{rail_L} (in)	0.0033	0.0033	0%
$_1$ (deg)	0.0905	0.0890	1.7%
$F_{lat_{1L}}$ (lb)	2770	2750	0.7%
W_{1L} (ft-lb/ft)	41	40	2.4%

empirically determine the critical speed of a conventional vehicle on tangent track. With a small perturbation (y_{W1}=0.05 in) introduced, the forward speed has been varied. Figure 5.1 shows the responses of the leading wheelset angles of attack following the imposed perturbation offset for three different forward speeds. For forward speeds below the critical speed, Figure 5.1a shows that the resulting oscillations dampen out, corresponding to stable vehicle operation. On the other hand, Figure 5.1c shows that perturbations introduced at speeds greater than the critical speed grow in magnitude, indicating inherent instability. At the critical speed, oscillations caused by the perturbation persist since there is no damping (see Figure 5.1b). The results are consistent with the eigenvector analysis of the linear model.

5.1.2 Scope and Approach of Dynamic Curving Study

This chapter focuses on the dynamic curving performance of conventional, self-steered, and forced-steered radial vehicles with new and Heumann wheels. The purpose of the study is to determine whether the transient curve entry characteristics of vehicles with alternate suspension designs and/or wheel profiles differ significantly from the curve entry behavior of conventional vehicles with standard new wheels. The results of the study are used to make some preliminary conclusions about the use of the steady-state curving analysis for design purposes. These conclusions are presented in Chapter 6.

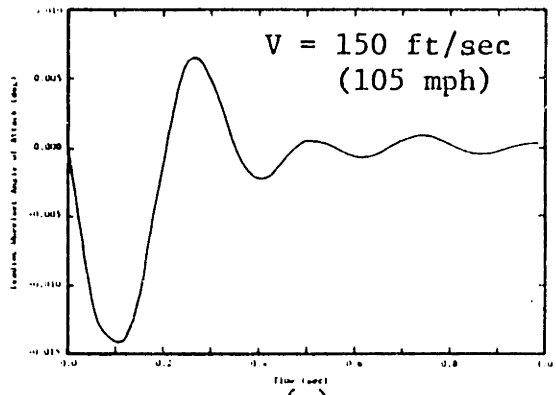

(a)

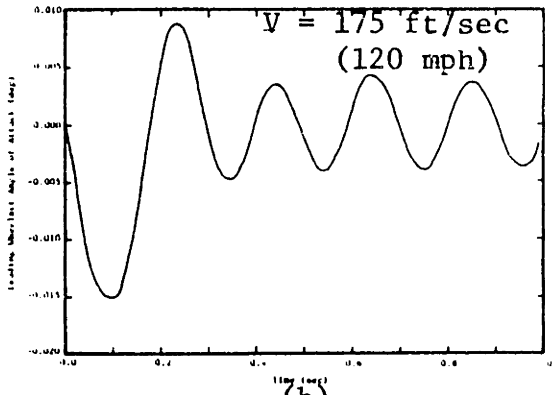

(b)

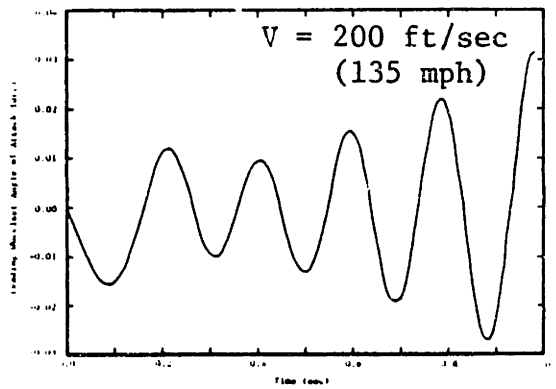

(c)

Figure 5.1 History of Leading Wheelset Angle of Attack of a Conventional Vehicle Operating on Tangent Track at (a) 150 ft/sec, (b) 175 ft/sec, and (c) 200 ft/sec in Presence of Perturbation

A limited study of the effect of transition spiral length on the curving performance of conventional vehicles with new wheels is also conducted. The length of the spiral curve transition track has a strong influence on the vehicle transient behavior and thus is an important track design variable.

In the curve entry simulations of this chapter, the following assumptions are made: (1) The vehicles enter the transition spiral track at the initial time (t = 0.0 sec) from centered tangent track positions. (2) The vehicles operate at constant forward speed, determined by the balanced running speed for the constant radius curve track. Table 5.2 lists the balance running speeds for different track curvatures used in the simulations. (3) The baseline transition spiral is 150 ft, which represents a typical value for transit systems. (4) Laterally stiff rails are used, i.e., $k_{rail} = 1.0 \times 10^7$ lb/ft. (5) The wheelsets are powered with axle drive torques of 420 ft-lb, representing 5% of the slip torque for axles with 50 HP traction motors operating at 50 mph.

The steady-state curving analysis assumes that yaw breakaway has occurred at each truck centerplate and thus a constant secondary yaw breakaway torque acts on each truck. A positive (or anti-curving) torque acts on the front truck degrading its ability to negotiate the curve and a negative torque acts on the rear truck helping it to negotiate the curve. Thus, in the steady-state analysis the two trucks behave differently, with the curving performance of the

TABLE 5.2

BALANCED RUNNING SPEEDS
ASSUMING 6 IN SUPERELEVATION
(i.e., $\phi_{SE} = 6.2°$)

DEGREE CURVE (deg)	CURVE RADIUS (ft)	BALANCED RUNNING SPEED	
		(ft/sec)	(mph)
2.5°	2290	90	60
5°	1146	60	45
10°	575	45	30
20°	288	30	20

front truck in general worse than the performance of the rear truck.

In the dynamic curving analysis, a different model of secondary yaw suspension is adopted. A coulomb damper which saturates at the breakaway torque acts between each truck and the carbody. For numerical reasons, the damper includes a linear viscous band at the origin. During dynamic conditions, the front and rear trucks display different behavior in general since truck and carbody yaw rates are present and thus yaw torques develop. Due to the linear viscous band, in steady-state the secondary yaw torques on the two trucks vanish since the truck and carbody yaw rates are zero. Thus, in the dynamic curving analysis, the two trucks behave identically in steady-state since no secondary yaw torques are imposed.

Therefore, in the dynamic curving simulations of this chapter, the results in steady-state do not agree with the results obtained with the steady-state curving analysis presented in Chapters 3 and 4. To evaluate the differences in results, a simulation study has been conducted for vehicles with and without secondary yaw breakaway torques. The results are compared in Table 5.3 for baseline conventional vehicles with new and Heumann wheels negotiating a 5° curve at a balanced running speed of 60 ft/sec. In the steady-state curving analysis, the breakaway torque is + 7500 ft-lb for the front truck and - 7500 ft-lb for the rear truck. In the dynamic curving analysis, secondary yaw torques do not develop in steady-state and thus the performance (of the front truck) is improved in comparison

TABLE 5.3

COMPARISON OF STEADY-STATE AND DYNAMIC CURVING RESULTS WITH AND WITHOUT SECONDARY YAW BREAKAWAY TORQUES

Baseline Conventional Vehicles Negotiating 5° Curve at Balance Speed of 60 ft/sec (45 mph); $k_{rail} = 1.0 \times 10^7$ lb/ft

HEUMANN WHEELS	Steady-State Curving Analysis (i.e., Constant Breakaway Torques: ± 7500 ft-lb)	Dynamic Curving Analysis in Steady-State (i.e., No Breakaway Torque)	Percent Change
Leading Wheelset Lateral Excursion y_{w1} (in)	0.2925	0.2658	9%
Leading Outer Rail Lateral Excursion, y_{rail_L} (in)	0.0027	0.0019	30%
Leading Wheelset Angle of Attack, ψ_{w1} (deg)	0.1979	0.1858	6%
Leading Outer Wheel Lateral Force, $F_{lat_{1L}}$ (lb)	2295	1570	32%
Leading Outer Wheel Work, W_{1L} (ft-lb/ft)	29	23	21%

NEW WHEELS	Steady-State Curving Analysis (i.e., Constant Breakaway Torques: ± 7500 ft-lb)	Dynamic Curving Analysis in Steady-State (i.e., No Breakaway Torque)	Percent Change
y_{w1} (in)	0.3233	0.3225	0.3%
y_{rail_L} (in)	0.0033	0.0025	24%
ψ_{w1} (deg)	0.0890	0.1053	18%
$F_{lat_{1L}}$ (lb)	2750	2060	25%
W_{1L} (ft-lb/ft)	40	36	10%

to the performance predicted by the steady-state curving analysis. The differences in performance do not present a serious limitation since (1) this chapter focuses on transient characteristics, and (2) due to actual dynamic effects, the secondary torque probably does not remain at the constant breakaway level. In summary, the steady-state curving analysis represents a more conservative design tool than the dynamic curving analysis to study steady-state performance. The dynamic curving analysis has been designed to study transient behavior (i.e., dynamic performance) during curve entry and negotiation.

5.2 Curve Entry Performance of a Conventional Vehicle

This section investigates the curve entry performance of conventional vehicles. The effect of track curvature, wheel/rail profile, and transition spiral length on the transient behavior of baseline conventional vehicles is discussed.

The nature of curve entry dynamics can be seen in the response of a baseline conventional vehicle with new wheels for which $k_{px} = 1.35 \times 10^5$ lb/ft negotiating a 150 ft transition spiral into a 10° curve at a balance speed of 45 ft/sec. Figures 5.2a and b show the wheelset lateral excursions and angles of attack, respectively, as functions of time. Figures 5.3a and b show the leading outer (i.e., flanging) wheel lateral force and contact work, respectively, as functions of time.

As the front truck enters the spiral curve, the leading wheelset

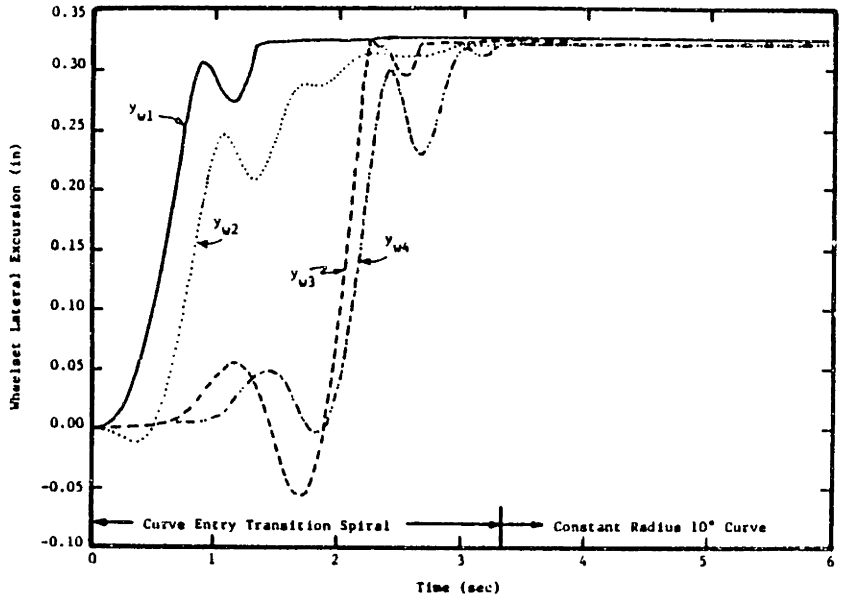

(a)

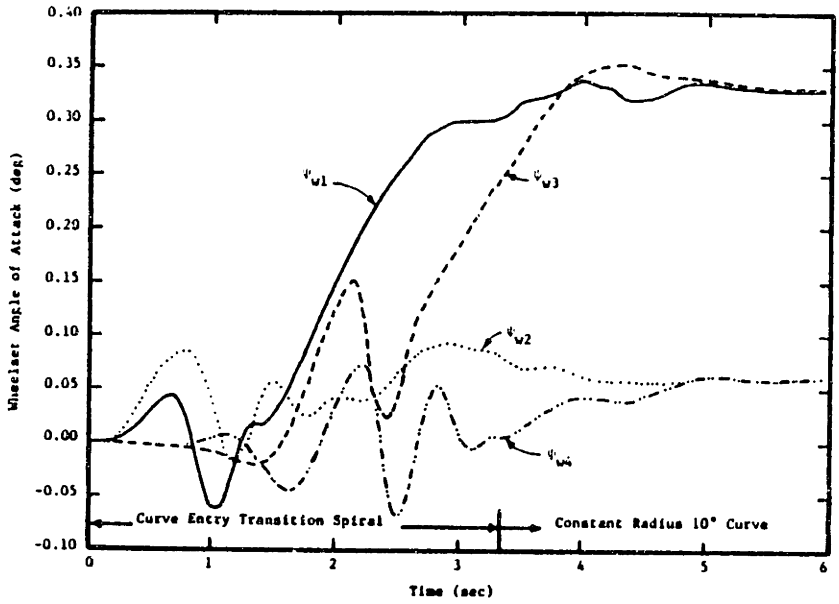

(b)

Figure 5.2: History of (a) Wheelset Lateral Excursions and (b) Angles of Attack of a Baseline Conventional Vehicle with New Wheels Negotiating a 150 ft Curve Entry Spiral into a 10° Curve at a Balance Speed of 45 ft/sec.

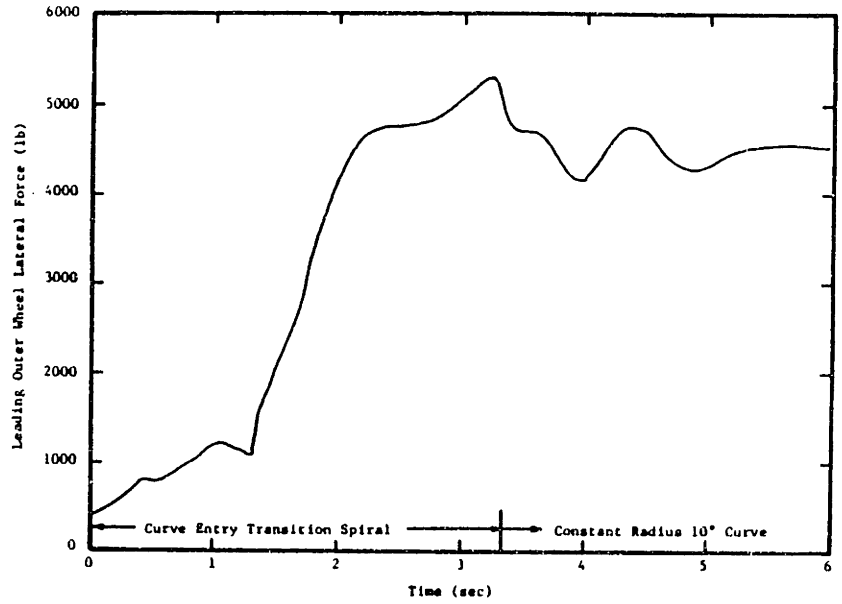

(a)

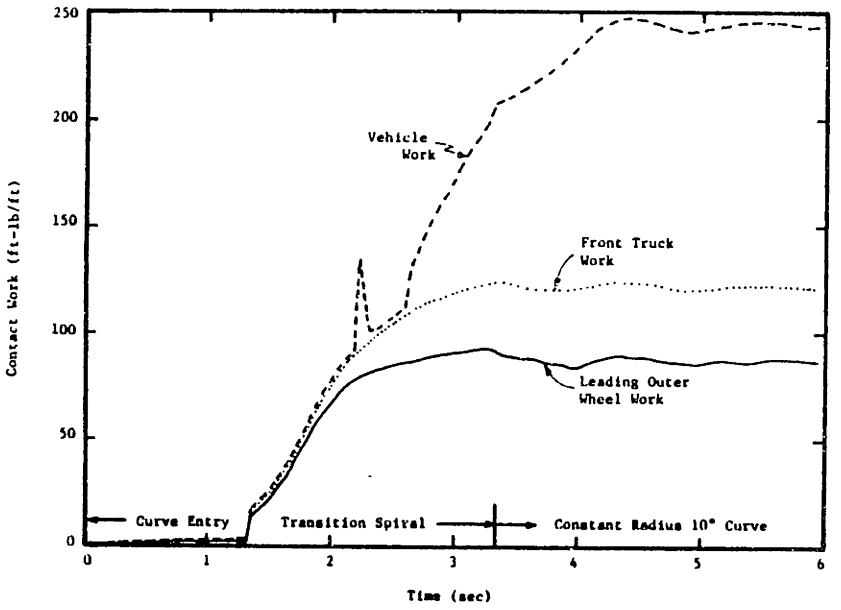

(b)

Figure 5.3 History of (a) Leading Outer (i.e., Flanging) Wheel Lateral Force and (b) Contact Work of a Baseline Conventional Vehicle with New Wheels, Negotiating a 150 ft Curve Entry Spiral into a 10° Curve at a Balance Speed of 45 ft/sec

rapidly displaces laterally toward the outer rail. The wheelset overshoots its desired rolling radius difference and thus the lateral displacement decreases slightly and then grows again. The leading outer wheel approaches its flange, but maintains single-point tread contact until it encounters the flange at t = 1.375 sec (i.e., 62 ft into the spiral). Two-point contact occurs at the leading outer wheel for the remainder of the simulation. The trailing wheelset of the front truck shows similar but somewhat lagged behavior. It displaces laterally maintaining single-point tread contact until the outer wheel impacts its flange at t = 3.000 sec (i.e., 135 ft into the spiral). It stays in two-point tread and flange contact for the remainder of the simulation.

The leading and trailing wheelsets of the rear truck displace rapidly toward the outer rail at t ≃ 2.0 sec (i.e., ≃ 90 ft into the spiral). The leading outer wheel of the rear truck impacts its flange at t ≃ 2.250 sec (i.e., 101 ft into the spiral) causing two-point contact to occur momentarily, and then bounces back into tread contact until t = 2.750 sec (i.e., 124 ft into the spiral). At all subsequent times two-point contact occurs at the leading outer wheel of the rear truck. The trailing wheelset of the rear truck maintains single-point tread contact during the entire transition spiral section. Two-point tread and flange contact occurs at the trailing outer wheel at t = 3.375 sec (i.e., 2 ft into the constant radius curve).

Figure 5.2b shows the angle of attack histories of the four wheelsets of the vehicle. As the vehicle enters the curve, the wheelsets of the front truck initially develop positive angles of attack. The wheelsets of the rear truck, which are still on tangent track, have zero angles. During negotiation of the transition spiral track, the angles of attack of all the wheelsets display oscillatory behavior. The oscillations disappear as the vehicle negotiates the constant radius curve track. In steady-state conditions, the leading wheelsets of the front and rear trucks develop angles of attack of ~ 0.33 deg and the trailing wheelsets develop angles of ~ 0.06 deg.

The lateral force at the leading outer wheel of the vehicle as a function of time is shown in Figure 5.3a. (This force is also called the flange force). The force increases rapidly at $t = 1.375$ sec when the leading outer wheel hits the flange and two-point contact develops. The force continues to increase, reaching a maximum of 5270 lb at $t = 3.250$ sec (i.e., 146 ft into the spiral) just before entering the constant radius curve. The peak force exceeds the steady-state force by 17%.

The leading outer wheel, front truck, and vehicle work as a function of time is shown in Figure 5.3b. The front truck work is the sum of the work expended at the contact patches at the four wheels of the front truck; similarly, the vehicle work is the sum of the work at all contact patches. At $t = 1.375$ sec, two-point contact develops at the leading outer wheel, and the work function

shows a sudden jump. As the vehicle continues through the curve, the contact work at the leading outer wheel and at the front truck continues to increase and each approaches a constant. The vehicle work rises rapidly at t = 2.250 sec when the leading outer wheel of the rear truck bounces into the flange and two-point contact occurs. The work decreases since single-point tread contact is restored and then increases at t = 2.750 sec when two-point contact again develops. The vehicle work continues to increase and then reaches a constant as steady-state conditions are approached.

In the following sections, the influences of track curvature, wheel/rail profile, and transition spiral length on the dynamic curving performance of baseline conventional vehicles are examined.

5.2.1 Effect of Track Curvature on Curve Entry Performance of a Conventional Vehicle

The track curvature is an important parameter influencing steady-state and dynamic curving performance. The steady-state results show that in general as tighter curves are negotiated, the flanging wheel contact work and lateral force increase. To determine the effect of track curvature on the transient behavior, a limited study of curve entry performance of conventional vehicles with new wheels has been conducted.

The response of a baseline conventional vehicle with new wheels negotiating a 150 ft curve entry spiral into a 2.5° curve at a balance speed of 90 ft/sec is shown in Figures 5.4 and 5.5. Figures 5.4a and b show the wheelset lateral excursion and angle

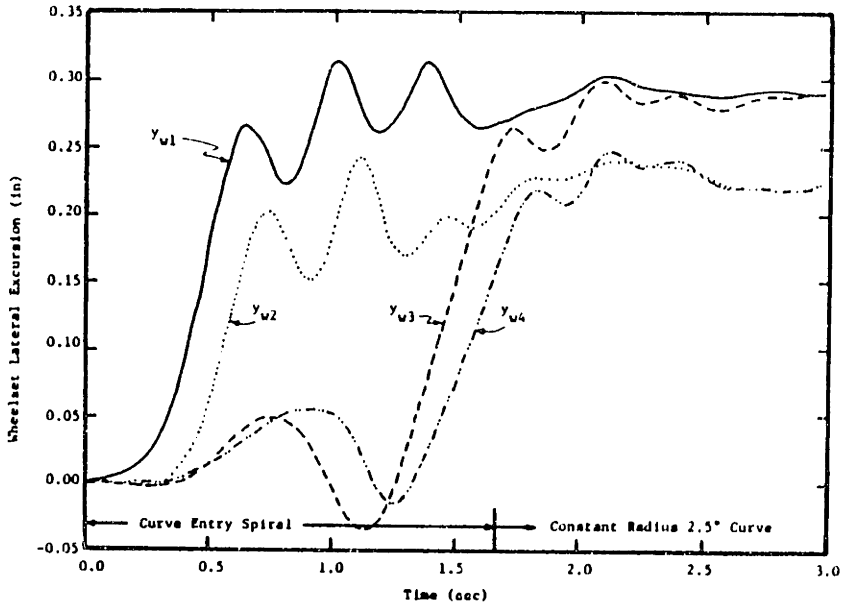

(a)

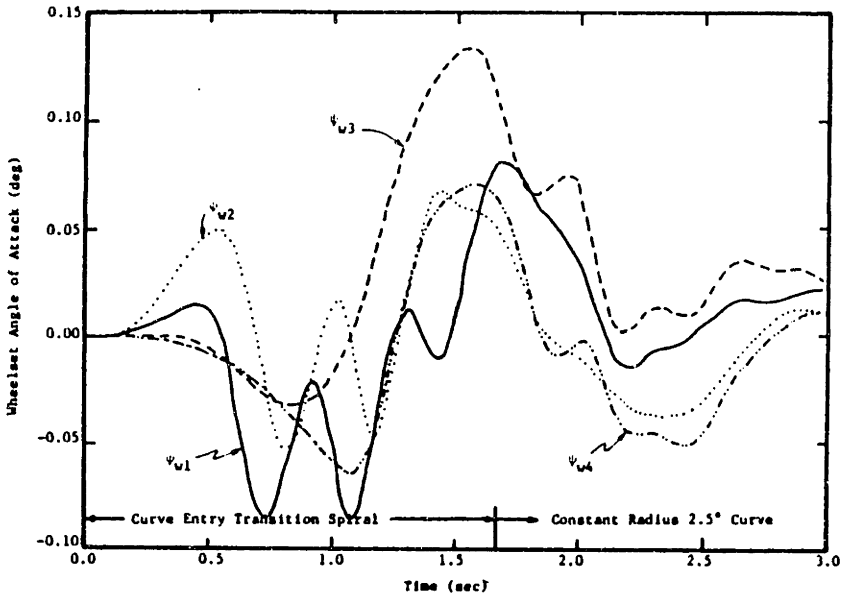

(b)

Figure 5.4: History of (a) Wheelset Lateral Excursions and (b) Angles of Attack of a Baseline Conventional Vehicle with New Wheels Negotiating a 150 ft Curve Entry Spiral into a 2.5° Curve at a Balance Speed of 90 ft/sec.

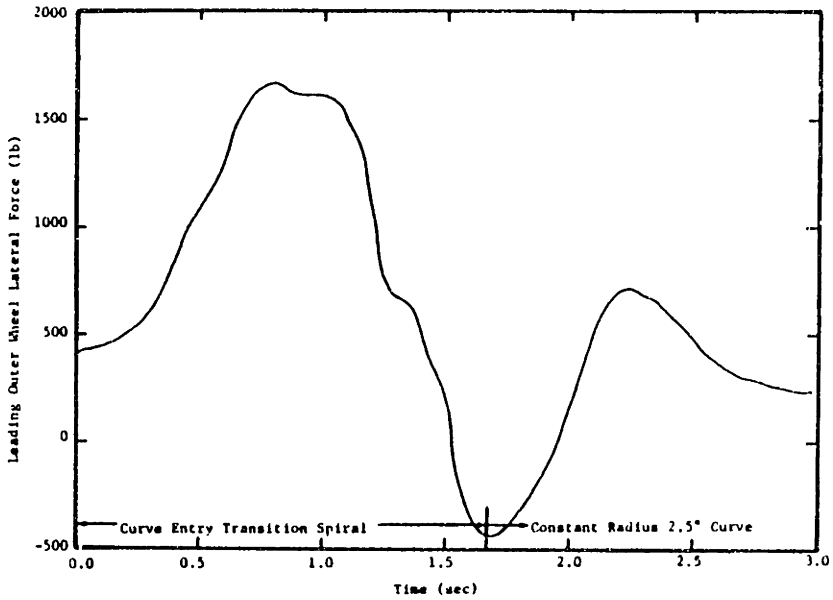

(a)

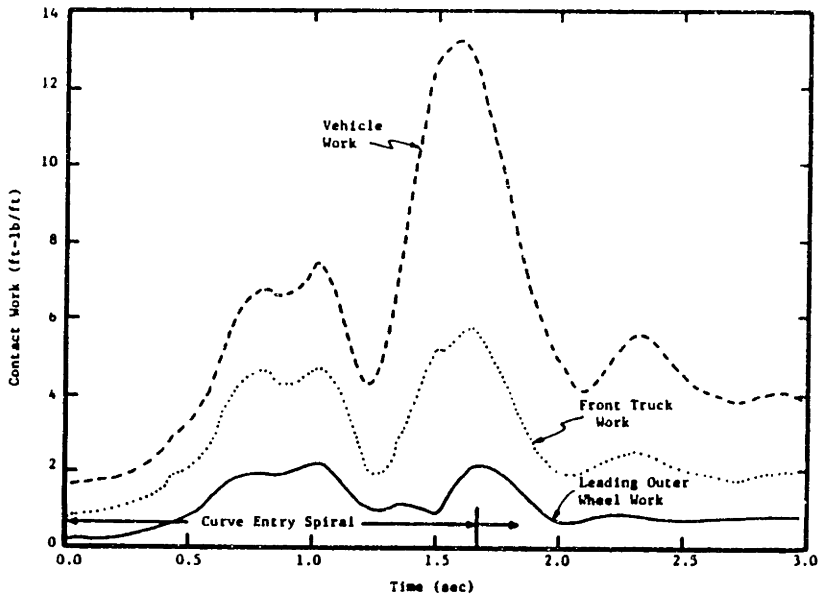

(b)

Figure 5.5: History of (a) Leading Outer (i.e., Flanging) Wheel Lateral Force and (b) Contact Work for a Baseline Conventional Vehicle with New Wheels Negotiating a 150 ft Curve Entry Spiral into a 2.5° Curve at a Balance Speed of 90 ft/sec.

of attack histories, respectively; Figures 5.5a and b show the flanging wheel lateral force and contact work histories, respectively. Single-point contact occurs at all wheels during the simulation. As the vehicle enters the transition spiral curve, the wheelsets of the front truck displace laterally toward the outer rail and oscillate, overshooting their desired positions (for the correct rolling radius difference). The wheelsets of the rear truck, which maintain their centered positions until they enter the curve, displace out and in slightly and then also displace laterally toward the outer rail and oscillate. In the constant radius curve section, the lateral excursions settle to the steady values: ~ 0.286 in for the leading wheelsets of the front and rear truck and ~ 0.221 in for the trailing wheelsets of the two trucks.

The wheelset angles of attack as a function of time, shown in Figure 5.4b exhibit sustained oscillatory behavior in the transition spiral curve. In the constant radius curve section, the oscillations continue but dampen. Steady-state conditions are not achieved until $t \sim 3.0$ sec (i.e., 120 ft into the constant radius curve).

Figure 5.5a shows the oscillatory behavior of the leading outer or flanging wheel lateral force as a function of time. The force increases as the vehicle enters the spiral curve, peaking at 1640 lb at $t = 0.751$ sec (i.e., 68 ft into the spiral). The force then decreases and eventually grows negative. As the vehicle enters the constant radius curve section, the force reaches a minimum of -440 lb at $t = 1.688$ sec (i.e., 2 ft into the constant radius curve).

The force increases and settles to its steady value of 340 lb by t = 3.0 sec (i.e., 120 ft into the constant radius curve).

The contact work expended at the leading outer wheel, at the front truck, and at the vehicle as a function of time is shown in Figure 5.5b. The work histories oscillate, until settling to their steady-state values: 1 ft-lb/ft for the leading outer wheel, 2 ft-lb/ft for the front truck, and 4 ft-lb/ft for the vehicle. The leading outer wheel work reaches a maximum of 2 ft-lb/ft at t = 1.000 sec (i.e., 90 ft into the spiral) and at t = 1.688 sec (i.e., 2 ft into the constant radius curve). The front truck and vehicle work reach maximum values of 6 and 13 ft-lb/ft, respectively, at t = 1.625 sec (i.e., 146 ft into the spiral). The maximum values occur when the wheelset angles of attack are extremum, indicative of large lateral creepages.

In summary, important transient behavior develops for a conventional vehicle with new wheels negotiating a 150 ft transition spiral into a shallow 2.5° curve at balance speed. The wheelset excursions and angles, the leading outer wheel lateral force, and the contact work significantly exceed their steady-state values. The wheelsets show sustained lateral and yaw oscillations in the transition spiral curve. These oscillations dampen out in the constant radius curve, and eventually steady-state conditions are achieved.

In contrast, the response of the vehicle traversing a 150 ft

spiral into a moderate 10° curve, shown in Figures 5.2 and 5.3, indicates that less significant transient behavior occurs. For instance, the peak flanging wheel force exceeds the steady-state force by only 17% for the vehicle running into the 10° curve, whereas the peak force exceeds the steady-state force by 388% for the vehicle negotiating the 2.5° curve. Table 5.4 summarizes the steady-state and peak flanging wheel force and contact work of a baseline conventional vehicle with new wheels entering a 2.5°, 5°, and 10° curve at balance speed. As tighter curves are traversed, the dynamic effects diminish. The wheelsets displace to the flange clearance and remain there. In comparison, for negotiation of shallow curves, the wheelsets approach the flanges but always remain in tread contact. The wheelsets exhibit "hunting"-type oscillations along the transition spiral, which result in significant dynamic behavior.

5.2.2 Effect of Wheel/Rail Profile on Curve Entry Performance of a Conventional Vehicle

The results of the steady-state studies presented in Chapters 3 and 4 emphasize the importance of wheel/rail profile on vehicle curving performance. In particular, the results suggest that single-point contact profiles, such as Heumann wheel profiles, offer improved performance in terms of decreased contact work in comparison to two-point contact profiles, such as new AAR wheel profiles. This section addresses the influence of wheel/rail profile on dynamic curving performance.

TABLE 5.4

LEADING OUTER WHEEL FORCE AND WORK OF A BASELINE CONVENTIONAL VEHICLE WITH NEW WHEELS NEGOTIATING A 150 FT CURVE ENTRY SPIRAL INTO A 2.5°, 5°, AND 10° CURVE

DEGREE CURVE (deg)	LEADING OUTER WHEEL LATERAL FORCE (lb)			LEADING OUTER WHEEL WORK (ft-lb/ft)		
	Steady-State	Peak	% Increase	Steady-State	Peak	% Increase
2.5°	340	1660	388%	1	2	100%
5°	2060	2650	29%	36	41	14%
10°	4520	5270	17%	87	93	7%

A curve entry simulation has been conducted to determine the dynamic response of a baseline conventional vehicle with Heumann wheels (for which $k_{px} = 6.50 \times 10^5$ lb/ft) negotiating a 150 ft transition spiral into a 10° curve at a balance speed of 45 ft/sec. The response histories are shown in Figures 5.6 and 5.7. The wheelset lateral excursions and angles of attack as functions of time are shown in Figures 5.6a and b, respectively. The leading outer wheel lateral force and contact work as functions of time are shown in Figures 5.7a and b, respectively. Since Heumann wheels are employed, single-point contact occurs at the wheels at all times.

As the vehicle enters the curve, the leading wheelset of the front truck displaces laterally toward the outer rail, as shown in Figure 5.6a. The leading outer wheel gradually rides up into the flange and stays in flange root contact. The trailing wheelset of the front truck increases and then decreases slightly, always staying near the centered position. The leading wheelset of the rear truck oscillates about the centered position and then smoothly displaces toward the outer rail. The trailing wheelset of the rear truck also oscillates about the centered position. The steady-state excursions are ~ 0.346 in for the leading wheelsets of the two trucks and ~ 0.034 in for the trailing wheelsets.

The angle of attack histories, shown in Figure 5.6b, reveal that the trailing wheelsets of both trucks remain near radial alignment during the simulation. For the leading wheelsets, the

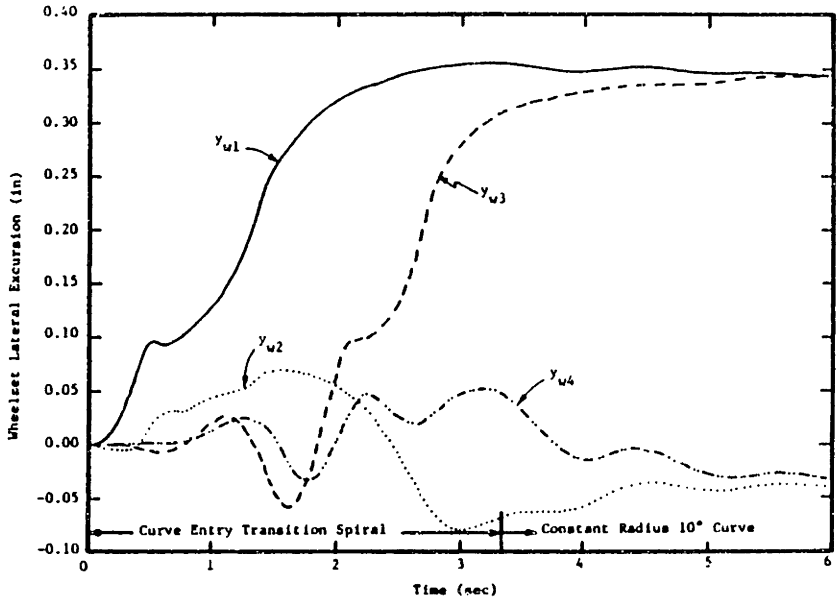

(a)

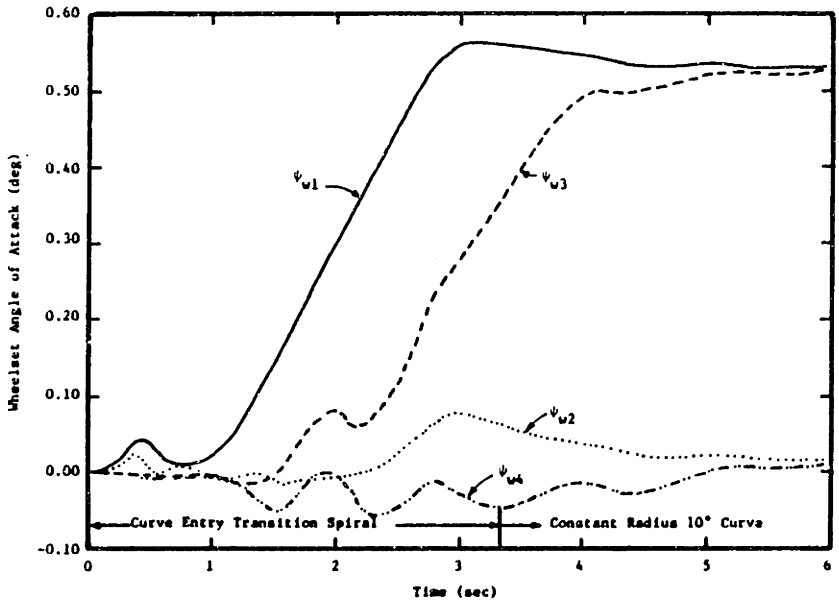

(b)

Figure 5.6: History of (a) Wheelset Lateral Excursions and (b) Angles of Attack of a Baseline Conventional Vehicle with Heumann Wheels Negotiating a 150 ft Curve Entry Spiral into a 10° Curve at a Balance Speed of 45 ft/sec.

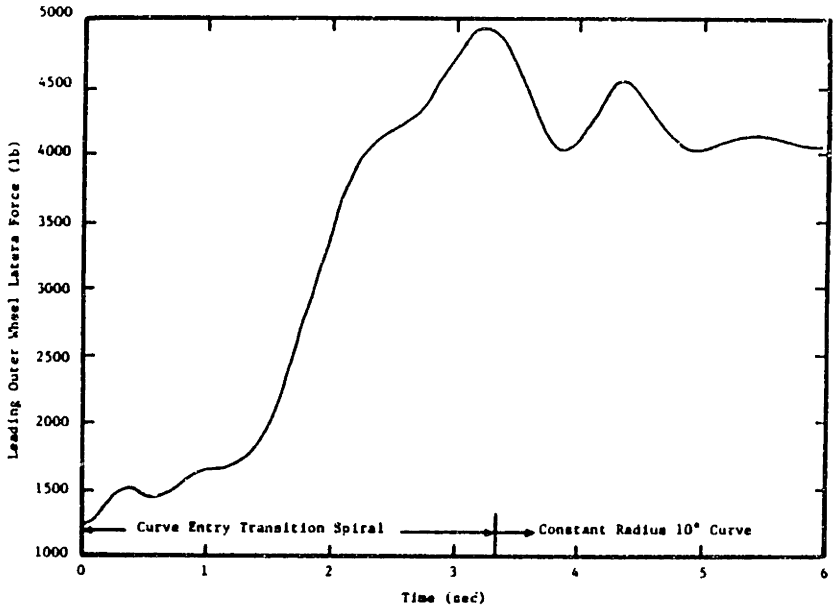

(a)

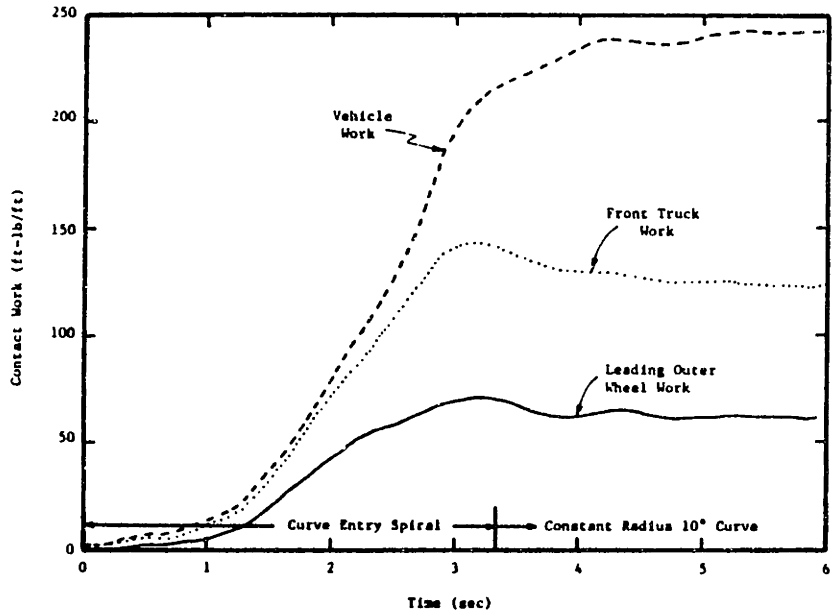

(b)

Figure 5.7: History of (a) Leading Outer (i.e., Flanging) Wheel Lateral Force and (b) Contact Work of a Baseline Conventional Vehicle with Heumann Wheels Negotiating a 150 ft Curve Entry Spiral into a 10° Curve at a Balance Speed of 45 ft/sec.

angles of attack increase and approach a constant as the vehicle negotiates the curve. The steady-state angles of attack are ~0.529 deg and ~ 0.013 deg for the leading and trailing wheelsets of the two trucks, respectively.

The leading outer wheel lateral force, shown in Figure 5.7a, increases as the vehicle enters the curve. It reaches a maximum of 4950 lb when the leading outer wheel rides up into the flange at t = 3.250 sec (i.e., 146 ft into the spiral curve). The force decreases in the constant radius section to a steady value of 4050 lb which is 22% less than the peak value.

Figure 5.7b shows the contact work for the leading outer wheel, the front truck, and the vehicle as a function of time. The contact work functions increase as the vehicle enters the curve and approach constant values. The maximum leading outer wheel work is 72 ft-lb/ft versus 62 ft-lb/ft for steady-state and occurs at t = 3.250 sec (i.e., 146 ft into the spiral). For the front truck and vehicle the maximum work is 144 and 243 ft-lb/ft, respectively. In contrast, the steady-state values are 121 and 242 ft-lb/ft, respectively. Dynamic effects have little influence on the contact work functions.

5.2.3 Effect of Spiral Length on Curve Entry Performance of a Conventional Vehicle

Previous studies [28] have indicated that the length of the curve entry or spiral transition track affects the transient performance of the vehicle. For instance, the length of the transition track influences the peak lateral force at the leading

outer or flanging wheel.

A study of the effect of spiral length on the peak flanging wheel lateral force of a conventional vehicle with new wheels has been conducted. In the study, the vehicle negotiates a transition spiral of varying length into a 10° curve at a balance speed of 45 ft/sec. The peak flanging force as a function of spiral length is shown in Figure 5.8. Reducing the spiral length increases the peak lateral force resulting from the initial flange contact. For short spiral lengths less than 75 ft, the peak force significantly exceeds the steady-state force. As the spiral length increases, the peak lateral force decreases rapidly and approaches the steady-state flange force. For very long spiral lengths (i.e., greater than the maximum value of 200 ft plotted in Figure 5.8) the peak and steady-state forces coincide implying that the steady-state force represents the maximum lateral force.

5.3 Curve Entry Performance of a Self-Steered Radial Vehicle

This section investigates the curve entry performance of self-steered radial vehicles. A baseline self-steered vehicle with new wheels (for which $k_{px} = 1.20 \times 10^5$ lb/ft, $k_{b2} = 1.0 \times 10^3$ ft-lb/rad, $k_{s2} = 1.0 \times 10^6$ lb/ft) was simulated through a 150 ft transition spiral curve into a 10° curve at a balance speed of 45 ft/sec. Response histories of wheelset lateral excursions and angles of attack are shown in Figures 5.9a and b, respectively. Histories of flanging wheel force and contact work are shown in Figures 5.10a

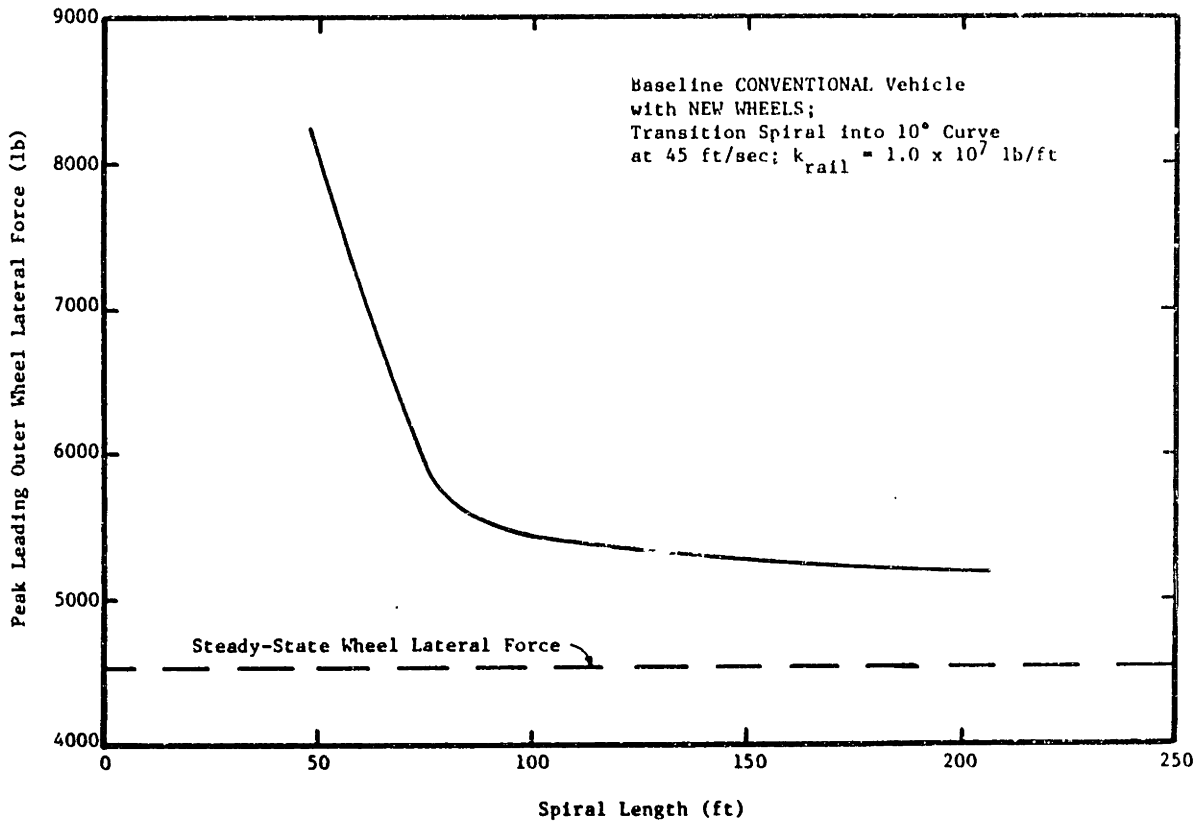

Figure 5.8: Effect of Curve Entry Spiral Length on the Peak Lateral Wheel Force of a Baseline Conventional Vehicle with New Wheels Entering a 10° Curve at a Balance Speed of 45 ft/sec.

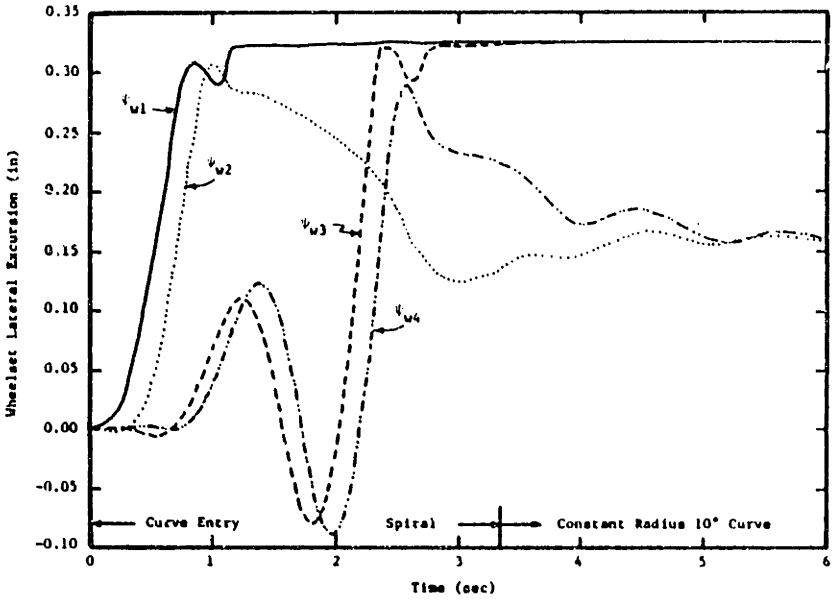

(a)

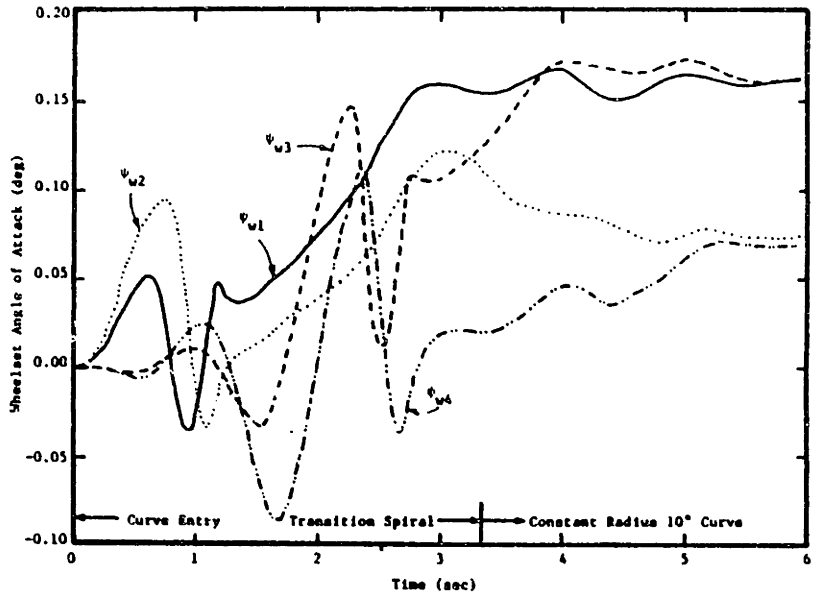

(b)

Figure 5.9: History of (a) Wheelset Lateral Excursions and (b) Angles of Attack of a Self-Steered Radial Vehicle with New Wheels Negotiating a 150 ft Curve Entry Spiral into a 10° Curve at a Balance Speed of 45 ft/sec.

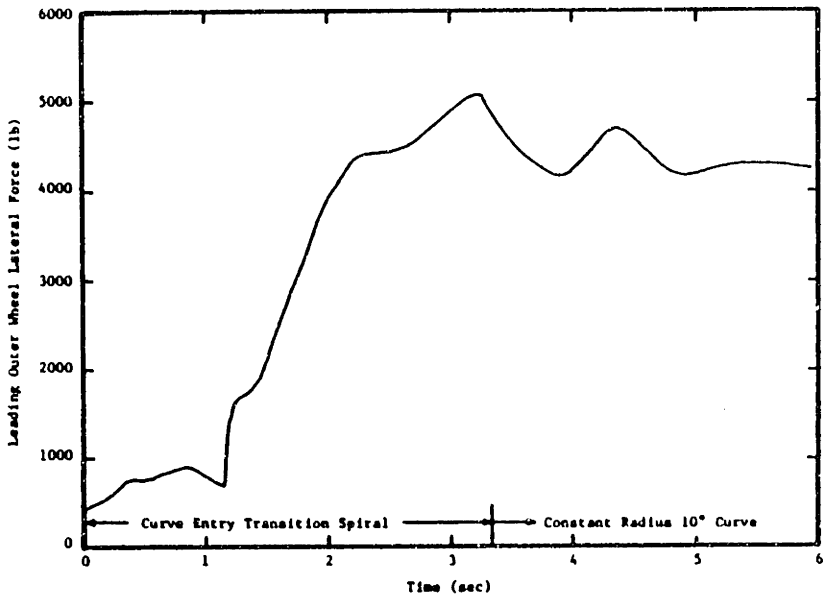

(a)

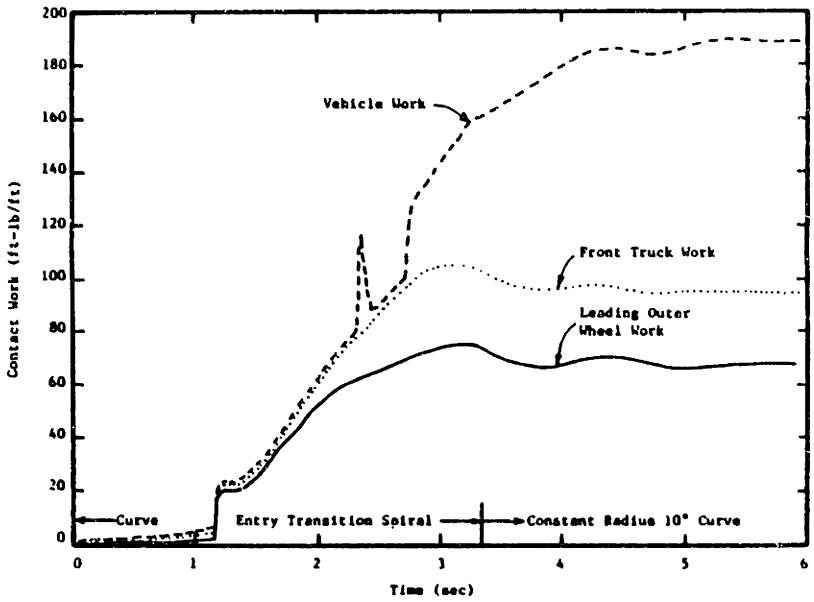

(b)

Figure 5.10: History of (a) Leading Outer (i.e., Flanging Wheel Lateral Force and (b) Contact Work of a Self-Steered Radial Vehicle with New Wheels Negotiating a 150 ft Curve Entry Spiral into a 10° Curve at a Balance Speed of 45 ft/sec.

and b, respectively.

As the front truck enters the spiral curve, the leading wheelset rapidly displaces toward the outer rail. The leading outer wheel approaches the flange, displaces inward slightly, and then hits the flange at t = 1.200 sec (i.e., 54 ft into the spiral curve). Two-point tread and flange contact occurs at the leading outer wheel and is maintained for the remainder of the simulation. The trailing wheelset of the front truck displaces laterally toward the outer rail but does not impact the flange and then displaces inward. Single-point tread occurs at both wheels of the trailing wheelset of the front truck during the simulation.

Once in the curve, the leading and trailing wheelsets of the rear truck both displace out and in and then approach the outer rail. The leading outer wheel of the rear truck hits the flange at t = 2.375 sec (i.e., 107 ft into the spiral curve) and two-point tread and flange contact occurs. It then bounces in, and single-point tread contact is restored until t = 2.750 sec (i.e., 124 ft into the spiral curve) at which time two-point contact again occurs. The leading outer wheel of the rear truck remains in two-point contact for the remainder of the simulation. The trailing wheelset of the rear truck displaces toward the outer rail and then returns slightly, always maintaining single-point tread contact at its wheels.

In steady-state, the leading wheelsets of the front and rear truck displace to 0.325 in; the trailing wheelsets of the two trucks

displace to 0.162 in. In comparison to the conventional vehicle response of Figure 5.2a, the trailing wheelsets of the front and rear self-steered trucks do not displace to the flange clearance in steady-state.

The wheelset angles of attack as a function of time are shown in Figure 5.9b. As the vehicle negotiates the spiral curve, the angles of attack of all the wheelsets oscillate, increasing and decreasing rapidly especially when two-point contact occurs. In the constant radius curve section, the oscillations dampen out and steady-state conditions are achieved. The steady-state angles of attack are: 0.162 deg for the leading wheelsets and 0.072 deg for the trailing wheelsets of the two trucks.

Figure 5.10a shows the leading outer wheel lateral force as a function of time. The force increases as the vehicle enters the spiral curve and jumps at t = 1.200 sec when the leading outer wheel impacts the flange and two-point contact occurs. The force continues to rise, peaking at 5090 lb at 3.250 sec (i.e., 146 ft into the spiral curve) and then settles to its steady-state value of 4260 lb. The peak force exceeds the steady-state force by 20%.

Figure 5.10b shows the leading outer wheel, front truck, and vehicle work as a function of time. The work increases as the vehicle negotiates the curve, increasing significantly at t = 1.200 sec when the leading outer wheel of the front truck bangs into the flange and two-point contact occurs. The vehicle work increases

significantly at t = 2.375 sec when the leading outer wheel of the rear truck impacts the flange and two-point contact occurs. The vehicle work then decreases, and increases again at t = 2.750 sec when flanging conditions are restored at the leading outer wheel of the rear truck. The work for the leading outer wheel, front truck, and vehicle continues to rise as the vehicle negotiates the curve. The leading outer wheel and front truck work reach maximum values of 75 and 106 ft-lb/ft, respectively, at t = 3.250 sec. The maximum work for the vehicle coincides with the steady-state work. Steady state conditions are achieved as the vehicle enters the constant radius curve. The steady-state work at the leading outer wheel, front truck, and vehicle is 67, 95, 190 ft-lb/ft, respectively.

5.3.1 Effect of Wheel/Rail Profile on the Curve Entry Performance Of A Self-Steered Radial Vehicle

This section discusses the influence of wheel/rail profile on the dynamic curving performance of a self-steered radial vehicle. A baseline self-steered vehicle with Heumann wheels (for which $k_{px} = 5.0 \times 10^5$ lb/ft, $k_{b2} = 1.0 \times 10^3$ ft-lb/rad, $k_{s2} = 1.0 \times 10^6$ lb/ft) was simulated through a 150 ft curve entry spiral into a 10° curve at a balance speed of 45 ft/sec. The response histories are shown in Figures 5.11 and 5.12. The wheelset lateral excursions and angles of attack as functions of time are shown in Figures 5.11a and b, respectively. The leading outer wheel lateral force and contact work as functions of time are shown in Figures 5.12a and b, respectively. For the simulation, single-point wheel/rail contact

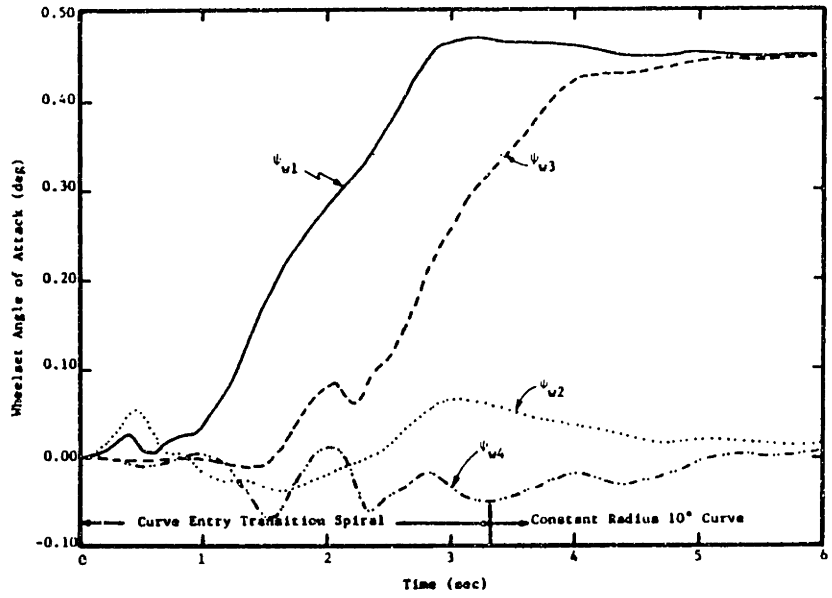

(a)

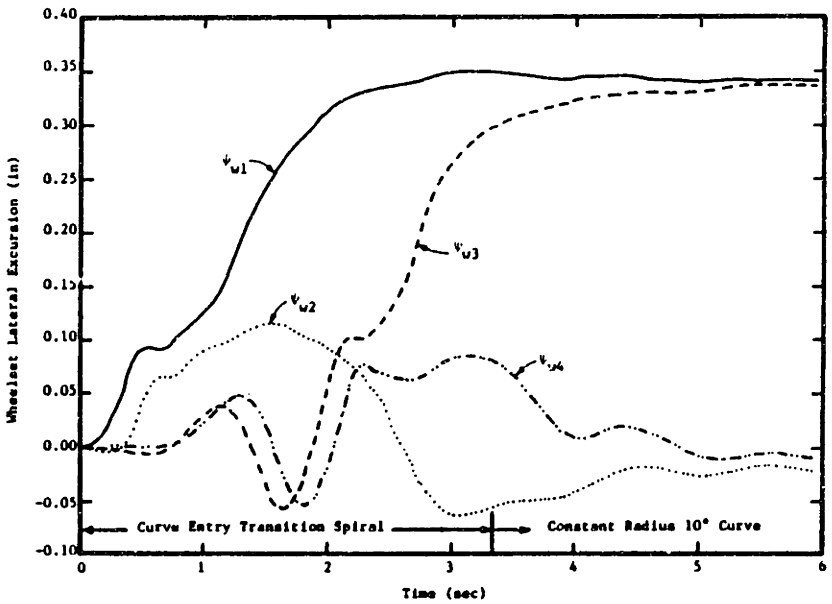

(b)

Figure 5.11: History of (a) Wheelset Lateral Excursions and (b) Angles of Attack of a Self-Steered Radial Vehicle with Heumann Wheels Negotiating a 150 ft Curve Entry Spiral into a 10° Curve at a Balance Speed of 45 ft/sec.

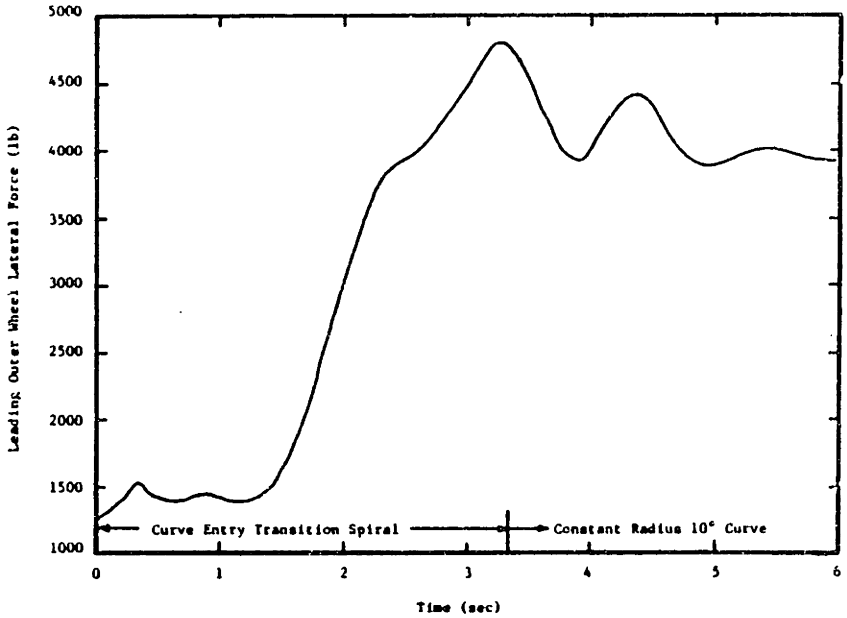

(a)

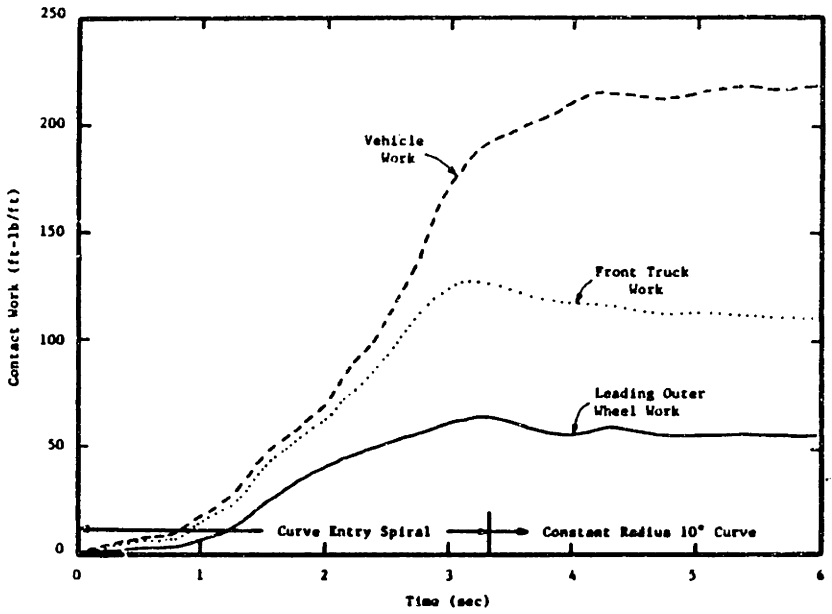

(b)

Figure 5.12: History of (a) Leading Outer (i.e., Flanging) Wheel Lateral Force and (b) Contact Work of a Self-Steered Radial Vehicle with Heumann Wheels Negotiating a 150 ft Curve Entry Spiral into a 10° Curve at a Balance Speed of 45 ft/sec.

occurs since Heumann wheels are employed. The dynamic response histories for the baseline self-steered vehicle with Heumann wheels are very similar in character to the histories for the baseline conventional vehicle with Heumann wheels shown in Figures 5.6 and 5.7.

As the vehicle negotiates the curve, the leading wheelset of the front truck displaces towards the outer rail and flange contact occurs. The leading outer wheel stays in flange contact for the remainder of the simulation. The trailing wheelset of the front truck stays near the centered position, increasing and decreasing slightly before reaching a steady value. The leading wheelset of the rear truck oscillates about the centered position and then displaces towards the outer rail. The trailing wheelset of the rear truck oscillates about the centered position and then settles to a steady value. The steady-state excursions are ~ 0.341 in for the leading wheelsets of the two trucks and ~ -0.013 in for the trailing wheelsets.

Figure 5.11b shows the wheelset angle of attack histories. The leading wheelsets of both trucks develop positive angles of attack as the vehicle negotiates the curve. The maximum deviation is 0.470 deg at t = 3.200 sec (i.e., 144 ft into the spiral curve) for the leading wheelset of the front trucks. The angles of attack of the trailing wheelsets oscillate about radially aligned positions. For the leading and trailing wheelsets

of the two trucks, the steady-state angles of attack are 0.446 deg and 0.010 deg, respectively.

The leading outer wheel lateral force, shown in Figure 5.12a, increases as the vehicle negotiates the curve. The force increases significantly as the leading outer wheel displaces laterally and flange contact occurs. The maximum lateral force is 4800 lb and occurs at t = 3.200 sec (i.e., 144 ft into the spiral curve). The force oscillates and then reaches a steady-state value of 3940 lb, which is 18% less than the peak value.

Figure 5.12b shows the contact work for the leading outer wheel, the front truck, and the vehicle as a function of time. The contact work functions increase as the vehicle enters the curve and approach constant values. The maximum leading outer wheel and front truck work is 64 and 128 ft-lb/ft, respectively, and occurs at t = 3.200 sec. The maximum vehicle work is 218 ft-lb/ft and occurs in steady-state conditions. For the leading outer wheel and front truck, the steady-state work is 56 and 109 ft-lb/ft, respectively. Dynamic effects have little influence on the contact work histories.

5.4 Curve Entry Performance of a Forced-Steered Radial Vehicle

The steady-state curving results of Chapters 3 and 4 indicate that forced-steered radial vehicles potentially offer significant performance benefits (in terms of decreased contact work) in comparison to conventional vehicle performance. This section addresses the dynamic curving performance of a forced-steered radial

vehicle. An L-type forced-steered vehicle has been selected for study for consistency with the earlier steady-state curving studies. The curvature steering gain is set to the pure rolling line gain. The study focuses on the performance of the FSR I forced-steered radial design, which has a soft primary longitudinal stiffness of $k_{px} = 7.0 \times 10^4$ lb/ft.

A baseline FSR I forced-steered vehicle with new wheels (for which $k_{b2} = 1.68 \times 10^5$ ft-lb/rad, $k_{s2} = 1.0 \times 10^6$ lb/ft) was simulated through a 150 ft transition spiral into a 10° curve at a balance speed of 45 ft/sec. Response histories of wheelset lateral excursions and angles of attack are shown in Figures 5.13a and b, respectively. Histories of flanging wheel force and contact work are shown in Figures 5.14a and b, respectively.

As the front truck enters the spiral curve, the leading wheelset rapidly displaces toward the outer rail. The leading outer wheel approaches the flange, displaces inward slightly, and then moves out impacting the flange at t = 1.200 sec (i.e., 54 ft into the spiral curve). Two-point tread and flange contact occurs at the leading outer wheel and is maintained during negotiation of the remaining spiral section and constant radius curve. The trailing wheelset of the front truck displaces laterally toward the outer rail, but the outer wheel does not impact the flange. The trailing wheelset then displaces inward. Single-point tread contact occurs at both wheels of the trailing wheelset of the front truck during the simulation.

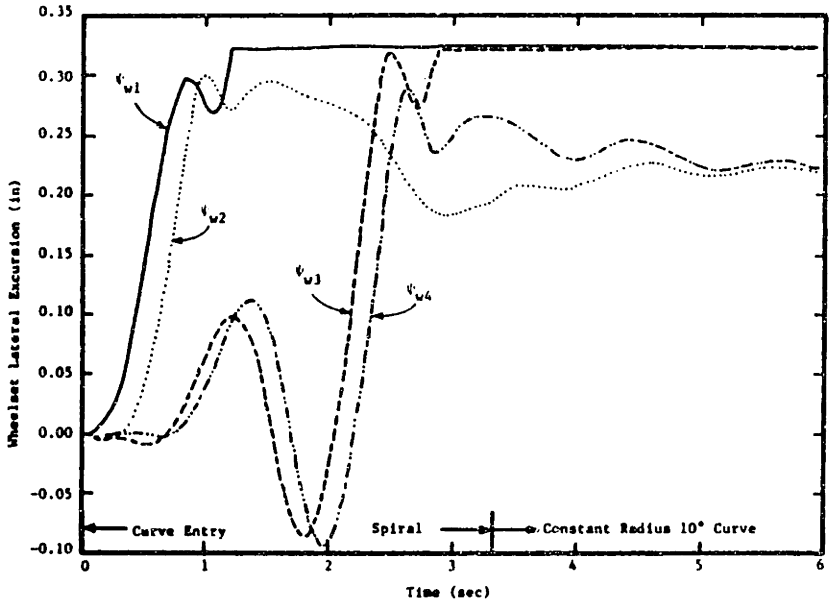

(a)

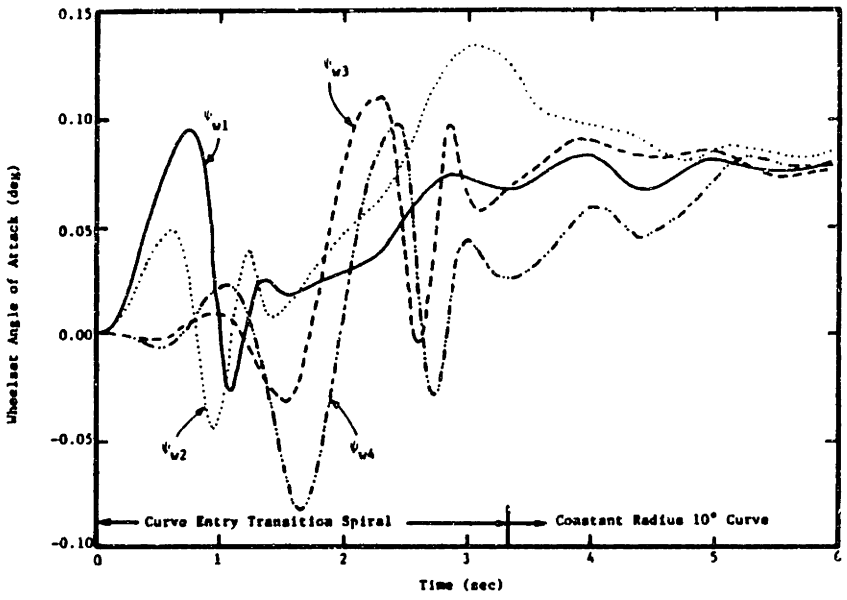

(b)

Figure 5.13: History of (a) Wheelset Lateral Excursions and (b) Angles of Attack of a FSR I Forced-Steered Radial Vehicle with New Wheels Negotiating a 150 ft Curve Entry Spiral into a 10° Curve at a Balance Speed of 45 ft/sec.

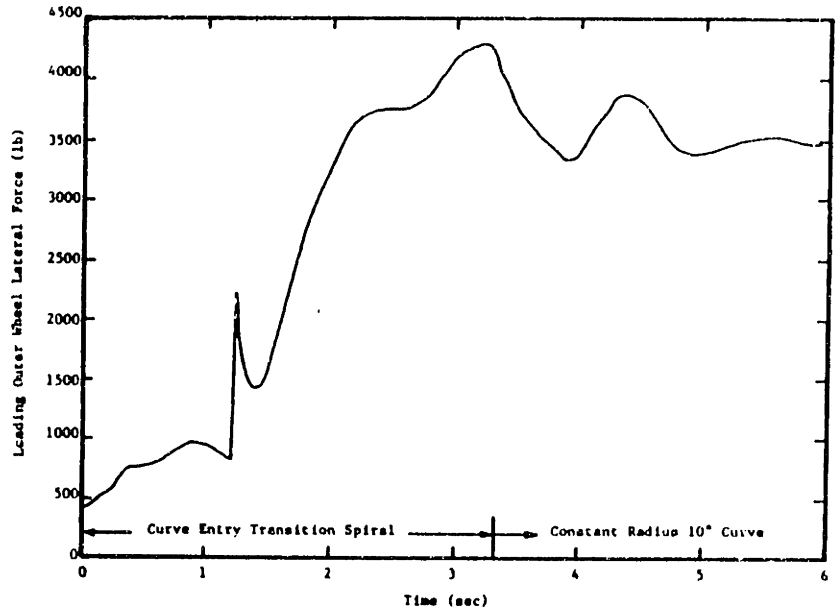

(a)

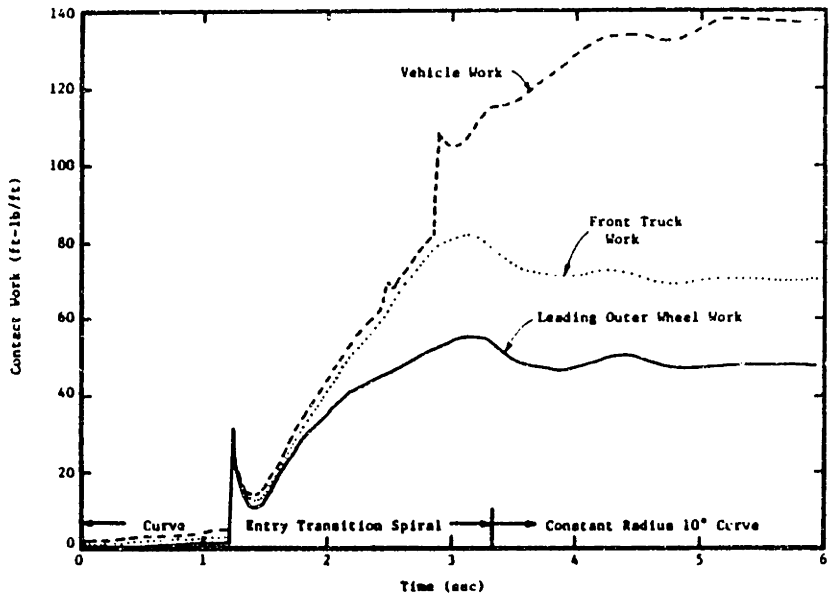

(b)

Figure 5.14: History of (a) Leading Outer (i.e., Flanging) Wheel Lateral Force and (b) Contact Work of a FSR I Forced-Steered Radial Vehicle with New Wheels Negotiating a 150 ft Curve Entry Spiral into a 10° Curve at a Balance Speed of 45 ft/sec.

As the rear truck enters the spiral curve, the leading and trailing wheelsets both displace out and in and then approach the outer rail. The leading outer wheel of the rear truck impacts the flange at t = 2.500 sec (i.e., 112 ft into the spiral) and two-point tread and flange contact occurs. The wheel rebounds back to single-point tread contact and maintains single-point contact until t = 2.875 sec (i.e., 129 ft into the spiral). The leading outer wheel of the rear truck then develops two-point tread and flange contact and maintains this condition for the remainder of the simulation. The trailing wheelset of the rear truck displaces toward the outer rail and then returns slightly. Single-point tread contact is maintained at the wheels of the trailing wheelset of the rear truck.

The steady-state lateral excursions are 0.324 in for the leading wheelsets and 0.223 in for the trailing wheelsets of the two trucks. The history of wheelset lateral excursions shown in Figure 5.13a for the FSR I forced-steered vehicle is very similar to the history of excursions shown in Figure 5.9a for the self-steered radial vehicle.

Figure 5.13b shows the wheelset angles of attack as a function of time. The angles of attack oscillate as the vehicle enters the curve. In the constant radius curve the oscillations dampen out and the angles of all wheelsets approach the same steady-state value of 0.079 deg. Ideally, the forced-steering action should position the wheelsets radially (i.e., yielding zero angles of attack). However, the pure rolling line steering gain slightly understeers the wheelsets,

as discussed in Chapter 3, and thus the wheelsets develop slightly positive angles of attack in steady-state. In comparison to the angles of attack of the self-steered vehicle (shown in Figure 5.9b), the leading and trailing wheelsets of the forced-steered vehicle adopt identical angles in steady-state.

The flanging wheel lateral force as a function of time is shown in Figure 5.14a. The force increases significantly at t = 1.200 sec (i.e., 54 ft into the spiral) when the leading outer wheel impacts the flange and two-point contact occurs. As the vehicle negotiates the curve, the force continues to increase. At t = 3.200 sec (i.e., 144 ft into the spiral curve) the maximum force of 4310 lb develops. The maximum force exceeds the steady-state force of 3480 lb by 24%.

The work expended at the leading outer wheel, the front truck, and the vehicle as a function of time is shown in Figure 5.14b. When the leading outer wheel impacts the flange at t = 1.200 sec, the work increases significantly. Following impact, the work decreases and then continues to rise. The work at the leading outer wheel and front truck reaches a maximum of 55 and 82 ft-lb/ft, respectively, at t = 3.200 sec. The vehicle work increases significantly at t = 2.875 sec when two-point contact develops at the leading outer wheel of the rear truck. The maximum vehicle work is 138 ft-lb/ft and occurs in steady-state conditions. The steady-state work at the leading outer wheel and front truck is 48 and 69 ft-lb/ft, respectively.

5.4.1 Effect of Wheel/Rail Profile on the Curve Entry Performance of a Forced-Steered Radial Vehicle

In this section, the influence of wheel/rail profile on the dynamic curving performance of a forced-steered radial vehicle is discussed. A dynamic simulation was conducted to determine the curve entry performance of a baseline FSR I forced-steered vehicle with Heumann wheels (for which $k_{b2} = 1.66 \times 10^6$ ft-lb/ft, $k_{s2} = 1.0 \times 10^6$ lb/ft) negotiating a 150 ft spiral into a 10° curve at a balance speed of 45 ft/sec. Response histories of wheelset lateral excursions and angles of attack are shown in Figures 5.15a and b, respectively. Histories of flanging wheel force and contact work are shown in Figures 5.16a and b, respectively.

As the vehicle enters the curve, the leading and trailing wheelsets of the front truck displace toward the outer rail, but maintain tread contact. The maximum lateral excursion occurs for the leading wheelset at t = 3.250 sec (i.e., 146 ft into the spiral curve) and is 0.248 in. The leading and trailing wheelsets of the rear truck increase and decrease slightly and then develop positive excursions. The steady-state excursions are ~ 0.158 in for the trailing wheelsets of the two trucks.

Figure 5.15b shows the wheelset angles of attack as a function of time. Very small angles of attack develop during the simulation. The largest magnitude is 0.073 deg, which occurs for the leading wheelset of the front truck at t = 2.875 sec (i.e., 129 ft into the spiral curve). In the curve entry spiral, the angles of attack

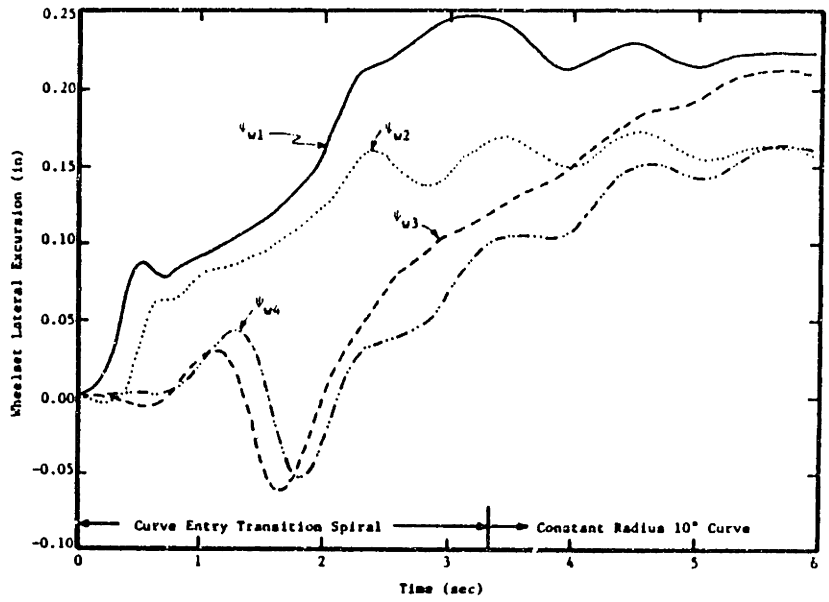

(a)

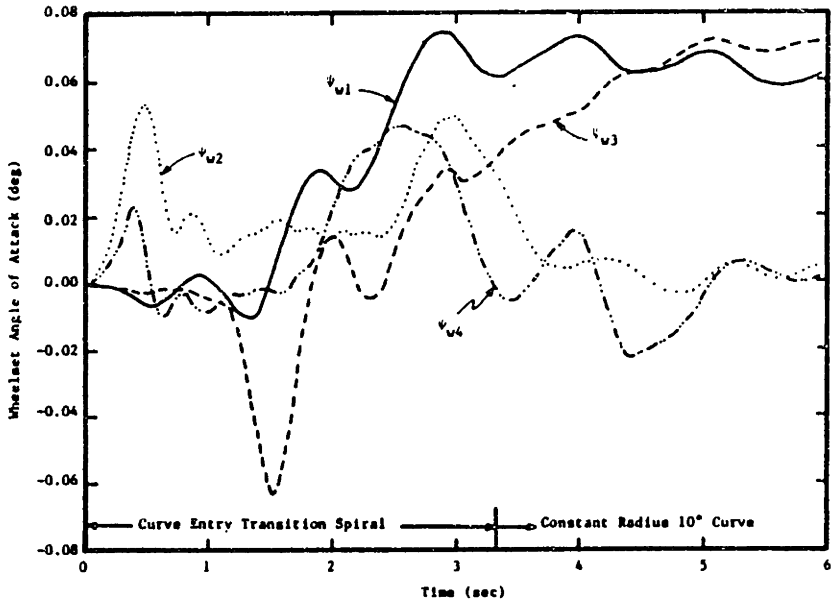

(b)

Figure 5.15: History of (a) Wheelset Lateral Excursions and (b) Angles of Attack of a FSR I Forced-Steered Radial Vehicle with Heumann Wheels Negotiating a 150 ft Curve Entry Spiral into a 10° Curve at a Balance Speed of 45 ft/sec.

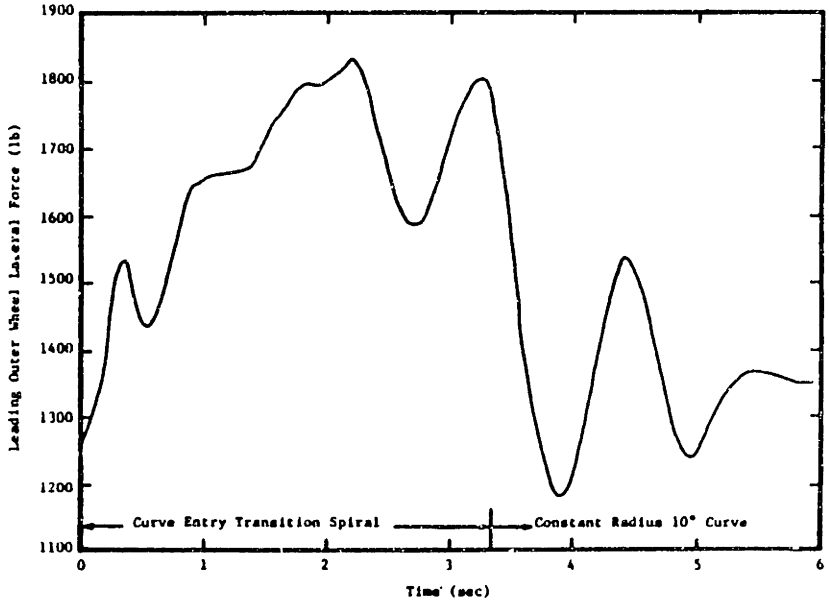

(a)

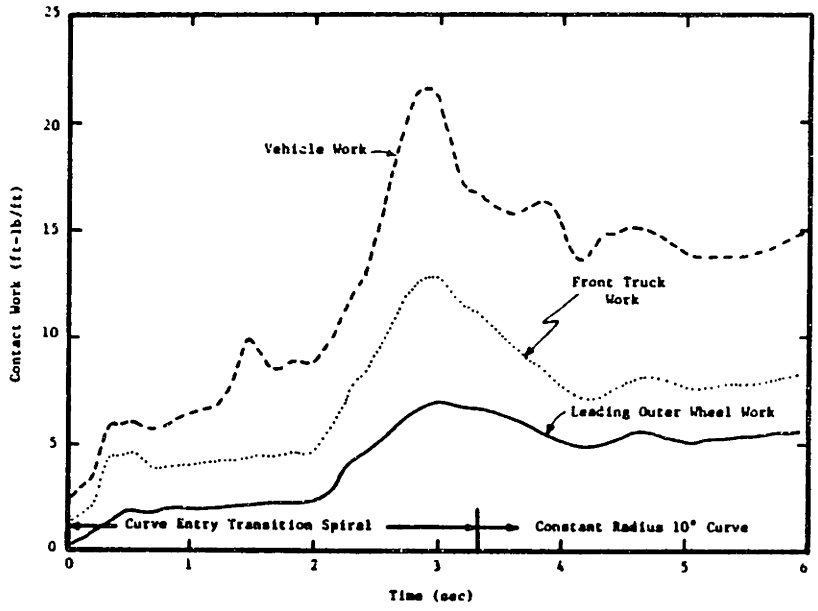

(b)

Figure 5.16: History of (a) Leading Outer (i.e., Flanging) Wheel Lateral Force and (b) Contact Work of a FSR I Forced-Steered Radial Vehicle with Heumann Wheels Negotiating a 150 ft Curve Entry Sprial into a 10° Curve at a Balance Speed of 45 ft/sec.

of all wheelsets oscillate about near radial positions. In the constant radius curve, the leading wheelsets of the front and rear trucks develop positive angles of attack; the trailing wheelsets approach perfect radial alignment. The steady-state angles are ~ 0.002 deg for the trailing wheelsets of the two trucks. The forced-steering action successfully positions the trailing wheelsets radially (since minimal flange forces act on the trailing wheelsets).

The leading outer wheel lateral force is shown in Figure 5.16a. The force is characterized by significant oscillations. The force increases to a maximum of 1820 lb at t = 2.250 sec (i.e., 101 ft into the spiral curve). As the vehicle enters the constant radius curve, the force decreases and reaches a steady-state value of 1350 lb. The peak force exceeds the steady-state force by 35%.

The work at the leading outer wheel, the front truck, and the vehicle is shown in Figure 5.16b. In comparison to the work expended by the other vehicles in previous simulations, the work for the forced-steered vehicle with Heumann wheels is very small. The maximum work is 7, 13, and 22 ft-lb/ft for the leading outer wheel, front truck, and total vehicle, respectively. The work in steady-state is 6, 7, and 14 ft-lb/ft, respectively. In this case, dynamic effects influence the contact work histories.

5.5 Comparative Curve Entry Performance of Conventional, Self-Steered, and Forced-Steered Radial Vehicles

The previous sections have examined the dynamic curve entry

performance of conventional, self-steered, and forced-steered radial vehicles with new and Heumann wheels. Baseline vehicles have been studied to ensure that the vehicles have identical linear critical speeds. This section compares the transient curving performance of the different vehicles.

The steady-state and peak values of the leading outer wheel lateral force and contact work are summarized in Tables 5.5 and 5.6 for vehicles with new and Heumann wheels, respectively. The tables show that the FSR I forced-steered vehicle offers improved performance in terms of decreased steady-state and peak forces and work in comparison to the conventional and self-steered vehicles. For example, the peak work is 55 ft-lb/ft for the forced-steered vehicle with new wheels in comparison to 93 and 75 ft-lb/ft for the conventional and self-steered vehicles, respectively. The tables also show that the peak/steady-state force and work ratios are highest for the forced-steered vehicle (in terms of percent increase), indicating that more dynamic behavior occurs for the forced-steered vehicle than for the self-steered or conventional vehicles. For example, for vehicles with new wheels, the peak work exceeds the steady-state work by 15% for the forced-steered vehicle and by 7 and 12% for the conventional and self-steered vehicles, respectively. Table 5.6 shows that the greatest improvement in performance is obtained with the forced-steered vehicle with Heumann wheels. The steady-state and peak work is 6 and 7 ft-lb/ft, respectively. However, this vehicle experiences the largest dynamic

TABLE 5.5

DYNAMIC CURVE ENTRY PERFORMANCE IN TERMS OF FLANGING WHEEL LATERAL FORCE AND CONTACT WORK FOR BASELINE VEHICLES WITH NEW WHEELS NEGOTIATING A 150 FT SPIRAL INTO A 10° CURVE AT A BALANCE SPEED OF 45 FT/SEC.

NEW WHEELS

	CONVENTIONAL			SELF-STEERED RADIAL			FORCED-STEERED RADIAL (FSR I)		
	Steady-State	Peak	% Increase	Steady-State	Peak	% Increase	Steady-State	Peak	% Increase
Flanging Wheel Lateral Force (lb)	4520	5270	17	4260	5090	20	3480	4310	24
Flanging Wheel Work (ft-lb/ft)	87	93	7	67	75	12	48	55	15

TABLE 5 6

DYNAMIC CURVE ENTRY PERFORMANCE IN TERMS OF FLANGING WHEEL LATERAL FORCE AND CONTACT WORK FOR BASELINE VEHICLES WITH HEUMANN WHEELS NEGOTIATING A 150 FT SPIRAL INTO A 10° CURVE AT A BALANCE SPEED OF 45 FT/SEC.

HEUMANN WHEELS

	CONVENTIONAL			SELF-STEERED RADIAL			FORCED-STEERED RADIAL (FSR I)		
	Steady-State	Peak	% Increase	Steady-State	Peak	% Increase	Steady-State	Peak	% Increase
Flanging Wheel Lateral Force (lb)	4050	4950	22	3940	4800	22	1350	1820	35
Flanging Wheel Work (ft-lb/ft)	62	72	16	56	64	14	6	7	17

overshoot in terms of percent. For instance, the peak work exceeds the steady-state work by 17%. The peak lateral force exceeds the steady-state force by 35%.

In summary, Tables 5.5 and 5.6 compare the important results of the dynamic curving study. The results suggest that significant performance improvements can be achieved by using forced-steered vehicles with Heumann wheels. Forced-steered vehicles experience more dynamic behavior in curve entry than conventional and self-steered vehicles. However, the magnitudes of the transient characteristics of the forced-steered vehicles are smaller than those which develop for conventional and self-steered vehicles indicating that the increased dynamic behavior is not critical.

This chapter has been intended to explore in a preliminary way the dynamic curving performance of conventional, self-steered, and forced-steered radial vehicles with new and Heumann wheels. The dynamic curving analysis used for the study incorporates a simple model of the secondary yaw suspension system. The model assumes that a coulomb damper element which saturates at the breakaway torque and has a linear viscous band acts between each truck and carbody. In steady-state conditions, the truck and carbody yaw rates vanish and thus no secondary yaw torques develop. The steady-state curving analysis assumes that breakaway has occurred at each truck centerpin, and thus includes constant secondary yaw breakaway torques. Due to the different models, the dynamic and

steady-state curving analyses do not predict the same steady-state behavior. The performance predicted by the steady-state analysis, such as wheel/rail force and work, is more conservative than that predicted by the dynamic curving analysis in steady-state.

6.0 CONCLUSIONS

6.1 Introduction

The ability to negotiate curves is critically important for rail passenger vehicles, especially in urban transit systems where sharp curves are often encountered. During curve negotiation, the wheelsets of conventional vehicles generally develop radial misalignments with the track which result in large wheel/rail contact forces. Several performance problems have been associated with the increased wheelset angles and wheel/rail forces, including increased wheel and rail wear, fuel consumption, and propensity for derailment. To minimize these performance problems, changes in vehicle suspension design and wheel profile have been proposed.

This thesis has investigated the steady-state and dynamic curving performance of rail passenger vehicles. In particular, studies have addressed the influence of suspension design and wheel/rail profile geometry on vehicle curving performance. The research philosophy has been to develop two main types of analytical approaches to investigate curving performance. The first of these is a nonlinear steady-state curving analysis that considers the steady-state performance of a single-truck/half-carbody model on smooth, constant radius curved track. This analysis is computationally efficient and is used for extensive parametric studies. The second analytical approach has been to develop a nonlinear, dynamic curving analysis to describe the dynamic response of a full vehicle model during curve entry and negotiation. This more comprehensive approach has been used to conduct simulations

of rail vehicle curve entry to study transient performance.

6.2 Implications of Steady-State and Dynamic Curving Results

The steady-state curving analysis, used to conduct the studies of Chapters 3 and 4, is an excellent tool for parametric investigations since it rapidly provides predictions of steady-state behavior. The predictions have corresponded to physically realizable and stable solutions, as determined by comparison with the results of the more comprehensive dynamic curving analysis. For the dynamic curving studies discussed in Chapter 5, transient effects are not significant and, thus, the steady-state curving analysis represents a satisfactory design tool. However, an exhaustive parametric study has not been conducted with the dynamic curving analysis to conclude that transient phenomenon during curving can be neglected for vehicle design.

The following paragraphs highlight guidelines for vehicle design based upon the results of this research.

Suspension Design

Suspension design plays a dominant role in determining the curving performance and stability of rail vehicles. For conventional vehicles, relatively stiff suspension components provide stable performance but restrict the ability of the wheelsets to align radially in curves. Soft suspension components allow improved wheelset alignment in curves but result in reduced vehicle stability.

Some improvement in the curving performance versus stability

tradeoff of conventional vehicles is achieved by using self-steered radial vehicles. Self-steered vehicles employ direct wheelset interconnections which allow for increased shear stiffness and reduced bending stiffness between the wheelsets for a given critical speed design, and therefore the curving performance is improved in comparison to conventional vehicle performance. The increased shear stiffness of self-steered vehicles provides improved alignment and reduced contact work at the leading wheelset as a result of steering forces generated by the trailing wheelset.

For tight curves, most often encountered in urban transit applications, a more significant improvement over conventional and self-steered vehicle performance can be achieved by forced-steering the wheelsets. Forced-steered vehicles utilize linkages between the carbody and truck to force the wheelsets into near radial alignment when traversing curves. For forced-steered vehicles, contact patch work can be substantially reduced without sacrificing tangent track critical speed.

Wheel/Rail Profile

The wheel/rail profile geometry is critically important in determining the curving performance and stability of rail vehicles. The forces and moments acting on the wheelsets are markedly different if two-point contact rather than single-point contact occurs at the flanging wheels. In general, a wheelset with single-point contact wheel profiles, such as Heumann wheels, develops a larger restoring moment (at the same lateral force) than a wheelset with two-point con-

tact wheel profiles, such as new AAR 1 in 20 wheels. As a result, the Heumann wheel profile is advantageous for curve negotiations. Heumann wheel profiles maintain single-point contact at all excursions and reduce the work expended during curving negotiation in comparison to two-point contact profiles.

Implications

The results of this research indicate that conventional vehicle designs with standard AAR new wheels may be sufficient for service in systems with few small radius curves, such as mainline systems. On the other hand, the results indicate the value of using more sophisticated configurations, such as forced-steered vehicles with Heumann wheels, for service in systems with many sharp curves, such as urban transit systems. The potential performance improvements of forced-steered vehicles with Heumann wheels imply significant savings in wheel and rail wear and lower operating costs. However, economic studies must be conducted to assess whether the performance improvements justify the additional costs of implementing the maintaining the steering linkages and of converting to alternate wheel profiles.

6.3 Recommendations for Future Work

The research described in this thesis forms part of a continuing program in the Vehicle Dynamics Laboratory at M.I.T. which aims to understand and predict the dynamic response of rail vehicles. This section focuses on extensions to the dynamic curving analysis which are recommended as future tasks.

- Reducing computation time for the dynamic analysis is an important goal which should be addressed. Program DYCURV, the computer coding of the dynamic curving analysis, should be optimized for computational efficiency. Alternative integration schemes, such as simple Euler and predictor-corrector algorithms, should be tried in an effort to increase computing speed. Law and Cooperrider [16] have reported that in general these schemes require smaller time steps for similar accuracy which can offset the savings in computations per step.

- Future work should address the vehicle response to track irregularities during curve negotiation. The dynamic curving analysis should be extended to account for these additional track inputs. As a first step, the response to cross-level and alignment irregularities intended to represent bolted rail should be analyzed.

- The dynamic curving analysis should be exercised to investigate the influence of wheel/rail and suspension nonlinearities on vehicle stability. In particular, the analysis should be used to study the onset of limit cycle behavior during curving. Currently, studies are being conducted to evaluate limit cycle phenomenon for a single wheelset negotiating curved track [54].

- Continued work is required to determine the influence of rail rollover on vehicle curving performance. Due to lateral wheel loads, the rails develop cant angles. Overturning motion of the rails influences the wheel/rail contact condition. The curving analysis should incorporate a means to modify the wheel/rail geometry data to account for rail rollover.

- For computational ease, the curving analysis neglects (1) the effective lateral mass of the rails, and (2) the influence of lateral rail velocity on the lateral creepages. The lateral mass of the rails is neglected since it is assumed that the lateral rail inertial forces are small in comparison to the stiffness and damping forces. The influence of lateral rail velocity on creepage is assumed to be small, since in many curving situations flanging occurs and the wheel/rail contact forces are saturated. However, these two assumptions should be evaluated more completely. The influence of rail mass and rail velocity may be critical in situations involving violent dynamic behavior, such as hunting during which the wheelsets hit the flanges and slam back and forth between the rails.

- The inclusion of longitudinal and vertical dynamics would make the dynamic curving analysis a more complete computational tool. Further, it would allow the influence of vehicle acceleration and deceleration to be evaluated as a means to recover from dynamic instability.

- Work is required to experimentally validate the steady-state and dynamic curving analyses and the curving performance indices. Experimental investigations of the curving and stability properties of vehicles with steered trucks and alternate wheel profiles should be conducted. The influence of wet or lubricated rails on vehicle curving performance and stability should also be studied. Existing data obtained from experiments at the Transportation Test Center [55] and at WMATA [28] should be compared with the predictions of the curving analy-

ses. Successful validation of linear models of rail vehicle dynamics on tangent track has been completed by members of the Vehicle Dynamics Laboratory [56].

- Establishing the validity of a wear index is a major priority. Limited experimental studies have been conducted by British Rail [33] and I.I.T. [34]. More comprehensive investigations of wear are required to better understand the causes and predict the development of wheel/rail wear.

REFERENCES

1. Boyd, P. L., Zaiko, J. P., and Jordan, W. L., "Effect of Wheel Taper and Primary Suspension Stiffness on Wheel/Rail Forces at the Washington Metropolitan Area Transit Authority," Vol. II Test Report, U.S.D.O.T. Interim Report, March, 1980.

2. Mekosh, G., "Design Feasibility Study for Modifying an Existing Heavy Rapid Rail Truck to a Steerable Configuration," Budd Company Project Memorandum, Report No. DOT-TSC-UM104-PM-80-49, December, 1980.

3. Cooperrider, N. K., and Wirth, J. L., "Wheel Tread Profile as a Rail Vehicle Design Parameter," A.S.M.E. Technical Report 82-WA/DSC-3, 1982.

4. Marcotte, P. P., Mathewson, K. J., and Caldwell, W. N., "Improved Wheel Tread Profiles for Heavy Freight Vehicles," J. of Engineering for Industry, Vol. 102, August, 1980, pp. 263-271.

5. Heumann, H., "Zur Frage des Radfeinumrisses," Organ 1934.

6. Eksergian, R., "Static Adjustments of Trucks on Curves," A.S.M.E. Transactions, Vol. 42, No. 1776, 1921.

7. Porter, S.R.M., "The Mechanics of a Locomotive on Curved Track," The Railway Gazette, 1935.

8. Vermeulen, P. J., and Johnson, K. L., "Contact of Nonspherical Elastic Bodies Transmitting Tangential Forces," J. of Applied Mechanics, Vol. 86, June, 1964, pp. 338-340.

9. Kalker, J. J., "On the Rolling Contact of Two Elastic Bodies in the Presence of Dry Friction," Ph.D. Thesis, Technische Hogeshoul, Delft, Netherlands, 1967.

10. Newland, D. E., "Steering a Flexible Railway Truck on Curved Track," J. of Engineering for Industry, A.S.M.E. Transactions, Series B, Vol. 91, No. 3, August, 1969, pp. 908-918.

11. Boocock, D., "Steady-State Motion of Railway Vehicles on Curved Tracks," J. of Mechanical Engineering Science, Vol. 11, No. 6, December, 1969, pp. 556-566.

12. Bell, C. E., Horak, D., and Hedrick, J. K., "Stability and Curving Mechanics of Rail Vehicles," J. of Dynamic Systems, Measurement, and Control, Vol. 103, September, 1981, pp. 181-190.

13. Horak, D., Bell, C. E., and Hedrick, J. K., "A Comparison of the Stability and Curving Performance of Radial and Conventional Rail Vehicle Trucks," J. of Dynamic Systems, Measurement and Control, Vol. 103, September, 1981, pp. 191-200.

14. Bell, C. E., and Hedrick, J. K., "Forced Steering of Rail Vehicles: Stability and Curving Mechanics," Vehicle System Dynamics, Vol. 10, pp. 357-386, 1981.

15. Elkins, J. A., and Gostling, R. J., "A General Quasi-Static Curving Theory for Railway Vehicles," Proc. 5th VSD-2nd IUTAM Symposium on the Dynamics of Vehicles on Roads and Tracks, 1978.

16. Law, E. H., and Cooperrider, N. K., "Nonlinear Dynamic and Steady-State Curving of Rail Vehicles," presented at the 1980 A.S.M.E. Winter Annual Meeting, San Francisco, CA, December, 1978.

17. Hedrick, J. K., Wormley, D. N., Arslan, A. V., and Chin, R., "Nonlinear Analysis and Design Tools for Rail Vehicles: Nonlinear Locomotive Dynamics," A.A.R. Report R-463, December, 1980.

18. Bell, C. E., "Curving Mechanics of Rail Vehicles," Ph.D. Thesis, Department of Mechanical Engineering, M.I.T., September, 1981.

19. Marcotte, P., Caldwell, W. N., and List, H. H., "Performance Analysis and Testing Conventional Three Piece Freight Car Truck Retrofitted to Provide Axle Steering," presented at the 1978 A.S.M.E. Winter Annual Meeting, San Francisco, CA, 1978.

20. Elkins, J. A., and Weinstock, H., "The Effects of Two-Point Contact on the Curving Behavior of Railroad Vehicles," presented at the 1982 A.S.M.E. Winter Annual Meeting, Phoenix, Arizona, November, 1982.

21. Mueller, C. Th., "Dynamics of Railway Vehicles on Curved Track," Interaction Between Vehicle and Track, The Institution of Mechanical Engineering Proceedings, Vol. 180, Part 3F, 1965 - 1966, pp. 45-57.

22. Smith, K., "Curve Entry and Curve Negotiation Characteristics of Two-Axle Trucks," M.S. Thesis, Illinois Institute of Technology, December, 1975.

23. Cooperrider, N. K., and Law, E. H., "The Nonlinear Dynamics of Rail Vehicles in Curve Entry and Negotiation," presented at the 7th IAVSD-IUTAM Symposium on the Dynamics of Vehicles on Roads and Tracks, Cambridge, U.K., September 7-11, 1981.

24. Clark, R. A., Eickhoff, B. M., and Hunt, G. A., "Prediction of the Dynamic Response of Vehicles to Lateral Track Irregularities," presented at the 7th IAVSD-IUTAM Symposium on the Dynamics of Vehicles on Roads and Tracks, Cambridge, U.K., September 7-11, 1981.

25. Duffek, W., and Jaschinski, A., "Efficient Implementation of Wheel-Rail Contact Mechanics in Dynamic Curving," presented at the 7th IAVSD-IUTAM Symposium on The Dynamics of Vehicles on Roads and Tracks, Cambridge, U.K., September 7-11, 1981.

26. Krolewski, S. M., "Model Development for Freight Car Dynamic Curving Simulation," S.M. Thesis, Department of Mechanical Engineering, M.I.T., June, 1982.

27. Elkins, J. A., "Analytic Studies of Curving Forces and Hunting Stability and Related Support for WMATA Phase II Truck Test Project," Interim Report, U.S.D.O.T.: UMTA, June, 1982.

28. DiMasi, F., "Outline of Principal Findings From WMATA Truck Tests," U.S.D.O.T. Memorandum to C.O. Phillips, November 23, 1981.

29. Bolton, P. J., Clayton, P., and McEwen, I. J., "Wear of Rail and Tyre Steels Under Rolling/Sliding Conditions," British Rail Research, presented at the ASME/ASNE Conference, August, 1980.

30. Gilchrist, A. O., and Brickle, B. V., "A Re-Examination of the Proneness to Derailment of a Railway Wheelset," J. of Mechanical Engineering Science, Vol. 18, No. 3, 1976, pp. 131 - 141.

31. Cherchas, D. B., "Determination of Railway Wheel Climb Probability Based on the Derailment Coefficient," J. of the Franklin Institute, Vol. 312, No. 1, July, 1981, pp. 31-40.

32. Doyle, G. R., "Conventional Versus Self-Steering Radial Truck for High-Speed Passenger Trains," ASME Report 79-RT-3, ASME/IEEE Joint Railroad Conference, 1979.

33. Bolton, P., "Wear of BS11 Rail Steels in Rolling/Sliding Contact with Class "D" Type Steel," British Railways Technical Note TNMET21, February, 1980.

34. Kumar, S., Prasanna Rao, D. L., and Rajkuma, B. R., "A Wheel-Rail Wear Study for Railroad Transit Systems," I.I.T. Report IIT-TRANS-80-1, August, 1980.

35. Kumar, S., Prasanna Rao, D. L., and Rajkuma, B. B., "Angle of Attack and Wheel-Rail Wear," F.R.A. Technical Report, DOT-FR-744-4301, December, 1981.

36. Elkins, J. A., and Allen, R. A., "Testing a Transit Vehicle for Wheel and Rail Wear," A.S.M.E. Transactions, Paper 81-WA/DSC-19, 1981.

37. Gogos, G., "Tilt Body Control of Rail Vehicles," S.B. Thesis, Department of Mechanical Engineering, M.I.T., June, 1980.

38. Ahlbeck, D. R., "The Effects of Track Modulus on Vehicle-Track Dynamic Interaction," IEEE/ASME Joint Railroad Conference, Erie, PA, April, 1982.

39. Cooperrider, N. K., and Law, E. H., "Data Book: Wheel/Rail Geometry for Five Wheel Profiles and Three Rail Profiles," Report No. ERC-R-75015, Department of Mechanical Engineering, Arizona State University, Tempe, Arizona 85281.

40. Kalker, J. J., "Survey of Wheel-Rail Rolling Contact Theory," Vehicle System Dynamics, Vol. 5, 1979, pp. 317 - 358.

41. List, H. A., Caldwell, W. N., and Marcotte, P., "Proposed Solutions to the Freight Car Truck Problems of Flange Wear and Truck Hunting," ASME Paper No. 75-WA-RT-8, 1976.

42. Scheffel, H., "The Hunting Stability and Curving Ability of Railway Vehicles," Rail International, No. 2, February, 1974, pp. 154-177.

43. Wickens, A. H., "Steering and Dynamic Stability of Railway Vehicles," Vehicle System Dynamics, Vol. 5, 1975/1976, pp. 15-46.

44. Scales, B. T., "Behavior of Bogies on Curves," Railway Engineering Journal, July, 1972, pp. 19-24.

45. Smith, R. E., "Steering Conversion of CTA 2400 Rapid Transit Truck, Volume I: Design Feasibility Study," Project Memorandum, U.S.D.O.T. Report No. DOT-TSC-UM104-PM-80-48, December, 1980.

46. Wormley, D. N., Hedrick, J. K., and Nagurka, M. L., "Stability and Curving Performance of Conventional and Advanced Rail Transit Vehicles," U.S.D.O.T. Interim Report, DTRS 57-80C-00152, November, 1982.

47. List, H. A., "Means for Improving the Steering Behavior of Railway Vehicles," Presented to the Annual Meeting of the Transportation Research Board, January 22, 1976.

48. Mekosh, G., "Technical Analysis for Modifying an Existing Heavy Rapid Rail Truck to a Steerable Configuration," Report for Contract No. DOT-TSC-1740, May, 1980.

49. Rabinowitz, P., Numerical Methods for Nonlinear Algebraic Equations Gordon and Breach Science Publishers, London, 1970.

50. Cooperrider, N. K., and Law, E. H., Rail Vehicle Dynamics, January, 1980.

51. Elkins, J. A., and Eickhoff, B. M., "Advances in Non-Linear Wheel/Rail Force Prediction Methods and Their Validation," Journal of Dynamic Systems, Measurement and Control, Vol. 104, No. 2, June, 1982, pp. 133-142.

52. Garg, D., and Weinstock, H., "Piecewise Linear Approximation of Lateral Forces in Rail-Wheel Contact," Transportation Systems Center, U.S.D.O.T., Report No. WP-743-C-10-100, August, 1980.

53. Shen, Z. Y., Hedrick, J. K., and Elkins, J. A., "A Comparison of Alternative Creep Force Models for Rail Vehicle Dynamic Analyses," to be presented at the 8th IAVSD Symposium, M.I.T., Cambridge, MA, August, 1983.

54. Aderbigbe, A., "Multiple Input Describing Function Analysis of the Lateral Motion of Rail Vehicle Systems," Ph.D. Thesis, Department of Mechanical Engineering, M.I.T., 1983.

55. Tuten, J. M., and Ahlbeck, D. R., "Characterization and Analysis of the Wheel/Rail Load Environment at the Facility for Accelerated Service Testing (FAST)," A.S.M.E. Technical Paper 81-WA/RT-13, 1981.

56. Horak, D., "Passenger Rail Vehicle Dynamics," Ph.D. Thesis, Department of Mechanical Engineering, M.I.T., 1981.

57. Sweet, L. M., and Sirak, J. A., "Nonlinear Wheelset Forces in Flange Contact, Part 1: Steady-State Analysis and Numerical Results," J. of Dynamic Systems, Measurement and Control, Vol. 101, No. 3, September, 1979, pp. 238-246.

APPENDIX A: DYNAMIC CURVING EQUATIONS OF MOTION OF A WHEELSET

A.1 Introduction

The basic element of the rail vehicle steering and support system is the wheelset. The contact and friction mechanisms which develop at the wheel/rail interfaces have a dominant effect on vehicle curving behavior. The curving performance of a vehicle is a direct function of the ability of its wheelsets to negotiate a curve.

The majority of previous steady-state and dynamic curving studies have assumed that each wheel of the vehicle contacts the rails at a single point. This is an acceptable approximation of tread contact, but for some wheel/rail profiles this represents a simplistic view of flange contact. For profiles with steep flanges including many U.S. profiles, two points of contact can occur simultaneously at the flanging wheel.

In this Appendix, an analytic model is developed to predict the dynamic curving performance of a rail vehicle wheelset. The model represents single-point and two-point wheel/rail contact at the flanging wheel and accounts for nonlinearities due to wheel/rail profile geometry and friction (creep) force saturation. The derivation assumes that (1) the wheelset maintains continuous wheel/rail contact as it traverses smooth, laterally flexible, right-handed curved track, and (2) the forward speed of the wheelset as well as the track curvature and superelevation (or bank) angle are known functions of the distance along the track. Wheelset and rail equations are derived by application of

Newtonian mechanics, resulting in force and moment dynamic equilibrium equations. By appropriate manipulation, a set of coupled scalar differential equations are generated which characterize the dynamic curving behavior of a wheelset in single-point or two-point contact at the flanging wheel. The governing equations represent a system of 5 states for the wheelset and 2 states for the rails. The wheelset has 2 states (i.e., 1 degree of freedom) to describe its lateral and yaw motions as well as a state to represent its spin speed. Each rail has a state to describe its lateral motion. When two-point contact occurs, the state of the rail at the flanging wheel is known due to a constraint relation which exists between the wheelset and rail lateral motions. Finally, an appropriate numerical solution procedure involving digital integration of the equations of motion is described.

A.2 Coordinate Systems

Six coordinate systems are established, each consisting of mutually-perpendicular right-handed axes x,y,z with corresponding unit vectors $\hat{i},\hat{j},\hat{k}$. The x,y, and z axes denote the longitudinal, lateral, and vertical directions, respectively, of each system. The coordinate systems are:

I	Inertial	Track-Related
H	Horizontal	
T	Track	

1	Yaws with wheelset	Wheelset-Related
2	Yaws and rolls with wheelset	
3	Wheelset (i.e., yaws, rolls, and pitches with wheelset)	

The first three systems are used to define the orientation of the track (which has variable geometry). The latter three systems are used to define the orientation of the wheelset.

Figure A.1 shows the inertial ("I"), horizontal ("H"), track ("T"), and wheelset ("W") coordinate systems. The inertial system, "I", is fixed in inertial space. The track system, "T", with origin O_T moves along the track centerline with tangential speed V and is superelevated relative to the horizontal system, "H". The x_T and y_T axes lie in the track plane (x_T points in the longitudinal direction and y_T points radially outward); the z_T axis is oriented normal to the track plane and points up. The "W" coordinate system has axes aligned with the principal directions of the wheelset (i.e., fixed in the directions of the three principal mass moments of inertia), with its origin at the wheelset's center of mass, W^*.

Relative to the inertial system, the track system is rotated due to curvature and superelevation angle. The orientation of the wheelset is specified relative to the track system by a yaw, roll, and pitch angle. Wheelset axes initially aligned with track axes are rotated successively through the following sequence: (1) yaw (ψ_w) about the z_T axis, (2) roll (ϕ_w) about the rotated x_T axis, and (3) pitch (θ_w) about the rotated y_T axis. Figure A.2 defines the different coordinate system rotations and

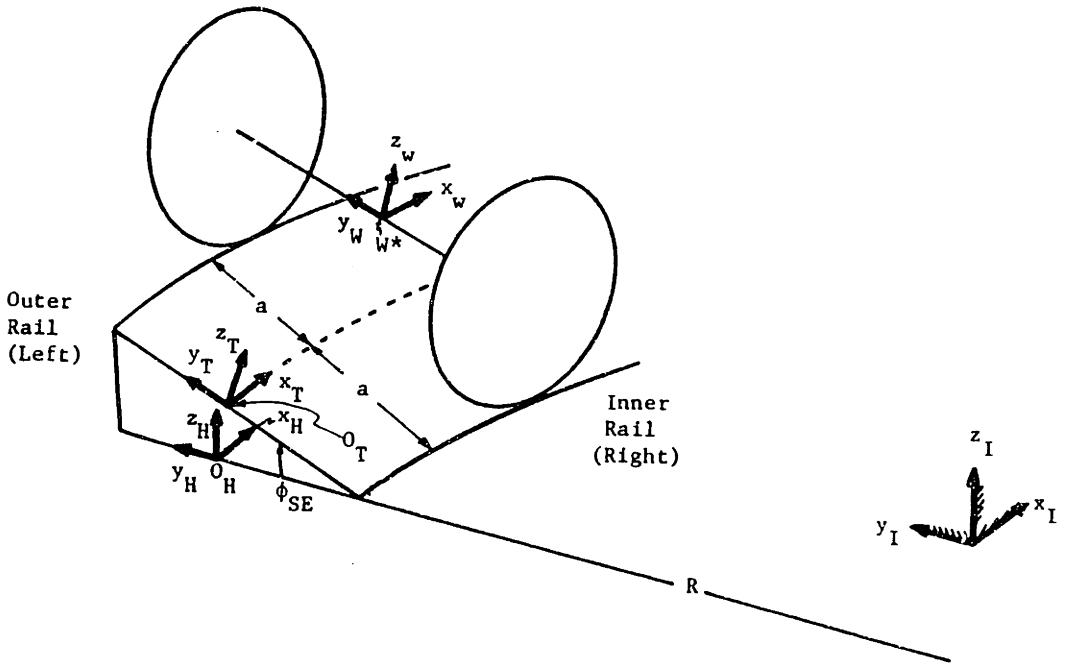

Figure A.1 Wheelset and Track Coordinate Systems

"I" → "H"

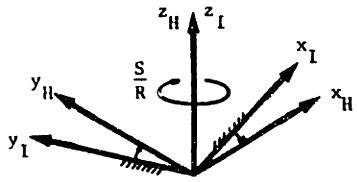

Rotation due to Curvature

$$\overset{I}{\omega}^{H} = -\frac{V}{R}\hat{k}_H$$

"H" → "T"

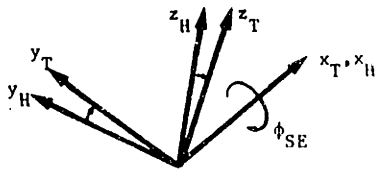

Superelevation, ϕ_{SE}

$$\overset{H}{\omega}^{T} = \dot{\phi}_{SE}\hat{i}_T$$

$$\begin{Bmatrix}\hat{i}_T\\ \hat{j}_T\\ \hat{k}_T\end{Bmatrix} = \underbrace{\begin{bmatrix}1 & 0 & 0\\ 0 & c\phi_{SE} & s\phi_{SE}\\ 0 & -s\phi_{SE} & c\phi_{SE}\end{bmatrix}}_{C_{T/H}}\begin{Bmatrix}\hat{i}_H\\ \hat{j}_H\\ \hat{k}_H\end{Bmatrix}$$

"T" → "1"

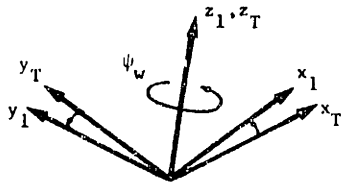

Yaw Angle, ψ_w

$$\overset{T}{\omega}^{1} = \dot{\psi}_w\hat{k}_1$$

$$\begin{Bmatrix}\hat{i}_1\\ \hat{j}_1\\ k_1\end{Bmatrix} = \underbrace{\begin{bmatrix}c\psi_w & s\psi_w & 0\\ -s\psi_w & c\psi_w & 0\\ 0 & 0 & 1\end{bmatrix}}_{C_{1/T}}\begin{Bmatrix}\hat{i}_T\\ \hat{j}_T\\ \hat{k}_T\end{Bmatrix}$$

"I" Inertial

"H" Horizontal

"T" Track

"1" Yaws with Wheelset

"1" → "2"

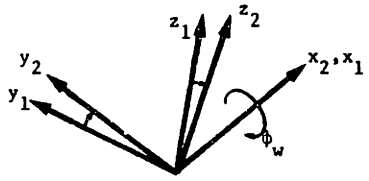

Roll Angle, ϕ_w

$$\overset{1}{\omega}^{2} = \dot{\phi}_w\hat{i}_2$$

$$\begin{Bmatrix}\hat{i}_2\\ \hat{j}_2\\ \hat{k}_2\end{Bmatrix} = \underbrace{\begin{bmatrix}1 & 0 & 0\\ 0 & c\phi_w & s\phi_w\\ 0 & -s\phi_w & c\phi_w\end{bmatrix}}_{C_{2/1}}\begin{Bmatrix}\hat{i}_1\\ \hat{j}_1\\ \hat{k}_1\end{Bmatrix}$$

"2" → "W"

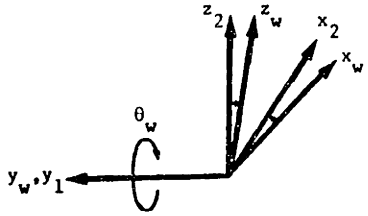

Pitch Angle, θ_w

$$\overset{I}{\omega}^{W} = \dot{\theta}_w\hat{j}_w$$

$$\begin{Bmatrix}\hat{i}_w\\ \hat{j}_w\\ \hat{k}_w\end{Bmatrix} = \underbrace{\begin{bmatrix}c\theta_w & 0 & -s\theta_w\\ 0 & 1 & 0\\ s\theta_w & 0 & c\theta_w\end{bmatrix}}_{C_{w/2}}\begin{Bmatrix}\hat{i}_2\\ \hat{j}_2\\ \hat{k}_2\end{Bmatrix}$$

"2" Yaws and Rolls with Wheelset

"W" Wheelset (i.e., yaws, rolls, and pitches with wheelset)

Figure A.2 Definition of Wheelset and Track Coordinate System Orientations (Rotations Only)
[The following notation is used: $s\alpha = \sin(\alpha)$, $c\alpha = \cos(\alpha)$]

corresponding transformation relations. The transformation relation for multiple rotations is obtained by matrix multiplication. For instance, the relation between the wheelset and track systems is:

$$\begin{Bmatrix} \hat{i}_W \\ \hat{j}_W \\ \hat{k}_W \end{Bmatrix} = [C_{W/T}] \begin{Bmatrix} \hat{i}_T \\ \hat{j}_T \\ \hat{k}_T \end{Bmatrix} \tag{A-1}$$

where the coordinate transformation matrix $[C_{W/T}]$ is found from matrix multiplication as follows:

$$[C_{W/T}] = [C_{W/2}][C_{2/1}][C_{1/T}] \tag{A-2}$$

Assuming small yaw, roll, and pitch angles, this coordinate transformation matrix is:

$$[C_{W/T}] = \begin{bmatrix} 1 & \psi_W & -\theta_W \\ -\psi_W & 1 & \phi_W \\ \theta_W & -\phi_W & 1 \end{bmatrix} \tag{A-3}$$

Finally, an important simplification occurs since the transformation matrices are orthogonal. As a result, matrix inversion is equivalent to the simpler transpose operation. Thus, the inverse relation:

$$\begin{Bmatrix} \hat{i}_T \\ \hat{j}_T \\ \hat{k}_T \end{Bmatrix} = [C_{T/W}] \begin{Bmatrix} \hat{i}_W \\ \hat{j}_W \\ \hat{k}_W \end{Bmatrix} \tag{A-4}$$

is easily obtained since:

$$[C_{T/W}] = [C_{W/T}]^{-1} = [C_{W/T}]^t \tag{A-5}$$

(where superscript t implies transpose).

In this Appendix, equations are developed to describe the dynamic behavior of a wheelset traversing right-handed curved track. For a wheelset moving along right-handed curved track, as shown in Figure A.1, positive lateral excursions, y_W, are associated with displacements toward the left rail (i.e., the outer or high rail). Thus, as the wheelset displaces laterally in the positive sense, flange contact occurs at the left wheel.

A.3 Acceleration of Wheelset Center of Mass

The inertial acceleration of the center of mass of the wheelset, $\underline{a}^{I_W^*}$, is:

$$\underline{a}^{I_W^*} = \underline{a}^{I_O_T} + \underline{\ddot{r}}^{W^*/O_T} + \underline{\ddot{r}}^{W^*/O_T} + \underline{\omega}^{I_T} \times \underline{r}^{W^*/O_T} + \underline{\omega}^{I_T} \times (\underline{\omega}^{I_T} \times \underline{r}^{W^*/O_T}) + 2\,\underline{\omega}^{I_T} \times \underline{\dot{r}}^{W^*/O_T} \tag{A-6}$$

where $\underline{a}^{I_O_T}$ is the inertial acceleration of point O_T (the origin of the "T" system), $\underline{\omega}^{I_T}$ and $\underline{\dot{\omega}}^{I_T}$ are the angular velocity and angular acceleration, respectively, of the "T" system relative to the "I" system, $\underline{r}^{W^*/O_T}$ is

the position vector from O_T to W^* (the center of mass of the wheelset "W"), and $\underset{\sim}{r}^{T\bullet W^*/O_T}$ and $\underset{\sim}{r}^{T\bullet\bullet W^*/O_T}$ are the first and second derivatives, respectively, taken in the "T" system of the position vector from O_T to W^*. Assuming small superelevation angle, the inertial acceleration of O_T is:

$$\underset{a}{I}\underset{\sim}{O_T} = \dot{V}\hat{i}_T - \frac{V^2}{R}\hat{j}_T + (a\ddot{\phi}_{SE} + \frac{V^2}{R}\phi_{SE})\hat{k}_T . \qquad \text{(A-7)}$$

In equation (A-7), a represents half the rail gage. The angular velocity of the "T" system with respect to the "I" system is:

$$\underset{\omega}{I}\underset{\sim}{T} = \dot{\phi}_{SE}\hat{i}_T - \frac{V}{R}\phi_{SE}\hat{j}_T - \frac{V}{R}\hat{k}_T . \qquad \text{(A-8)}$$

The displacement of W^* from O_T is:

$$\underset{\sim}{r}^{W^*/O_T} = x_W\hat{i}_T + y_W\hat{j}_T + (z_W + r_o)\hat{k}_T \qquad \text{(A-9)}$$

where x_W, y_W, and z_W represent small longitudinal, lateral, and vertical displacements, respectively, of the wheelset center of mass. Substituting equations (A-7) - (A-9) into (A-6) yields the inertial acceleration of the center of mass of the wheelset:

$$\underset{a}{I}\underset{\sim}{W^*} = [\ddot{x}_W + \dot{V}]\hat{i}_T + [\ddot{y}_W - r_o\ddot{\phi}_{SE} - \frac{V^2}{R}]\hat{j}_T$$

$$+ [\ddot{z}_W + a\ddot{\phi}_{SE} + \frac{V^2}{R}\phi_{SE}]\hat{k}_T . \qquad \text{(A-10)}$$

A.4 Rate of Angular Momentum of Wheelset

From Figure A.2, the angular velocity of the wheelset or "W" system relative to the "I" system is:

$$\underline{\omega}^{I_W} = -\frac{V}{R}\hat{k}_H + \dot{\phi}_{SE}\hat{i}_T + \dot{\psi}_W\hat{k}_1 + \dot{\phi}_W\hat{i}_2 + \dot{\theta}_W\hat{j}_w \quad . \tag{A-11}$$

Assuming small angles, equation (A-11) simplifies to:

$$\underline{\omega}^{I_W} = \omega_{WX}\hat{i}_2 + \omega_{WY}\hat{j}_2 + \omega_{WZ}\hat{k}_2 \tag{A-12}$$

where the components are:

$$\omega_{WX} = \dot{\phi}_{SE} + \dot{\phi}_W$$

$$\omega_{WY} = \dot{\theta}_W \tag{A-13}$$

$$\omega_{WZ} = \dot{\psi}_W - \frac{V}{R} \quad .$$

Since the "2" system is aligned with the principal directions of the wheelset, the angular momentum of the wheelset about its center of mass is given by:

$$\underline{H}^{W/W^*} = I_{WX}\omega_{WX}\hat{i}_2 + I_{WY}\omega_{WY}\hat{j}_2 + I_{WX}\omega_{WZ}\hat{k}_2 \tag{A-14}$$

where I_{WX} and I_{WY} are the roll and pitch principal mass moments of inertia of the wheelset, respectively. In equation (A-14), the yaw and roll moments of inertia are assumed identical due to symmetry.

The time rate of change of angular momentum is expressed by:

$$\underline{H}^{I\bullet W/W^*} = \underline{H}^{2\bullet W/W^*} + \underline{\omega}^{I_2} \times \underline{H}^{W/W^*} \tag{A-15}$$

where $\underline{H}^{I\bullet W/W^*}$ and $\underline{H}^{2\bullet W/W^*}$ are the first derivatives of the angular momen-

tum in the "I" and "2" systems, respectively, and where $\overline{{}^{I}\omega}^{2}$ is the angular velocity of the "2" system relative to the "I" system. Since the "2" coordinate system does not spin (pitch) with the wheelset, its angular velocity with respect to the "I" system is:

$$\overline{{}^{I}\omega}^{2} = \omega_{WX}\hat{i}_2 + \omega_{WZ}\hat{k}_2 \tag{A-16}$$

where ω_{WX} and ω_{WY} are defined in equation (A-13). Substituting equations (A-13), (A-14), and (A-16) into (A-15) and neglecting smaller order terms gives the inertial time rate of change of angular momentum:

$$\begin{aligned}\overline{{}^{I}\dot{H}}^{W/W^*} &= [I_{WX}(\ddot{\phi}_{SE} + \ddot{\phi}_W) - I_{WY}\dot{\theta}_W(\dot{\psi}_W - \frac{V}{R})]\hat{i}_2 \\ &+ [I_{WY}\ddot{\theta}_W]\hat{j}_2 \\ &+ [I_{WX}(\ddot{\psi}_W - \frac{\dot{V}}{R} - V(\frac{\dot{I}}{R})) + I_{WY}\dot{\theta}_W(\dot{\phi}_{SE} + \dot{\phi}_W)]\hat{k}_2.\end{aligned} \tag{A-17}$$

A.5 Wheelset Forces and Moments

As a wheelset negotiates a curve, partial slip cr creepage occurs at the wheel/rail contact patches. Due to normal loads acting on the slipping wheelset, friction-type forces known as creep forces are generated. The creep forces depend upon the amounts of pure-roll and pure-slip at each contact patch. In addition to creep forces, normal (or reaction) forces act at each contact patch to equilibrate wheelset loads.

Other external forces and moments acting on the wheelset are:

- Body forces including wheelset weight and other loads carried by the wheelset from the truck, carbody above.

- Suspension forces and moments which depend upon the truck configuration (e.g., conventional transit, radial, etc.)

- Thrust forces and traction (driving/braking) moments which depend upon the truck type (e.g., powered truck)

In the following sections, normal forces and creep forces/moments are discussed.

A.5.1 Normal Forces

Normal forces act at each wheel/rail contact patch. The left and right normal forces, F_{NL} and F_{NR}, respectively, are shown in Figure A.3 for a wheelset in single-point contact. Also shown in Figure A.3 are the left and right contact angles (δ_L,δ_R), the left and right rolling radii (r_L,r_R), and the wheelset roll angle relative to the track plane (ϕ_W).

Each normal force acts perpendicular to the contact patch plane and can be resolved into lateral and vertical components in the track plane. For single-point wheel/rail contact at the left and right wheels, the resolved normal force components are:

$$\begin{aligned} F_{NYL} &= -F_{NL}\sin(\delta_L + \phi_w) \\ F_{NZL} &= F_{NL}\cos(\delta_L + \phi_w) \\ F_{NYR} &= F_{NR}\sin(\delta_R - \phi_W) \\ F_{NZR} &= F_{NR}\cos(\delta_R - \phi_W) \end{aligned} \qquad \text{(A-18)}$$

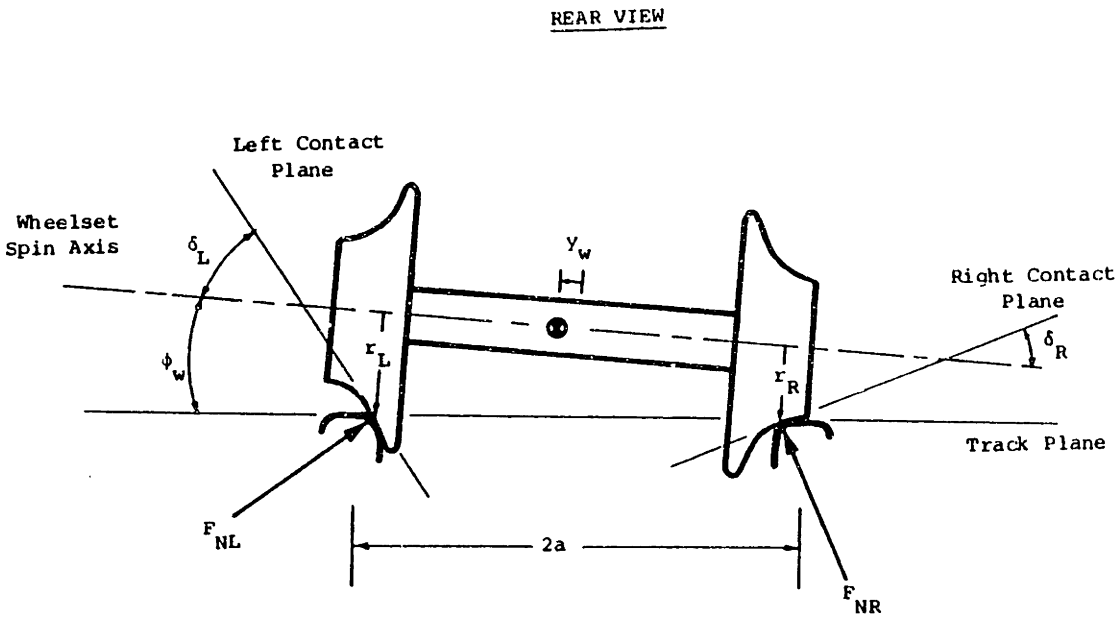

Figure A.3 Wheel/Rail Geometry and Normal Forces Assuming Single-Point Contact

where F_{NYL}, F_{NYR} = left, right normal force in lateral "track" direction

F_{NZL}, F_{NZR} = left, right normal force in vertical "track" direction

The sum of the lateral components of the normal forces is sometimes referred to as the "gravitational stiffness force".

A.5.2 Creep Forces and Moments

In general, rolling/sliding contact theories predict longitudinal and lateral components of creep force in the plane of the contact patch and a creep moment normal to the patch. Contact patch coordinate systems as well as the transformation relations between the contact patch and track axes are defined in Figure A.4. The creep forces and moments at the left, right contact patches are:

$$\begin{aligned} \bar{F}_{CL} &= F_{CPXL}\hat{i}_{CL} + F_{CPYL}\hat{j}_{CL} \\ \bar{F}_{CR} &= F_{CPXR}\hat{i}_{CR} + F_{CPYR}\hat{j}_{CR} \\ \bar{M}_{CL} &= M_{CPZL}\hat{k}_{CL} \\ \bar{M}_{CR} &= M_{CPZR}\hat{k}_{CR} \end{aligned} \qquad \text{(A-19)}$$

where F_{CPXL}, F_{CPXR} = left, right creep force in longitudinal contact patch direction

F_{CPYL}, F_{CPYR} = left, right creep force in lateral contact patch direction

M_{CPZL}, M_{CPZR} = left, right creep moment normal to contact patch

and where $\hat{i}_{CL}$, $\hat{j}_{CL}$, $\hat{k}_{CL}$ and $\hat{i}_{CR}$, $\hat{j}_{CR}$, $\hat{k}_{CR}$ are unit vectors along the left and right contact patch coordinate systems, respectively.

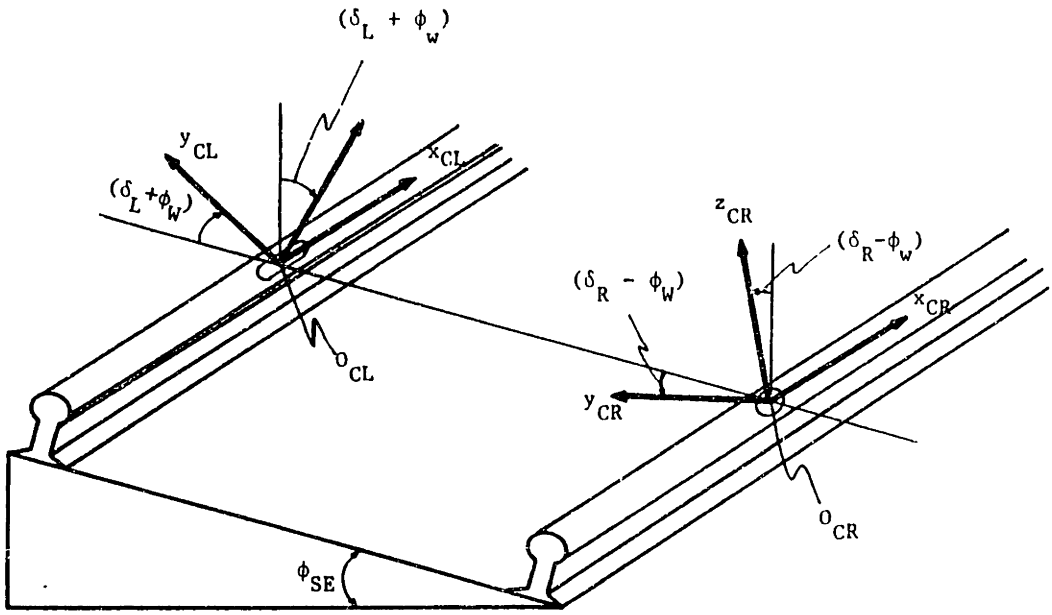

$$\begin{Bmatrix} \hat{i}_{CL} \\ \hat{j}_{CL} \\ \hat{k}_{CL} \end{Bmatrix} \begin{bmatrix} 1 & 0 & 0 \\ 0 & c(\delta_L+\phi_w) & s(\delta_L+\phi_w) \\ 0 & -s(\delta_L+\phi_w) & c(\delta_L+\phi_w) \end{bmatrix} \begin{Bmatrix} \hat{i}_j \\ \hat{j}_T \\ \hat{k}_T \end{Bmatrix} ; \begin{Bmatrix} \hat{i}_{CR} \\ \hat{j}_{CR} \\ \hat{k}_{CR} \end{Bmatrix} = \begin{bmatrix} 1 & 0 & 0 \\ 0 & c(\delta_R-\phi_w) & s(\delta_R-\phi_w) \\ 0 & s(\delta_R-\phi_w) & c(\delta_R-\phi_w) \end{bmatrix} \begin{Bmatrix} \hat{i}_T \\ \hat{j}_T \\ \hat{k}_T \end{Bmatrix}$$

Figure A.4 Contact Patch Coordinate Systems

Performing the coordinate transformations gives the creep forces and moments resolved in the track system as follows:

Left Contact Patch:

$$
\begin{aligned}
F_{CXL} &= F_{CPXL} \\
F_{CYL} &= F_{CPYL}\cos(\delta_L + \phi_W) \\
F_{CZL} &= F_{CPYL}\sin(\delta_L + \phi_W) \\
M_{CXL} &= 0 \\
M_{CYL} &= -M_{CPZL}\sin(\delta_L + \phi_W) \\
M_{CZL} &= M_{CPZL}\cos(\delta_L + \phi_W)
\end{aligned}
\qquad \text{(A-20)}
$$

Right Contact Patch:

$$
\begin{aligned}
F_{CXR} &= F_{CPXR} \\
F_{CYR} &= F_{CPYR}\cos(\delta_R - \phi_W) \\
F_{CZR} &= -F_{CPYR}\sin(\delta_R - \phi_W) \\
M_{CXR} &= 0 \\
M_{CYR} &= M_{CPZR}\sin(\delta_R - \phi_W) \\
M_{CZR} &= M_{CPZR}\cos(\delta_R - \phi_W)
\end{aligned}
\qquad \text{(A-21)}
$$

A.5.2.1 Heuristic Creep Model

A heuristic nonlinear creep force model is adopted in this analysis. The creep forces and moments are initially using Kalker's linear theory [40]. At each wheel/rail interface, the longitudinal and

lateral contact patch components of creep force are:

$$F'_{CPX} = -f_{33}\xi_x$$
$$F'_{CPY} = -f_{11}\xi_y - f_{12}\xi_{sp} \qquad \text{(A-22)}$$

and the spin creep moment acting normal to the contact patch is:

$$M'_{CPZ} = f_{12}\xi_y - f_{22}\xi_{sp} \qquad \text{(A-23)}$$

where f_{11}, f_{12}, f_{22}, and f_{33} are the lateral, lateral/spin, spin, and longitudinal creep coefficients, respectively, and ξ_x, ξ_y, and ξ_{sp} are the longitudinal, lateral, and spin contact patch creepages, respectively. The creepages are the relative wheel/rail velocities at the contact patch normalized by the nominal forward velocity. They are derived in the following section (A.5.2.2).

The creep coefficients f_{11}, f_{12}, f_{22}, and f_{33} are functions of the wheel/rail geometry, material properties, and normal load. They are computed according to Kalker's linear theory [40], which assumes that the shape and dimensions of the contact area (as well as the distribution of the normal stress) are given by the Hertz solution for two elastic bodies in contact. In this solution, the contact patch is elliptical. The creep coefficients are then typically reduced by 50% to account for discrepancies between field and laboratory test data due to contaminated rail conditions in the field.

The creep coefficients depend on the normal load, F_N, in the following way:

$$f_{11} = \left(\frac{F_N}{F_N^*}\right)^{2/3} f_{11}^*$$

$$f_{12} = \left(\frac{F_N}{F_N^*}\right) f_{12}^*$$

$$f_{22} = \left(\frac{F_N}{F_N^*}\right)^{4/3} f_{22}^* \qquad \text{(A-24)}$$

$$f_{33} = \left(\frac{F_N}{F_N^*}\right) f_{33}^*$$

In equation (A-24), f_{ij}^* are nominal creep coefficients computed for the nominal normal load F_N^*; f_{ij} are creep coefficients for normal load F_N.

The magnitude of the resultant creep force cannot exceed the amount of available adhesion, μF_N, at the wheel/rail contact interface. Accordingly, the resultant creep force is saturated using a modified Vermeulen-Johnson model [8] which includes the effect of spin creepage. A saturation coefficient, ε, is calculated by:

$$\varepsilon = \begin{cases} \frac{1}{\beta}[\beta - \frac{1}{3}\beta^2 + \frac{1}{27}\beta^3] \ldots \text{For } \beta < 3 \\ \\ \frac{1}{\beta} \ldots\ldots\ldots\ldots\ldots\ldots \text{For } \beta \geq 3 \end{cases} \qquad \text{(A-25)}$$

where β is the normalized unlimited resultant creep force:

$$\beta = \frac{1}{\mu F_N} \sqrt{(F'_{CPX})^2 + (F'_{CPY})^2} \quad . \tag{A-26}$$

The saturated contact patch creep forces and moment are then:

$$\left.\begin{aligned} F_{CPX} &= \varepsilon F'_{CPX} \\ F_{CPY} &= \varepsilon F'_{CPY} \\ M_{CPZ} &= \varepsilon M'_{CPZ} \quad . \end{aligned}\right\} \tag{A-27}$$

These equations predict a resultant creep force which agrees with linear Kalker Theory for small creepages and which saturates to the adhesion limit for larger creepages, as shown in Figure A.5.

A.5.2.2 Derivation of Creepages for Dynamic Curving

The creepages are the relative velocities of the wheel and rail at the contact patch normalized with respect to the nominal forward velocity. The longitudinal and lateral components of creepage at the left contact patch, ξ_{XL} and ξ_{YL}, respectively, are:

$$\left.\begin{aligned} \xi_{XL} &= \frac{1}{V} \left(\bar{V}^{O_{CL}}_{rel} \cdot \hat{i}_{CL} \right) \\ \xi_{YL} &= \frac{1}{V} \left(\bar{V}^{O_{CL}}_{rel} \cdot \hat{j}_{CL} \right) \end{aligned}\right\} \tag{A-28}$$

where $\bar{V}^{O_{CL}}_{rel}$ is the relative wheel/rail velocity at the left contact patch*, i.e., the velocity of O_{CL} on the wheel with respect to the rail.

*O_{CL} is the origin of the left contact patch coordinate system.

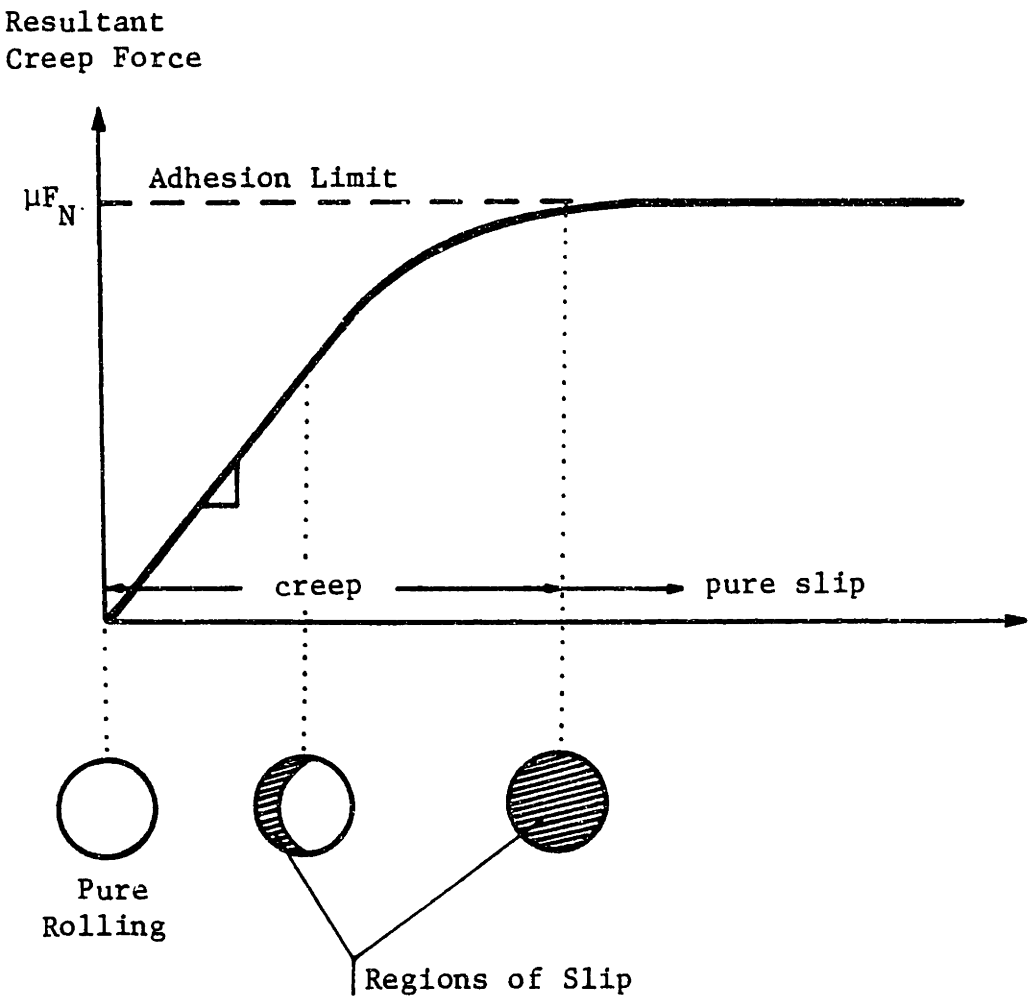

Figure A.5 Contact Patch Creep Force vs. Creepage Relation

For small wheelset roll and yaw angles,

$$\bar{V}^{O_{CL}}_{rel} = [\dot{x}_W + V(1 + \frac{a}{R}) - r_L\dot{\theta}_W - a\dot{\psi}_W]\hat{i}_T$$

$$+ [\dot{y}_W + r_L(\dot{\phi}_W - \dot{\theta}_W\psi_W) - \dot{y}_{rail_L}]\hat{j}_T$$

$$+ [\dot{z}_W + a\dot{\phi}_W - \Delta_{XL}\dot{\theta}_W]\hat{k}_T \ . \qquad \text{(A-29)}$$

In equation (A-29), $\dot{y}_{rail_L}$ is the left rail lateral velocity. Also, Δ_{XL} is the longitudinal displacement of the contact patch from under the wheelset centerline due to yaw.* For a positive wheelset yaw angle, the left contact patch displaces forward a distance Δ_{XL} and the right contact patch displaces backward a distance Δ_{XR}, as shown in Figure A.6. Transforming equation (A-29) to contact patch coordinates and assuming no relative velocity normal to the contact patch implies the following constraint relation obtained by setting the coefficient of $\hat{k}_{CL}$ to zero.

$$\dot{z}_W + a\dot{\phi}_W - \Delta_{XL}\dot{\theta}_W = [\dot{y}_W + r_L(\dot{\phi}_W - \dot{\theta}_W\psi_W) - \dot{y}_{rail_L}]\tan(\delta_L+\phi_W) \qquad \text{(A-30)}$$

Using this constraint in equation (A-29) and evaluating equation (A-28) results in the following expressions for the longitudinal and lateral creepages at the left contact patch, ξ_{XL} and ξ_{YL}, respectively:

$$\left.\begin{aligned} \xi_{XL} &= \frac{1}{V}[\dot{x}_W + V(1 + \frac{a}{R}) - r_L\dot{\theta}_W - a\dot{\psi}_W] \\ \xi_{YL} &= \frac{1}{V}[\dot{y}_W + r_L(\dot{\phi}_W - \dot{\theta}_W\psi_W) - \dot{y}_{rail_L}]/\cos(\delta_L + \phi_w) \end{aligned}\right\} \qquad \text{(A-31)}$$

*In [30] the longitudinal shift of the contact patch, Δ_{XL}, was derived for steady-state conditions as: $\Delta_{XL} = r_L\psi_W\tan(\delta_L + \phi_W)$.

PLAN
VIEW:

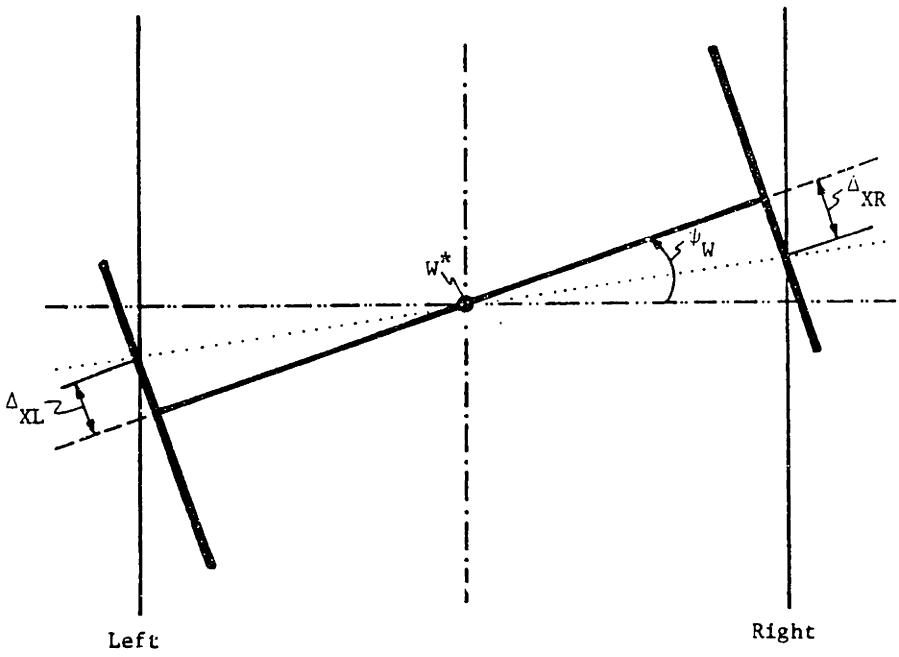

Figure A.6 Longitudinal Displacement of Contact Points Due to Wheelset Yaw

The spin creepage at the left contact patch, ξ_{SPL}, is:

$$\xi_{SPL} = \frac{1}{V}(\bar{\omega}_{rel} \cdot \hat{k}_{CL}) \tag{A-32}$$

where $\bar{\omega}_{rel}$ is the relative wheel/rail angular velocity given by:

$$\bar{\omega}_{rel} = \dot{\phi}_W \hat{i}_2 + \dot{\theta}_W \hat{j}_2 + (\dot{\psi}_W - \frac{V}{R})\hat{k}_2 \ . \tag{A-33}$$

The spin creepage is obtained by transforming equation (A-33) to left contact patch coordinates, evaluating equation (A-32), and assuming small wheelset angles.

$$\xi_{SPL} = \frac{1}{V}[-\dot{\theta}_W \sin(\delta_L + \phi_W) + (\dot{\psi}_W - \frac{V}{R} + \phi_W \dot{\theta}_W)\cos(\delta_L + \phi_W)] \tag{A-34}$$

A similar development results in expressions for the creepages at the right contact patch:

$$\left.\begin{aligned} \xi_{XR} &= \frac{1}{V}[\dot{x}_W + V(1 - \frac{a}{R}) - r_R \dot{\theta}_W + a\dot{\psi}_W] \\ \xi_{YR} &= \frac{1}{V}[\dot{y}_W + r_R(\dot{\phi}_W - \dot{\theta}_W \psi_W) - \dot{y}_{rail_R}]/\cos(\delta_R - \phi_W) \\ \xi_{SPR} &= \frac{1}{V}[\dot{\theta}_w \sin(\delta_R - \phi_W) + (\dot{\psi}_W - \frac{V}{R} - \phi_W \dot{\theta}_W)\cos(\delta_R - \phi_W)] \end{aligned}\right\} \tag{A-35}$$

A.5.2.3 Definition of Contact Patch Work

The work expended at the wheel/rail contact patches has been proposed as a curving performance index [29]. The contact patch work is related to wheel and track wear.

Contact patch work is defined as the dot product of the resultant creep force and creepage vectors, as follows:

$$W = F_{CPX}\xi_X + F_{CPY}\xi_Y + M_{CP}\xi_{SP} \tag{A-36}$$

The work index, W, represents the work expended at the contact patch per unit distance along the track. As such, W has units of work per distance or force.

If creepage occurs, work is expended at the contact patch. This is verified by substituting equations (A-22), (A-23), and (A-27) into equation (A-36) yielding:

$$W = -[f_{33}\xi_X^2 + f_{11}\xi_Y^2 + f_{22}\xi_{SP}^2] \tag{A-37}$$

Since the creep coefficients, f_{11}, f_{22}, and f_{33}, and the saturation coefficient, ε, are positive numbers, the work index is negative. Thus, work is always expended at the contact patch.

The work, W, is related to the power dissipated at the contact patch as follows:

$$P = VW \tag{A-38}$$

where V is the vehicle speed (assumed constant). Equation (A-38) represents the power dissipated by friction.

A.6 Wheelset Equations of Motion

The wheelset equations of motion are derived by direct application of Newtonian mechanics prescribed by the principles of linear and angular momentum. The principle of linear momentum states that the net

external force acting on the wheelset is equal to the product of the mass of the wheelset, m_W, and the inertial acceleration of the center of mass, $\underline{a}^{I_{W^*}}$. Thus,

$$\bar{F} = m_W \underline{a}^{I_{W^*}} \tag{A-39}$$

where $\bar{F}$ represents the sum of all external forces acting on the wheelset, including creep and normal forces. The principle of angular momentum states that the net external moment acting about the center of mass of the wheelset is equal to the time rate of change of angular momentum about the center of mass.

$$\bar{M}^{W^*} = \underline{H}^{I \cdot W/W^*} \tag{A-40}$$

where $\bar{M}^{W^*}$ is the sum of all external moments acting about the center of mass of the wheelset. Equations (A-39) and (A-40) represent six scalar differential equations of motion for the wheelset.

A simple model of the track is adopted in which each rail is assumed to have lateral freedom only. In this model, overturning motion of the rails is neglected. Figure A.7 shows the mass-spring-viscous damper arrangement used to model each rail. The equation of motion for each rail is:

$$-F_y = m_r \ddot{y}_{rail} + c_r \dot{y}_{rail} + k_r y_{rail} \tag{A-41}$$

where F_y is the net lateral wheel force composed of creep and normal forces; m_r is the effective lateral rail mass, c_r is the effective lateral rail damping, k_r is the effective lateral rail stiffness, and y_{rail} is the lateral rail displacement. Equation (A-38) represents

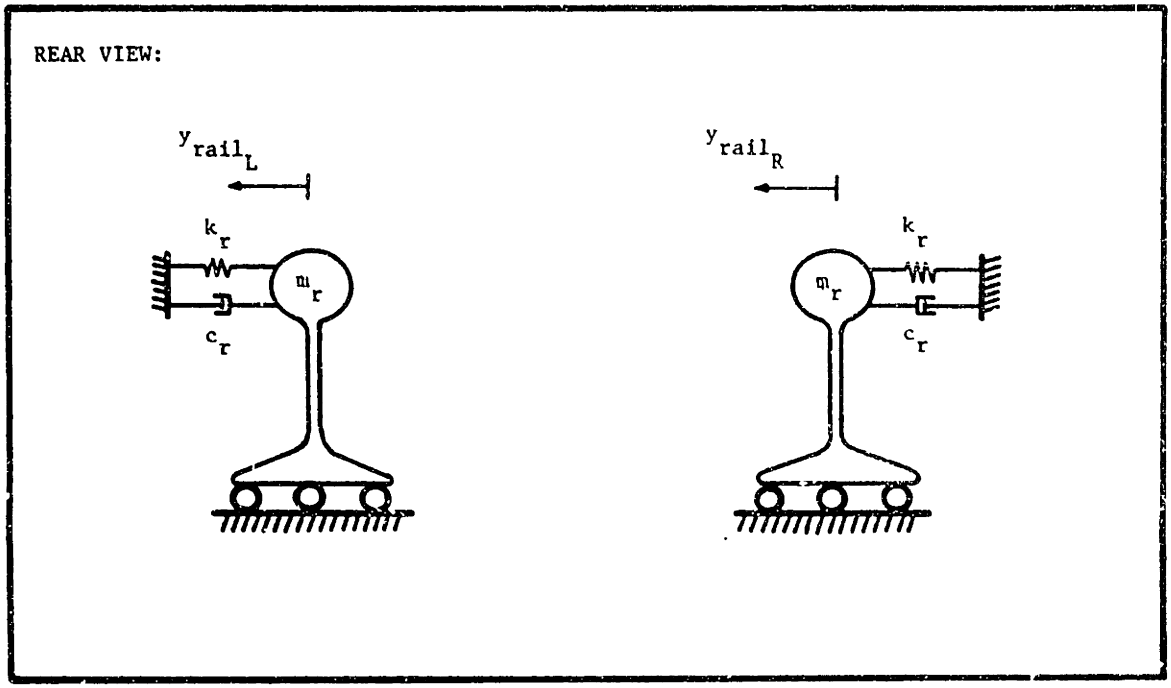

Figure A.7 Lateral Track Model

the scalar differential equations of motion for the left and right rails.

A.6.1 Single-Point Contact

This section develops the dynamic curving equations of motion of a wheelset in single-point contact at the left and right wheels. A free-body diagram is shown in Figure A.8. From equation (A-39), the vector force equation of motion is:

$$\bar{F}_{CL} + \bar{F}_{CR} + \bar{F}_{NL} + \bar{F}_{NR} + \bar{F}_{susp_W} + \bar{F}_{axle} = m_W \underline{a}^{I_{W^*}} \tag{A-42}$$

where $\bar{F}_{CL}$, $\bar{F}_{CR}$ are creep forces and $\bar{F}_{NL}$, $\bar{F}_{NR}$ are normal forces at the left, right contact points, respectively, $\bar{F}_{susp}$ are suspension forces, $\bar{F}_{axle}$ are axle forces, $m_W = W_w/g$ is the wheelset mass, and $\underline{a}^{I_{W^*}}$ is the inertial acceleration of the center of mass of the wheelset given by equation (A-10). The axle forces consist of longitudinal thrust, F_t, and wheelset weight, W_w, as follows:

$$\bar{F}_{axle} = F_t \hat{i}_T - W_w \hat{k}_H \tag{A-43}$$

Assuming small angles, equation (A-42) is equivalent to the following three scalar equations of motion resolved along track coordinates.

Wheelset Longitudinal Equation

$$\frac{W_w}{g} (\ddot{x}_W + \dot{V}) = F_{CXL} + F_{CXR} + F_{susp_{x_W}} + F_t \tag{A-44}$$

Wheelset Lateral Equation

$$\left.\begin{aligned} \frac{W_w}{g} (\ddot{y}_W - r_o \ddot{\phi}_{SE}) = F_{CYL} + F_{CYR} + F_{NYL} + F_{NYR} + F_{susp_{y_W}} \\ + W_w(\phi_d - \phi_W) \end{aligned}\right\} \tag{A-45}$$

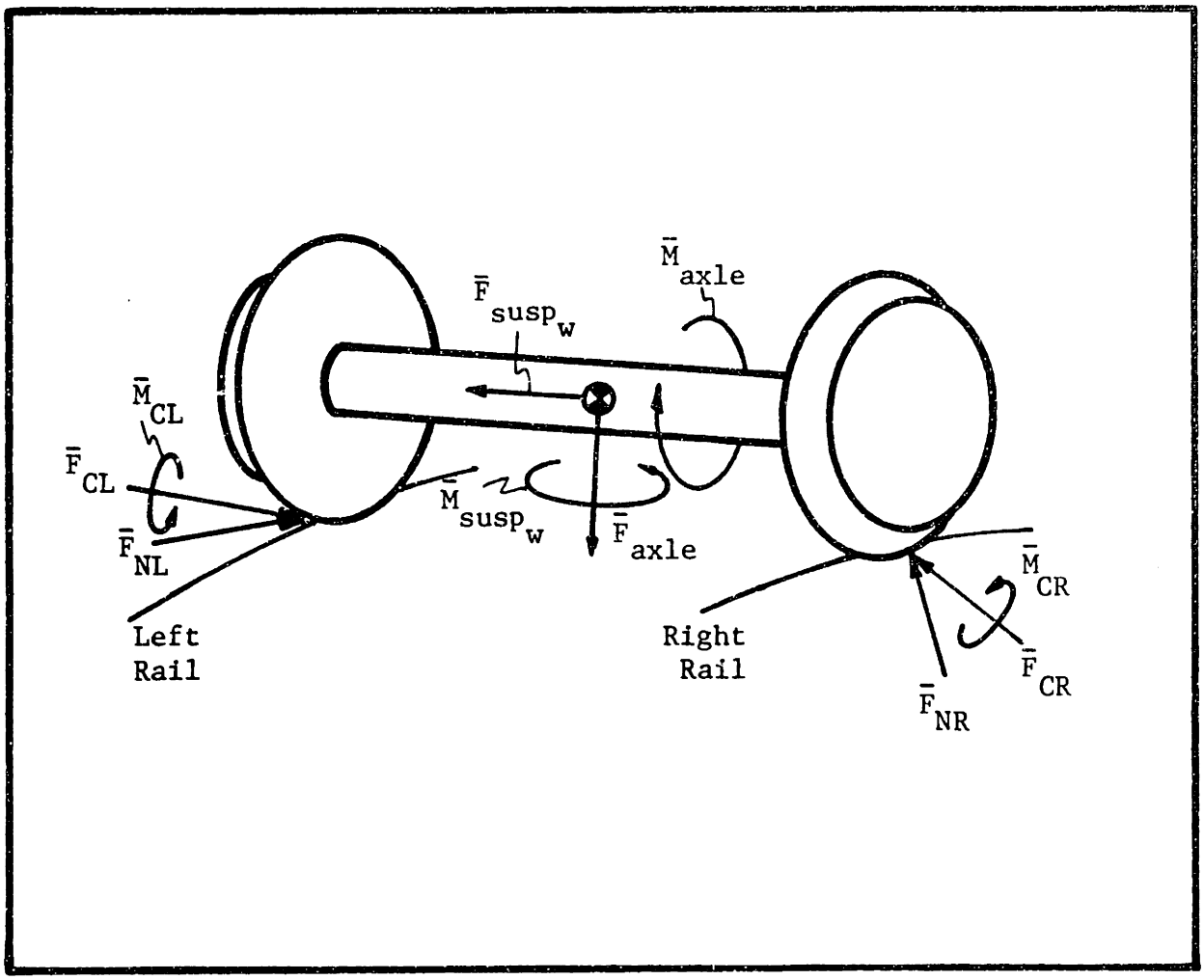

Figure A.8 Free-Body Diagram of Wheelset in Single-Point Contact

Wheelset Vertical Equation

$$\frac{W_w}{g}(\ddot{z}_W + a\ddot{\phi}_{SE}) = F_{CZL} + F_{CZR} + F_{NZL} + F_{NZR} + F_{susp_{z_W}} - W_w \qquad (A-46)$$

In equation (A-45), ϕ_d represents the cant deficient, given by

$$\phi_d = \frac{V^2}{Rg} - \phi_{SE} \cdot \qquad (A-47)$$

The cant deficiency is an angular measure of the lateral unbalance between centrifugal and gravitational forces.

The vector moment equation of motion, equation (A-40), is defined by:

$$\bar{R}_L \times (\bar{F}_{CL} + \bar{F}_{NL}) + \bar{R}_R \times (\bar{F}_{CR} + \bar{F}_{NR}) + \bar{M}_{CL} + \bar{M}_{CR} + \bar{M}_{susp_W} + \bar{M}_{axle} = \overset{I\cdot W/W^*}{\bar{H}} \qquad (A-48)$$

where $\bar{R}_L$, $\bar{R}_R$ are displacement vectors from the wheelset center of mass to the left, right contact points, $\bar{M}_{CL}$, $\bar{M}_{CR}$ are the creep moments at the left, right contact points, $\bar{M}_{susp_W}$ are suspension moments, $\bar{M}_{axle}$ are axle moments (e.g., drive/brake torque, $T_d\hat{j}_2$) and $\overset{I\cdot W/W^*}{\bar{H}}$ is the inertial time rate of change of angular momentum, specified by equation (A-17). The displacement vectors, $\bar{R}_L$ and $\bar{R}_R$ are given by

$$\left.\begin{aligned} \bar{R}_L &= -[\{a - r_L\tan(\delta_L+\phi_W)\}\psi_W]\hat{i}_T + a\hat{j}_T - r_L\hat{k}_T \\ \bar{R}_R &= [\{a - r_R\tan(\delta_R-\phi_W)\}\psi_W]\hat{i}_T - a\hat{j}_T - r_R\hat{k}_T \end{aligned}\right\} \qquad (A-49)$$

where small yaw and roll angles have been assumed and the longitudinal

displacements of the contact points with wheelset yaw have been taken into account. Substituting expressions (A-49) into equation (A-48), expanding, and neglecting smaller order terms gives the following three scalar equations resolved along "2" system coordinates.

Wheelset Roll Equation

$$I_{WX}(\ddot{\phi}_W + \ddot{\phi}_{SE}) = I_{WY}\dot{\theta}_W(\dot{\psi}_W - \frac{V}{R}) + a(F_{CZL} + F_{NZL})$$
$$+ r_L(F_{CYL} + F_{NYL} - \psi_W F_{CXL}) - a(F_{CZR} + F_{NZR})$$
$$+ r_R(F_{CYR} + F_{NYR} - \psi_W F_{CXR})$$
$$+ M_{susp_{X_W}} + \psi_W(M_{CYL} + M_{CYR}) \qquad \text{(A-50)}$$

Wheelset Spin Equation

$$I_{WY}\ddot{\theta}_W = -r_L[F_{CXL} + \psi_W\{F_{CYL} + F_{CZL}\tan(\delta_L + \phi_W)\ ]$$
$$- r_R[F_{CXR} + \psi_W\{F_{CYR} - F_{CZR}\tan(\delta_R - \phi_W)\}\ ]$$
$$+ M_{CYL} + M_{CYR} + M_{susp_{y_W}} + \dot{\phi}_W(M_{CZL} + M_{CZR})$$
$$+ T_d \qquad \text{(A-51)}$$

Wheelset Yaw Equation

$$I_{WX}(\ddot{\psi}_W - \frac{\dot{V}}{R} - V(\frac{\dot{I}}{R})) = -I_{WY}\dot{\theta}_W(\dot{\phi}_W + \dot{\phi}_{SE})$$
$$- a(F_{CXL} - F_{CXR}) - \psi_W\{(a - r_L\tan(\delta_L + \phi_W))(F_{CYL} + F_{NYL})$$

$$-(a-r_R\tan(\delta_R - \phi_W))(F_{CYR} + F_{NYR})\} + M_{CZL} + M_{CZR}$$

$$+M_{susp_{z_W}} - \phi_W(M_{CYL} + M_{CYR}) \qquad \text{(A-52)}$$

In these equations, the longitudinal creep moments, M_{CXL} and M_{CXR}, have been set to zero as was shown in equations (A-20) and (A-21). Also, relations (A-18) have been used to simplify the wheelset spin equation, equation (A-51). As expected, normal forces do not (explicitly) appear in this equation.

The dynamics of the rails are approximated using the lateral rail model shown in Figure A.7. The equations of motion of the left and right rails are determined by equation (A-41).

Left Rail Lateral Equation

$$m_r\ddot{y}_{rail_L} + c_r\dot{y}_{rail_L} + k_r y_{rail_L} = -F_{NYL} - F_{CYL} \qquad \text{(A-53)}$$

Right Rail Lateral Equation

$$m_r\ddot{y}_{rail_R} + c_r\dot{y}_{rail_R} + k_r y_{rail_R} = -F_{NYR} - F_{CYR} \qquad \text{(A-54)}$$

Equations (A-44) - (A-47) and (A-50) - (A-52) represent six wheelset equations of motion; equations (A-53) and (A-54) represent two rail equations of motion. This system of 8 equations describes the dynamic behavior of a wheelset in single-point contact as it negotiates laterally flexible, curved track. Mathematically, these equations are coupled, nonlinear, scalar, differential equations. They can be solved for the time histories of the following 8 indepen-

dent variables: x_W, y_W, $\dot{\theta}_W$, $\dot{\psi}_W$, F_{NZL}, F_{NZR}, y_{rail_L}, y_{rail_R}. This assumes that F_t, T_d, wheelset mqss and inertia properties, and suspension forces and moments are known input data. Also, V, R, and ϕ_{SE} are assumed known functions of distance along the track. For continuous wheel/rail contact, the following geometry are known functions of y_W, y_{rail_L}, and y_{rail_R} for a given wheel/rail profile: z_W, ϕ_W, r_L, r_R, δ_L, δ_R. Thus, the wheelset vertical displacement, z_W, and the wheelset roll angle, ϕ_W, can be written in terms of the state variables y_W, y_{rail_L}, and y_{rail_R}. Similarly, the wheelset vertical velocity and roll angle rate are functions of the wheelset and rail lateral velocities.

It is convenient to calculate the normal forces from the wheelset vertical and roll equations. Simultaneous solution of equations (A-46) and (A-50) gives the normal forces at the left and right wheel/rail contact patches as follows:

$$\left.\begin{aligned} F_{NL} &= \frac{\nu_L}{\Delta_1} \\ F_{NR} &= \frac{\nu_R}{\Delta_1} \end{aligned}\right\} \qquad \text{(A-55)}$$

where

$$\nu_L = F_Z^*\{a\cos(\delta_R-\phi_W)-r_R\sin(\delta_R-\phi_W)\} + M_\phi^*\cos(\delta_R-\phi_W)$$

$$\nu_R = F_Z^*\{a\cos(\delta_L+\phi_W)-r_L\sin(\delta_L+\phi_W)\} - M_\phi^*\cos(\delta_L+\phi_W)$$

and

$$\Delta_1 = 2a\cos(\delta_L+\phi_W)\cos(\delta_R-\phi_W)-r_R\cos(\delta_L+\phi_W)\sin(\delta_R-\phi_W)$$
$$-r_L\sin(\delta_L+\phi_W)\cos(\delta_R-\phi_W)$$

In the expressions for ν_L and ν_R, F_Z^* is an equivalent vertical force and M_ϕ^* is an equivalent roll moment given by:

$$F_Z^* = -F_{CZL} - F_{CZR} - F_{susp_{z_W}} + \frac{W_w}{g}(\ddot{z}_W + a\ddot{\phi}_{SE}) + W_w$$

and

$$M_\phi^* = a(F_{CZR} - F_{CZL}) - r_L(F_{CYL} - \psi_W F_{CXL})$$
$$-r_R(F_{CYR} - \psi_W F_{CXR}) - \psi_W(M_{CYL} + M_{CYR}) - M_{susp_{x_W}}$$
$$+I_{WX}(\ddot{\phi}_W + \ddot{\phi}_{SE}) - I_{WY}\dot{\theta}_W(\dot{\psi}_W - \frac{V}{R})$$

The normal forces, F_{NL} and F_{NR}, are resolved into lateral and vertical components according to equations (A-18).

A.6.2 Two-Point Contact

The previous development is appropriate for a wheelset which maintains single-point wheel/rail contact at both wheels for all lateral displacements. This continuous single-point contact approximation is appropriate for some wheel/rail profiles, particularly many European profiles. As the wheelset displaces laterally, the point of contact at the outer wheel shifts smoothly from the tread to the flange, while the inner wheel maintains tread contact. For other profiles with steep flanges, such as many U.S. wheel/rail profiles, two points of contact can develop at the flanging wheel. As before, single-point tread contact occurs at both the inner and outer wheels for a net wheelset ex-

cursion less than the flange clearance. Two-point contact occurs at the flanging wheel and single-point contact occurs at the inner wheel for a wheelset displacement (relative to the flanging wheel rail) equal to the flange clearance. Single-point flange contact occurs at the flanging wheel for net excursions greater than the flange clearance. This represents a dangerous situation conducive to derailment.

For a wheelset negotiating a right-handed curved track, the left wheel represents the outer or flanging wheel. Figure A.9 shows the contact condition at the left wheel as the wheelset displaces laterally. Single-point tread contact (Figure A.9a) and single-point flange contact (Figure A.9c) occur for net excursions less than and greater than the flange clearance, respectively. Two-point contact occurs for a wheelset excursion (with respect to the left rail) equal to the flange clearance. Two-point contact is depicted in Figure A.9b where the rail head is shown to contact simultaneously both the tread and flange of the left wheel.

For a wheelset in two-point contact*, the displacement relative to the left rail is fixed at the flange clearance, y_{fc}, or mathematically,

$$y_W - y_{rail_L} = y_{fc} \tag{A-56}$$

Equation (A-56) represents a constraint relation which can be used to specify the contact geometry (rolling radius, contact angle) of the

*The terminology assumes that the two points of contact occur at the flanging wheel. "A wheelset in two-point contact" actually has three points of wheel/rail contact, two at the flanging or outer wheel and one at the inner wheel.

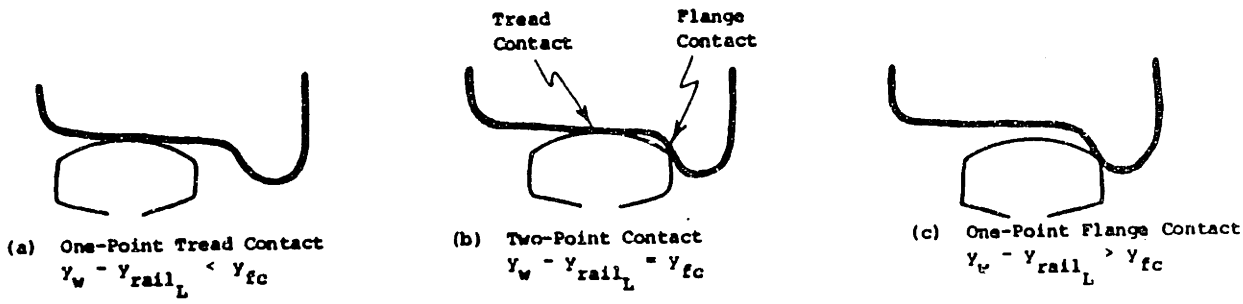

Figure A.9 Left Wheel/Rail Contact

tread and flange contact points of the left wheel. Differentiation of equation (A-56) gives the relation between the wheelset and left rail lateral velocities and accelerations:

$$\left.\begin{aligned} \dot{y}_W &= \dot{y}_{rail_L} \\ \ddot{y}_W &= \ddot{y}_{rail_L} \end{aligned}\right\} \quad (A\text{-}57)$$

Figure A.10 shows the wheel/rail forces acting on a wheelset in two-point contact. The equations of motion describing a wheelset in two-point contact at the left wheel are similar to the equations derived for a wheelset in single-point contact, with new terms to account for the additional contact patch. The expressions derived for single-point contact at the left, such as the normal force, the creep force and moment, and the creepages at the left, are correct for two-point contact. Now, however, these expressions apply to a left tread and left flange contact patch when the appropriate contact geometry is used. The notation is subscripts LT and LF for left tread and left flange contact patch, respectively, in place of subscript L (for left contact patch) of the single-point contact derivation.

Assuming small yaw and roll angles, the equations of motion of a wheelset in two-point contact at the left wheel are given below.

Wheelset Longitudinal Equation

$$\frac{W_w}{g}(\ddot{x}_W + \dot{V}) = F_{CXLT} + F_{CXLF} + F_{CXR} + F_{susp_{x_W}} + F_t \quad (A\text{-}58)$$

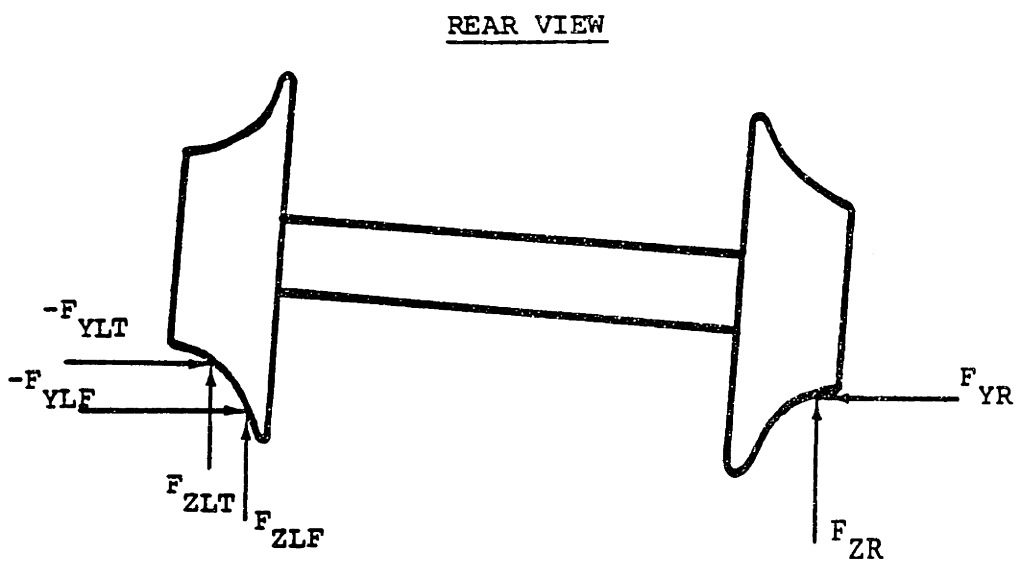

Wheel Forces

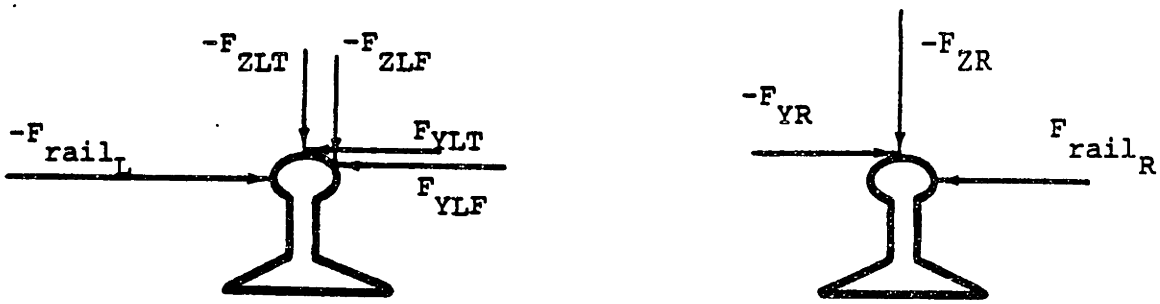

Rail Forces

Figure A.10 Wheel and Rail Forces for Two-Point Contact

Wheelset Lateral Equation

$$\frac{W_w}{g}(\ddot{y}_W - r_o\ddot{\phi}_{SE}) = F_{CYLT} + F_{CYLF} + F_{CYR} + F_{NYLT}$$

$$+ F_{NYLF} + F_{NYR} + F_{susp_{y_W}} + W_w(\phi_d - \phi_W) \qquad \text{(A-59)}$$

Wheelset Vertical Equation

$$\frac{W_w}{g}(\ddot{z}_W + a\ddot{\phi}_{SE}) = F_{CZLT} + F_{CZLF} + F_{CZR} + F_{NZLT}$$

$$+ F_{NZLF} + F_{NZR} + F_{susp_{z_W}} - W_w \qquad \text{(A-60)}$$

Wheelset Roll Equation

$$I_{WX}(\ddot{\phi}_W + \ddot{\phi}_{SE}) = I_{WY}\dot{\theta}_W(\dot{\psi}_W - \frac{V}{R}) + a(F_{CZLT} + F_{CZLF} + F_{NZLT} + F_{NZLF})$$

$$+ r_{LT}(F_{CYLT} + F_{NYLT} - \psi_W F_{CXLT}) + r_{LF}(F_{CYLF} + F_{NYLF} - \psi_W F_{CXLF})$$

$$- a(F_{CZR} + F_{NZR}) + r_R(F_{CYR} + F_{NYR} - \psi_W F_{CXR})$$

$$+ M_{susp_{x_W}} + \psi_W(M_{CYLT} + M_{CYLF} + M_{CYR}) \qquad \text{(A-61)}$$

Wheelset Spin Equation

$$I_{WY}\ddot{\theta}_W = -r_{LT}[F_{CXLT} + \psi_W\{F_{CYLT} + F_{CZLT}\tan(\delta_{LT} + \phi_W)\}]$$

$$- r_{LF}[F_{CXLF} + \psi_W\{F_{CYLF} + F_{CZLF}\tan(\delta_{LF} + \phi_W)\}]$$

$$- r_R[F_{CXR} + \psi_W\{F_{CYR} - F_{CZR}\tan(\delta_R - \phi_W)\}]$$

$$+ M_{CYLT} + M_{CYLF} + M_{CYR} + M_{susp_{y_W}}$$

$$+ \phi_W(M_{CZLT} + M_{CZLF} + M_{CZR}) + T_d \qquad \text{(A-62)}$$

Wheelset Yaw Equation

$$I_{WX}[\ddot{\psi}_X - \frac{\dot{V}}{R} - V(\frac{\dot{i}}{R})] = -I_{WY}\dot{\theta}_W(\dot{\phi}_W + \dot{\phi}_{SE})$$

$$-a(F_{CXLT} + F_{CXLF} - F_{CXR}) - \psi_W\{(a-r_{LT}\tan(\delta_{LT}+\phi_W))(F_{CYLT}+F_{NYLT})$$

$$+(a-r_{LF}\tan(\delta_{LF}+\phi_W))(F_{CYLF}+F_{NYLF})-(a-r_R\tan(\delta_R-\phi_W))(F_{CYR}+F_{NYR})\}$$

$$+M_{CZLT} + M_{CZLF} + M_{CZR} + M_{susp_{z_W}}$$

$$+\phi_W(M_{CYLT} + M_{CYLF} + M_{CYR}) \qquad \text{(A-63)}$$

Left Rail Lateral Equation

$$m_r\ddot{y}_{rail_L} + c_r\dot{y}_{rail_L} + k_r y_{rail_L} = -F_{NYLT} - F_{NYLF} - F_{CYLT} - F_{CYLF} \qquad \text{(A-64)}$$

Right Rail Lateral Equation

$$m_r\ddot{y}_{rail_R} + c_r\dot{y}_{rail_R} + k_r y_{rail_R} = -F_{NYR} - F_{CYR} \qquad \text{(A-65)}$$

Equations (A-58) - (A-65) represent 8 coupled, nonlinear, differential equations of motion. The equations describe the dynamic behavior of a wheelset in two-point contact at the left wheel as it negotiates laterally flexible, right-handed curved track. The equations can be solved for the time histories of the following 8 independent variables: x_W, y_W, $\dot{\theta}_W$, ψ_W, F_{NZLT}, F_{NZLF}, F_{NZR}, y_{rail_R}. The left rail lateral displacement, y_{rail_L}, is a known function of the wheelset lateral excursion, y_W, according to equation (A-56). Similarly, $\dot{y}_{rail_L}$ and $\dot{y}_{rail_L}$ are given by equations (A-57).

The normal forces are determined by solving simultaneously the wheelset vertical and roll equations, the left rail lateral equation, and the two-point contact constraint relations. By manipulation of equations (A-60), (A-61), and (A-64) with (A-56) and (A-57), the normal forces at the left tread, left flange, and right wheel/rail contact patches, F_{NLT}, F_{NLF}, and F_{NR}, respectively, are:

$$\left.\begin{aligned} F_{NLT} &= \frac{\nu_{LT}}{\Delta_2} \\ F_{NLF} &= \frac{\nu_{LF}}{\Delta_2} \\ F_{NR} &= \frac{\nu_{2R}}{\Delta_2} \end{aligned}\right\} \quad \text{(A-66)}$$

where

$$\nu_{LT} = F_y^{**}\{2a\cos(\delta_{LF}+\phi_W)\cos(\delta_R-\phi_W) - r_{LF}\sin(\delta_{LF}+\phi_W)\cos(\delta_R-\phi_W)$$
$$-r_R\cos(\delta_{LF}+\phi_W)\sin(\delta_R-\phi_W)\} + F_Z^{**}\{\sin(\delta_{LF}+\phi_W)[a\cos(\delta_R-\phi_W)$$
$$-r_R\sin(\delta_R-\phi_W)]\} + M_\phi^{**}\sin(\delta_{LF}+\phi_W)\cos(\delta_R-\phi_W)$$

$$\nu_{LF} = F_y^{**}\{-2a\cos(\delta_{LT}+\phi_W)\cos(\delta_R-\phi_W)+r_{LT}\sin(\delta_{LT}+\phi_W)\cos(\delta_R-\phi_W)$$
$$+r_R\cos(\delta_{LT}+\phi_W)\sin(\delta_R-\phi_W)\} - F_Z^{**}\{\sin(\delta_{LT}+\phi_W)[a\cos(\delta_R-\phi_W)$$
$$-r_R\sin(\delta_R-\phi_W)]\} - M_\phi^{**}\sin(\delta_{LT}+\phi_W)\cos(\delta_R-\phi_W)$$

$$\nu_{2R} = F_y^{**}\{r_{LF}\cos(\delta_{LT}+\phi_W)\sin(\delta_{LF}+\phi_W)-r_{LT}\sin(\delta_{LT}+\phi_W)\cos(\delta_{LF}+\phi_W)\}$$
$$+ F_z^{**}\{a[\cos(\delta_{LT}+\phi_W)\sin(\delta_{LF}+\phi_W)-\sin(\delta_{LT}+\phi_W)\cos(\delta_{LF}+\phi_W)]$$
$$+ (r_{LF}-r_{LT})\sin(\delta_{LT}+\phi_W)\sin(\delta_{LF}+\phi_W)\} - M_\phi^{**}\{\cos(\delta_{LT}+\phi_W)\sin(\delta_{LF}+\phi_W)$$
$$-\sin(\delta_{LT}+\phi_W)\cos(\delta_{LF}+\phi_W)\}$$

and

$$\Delta_2 = [2a\cos(\delta_R-\phi_W)-r_R\sin(\delta_R-\phi_W)]\{\cos(\delta_{LT}+\phi_W)\sin(\delta_{LF}+\phi_W)$$
$$-\sin(\delta_{LT}+\phi_W)\cos(\delta_{LF}+\phi_W)\} + (r_{LF}-r_{LT})\sin(\delta_{LT}+\phi_W)\sin(\delta_{LF}+\phi_W)\cos(\delta_R-\phi_W)$$

In the expressions for δ_{LT}, δ_{LF}, and δ_{2R}, the equivalent lateral force, vertical force, and roll moment, F_y^*, F_z^*, and M_ϕ^* respectively, are:

$$F_y^{**} = -F_{CYLT} - F_{CYLF} - m_r\ddot{y}_W - c_r\dot{y}_W - k_r(y_W - y_{fc})$$

$$F_z^{**} = -F_{CZLT} - F_{CZLF} - F_{CZR} - F_{susp_{Z_W}} + \frac{W_w}{g}(\ddot{z}_W+a\ddot{\phi}_{SE}) + W_w$$

and

$$M_\phi^{**} = -a(F_{CZLT}+F_{CZLF}-F_{CZR}) - r_{LT}(F_{CYLT}-\psi_W F_{CXLT})$$
$$-r_{LF}(F_{CYLF}-\psi_W F_{CXLF}) - r_R(F_{CYR}-\psi_W F_{CXR})$$
$$-\psi_w(M_{CYLT} + M_{CYLF} + M_{CYR}) - M_{susp_{x_W}} + I_{WX}(\ddot{\phi}_W + \ddot{\phi}_{SE})$$
$$-I_{WY}\dot{\theta}_W(\dot{\psi}_W - V/R)$$

The normal forces, F_{NLT}, F_{NLF}, and F_{NR}, given by equations (A-66), are resolved into lateral and vertical components by relations similar to equations (A-18) but modified to account for a tread and flange con-

tact patch at the left.

This development assumes that two-point contact occurs at the outer or left wheel. However, two-point contact can occur at the inner or right wheel during violent curve entry and hunting conditions and during negotiation of reverse curves. The derivation of the equations of motion of a wheelset in two-point contact at the right wheel follows directly from the above analysis, and is not presented here.

A.7 Wheelset Numerical Methods

The equations of motion developed in Section A.6 describe the dynamic behavior of a wheelset negotiating flexible, curved track of variable geometry. In this section, a general method for wheelset analysis is presented which accounts for both single-point and two-point wheel/rail contact. In addition, the numerical technique to solve the wheelset equations is discussed.

Due to suspension forces and moments, the wheelset equations of motion are coupled to the vehicle equations of motion. The details of the suspension forces and moments and the vehicle equations are presented in Appendix B.

In a dynamic curving analysis the wheelset lateral dynamics are extremely important since they determine whether or not flanging occurs. The lateral dynamics are virtually decoupled from the longitudinal dynamics. As a result, wheelset longitudinal dynamics are neglected. Thus, by assumption, x_W, $\dot{x}_W$, and $\ddot{x}_W$ are zero. As an

additional benefit, this assumption eliminates a degree of freedom (for each wheelset), and reduces computer simulation time.

It is also assumed that the effective lateral mass of the rail, m_r, is zero. This is justified since the rail lateral stiffness and viscous damping forces dominate. Further, it is assumed that the influence of lateral rail velocity on lateral creepage is negligible.* British Rail [24] has suggested that this approximation is reasonable since the lateral creep force is generally saturated during flange contact.

A flowchart of a general method for wheelset analysis is shown in Figure A.11. At each time step, the single-point contact wheelset equations are solved and the solution is checked for consistency. The single-point contact solution is consistent if (1) a single-point contact wheel-rail profile is used, or (2) a two-point contact profile is used but the net excursion at the left and right wheels is not equal to the flange clearance. In the latter case, single-point tread contact occurs if the net wheelset excursion is less than the flange clearance; single-point flange contact occurs if the net excursion is greater than the flange clearance. If the solution is inconsistent, the wheelset equations appropriate for two-point contact at the left or right wheel are solved (depending whether the net excursion equals the flange clearance at the left or right wheel). By necessity, the two-point contact solution must be consistent. This implies that

*These assumptions, i.e., neglecting the rail mass and the effect of rail lateral velocity on lateral creepage, simplify the computational aspects of the dynamic curving analysis.

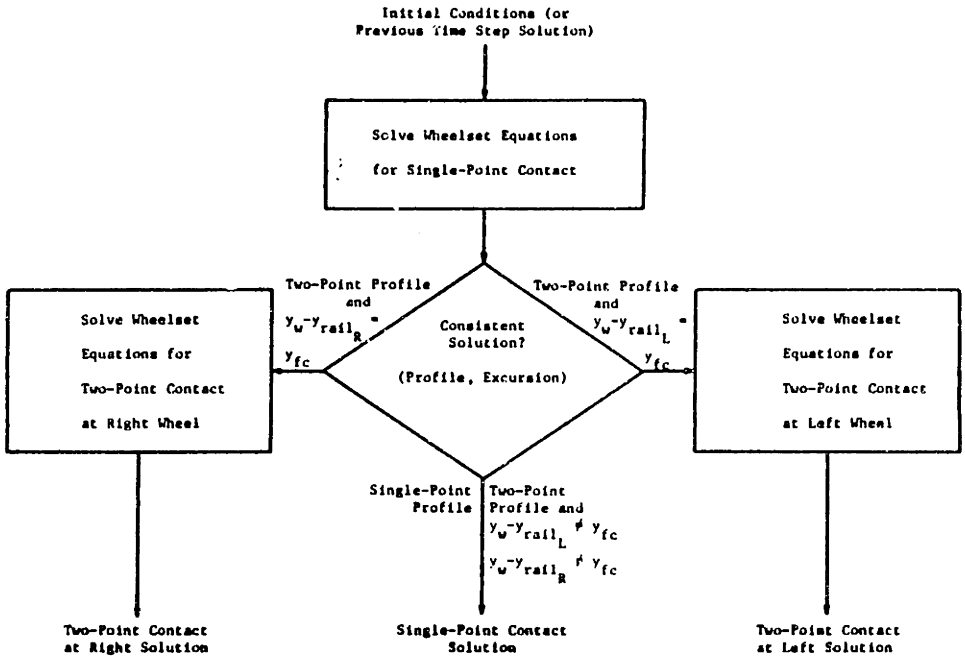

Figure A.11 Wheelset Dynamic Curving Analysis at One Time-Step

(1) the net wheelset excursion is equal to the flange clearance, and (2) two points of contact actually exist (i.e., positive normal forces act at both contact patches of the flanging wheel).

The single-point and two-point contact wheelset equations are solved via a fourth order Runge-Kutta integration algorithm. The method requires that the equations of motion are transformed to a system of first-order differential equations.

A.7.1 Single-Point Contact

For a wheelset in single-point contact, the solution approach is to solve the wheelset lateral, yaw, and spin equations and the left and right rail lateral equations for the following states:

$$\begin{aligned} X_1 &= y_W \\ X_2 &= \psi_W \\ X_3 &= \dot{\theta}_W \\ X_4 &= \dot{y}_W \\ X_5 &= \dot{\psi}_W \\ X_6 &= y_{rail_R} \\ X_7 &= y_{rail_L} \end{aligned} \qquad \text{(A-67)}$$

The seven first order differential equations of motion are:

$$\dot{X}_1 = X_4$$

$$\dot{X}_2 = X_5$$

Wheelset Spin [Equation (A-51)]

$$\dot{X}_3 = f(X_1, X_2, \ldots, X_7, \bar{F}_{susp_W}, \bar{M}_{susp_W})$$

Wheelset Lateral [Equation (A-45)]

$$\dot{X}_4 = f(X_1, X_2, \ldots, X_7, \bar{F}_{susp_W}, \bar{M}_{susp_W}) \qquad \text{(A-68)}$$

Wheelset Yaw [Equation (A-52)]

$$\dot{X}_5 = f(X_1, X_2, \ldots, X_7, \bar{F}_{susp_W}, \bar{M}_{susp_W})$$

Right Rail Lateral [Equation (A-54)]

$$\dot{X}_6 = f(X_1, X_2, \ldots, X_7, \bar{F}_{susp_W}, \bar{M}_{susp_W})$$

Left Rail Lateral [Equation (A-53)]

$$\dot{X}_7 = f(X_1, X_2, \ldots, \bar{X}_7, \bar{F}_{susp_W}, \bar{M}_{susp_W})$$

The normal forces at the left and right contact patches, F_{NL} and F_{NR}, are calculated from the wheelset vertical and roll equations according to equations (A-55). In these equations, the normal forces are given as a function of the creep forces and moments. However, the creep forces and moments depend on the normal forces. Thus, at each time step an iterative scheme is required to solve for the wheel/rail forces and moments, as shown in Figure A.12. In equations (A-55), the normal forces are also a function of the suspension forces and moments. The wheelset suspension force, $\bar{F}_{susp_W}$, and moment, $\bar{M}_{susp_W}$, couple equations (A-68) to the vehicle equations of motion and are presented in Appendix B.

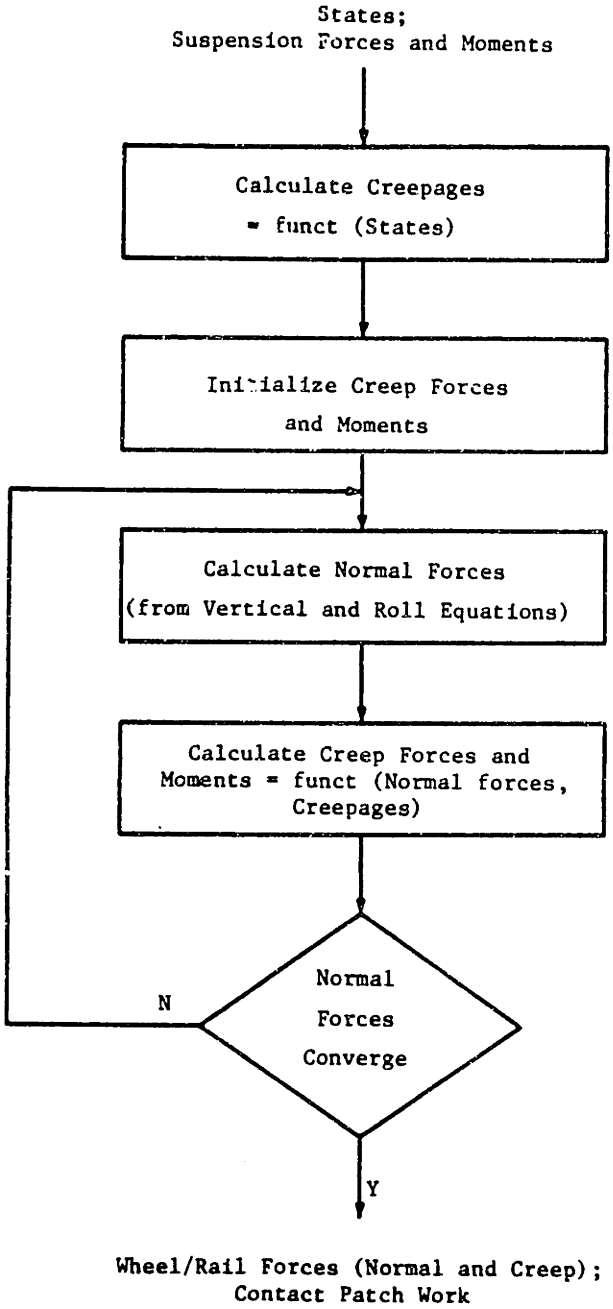

Figure A.12 Wheel/Rail Force Calculation at One Time-Step

A.7.2 Two-Point Contact

For a wheelset in two-point contact at the left wheel, states X_1 and X_7 are dependent due to the contact constraint relation (A-56). The left rail lateral displacement is a known function of the wheelset lateral displacement. In this case, six first order differential equations are written:

$$\dot{X}_1 = X_4$$

$$\dot{X}_2 = X_5$$

Wheelset Spin [Equation (A-62)]

$$\dot{X}_3 = f(X_1, X_2, \ldots, X_6, \bar{F}_{susp_W}, \bar{M}_{susp_W})$$

Wheelset Lateral [Equation (A-59)]

$$\dot{X}_4 = f(X_1, X_2, \ldots, X_6, \bar{F}_{susp_W}, \bar{M}_{susp_W})$$

Wheelset Yaw [Equation (A-63)] (A-69)

$$\dot{X}_5 = f(X_1, X_2, \ldots, X_6, \bar{F}_{susp_W}, \bar{M}_{susp_W})$$

Right Rail Lateral [Equation (A-65)]

$$\dot{X}_6 = f(X_1, X_2, \ldots, X_6, \bar{F}_{susp_W}, \bar{M}_{susp_W})$$

The wheelset vertical and roll equations and the left rail lateral equation are used to calculate the normal force at the left tread, left flange, and right contact patch, F_{NLT}, F_{NLF}, and F_{NR}, respectively, according to equations (A-65). At each time step, an iterative scheme similar to the method shown in Figure A.12 is used. The left rail

lateral displacement, velocity, and acceleration are specified by equations (A-56) and (A-57). Equations (A-69) are coupled to the vehicle equations of motion by the wheelset suspension force and moment, $\bar{F}_{susp_W}$ and $\bar{M}_{susp_W}$, respectively. These are discussed in Appendix B.

Equations (A-68) are appropriate for a wheelset in single-point contact at the left and right wheels; equations (A-69) are appropriate for a wheelset in two-point contact at the left wheel (and single-point contact at the right wheel). Following a parallel derivation, equations of motion similar to equations (A-69) can be written for a wheelset in two-point contact at the right wheel. In such a case, states X_1 and X_6 are dependent.

Equations (A-68), (A-69), and the equations for a wheelset in two-point contact at the right wheel represent sets of coupled, scalar, first order differential equations which characterize the behavior of a wheelset as it traverses flexible, curved track. These governing equations represent a system of 7 states: 5 states for the wheelset and 2 states for the rails. The wheelset has 2 states (i.e., 1 degree of freedom) to describe its lateral and yaw motions, as well as a state to represent its spin speed. Each rail has a state to describe its lateral deflection. When two-point contact occurs, the state of the rail at the flanging wheel is known due to a constraint relation which exists between the wheelset and rail lateral displacements.

APPENDIX B

DYNAMIC CURVING EQUATIONS OF MOTION OF A RAIL VEHICLE MODEL

B.1 Introduction

In this Appendix, the dynamic curving equations of motion of a rail vehicle model are developed. The vehicle model is shown schematically in Figure B.1. The vehicle model incorporates the nonlinear wheelset model described in Appendix A. In addition, it includes a generic truck model that can represent arbitrary interconnections between the wheelsets, truck frames, bolsters, and carbody. Thus, conventional, self-steered radial, and forced-steered radial truck configurations can be modelled. In addition to the wheel/rail nonlinearities of the wheelset model, nonlinear suspension effects are included in the vehicle model.

B.2 Coordinate Systems

The front and rear truck frames, the front and rear bolsters, and the carbody are assumed to be rigid bodies. For each rigid body, a "body-fixed" coordinate system is established, consisting of mutually-perpendicular, right-handed axes x, y, z with corresponding unit vectors $\hat{i}$, $\hat{j}$, $\hat{k}$. The x, y, and z axes denote the longitudinal, lateral, and vertical directions, respectively. The axes of each coordinate system are aligned with the principal directions (i.e., in the directions of the principal mass moments of inertia) and the origin of each system is located at the center of mass.

Figure B.2 shows the following "body-fixed" coordinate systems: "F1" and "F2" for the front and rear truck frames, respectively; "B1"

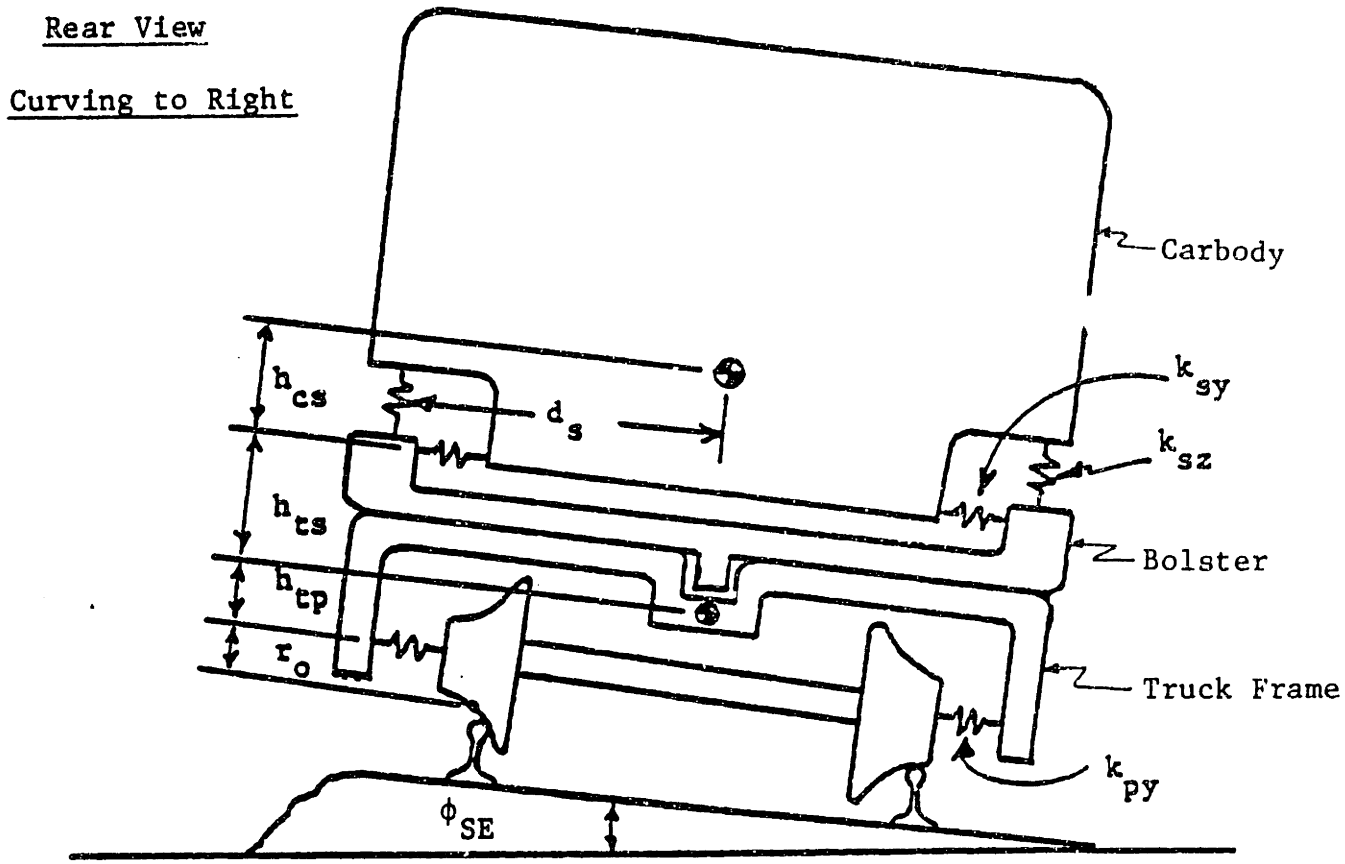

Figure B.1 Rail Vehicle Model During Curving, Rear View

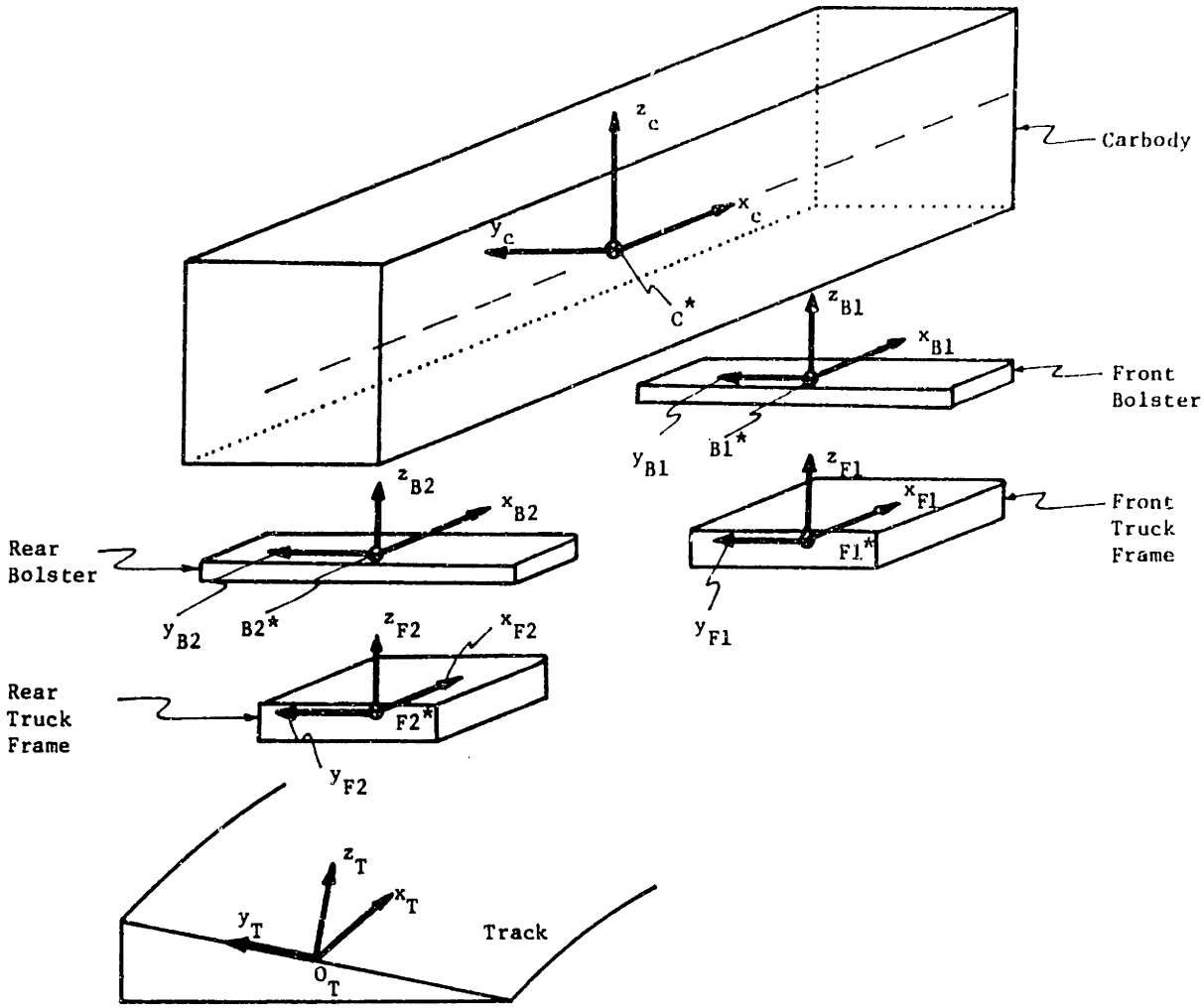

Figure B.2 Rail Vehicle Model Coordinate Systems

and "B2" for the front and rear bolsters, repectively; and "C" for the carbody. The centers of mass are denoted with asterisks. Figure B.2 also shows the track coordinate system, "T". This system moves along the superelevated track centerline with tangential speed V, as described in Appendix A (Section A.2).

In addition to "body-fixed" coordinate systems, intermediate coordinate systems are used to define the orientation of each rigid body. Table B.1 summarizes the coordinate systems used in the analysis. (For simplicity, the table does not list separate coordinate systems for the front and rear trucks and bolsters. System "F" represents "F1" for the front truck and "F2" for the rear truck, etc.) Coordinate systems "3" and "4" are intermediate systems used to define the orientation of the truck frame and carbody, respectively.

TABLE B.1 COORDINATE SYSTEMS

T	Track
3	"Intermediate" Truck Frame (Yaws with Truck Frame)
F	Truck Frame (Yaws and Rolls with Truck Frame)
B	Bolster (Yaws with Bolster)
4	"Intermediate" Carbody (Yaws with Carbody)
C	Carbody (Yaws and Rolls with Carbody)

Figures B.3, B.4, and B.5 show the coordinate system rotations and the corresponding transformation relations used to define the

"T" → "3"

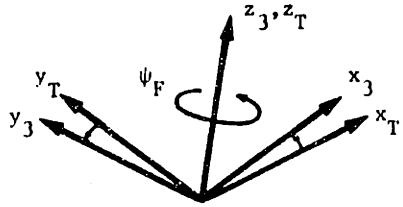

Yaw Angle, ψ_F

$$\underline{\omega}^{T_3} = \dot{\psi}_F \hat{k}_3$$

$$\begin{Bmatrix} \hat{i}_3 \\ \hat{j}_3 \\ \hat{k}_3 \end{Bmatrix} = \underbrace{\begin{bmatrix} c\psi_F & s\psi_F & 0 \\ -s\psi_F & c\psi_F & 0 \\ 0 & 0 & 1 \end{bmatrix}}_{C_{3/T}} \begin{Bmatrix} \hat{i}_T \\ \hat{j}_T \\ \hat{k}_T \end{Bmatrix}$$

"T" Track

"3" Yaws with Truck

"3" → "F"

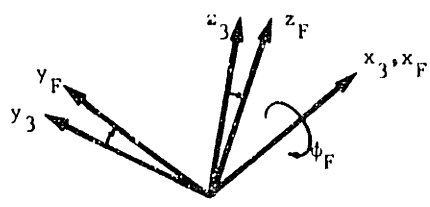

Roll Angle, ϕ_F

$$\underline{\omega}^{3_F} = \dot{\phi}_F \hat{i}_F$$

$$\begin{Bmatrix} \hat{i}_F \\ \hat{j}_F \\ \hat{k}_F \end{Bmatrix} = \underbrace{\begin{bmatrix} 1 & 0 & 0 \\ 0 & c\phi_F & s\phi_F \\ 0 & -s\phi_F & -s\phi_F \end{bmatrix}}_{C_{F/3}} \begin{Bmatrix} \hat{i}_3 \\ \hat{j}_3 \\ \hat{k}_3 \end{Bmatrix}$$

"F" Truck Frame

(Yaws and Rolls Relative to Track)

The following notation is used: $s\alpha = \sin(\alpha)$, $c\alpha = \cos(\alpha)$

Figure B.3 Definition of Truck Frame Orientation (Rotation Only)

"F" → "B"

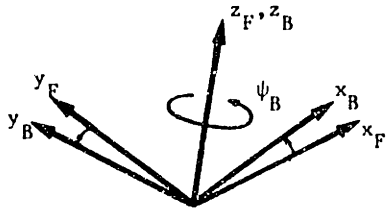

Yaw Angle, ψ_B

$$\overline{\omega}^{F_B} = \dot{\psi}_B \hat{k}_B$$

$$\begin{Bmatrix} \hat{i}_B \\ \hat{j}_B \\ \hat{k}_B \end{Bmatrix} = \underbrace{\begin{bmatrix} c\psi_B & s\psi_B & 0 \\ -s\psi_B & c\psi_B & 0 \\ 0 & 0 & 1 \end{bmatrix}}_{C_{B/F}} \begin{Bmatrix} \hat{i}_F \\ \hat{j}_F \\ \hat{k}_F \end{Bmatrix}$$

"F" Truck Frame

"B" Bolster
(Yaws with Bolster)

The following notation is used: $s\alpha = \sin(\alpha)$, $c\alpha = \cos(\alpha)$

Figure B.4 Definition of Bolster Orientation (Rotation Only)

"T" → "4"

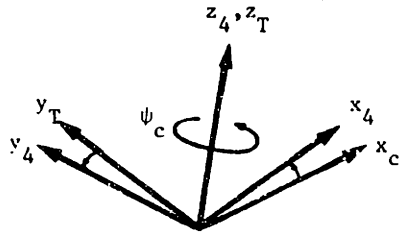

Yaw Angle, ψ_c

$$\underline{\omega}^{T_4} = \dot{\psi}_c \hat{k}_4$$

$$\begin{Bmatrix} \hat{i}_4 \\ \hat{j}_4 \\ \hat{k}_4 \end{Bmatrix} = \underbrace{\begin{bmatrix} c\psi_c & s\psi_c & 0 \\ -s\psi_c & c\psi_c & 0 \\ 0 & 0 & 1 \end{bmatrix}}_{C_{4/T}} \begin{Bmatrix} \hat{i}_T \\ \hat{j}_T \\ \hat{k}_T \end{Bmatrix}$$

"T" Track

"4" Yaws with Carbody

"4" → "C"

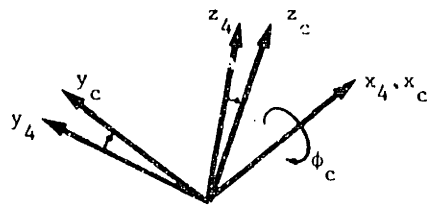

Roll Angle, ϕ_c

$$\underline{\omega}^{4_c} = \dot{\phi}_c \hat{i}_c$$

$$\begin{Bmatrix} \hat{i}_c \\ \hat{j}_c \\ \hat{k}_c \end{Bmatrix} = \underbrace{\begin{bmatrix} 1 & 0 & 0 \\ 0 & c\phi_c & s\phi_c \\ 0 & -s\phi_c & c\phi_c \end{bmatrix}}_{C_{c/4}} \begin{Bmatrix} \hat{i}_4 \\ \hat{j}_4 \\ \hat{k}_4 \end{Bmatrix}$$

"C" Carbody

(Yaws and Rolls Relative to Track)

The following notation is used: $s\alpha = \sin(\alpha)$, $c\alpha = \cos(\alpha)$

Figure B.5 Definition of Carbody Orientation (Rotation Only)

orientation of the truck frame, bolster, and carbody, respectively. The orientation of the truck frame and carbody is specified relative to the track coordinate system by yaw and roll angles. The sequence of rotations for the truck frame and carbody is yaw displacement about the z_T axis followed by roll displacement about the rotated x_T axis. The orientation of the bolster is specified relative to the truck frame by a yaw angle about the z_F axis. It is assumed that the truck frame, bolster, and carbody do not pitch and thus rotations about the rotated y_T axis are neglected.

As discussed in Section A.2, transformation relations for multiple rotations are obtained by matrix multiplication. Performing the multiplication and assuming small angles gives the following relation between the truck frame and track systems.

$$\begin{Bmatrix} \hat{i}_F \\ \hat{j}_F \\ \hat{k}_F \end{Bmatrix} = \begin{bmatrix} 1 & \psi_F & 0 \\ -\psi_F & 1 & \frac{1}{2}(\phi_{W1}+\phi_{W2}) \\ 0 & -\frac{1}{2}(\phi_{W1}+\phi_{W2}) & 1 \end{bmatrix} \begin{Bmatrix} \hat{i}_T \\ \hat{j}_T \\ \hat{k}_T \end{Bmatrix} \qquad \text{(B-1)}$$

where the truck frame roll angle is assumed to be the average of the leading and trailing wheelset roll angles, ϕ_{W1} and ϕ_{W2}. (For analysis of the rear truck, angles ϕ_{W1} and ϕ_{W2} correspond to ϕ_{W3} and ϕ_{W4}, respectively,) Similarly, the relation between the bolster and track systems is:

$$\begin{Bmatrix} \hat{i}_B \\ \hat{j}_B \\ \hat{k}_B \end{Bmatrix} = \begin{bmatrix} 1 & \psi_B & 0 \\ -\psi_B & 1 & \frac{1}{2}(\phi_{W1}+\phi_{W2}) \\ 0 & -\frac{1}{2}(\phi_{W1}+\phi_{W2}) & 1 \end{bmatrix} \begin{Bmatrix} \hat{i}_T \\ \hat{j}_T \\ \hat{k}_T \end{Bmatrix} \qquad \text{(B-2)}$$

since the bolster rolls with the truck frame. The transformation relation between the carbody and track systems for small yaw and roll angles is:

$$\begin{Bmatrix} \hat{i}_C \\ j_C \\ \hat{k}_C \end{Bmatrix} = \begin{bmatrix} 1 & \psi_C & 0 \\ -\psi_C & 1 & \phi_C \\ 0 & -\phi_C & 1 \end{bmatrix} \begin{Bmatrix} \hat{i}_T \\ \hat{j}_T \\ \hat{k}_T \end{Bmatrix} \qquad \text{(B-3)}$$

B.3 Acceleration of Center of Mass

The inertial acceleration of the center of mass of the truck, bolster, carbody, or any rigid body Q with center of mass Q^* moving along the track is defined by:

$$\begin{aligned} \underset{a}{I}\underline{Q}^* &= \underset{a}{I}\underline{O}_T + \underset{r}{T}\ddot{\underline{Q}}^*/O_T + \underset{\omega}{I}\underline{T} \times \underline{\dot{r}}^*/O_T \\ &\quad + \underset{\omega}{I}\underline{T} \times \left(\underset{\omega}{I}\underline{T} \times \underline{r}^*/O_T \right) + 2 \underset{\omega}{I}\underline{T} \times \underset{r}{T}\underline{\dot{Q}}^* O_T \end{aligned} \qquad \text{(B-4)}$$

where $\underset{a}{I}\underline{O}_T$ is the inertial acceleration of point O_T given by equation (A-7), $\underset{\omega}{I}\underline{T}$ is the angular velocity of the "T" system relative to the "I" system given by equation (A-8), and $\underline{r}^*/O_T$ is the displacement vector from O_T to Q^*.

B.3.1 Acceleration of Truck Frame/Bolster Center of Mass

The displacement of the center of mass of the truck frame, F^*, relative to point O_T is $\bar{r}^{F^*/O_T}$ given by:

$$\bar{r}^{F^*/O_T} = x_F\hat{i}_T + y_F\hat{j}_T + (z_F + r_o + h_{tp})\hat{k}_T \tag{B-5}$$

where x_F, y_F, and z_F represent small longitudinal, lateral, and vertical displacements, respectively, of the truck frame center of mass. Substituting equation (B-5) into (B-4) and setting $Q^* = F^*$ gives the acceleration of the center of mass of the truck frame:

$$\bar{a}^{F^*} = [\ddot{x}_F + \dot{V}]\hat{i}_T + [\ddot{y}_F - (r_o + h_{tp})\ddot{\phi}_{SE} - \frac{V^2}{R}]\hat{j}_T + [\ddot{z}_F + a\ddot{\phi}_{SE} + \frac{V^2}{R}\phi_{SE}]\hat{k}_T \tag{B-6}$$

It is assumed that the only relative displacement between the truck frame and bolster is yaw rotation. In translation, the truck frame and bolster execute the same motions. Thus, the acceleration of the center of mass of the bolster is given by equation (B-6). (This assumes that the vertical distance between the centers of mass of the truck frame and bolster is small relative to $(r_o + h_{tp})$.

B.3.2 Acceleration of Carbody Center of Mass

The displacement of the center of mass of the carbody, C^*, from point O_T, denoted by $\bar{r}^{C^*/O_T}$, is

$$\bar{r}^{C^*/O_T} = x_C\hat{i}_T + y_C\hat{j}_T + (z_C + r_o + h_{tp} + h_{ts} + h_{cs})\hat{k}_T \tag{B-7}$$

where x_C, y_C, and z_C represent small longitudinal, lateral, and verti-

cal carbody displacements, respectively. Substituting into equation (B-4) with $Q^* = C^*$ yields the acceleration of the center of mass of the carbody:

$$\underline{a}^{C^*} = [\ddot{x}_C + \dot{V}]\hat{i}_T + [\ddot{y}_C - (r_o+h_{tp}+h_{ts}+h_{cs})\ddot{\phi}_{SE} - \frac{V^2}{R}]\hat{j}_T$$

$$+ [\ddot{z}_C + a\ddot{\phi}_{SE} + \frac{V^2}{R}\phi_{SE}]\hat{k}_T \qquad \text{(B-8)}$$

B.4 Rate of Angular Momentum

B.4.1 Rate of Angular Momentum of Truck Frame and Bolster

The angular velocity of the truck frame, "F", in inertial space "I" is:

$$\underline{\omega}^{F} = -\frac{V}{R}\hat{k}_H + \dot{\phi}_{SE}i_T + \dot{\psi}_F\hat{k}_3 + \frac{1}{2}(\dot{\phi}_{W1}+\dot{\phi}_{W2})\hat{i}_F \qquad \text{(B-9)}$$

Assuming small angles, equation (B-9) is equivalent to

$$\underline{\omega}^{F} = \omega_{FX}\hat{i}_F + \omega_{FZ}\hat{k}_F \qquad \text{(B-10)}$$

by transformation where the components are

$$\left.\begin{aligned}\omega_{FX} &= \dot{\phi}_{SE} + \frac{1}{2}(\dot{\phi}_{W1} + \dot{\phi}_{W2}) \\ \omega_{FZ} &= \dot{\psi}_F - \frac{V}{R}.\end{aligned}\right\} \qquad \text{(B-11)}$$

The angular momentum of the truck frame about its center of mass is given by

$$\bar{H}^{F/F^*} = I_{FX}\omega_{FX}\hat{i}_F + I_{FZ}\omega_{FZ}\hat{k}_F \qquad \text{(B-12)}$$

where I_{FX} and I_{FZ} are the roll and yaw principal mass moments of inertia of the truck frame, respectively.

The inertial time rate of change of angular momentum is expressed by:

$$\underline{\underline{H}}^{I\bullet F/F^*} = \underline{\underline{H}}^{F\bullet F/F^*} + \underline{\omega}^{IF} \times \underline{\underline{H}}^{F/F^*} \tag{B-13}$$

where $\underline{\underline{H}}^{I\bullet F/F^*}$ and $\underline{\underline{H}}^{F\bullet F/F^*}$ are the time rates of change (i.e., first derivatives) of the angular momentum in the "I" and "F" systems, respectively. Substituting equations (B-10), (B-11), and (B-12) into (B-13) and neglecting smaller order terms gives the inertial time rate of change of angular momentum of the truck frame:

$$\begin{aligned}\underline{\underline{H}}^{I\bullet F/F^*} &= [I_{FX}\{\ddot{\phi}_{SE} + \tfrac{1}{2}(\ddot{\phi}_{W1} + \ddot{\phi}_{W2})\}]\hat{i}_F \\ &+ [I_{FZ}\{\ddot{\psi}_F - \frac{\dot{V}}{R} - V(\dot{1/R})\}]\hat{k}_F\end{aligned} \tag{B-14}$$

By parallel arguments, the inertial time rate of change of angular momentum of the bolster is:

$$\begin{aligned}\underline{\underline{H}}^{I\bullet B/B^*} &= [I_{BX}\{\ddot{\phi}_{SE} + \tfrac{1}{2}(\ddot{\phi}_{W1} + \ddot{\phi}_{W2})\}]\hat{i}_B \\ &+ [I_{BZ}\{\ddot{\psi}_B - \frac{\dot{V}}{R} - V(1/R)\}]\hat{k}_B\end{aligned} \tag{B-15}$$

where small angles have been assumed and smaller order terms have been neglected.

B.4.2 Rate of Angular Momentum of Carbody

The angular velocity of the carbody "C" with respect to inertial space "I" is:

$$\underline{\omega}^{IC} = -\frac{V}{R}\hat{k}_H + \dot{\phi}_{SE}\hat{i}_T + \dot{\psi}_C\hat{k}_4 + \dot{\phi}_C\hat{k}_C \tag{B-16}$$

In carbody coordinates, equation (B-16) is equivalent to:

$$\underline{\omega}^{I\underline{C}} = (\dot{\phi}_{SE} + \dot{\phi}_C)\hat{i}_C + (\dot{\psi}_C - \frac{V}{R})\hat{k}_C \tag{B-17}$$

where smaller order terms have been neglected. The inertial times rate of change of angular momentum of the carbody is derived by following a development similar to the derivation in Section B.4.1 for the truck frame. The result is:

$$\underline{H}^{\underline{\cdot}C/C^*} = [I_{CX}(\ddot{\phi}_{SE} + \ddot{\phi}_C)]\hat{i}_c + [I_{CZ}\{\ddot{\psi}_C - \dot{V}/R - V(1/R)^{\cdot}\}]\hat{k}_c \tag{B-18}$$

where I_{CX} and I_{CZ} are the roll and yaw principal mass moments of inertia of the carbody, respectively. In deriving equation (B-16), small angles have been assumed and smaller order terms have been neglected.

B.5 Forces and Moments

This section focuses on the internal suspension forces and moments acting on the wheelsets, trucks, bolsters, and carbody of the rail vehicle model shown in Figure B.1. The vehicle model incorporates a generic truck model capable of representing conventional, self-steered radial, and several forced-steered radial truck designs.

A schematic of the generic truck model is shown in Figure B.6. The geometric offsets, $\Delta\psi_1$, $\Delta\psi_2$, Δy_1, Δy_2, represent the effects of forced-steering linkages and are given by the following steering relations.

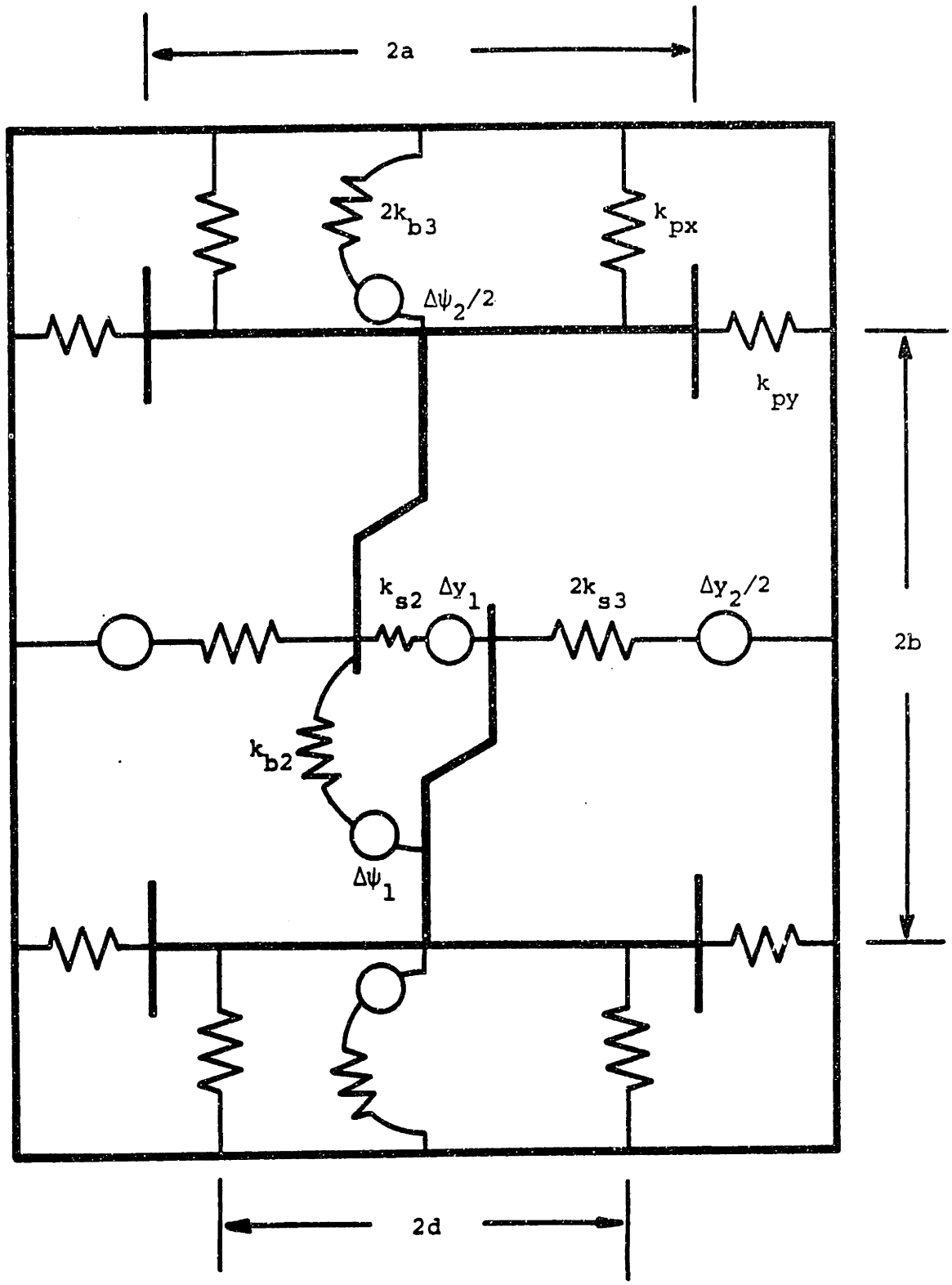

Figure B.6 Generic Truck Model

Yaw Offset Relation

$$\Delta\psi_1 = \Delta\psi_2 = \pm 2G_1\left(\frac{\psi_{W1} + \psi_{W2}}{2} - \psi_B\right) \pm 2G_2\left(\frac{y_{W1} - y_{W2}}{2b} - \psi_B\right)$$
$$\pm 2G_3\left(\frac{y_{W1} + y_{W2}}{2} - y_F\right) \pm 2G_4(\psi_F - \psi_B)$$
$$\pm 2G_5\left(\frac{\psi_{W1} + \psi_{W2}}{2} - \psi_F\right) \pm 2G_6\left(\frac{y_{W1} - y_{W2}}{2b} - \psi_F\right) \quad \text{(B-19)}$$

Lateral Offset Relation

$$\Delta y_1 = \Delta y_2 = 2H_1\left(\frac{y_{W1} + y_{W2}}{2} - y_C\right) + 2H_2(y_F - y_C) + 2H_3\left(\frac{y_{W1} + y_{W2}}{2} - y_F\right) \quad \text{(B-20)}$$

The G_i's in equation (B-19) are curvature steering gains and the H_i's in equation (B-20) are cant deficient steering gains. The suspension system of the generic truck model produces suspension forces and moments which act on the wheelsets, truck frame, bolster, and carbody. Expressions for the suspension forces and moments due to the steering linkages are derived in [46].

B.5.1 Wheelset Suspension Forces and Moments

Suspension forces and moments act on each wheelset due to primary longitudinal and lateral suspension elements, self-steered and forced-steered linkages, and loads carried from above. Figure B.7 shows the lateral and vertical suspension forces, $F_{suspy_{wi}}$ and $F_{suspz_{wi}}$, and the equivalent roll and yaw suspension moments, $M_{suspx_{wi}}$ and $M_{suspz_{wi}}$, respectively, acting on wheelset i. In this analysis, the longitudinal suspension force, $F_{suspx_{wi}}$, is zero since the analysis neglects the wheelset longitudinal degree of freedom. The spin sus-

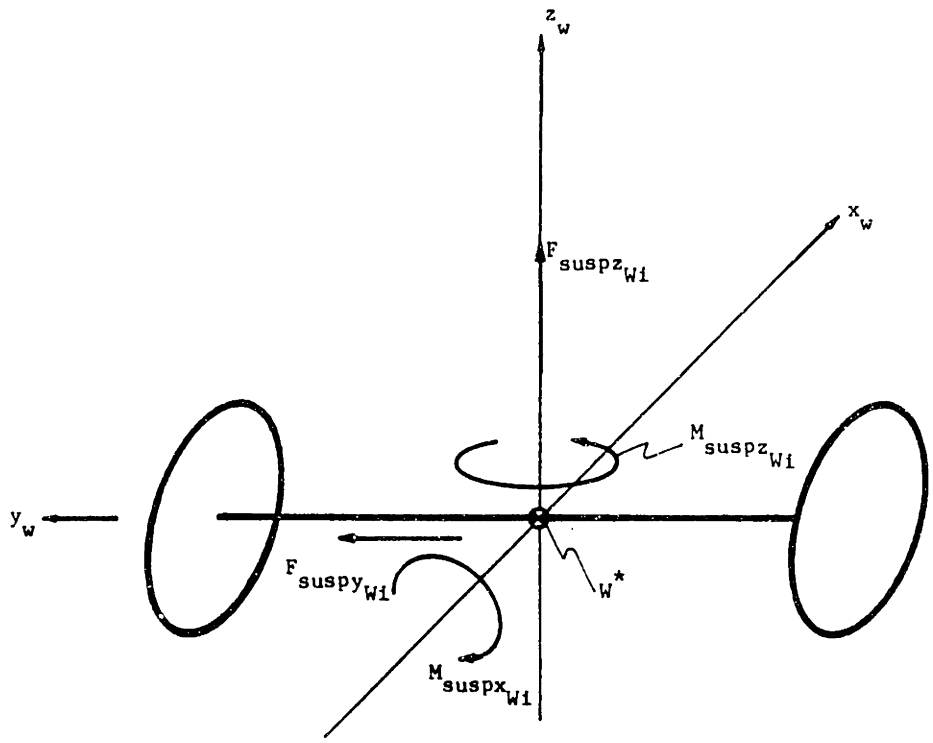

Figure B.7 Suspension Forces and Moments Acting on Wheelset i

sion moment, $M_{suspy_{wi}}$, is also zero since no moments develop about the spin axis due to suspension components.

The lateral suspension force, $F_{suspy_{wi}}$, and yaw suspension moment, $M_{suspy_{wi}}$, acting on the leading wheelset of the front and rear trucks are given by the expressions below.

Leading Wheelset Lateral (i = 1 Front Truck;
i = 3 Rear Truck)

$$F_{suspy_{wi}} = [-2k_{py} - \{G_3 \pm (\frac{G_2+G_6}{b})\}^2 (k_{b2}+k_{b3}) - (H_1-H_3+1)^2 (k_{s2}+k_{s3}) - k_{s3}] y_{w1}$$

$$+ [\{G_3 \pm (\frac{G_2+G_6}{b})\} \{1 \mp (G_1+G_5)\} (k_{b2}+k_{b3}) + b(H_1+H_3+1)(k_{s2}+k_{s3})$$

$$+ bk_{s3}] (\psi_{w1} - \frac{b}{R})$$

$$+ [-\{G_3^2 - (\frac{G_2+G_6}{b})\}^2 (k_{b2}+k_{b3}) - \{(H_1+H_3)^2 - 1\} (k_{s2}+k_{s3}) - k_{s3}] y_{w2}$$

$$+ [\{-G_3 \mp (\frac{G_2+G_6}{b})\} \{1 \pm (G_1+G_5)\} (k_{b2}+k_{b3}) + b(H_1+H_3+1)(k_{s2}+k_{s3})$$

$$- bk_{s3}] (\psi_{w2} + \frac{b}{R})$$

$$+ [2k_{py} + 2G_3 \{G_3 \pm (\frac{G_2+G_6}{b})\} (k_{b2}+k_{b3}) - 2(H_2-H_3)(H_1+H_3+1)(k_{s2}+k_{s3})$$

$$+ 2k_{s3}] y_F$$

$$+ [2bk_{py} + 2(G_4-G_5-G_6) \{\mp G_3 - (\frac{G_2+G_6}{b})\} (k_{b2}+k_{b3})] \psi_F$$

$$+ [2(G_1+G_2+G_4) \{\pm G_3 + (\frac{G_2+G_6}{b})\} (k_{b2}+k_{b3})] \psi_B$$

$$+[2(H_1+H_2)(H_1+H_3+1)(k_{s2}+k_{s3})]y_c$$

$$+[-2C_{py}-(C_{s2}+2C_{s3})]2\dot{y}_{w1}+[b(C_{s2}+2C_{s3})](\dot{\psi}_{w1}-b(1/\dot{R}))$$

$$+[C_{s2}]\dot{y}_{w2}+[bC_{s2}](\dot{\psi}_{w2}+b(1/\dot{R}))$$

$$+[2C_{py}+2C_{s3}]\dot{y}_F+[2bC_{py}]\dot{\psi}_F \qquad \text{(B-21)}$$

Leading Wheelset Yaw (i = 1 Front Truck; i = 3 Rear Truck)

$$M_{suspz_{wi}} = [\{G_3 \pm (\frac{G_2+G_6}{b})\}\{1 \mp (G_1+G_5)\}(k_{b2}+k_{b3})$$

$$+b(H_1+H_3+1)(k_{s2}+k_{s3})+bk_{s3}]y_{w1}$$

$$+[-2d_p^2k_{px}-(G_1+G_5 \mp 1)^2(k_{b2}+k_{b3})-b^2(k_{s2}+k_{s3})$$

$$-k_{b3}-b^2k_{s3}](\psi_{w1}-\frac{b}{R})$$

$$+[\{G_3 \mp (\frac{G_2+G_6}{b})\}\{1 \mp (G_1+G_5)\}(k_{b2}+k_{b3})$$

$$+b(H_1+H_3-1)(k_{s2}+k_{s3})+bk_{s3}]y_{w2}$$

$$+[\{1-(G_1+G_5)^2\}(k_{b2}+k_{b3})-b^2(k_{s2}+k_{s3})$$

$$-k_{b3}+b^2k_{s3}](\psi_{w2}+\frac{b}{R})$$

$$+[2G_3\{-1 \pm (G_1+G_5)\}(k_{b2}+k_{b3})+2b(H_2-H_3)(k_{s2}+k_{s3})-2bk_{s3}]y_F$$

$$+[2d_p^2k_{px}+2(G_4-G_5-G_6)\{\pm 1-(G_1+G_5)\}(k_{b2}+k_{b3})+2k_{b3}]\psi_F$$

$$+[2(G_1+G_2+G_4)(G_1+G_5\mp1)(k_{b2}+k_{b3})]\psi_B$$

$$+[-2b(H_1+H_2)(k_{s2}+k_{s3})]y_c$$

$$+[b(C_{s2}+2C_{s3})]\dot{y}_{w1} + [-2d_p^2C_{px}-C_{b2}-2C_{b3}-b^2(C_{s2}+2C_{s3})](\dot{\psi}_{w1}-b(1/R))$$

$$+[-bC_{s2}]\dot{y}_{w2} + [C_{b2}-b^2C_{s2}](\dot{\psi}_{w2} + b(1/\dot{R}))$$

$$+[-2bC_{s3}]\dot{y}_F + [2d_p^2C_{px} + 2C_{b3}]\dot{\psi}_F \qquad \text{(B-22)}$$

In these equations, as well as the equations that follow, the notation $\mp$ implies + for the front truck and - for the rear truck. Also, y_{w1} and y_{w2} represent the lateral excursions of the leading and trailing wheelsets of the truck, respectively, ψ_{w1} and ψ_{w2} denote the yaw angles of the leading and trailing wheelsets, respectively. For analysis of the rear truck, y_{w1}, y_{w2}, ψ_{w1}, and ψ_{w2} correspond to y_{w3}, y_{w4}, ψ_{w3}, and ψ_{w4}, respectively.

Due to the suspension arrangement, a lateral force, $F_{suspy_{wi}}$, and a yaw moment, $M_{suspz_{wi}}$, act on the trailing wheelsets of the front and rear trucks.

Trailing Wheelset Lateral (i = 2 Front Truck;
i = 4 Rear Truck)

$$F_{suspy_{wi}} = \left[-\left|G_3^2-\left(\frac{G_2+G_6}{b}\right)^2\right|(k_{b2}+k_{b3})-\left|(H_1+H_3)^2-1\right|(k_{s2}+k_{s3})-k_{s3}\right]y_{w1}$$

$$+\left[\left|G_3\mp\left(\frac{G_2+G_6}{b}\right)\right|\left|1\mp(G_1+G_5)\right|(k_{b2}+k_{b3})\right.$$

$$+b(H_1+H_3-1)(k_{s2}+k_{s2})+bk_{s3}](\psi_{w1} - \frac{b}{R})$$

$$+[-2k_{py}-\left\{G_3\mp(\frac{G_2+G_6}{b})\right\}^2(k_{b2}+k_{b3})-(H_1+H_3-1)^2(k_{s2}+k_{s3})-k_{s3}]y_{w2}$$

$$+[\left\{-G_3\pm(\frac{G_2+G_6}{b})\right\}\left\{1\pm(G_1+G_5)\right\}(k_{b2}+k_{b3})$$

$$+b(H_1+H_3-1)(k_{s2}+k_{s3})-bk_{s3}](\psi_{w2} + \frac{b}{R})$$

$$+[2k_{py}+2G_3\left\{G_3\mp(\frac{G_2+G_6}{b})\right\}(k_{b2}+k_{b3})$$

$$-2(H_2-H_3)(H_1+H_3-1)(k_{s2}+k_{s3})+2k_{s3}]y_F$$

$$+[-2k_{py}b+2(G_4-G_5-G_6)\left\{\mp G_3+(\frac{G_2+G_6}{b})\right\}(k_{b2}+k_{b3})]\psi_F$$

$$+[2(G_1+G_2+G_4)\left\{\pm G_3-(\frac{G_2+G_6}{b})\right\}(k_{b2}+k_{b3})]\psi_B$$

$$+[2(H_1+H_2)(H_1+H_3-1)(k_{s2}+k_{s3})]y_c$$

$$+[C_{s2}]\dot{y}_{w1} \qquad +[-bC_{s2}](\dot{\psi}_{w1} - b(1/\dot{R}))$$

$$+[-2C_{py}-(C_{s2}+2C_{s3})]\dot{y}_{w2} + [-b(C_{s2}+2C_{s3})](\dot{\psi}_{w2}+b(1/\dot{R}))$$

$$+[2C_{py}+2C_{s3}]\dot{y}_F \qquad + [-2bC_{py}]\dot{\psi}_F \qquad \text{(B-23)}$$

Trailing Wheelset Yaw (i = 2 Front Truck;
i = 4 Rear Truck)

$$M_{suspz_{wi}} = [\left\{-G_3\mp(\frac{G_2+G_6}{b})\right\}\left\{1\pm(G_1+G_5)\right\}(k_{b2}+k_{b3})$$

$$+b(H_1+H_3+1)(k_{s2}+k_{s3})-bk_{s3}]y_{w1}$$

$$+[\{1-(G_1+G_5)^2\}(k_{b2}+k_{b3})-b^2(k_{s2}+k_{s3})-k_{b3}-b^2k_{s3}](\psi_{w1}-\frac{b}{R})$$

$$+[\{-G_3\pm(\frac{G_2+G_6}{b})\}\{1\pm(G_1+G_5)\}(k_{b2}+k_{b3})$$

$$+b(H_1+H_3-1)(k_{s2}+k_{s3})-bk_{s3}]y_{w2}$$

$$+[-2d_p^2k_{px}-\{1\pm(G_1+G_5)\}^2(k_{b2}+k_{b3})-b^2(k_{s2}+k_{s3})$$

$$-k_{b3}-b^2k_{s3}](\psi_{w2}+\frac{b}{R})$$

$$+[2G_3\{1\pm(G_1+G_5)\}(k_{b2}+k_{b3})+2b(H_2-H_3)(k_{s2}+k_{s3})+2bk_{s3}]y_F$$

$$+[2d_p^2k_{px}+2(G_4-G_5-G_6)\{\mp1-(G_1+G_5)\}(k_{b2}+k_{b3})+2k_{b3})\psi_F$$

$$+[2(G_1+G_2+G_4)(G_1+G_5\pm1)(k_{b2}+k_{b3})]\psi_B$$

$$+[-2b(H_1+H_2)(k_{s2}+k_{s3})]y_c$$

$$+[bC_{s2}]\dot{y}_{w1} \qquad +[C_{b2}-b^2C_{s2}](\dot{\psi}_{w1}-b(1/R))$$

$$+[-b(C_{s2}+2C_{s3})]\dot{y}_{w2}+[-2d_p^2C_{px}-\{C_{b2}+2C_{b3}+b^2(C_{s2}+2C_{s3})\}](\dot{\psi}_{w2}+b(1/R))$$

$$+[2bC_{s3}]\dot{y}_F + [2d_p^2C_{px} + 2C_{b3}]\dot{\psi}_F \qquad \text{(B-24)}$$

The vertical suspension force, $F_{suspz_{wi}}$, is equal to the load carried vertically by the leading and trailing wheelsets, i.e.,

$$F_{suspz_{wi}} = -[\frac{1}{2}(W_F+W_B)+\frac{1}{4}W_C], \qquad i = 1,2,3,4. \qquad (B-25)$$

The roll suspension moment, $M_{suspx_{wi}}$, is due to the truck frame, bolster, and carbody weights as follows.

$$M_{suspx_{wi}} = -\frac{1}{2}(W_F+W_B)[\phi_d = \frac{1}{2}(\phi_{w1}+\phi_{w2})]h_{tp}$$

$$-\frac{1}{4}W_c[\phi_d-\phi_c](h_{cs}+h_{ts}+h_{tp})$$

$$-\frac{1}{2}(W_F+W_B)[y_F+\frac{b^2}{R}-y_{wi}]$$

$$-\frac{1}{4}W_c(y_c+\frac{\ell_s^2}{R}-y_{wi}), \quad i = 1,2,3,4. \qquad (B-26)$$

In equation (B-25) and (B-26), i = 1,2 for the leading, trailing wheelsets of the front truck, and i = 3,4 for the leading, trailing wheelsets of the rear truck. For analysis of the rear truck, ϕ_{w1} and ϕ_{w2} in equation (B-26) correspond to ϕ_{w3} and ϕ_{w4}, respectively.

B.5.2 Truck Frame and Bolster Suspension Forces and Moments

In this section, expressions for the suspension forces and moments acting on the truck frame and bolster are presented. In a conventional rail vehicle, suspension forces and moments act due to the primary and secondary suspension systems. In an advanced design vehicle with steerable trucks, the steering linkages exert additional forces and moments on the trucks and bolsters.

The secondary suspension system acting between the truck, bolster, and carbody is modelled as follows. The carbody is coupled to the bolster via parallel spring/viscous damper elements in the lateral and vertical directions and a torsional spring/viscous damper combination in the yaw direction. The bolster is connected to the truck frame by a torsional coulomb damper which saturates at the breakaway torque. The damper allows yaw motion between the truck frame and bolster. In all directions except yaw the bolster and truck frame follow identical motions. In forced-steered vehicle designs, the steering linkages are physically connected to the bolster.

Due to the suspension system, an equivalent lateral force and yaw moment act at the center of mass of each truck frame. The lateral suspension force, $F_{suspy_{Fi}}$, and yaw suspension moment, $M_{suspz_{Fi}}$, acting on truck frame i (i = 1 for front truck; i = 2 for rear truck) are shown in Figure B.8 and are given by the following equations.

<u>Truck Frame Lateral</u> (i = 1 Front Truck;
i = 2 Rear Truck)

$$F_{suspy_{Fi}} = [2k_{py}+2G_3\left|G_3\pm\left(\frac{G_2+G_6}{b}\right)\right|(k_{b2}+k_{b3})$$

$$-2(H_2-H_3)(H_1+H_3+1)(k_{s2}+k_{s3})+2k_{s3}]y_{w1}$$

$$+[2G_3\left|-1\pm(G_1+G_5)\right|(k_{b2}+k_{b3})+2b(H_2-H_3)(k_{s2}+k_{s3})-2bk_{s3}](\psi_{w1}-\frac{b}{R})$$

$$+[2k_{py}+2H_3\left|G_3\mp\left(\frac{G_2+G_6}{b}\right)(k_{b2}+k_{b3})\right|$$

$$-2(H_2-H_3)(H_1+H_3-1)(k_{s2}+k_{s3})+2k_{s3}]y_{w2}$$

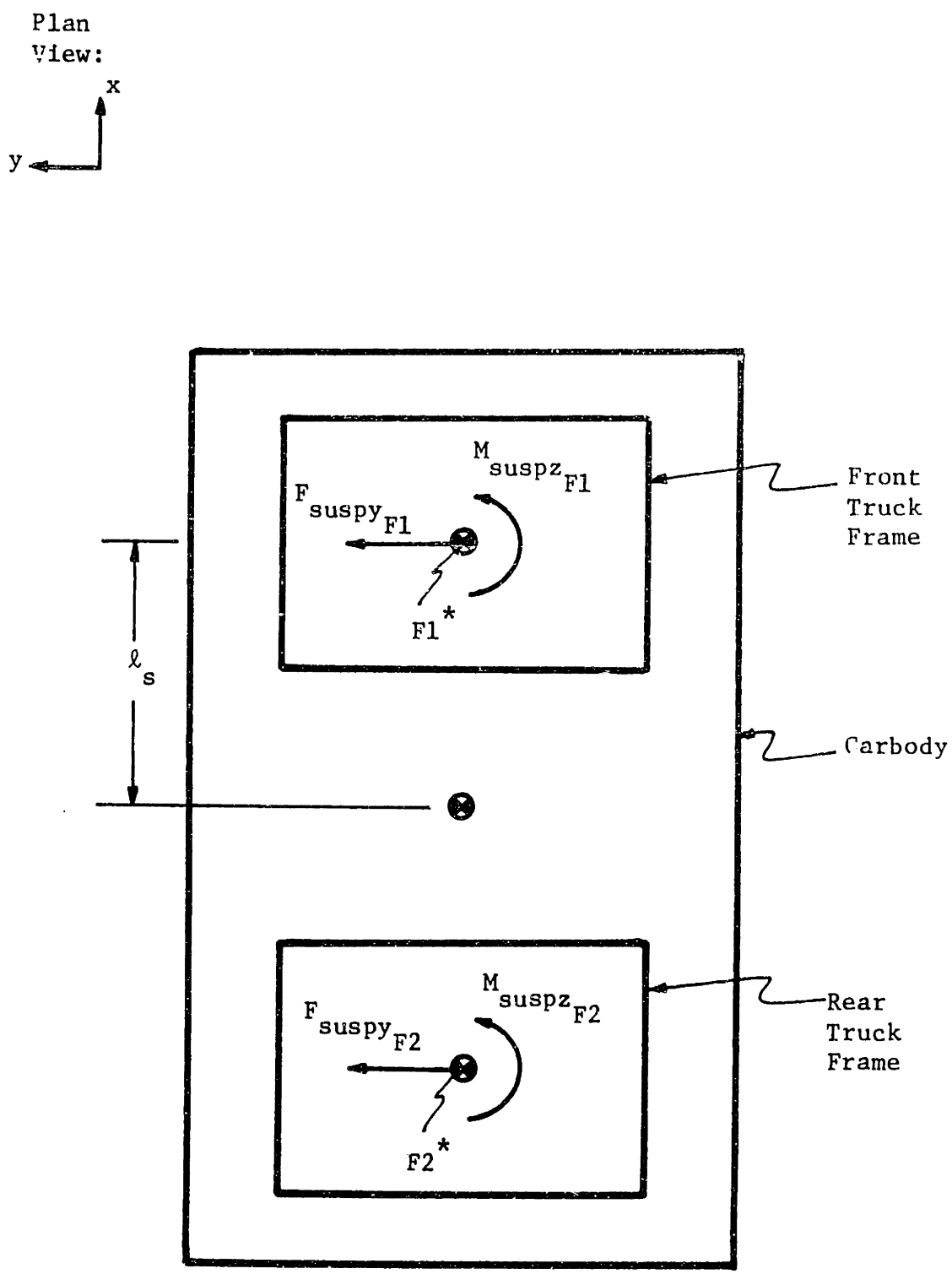

Figure B.8 Lateral Suspension Forces and Yaw Suspension Moments Acting on Truck Frame

$$+[2G_3\left|1\pm(G_1+G_5)\right|(k_{b2}+k_{b3})+2b(H_2-H_3)(k_{s2}+k_{s3})+2bk_{s3}](\psi_{w2}+\frac{b}{R})$$

$$+[-4k_{py}-2k_{sy}-4G_3^2(k_{b2}+k_{b3})-4(H_2-H_3)^2(k_{s2}+k_{s3})-4k_{s3}]y_F$$

$$+[\pm 4G_3(G_4-G_5-G_6)(k_{b2}+k_{b3})]\psi_F$$

$$+[\mp 4G_3(G_1+G_2+G_4)(k_{b2}+k_{b3})]\psi_B$$

$$+[2k_{sy}+4(H_1+H_2)(H_2-H_3)(k_{s2}+k_{s3})]y_c$$

$$+[\pm 2k_{sy}\ell_s](\psi_c \pm \frac{\ell_s}{R})$$

$$+[2C_{py}+2C_{s3}]\dot{y}_{w1} \qquad +[-2bC_{s3}](\dot{\psi}_{w1} - b(1/R))$$

$$+[2C_{py}+2C_{s3}]\dot{y}_{w2} \qquad +[+2bC_{s3}](\dot{\psi}_{w2}+b(1/R))$$

$$+[-4C_{py}-2C_{sy}-4C_{s3}]\dot{y}_F + [2C_{sy}]\dot{y}_c$$

$$+[\pm 2C_{sy}\ell_s](\dot{\psi}_c \pm \ell_s(1/R)) \qquad \text{(B-27)}$$

Truck Frame Yaw (i = 1 Front Truck; i = 2 Rear Truck)

$$M_{suspz_{Fi}} = [2bk_{py}+2\left|\mp G_3-(\frac{G_2+G_6}{b})\right|(G_4-G_5-G_6)(k_{b2}+k_{b3})]y_{w1}$$

$$+[2d_p^2k_{px}+2(G_4-G_5-G_6)\left|\pm 1-(G_1+G_5)\right|(k_{b2}+k_{b3})+2k_{b3}](\psi_{w1}-\frac{b}{R})$$

$$+[-2bk_{py}+2\left|\mp G_3+(\frac{G_2+G_6}{b})\right|(G_4-G_5-G_6)(k_{b2}+k_{b3})]y_{w2}$$

$$+[2d_p^2 k_{px}+2(G_4-G_5-G_6)\left|\mp 1-(G_1+G_5)\right|(k_{b2}+k_{b3})+2k_{b3}](\psi_{w2}+\frac{b}{R})$$

$$+[\pm 4G_3(G_4-G_5-G_6)(k_{b2}+k_{b3})]y_F$$

$$+[-4d_p^2 k_{px}-4b^2 k_{py}-4(G_4-G_5-G_6)^2(k_{b2}+k_{b3})-4k_{b3}]\psi_F$$

$$+[4(G_4-G_5-G_6)(G_1+G_2+G_4)(k_{b2}+k_{b3})]\psi_B$$

$$+[2bC_{py}]\dot{y}_{w1} + [2d_p^2 C_{px}+2C_{b3}](\dot{\psi}_{w1}-b(1/R))$$

$$+[-2bC_{py}]\dot{y}_{w2} + [2d_p^2 C_{px}+2C_{b3}](\dot{\psi}_{w2}+b(1/R))$$

$$+[-4d_p^2 C_{px}-4b^2 C_{py}-4C_{b3}]\dot{\psi}_F - T_{coul} \qquad \text{(B-28)}$$

In equation (B-28), T_{coul} represents the coulomb friction yaw moment acting on the truck frame due to interaction with the bolster. For numerical purposes, the model of coulomb friction is modified to include a linear viscous band at the origin, as follows:

$$T_{coul} = \begin{cases} T_o \quad \ldots\ldots\ldots\ldots \text{ for } (\dot{\psi}_F-\dot{\psi}_B) \geq T_o/k_o \\ k_o(\dot{\psi}_F-\dot{\psi}_B) \ldots\ldots\ldots \text{ for } -T_o/k_o < (\dot{\psi}_F-\dot{\psi}_B) < T_o/k_o \\ -T_o \quad \ldots\ldots\ldots\ldots \text{ for } (\dot{\psi}_F-\dot{\psi}_B) \leq -T_o/k_o \end{cases} \qquad \text{(B-29)}$$

At low relative yaw rates between the bolster and truck frame, the model assumes viscous damping occurs. At higher relative yaw rates, the model assumes coulomb damping occurs with the frictional torque saturating at the centerplate breakaway value. The coulomb friction

characteristic of equation (B-29) is shown in Figure B.9. This method approximates the frictional torque levels below $|T_o|$ (during "stopped conditions"). The selection of the width of the linear viscous band is important. Too wide a band will produce viscous damping results. However, if the band is too narrow, it will be missed during "stopped conditions" by discrete integration.

A net yaw moment acts on the bolster due to the coulomb friction element and due to the steering linkages of forced-steered vehicle designs. The yaw suspension moment, $M_{suspz_{Bi}}$, acting on bolster i (i = 1 for front bolster; i = 2 for rear bolster) is shown in Figure B.10 and is given by equation (B-30).

Bolster Yaw (i = 1 Front Bolster; i = 2 Rear Bolster)

$$
\begin{aligned}
M_{suspz_{Bi}} = {} & [2(G_1+G_2+G_4)(\pm G_3+\frac{G_2+G_6}{b})(k_{b2}+k_{b3})]y_{w1} \\
& +[2(G_1+G_2+G_4)(G_1+G_5\mp 1)(k_{b2}+k_{b3})](\psi_{w1}-\frac{b}{R}) \\
& +[\pm 2(G_1+G_2+G_4)(G_3\mp\frac{G_2+G_6}{b})(k_{b2}+k_{b3})]y_{w2} \\
& +[2(G_1+G_2+G_4)(G_1+G_5\pm 1)(k_{b2}+k_{b3})](\psi_{w2}+\frac{b}{R}) \\
& +[\mp 4G_3(G_1+G_2+G_4)(k_{b2}+k_{b3})]y_F \\
& +[4(G_1+G_2+G_4)(G_4-G_5-G_6)(k_{b2}+k_{b3})]\psi_F \\
& +[-k_{s\psi}-4(G_1+G_2+G_4)^2(k_{b2}+k_{b3})]\psi_B
\end{aligned}
$$

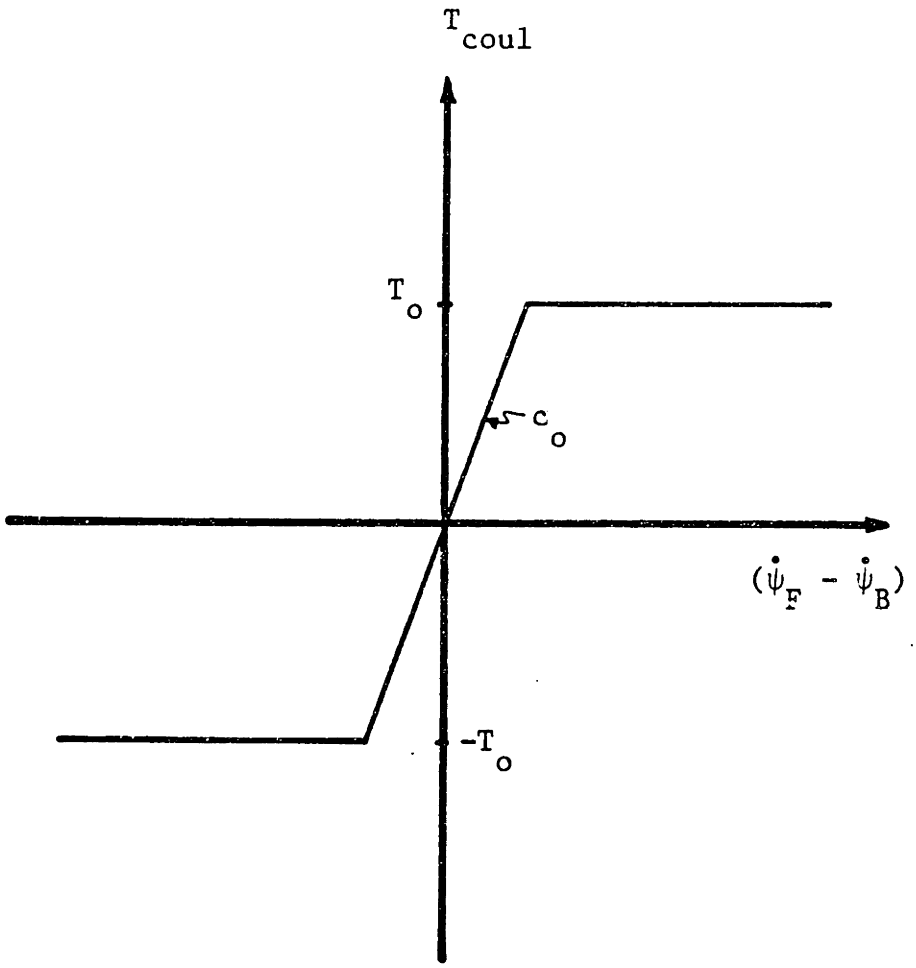

Figure B.9 Truck Frame/Bolster Yaw Suspension Characteristic

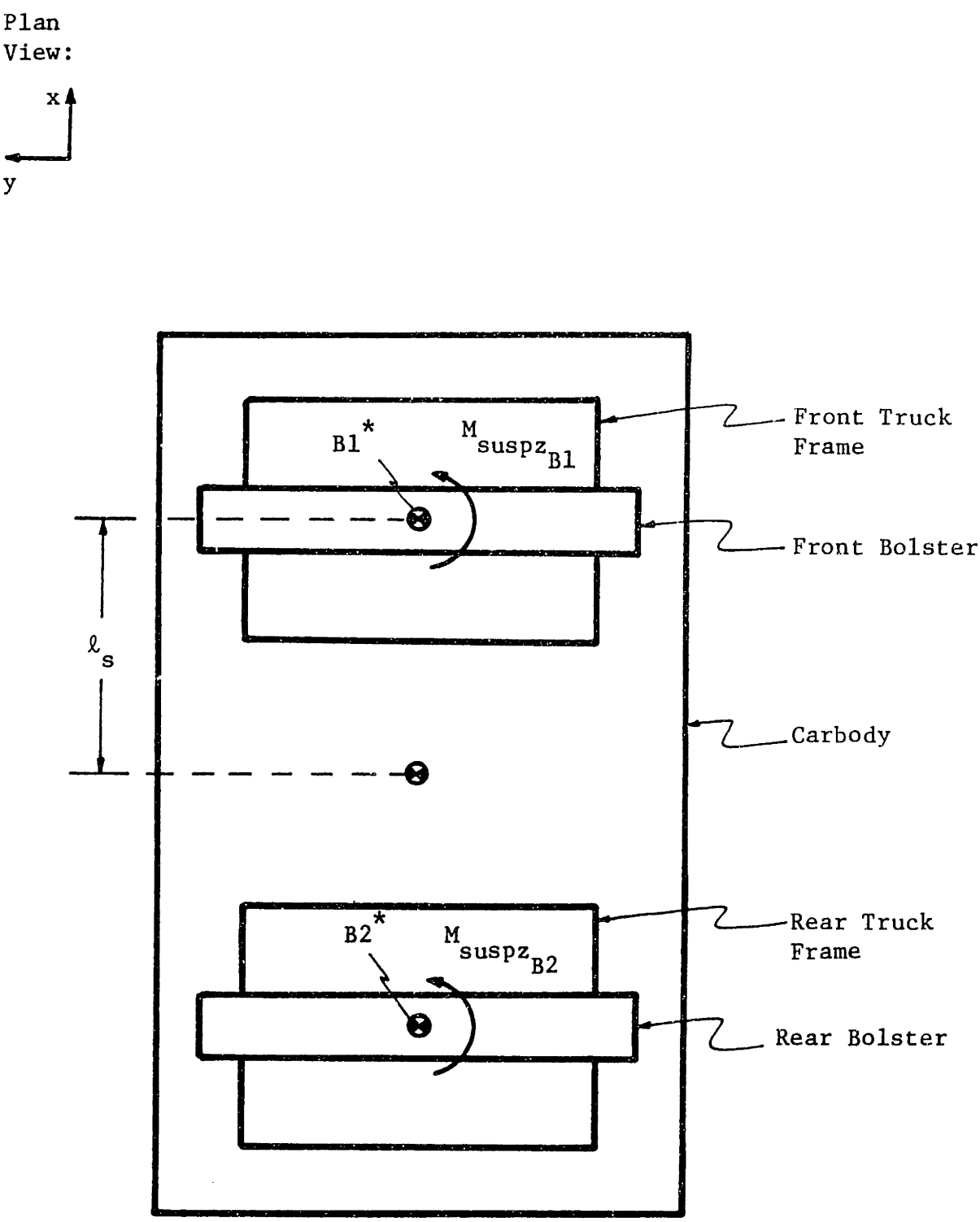

Figure B.10 Yaw Suspension Moments Acting on Bolsters

$$+[k_{s\psi}](\psi_c \pm \frac{\ell_s}{R})$$

$$+[-C_{s\psi}]\dot{\psi}_B + [C_{s\psi}](\dot{\psi}_c \pm \ell_s(1/\dot{R})) + T_{coul} \qquad \text{(B-30)}$$

B.5.3 Carbody Suspension Forces and Moments

Suspension forces and moments act on the carbody due to the secondary suspension system and due to the steering linkages of forced-steered vehicle designs. It is convenient to consider the influence of the front and rear trucks separately on the carbody suspension forces and moments. Figure B.11 shows the effective lateral force, $F_{suspy_{Ci}}$, yaw moment, $M_{suspz_{Ci}}$, and roll moment, $M_{suspx_{Ci}}$, acting on the carbody due to truck i(i = 1 for front truck; i = 2 for rear truck). The lateral suspension force and yaw and roll suspension moments are given by the following equations.

Carbody Lateral

$$F_{suspy_{Ci}} = [2(H_1+H_2)(H_1+H_3+1)(k_{s2}+k_{s3})]y_{w1}$$

$$+ [-2b(H_1+H_2)(k_{s2}+k_{s3})](\psi_{w1} - \frac{b}{R})$$

$$+ [2(H_1+H_2)(H_1+H_3-1)(k_{s2}+k_{s3})]y_{w2}$$

$$+[-2b(H_1+H_2)(k_{s2}+k_{s3})](\psi_{w2} + \frac{b}{R})$$

$$+[2k_{sy}+4(H_1+H_2)(H_2-H_3)(k_{s2}+k_{s3})]y_F$$

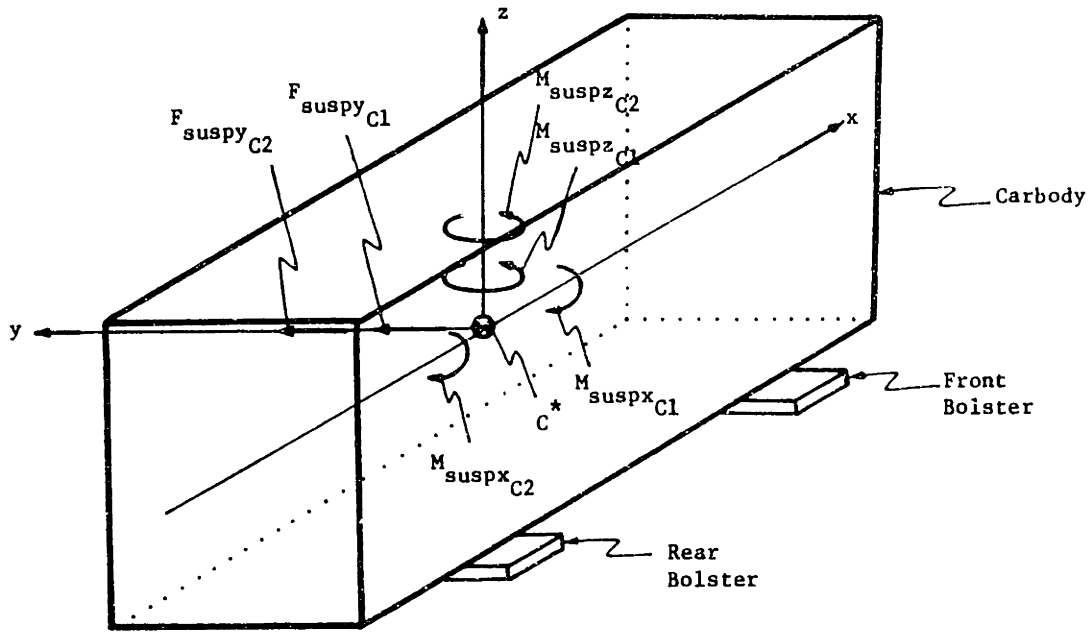

Figure B.11 Suspension Forces and Moments Acting on Carbody

$$+[-2k_{sy}-4(H_1+H_2)^2(k_{s2}+k_{s3})]y_c$$

$$+[2C_{sy}]\dot{y}_B + [-2C_{sy}]\dot{y}_c$$

$$+[-2h_{cs}k_{sy}]\phi_c + [-2h_{cs}C_{sy}]\dot{\phi}_c \qquad \text{(B-31)}$$

Carbody Yaw

$$M_{suspz_{Ci}} = [\pm 2\ell_s k_{sy}]y_F + [k_{s\psi}]\psi_B$$

$$+[-2\ell_s^2 k_{sy} - k_{s\psi}](\psi_c \pm \frac{\ell_s}{R})$$

$$+[\pm 2\ell_s C_{sy}]\dot{y}_F + [C_{s\psi}]\dot{\psi}_B$$

$$+[-2\ell_s^2 C_{sy} - C_{s\psi}](\dot{\psi}_c \pm \ell_s(1/R)) \qquad \text{(B-32)}$$

Carbody Roll

$$M_{suspx_{Ci}} = [-2k_{sy}h_{cs}^2 - 2k_{sz}d_s^2]\phi_c$$

$$+ [-2C_{sy}h_{cs}^2 - 2C_{sz}d_s^2]\dot{\phi}_c \qquad \text{(B-33)}$$

The dynamics of the front and rear trucks (and bolsters) are coupled due to connection via the carbody. In steady-state curving conditions, the effect of coupling between the trucks is negligible (for typical secondary suspension parameters). The suspension forces

and moments from the carbody acting on the front and rear trucks are equal and opposite. In dynamic curving situations, such as curve entry and exit, the forces and moments acting on the front and rear trucks are not equal and opposite. The trucks do not behave independently and, thus, a full vehicle model is required.

In the next section, the equations of motion are developed for a full vehicle model.

B.6 Equations of Motion

The wheelsets, trucks, bolsters, and carbody are assumed to be rigid bodies. The equations of motion are derived by direct application of Newtonian mechanics. As discussed in Appendix A (Section A.6), the principles of linear and angular momentum give six scalar differential equations for each rigid body. The equations represent three dynamic force equilibrium equations and three dynamic moment equilibrium equations.

B.6.1 Wheelset Equations of Motion

The equations of motion of a wheelset in single-point and two-point contact at the flanging wheel are developed in Appendix A. For a wheelset in single-point contact, the first order differential equations of motion are given in equations (A-68). For a wheelset in two-point contact at the flanging wheel, the equations are given in equations (A-70). The wheelset suspension forces and moments are presented in Section B.5.1. The lateral suspension force and yaw suspension moment acting on the wheelsets are listed in equations (B-21) -

(B-24); the vertical suspension force and roll suspension moment are given in equations (B-25) and (B-26).

B.6.2 Truck Frame and Bolster Equations of Motion

In this section, the lateral and yaw equations of motion of the truck frame and bolster are presented. The lateral equation is obtained by applying the principle of linear momentum in the lateral direction. Taking into account the lateral components of truck frame and bolster weight (since the truck frame and bolster move together laterally) and assuming small angles, the lateral equation of motion is:

TRUCK FRAME/BOLSTER LATERAL EQUATION

$$\frac{(W_F + W_B)}{g}[\ddot{y}_F - (r_o+h_{tp})\ddot{\phi}_{SE}] = (W_F+W_B)[\phi_d - \frac{1}{2}(\phi_{w1}+\phi_{w2})] + F_{suspy_F} \quad \text{(B-34)}$$

The truck frame yaw equation is obtained by applying the principle of angular momentum in the yaw direction. Assuming small angles, the truck frame yaw equation of motion is:

TRUCK FRAME YAW EQUATION

$$I_{FZ}[\ddot{\psi}_F - \frac{\dot{V}}{R} - V(\dot{1/R})] = M_{suspz_F} \quad \text{(B-35)}$$

Similarly, the bolster yaw equation of motion is:

BOLSTER YAW EQUATION

$$I_{BZ}[\ddot{\psi}_B - \frac{\dot{V}}{R} - V(\dot{1/R})] = M_{suspz_B} \quad \text{(B-36)}$$

The truck frame lateral suspension force, F_{suspy_F}, in equation (B-34), the truck frame yaw suspension moment, M_{suspz_F}, in equation (B-35), and the bolster yaw suspension moment, M_{suspz_B}, in equation (B-36) are defined in equations (B-27), (B-28), and (B-30), respectively.

B.6.3 Carbody Equations of Motion

The lateral and yaw equations of motion of the carbody are presented in this section. The lateral equation of motion is derived by applying the principle of linear momentum in the lateral direction and accounting for the contributions of the lateral suspension forces from the front and rear trucks. The equation is:

CARBODY LATERAL EQUATION

$$\frac{W_c}{g}[\ddot{y}_c - (r_o+h_{tp}+h_{ts}+h_{cs})\ddot{\phi}_{SE}] = W_c(\phi_d - \phi_c) + F_{suspy_{C1}} + F_{suspy_{C2}} \qquad \text{(B-37)}$$

where the lateral component of the carbody weight is included and small angles are assumed.

The yaw equation of motion is obtained by invoking the principle of angular momentum in the yaw direction and including the influence of the yaw suspension moments from the front and rear trucks. Assuming small angles, the carbody yaw equation is:

CARBODY YAW EQUATION

$$I_{cz}[\ddot{\psi}_c - \frac{\dot{V}}{R} - V(1/R)] = M_{suspz_{C1}} + M_{suspz_{C2}} \quad \text{(B-38)}$$

Similarly, the carbody roll equation of motion is derived by applying the principle of angular momentum in the roll direction.

CARBODY ROLL EQUATION

$$I_{cx}[\ddot{\phi}_c + \ddot{\phi}_{SE}] = M_{suspx_{C1}} + M_{suspx_{C2}} \quad \text{(B-39)}$$

The carbody roll angle, ϕ_c, is the angular displacement about a longitudinal axis passing through the carbody center of mass. When $\phi_c = 0$, the carbody is parallel to the track plane.

The carbody lateral suspension forces, $F_{suspy_{Ci}}$, in equation (B-37), the yaw suspension moments, $M_{suspz_{Ci}}$, in equation (B-38), and the roll suspension moments, $M_{suspx_{Ci}}$, in equation (B-39) are defined in equations (B-31), (B-32), and (B-33), respectively.

B.6.4 Modified Carbody Yaw Equation of Motion

In the development above, a detailed model of truck frame-bolster-carbody interaction has been assumed which includes a degree of freedom for bolster yaw motions. In the model, the carbody is connected to each bolster by yaw suspension stiffness and damping elements. Physically, the stiffness and damping are provided by anchor rods which offer large torsional resistance. The model also includes a (modified)

coulomb friction element between the bolster and truck frame to represent the effect of the friction pads at the truck centerplate. The truck frame-bolster yaw suspension characteristic is shown in Figure B.12.

Since the secondary yaw stiffness between the carbody and bolster is very large,* it is reasonable to model the bolster as rigidly coupled to the carbody in yaw. This simplifies the analysis by eliminating a degree of freedom for bolster yaw. In the following, it is assumed that each bolster yaws with the carbody, but displaces laterally and rolls with the truck frame. For forced-steered vehicles, this implies that the steering linkages are effectively connected to the carbody.

Since each bolster yaws with the carbody, the bolster yaw angle, ψ_B, is a function of the carbody yaw angle, ψ_c, given by

$$\psi_B \approx \psi_c \pm \frac{\ell_s}{R} \qquad \text{(B-40)}$$

Substituting equation (B-40) into the bolster and carbody yaw equations of motion and combining terms results in the following equation for carbody/bolster yaw:

---

*In addition to large secondary yaw stiffness (>5.0 x 10^6 ft-lb/rad), the bolster weight (~1500 lb) is small (relative to truck frame and carbody weights). Thus, the natural frequency of yaw oscillation of the bolster (~15 Hz) is large relative to the truck frame and carbody natural frequencies.

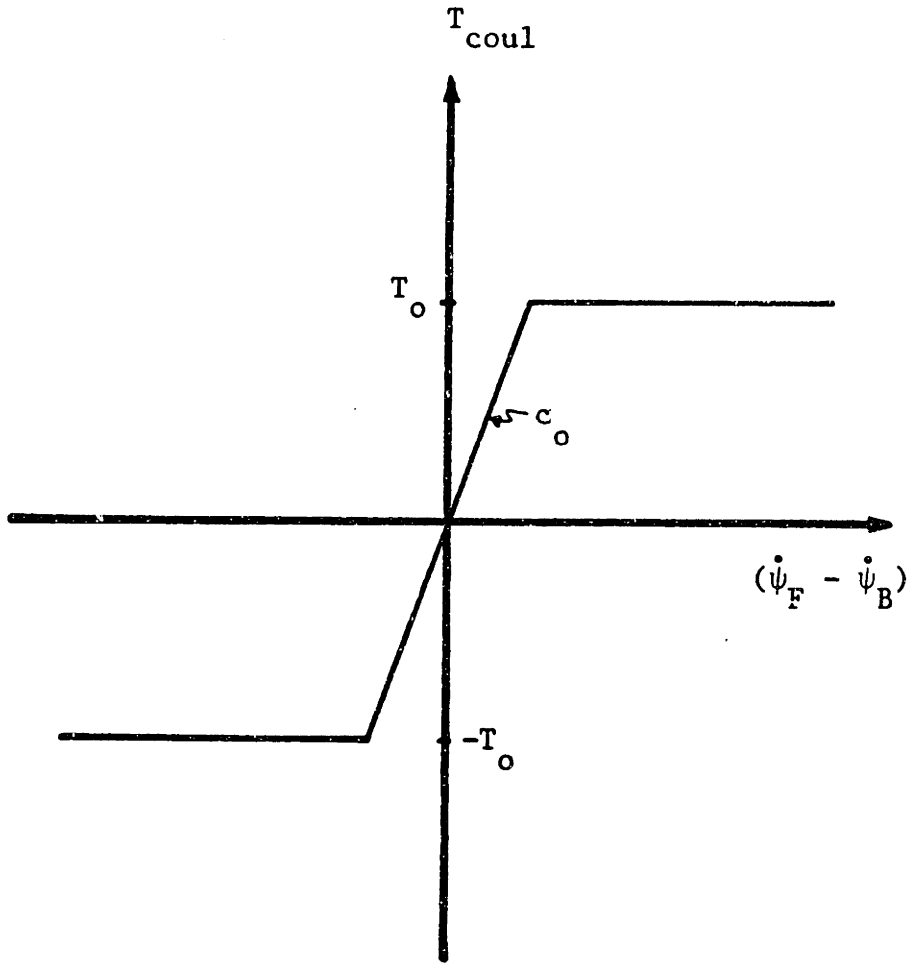

Figure B.12: Truck Frame/Bolster Yaw Suspension Characteristic

CARBODY/BOLSTER YAW EQUATION

$$I^*_{cz}[\ddot{\psi}_c - \frac{\dot{V}}{R} - V(1/R)] = M^*_{suspz_{C1}} + M^*_{suspz_{C2}} \qquad \text{(B-41)}$$

where I^*_{CZ} is the yaw moment of inertia of the carbody and front and rear bolsters (about a vertical axis through the carbody center of mass) and $M^*_{suspz_{Ci}}$ is the suspension yaw moment acting on the carbody and bolster due to interaction with truck i. The expression for the suspension yaw moment, $M^*_{suspz_{Ci}}$, is obtained by summing the suspension yaw moments on the carbody and bolster, i.e.,

CARBODY/BOLSTER YAW

$$\begin{aligned}
M^*_{suspz_{Ci}} = {} & [2(G_1+G_2+G_4)(\pm G_3 + \frac{G_2+G_6}{b})(k_{b2}+k_{b3})]y_{w1} \\
& + [2(G_1+G_2+G_4)+(G_1+G_5\mp 1)(k_{b2}+k_{b3})](\psi_{w1} - \frac{b}{R}) \\
& + [\pm 2(G_1+G_2+G_4)(G_3 \mp \frac{G_2+G_6}{b})(k_{b2}+k_{b3})]y_{w2} \\
& + [2(G_1+G_2+G_4)(G_1+G_5\pm 1)(k_{b2}+k_{b3})](\psi_{w2} + \frac{b}{R}) \\
& + [\pm 2\ell_s k_{sy} \mp 4G_3(G_1+G_2+G_4)(k_{b2}+k_{b3})]y_F \\
& + [4(G_1+G_2+G_4)(G_4-G_5-G_6)(k_{b2}+k_{b3})]\psi_F \\
& + [-2\ell_s^2 k_{sy} - 4(G_1+G_2+G_4)^2(k_{b2}+k_{b3})](\psi_c \pm \frac{\ell_s}{R})
\end{aligned}$$

$$+[\pm 2\ell_s C_{sy}]\dot{y}_F + [-2\ell_s^2 C_{sy}](\dot{\psi}_c \pm \ell_s(1/R))$$

$$+T_{coul} \qquad \text{(B-42)}$$

B.7 Numerical Methods

The equations of motion presented in Section B.6 describe the dynamic behavior of the wheelsets, trucks, bolsters, and carbody of a rail vehicle model as it traverses flexible, curved track. The equations of motion are solved by digital integration using a fourth-order Runge-Kutta scheme, which requires that the equations be in first order form. In this section, the equations of motion of the full vehicle model are cast in a form convenient for computer manipulation. In a sense, this section represents a continuation of Section A.7 of Appendix A which presented the first order differential equations of motion of a wheelset.

The full vehicle model is represented by 42 states: 20 states for the 4 wheelsets, 8 states for the 2 trucks, 6 states for the carbody, and 8 states for the rails. These states are listed in Table B.2. Each wheelset has 2 states (1 degree of freedom) to describe lateral motions (y_{Wi}, $\dot{y}_{Wi}$) 2 states to describe yaw motions (ψ_{Wi}, $\dot{\psi}_{Wi}$), and a state to represent spin speed ($\dot{\theta}_{Wi}$). In addition, the rails in contact with each wheelset have 2 states to describe lateral deflections ($y_{rail_{Ri}}$, $y_{rail_{Li}}$). Each truck frame is characterized by 2 states for lateral motions (y_{Fi}, $\dot{y}_{Fi}$) and 2 states for yaw motions (ψ_{Fi}, $\dot{\psi}_{Fi}$). The carbody has 2 states for lateral motions (y_C, $\dot{y}_C$), 2 states for yaw

motions (ψ_c, $\dot{\psi}_c$), and 2 states for roll motions (ϕ_c, $\dot{\phi}_c$).

Assuming that single-point contact occurs at all wheels of the vehicle, the first order differential equations of motion are given by the following equations.

SINGLE-POINT CONTACT VEHICLE EQUATIONS

$$
\begin{aligned}
\dot{X}_1 &= X_4 \\
\dot{X}_2 &= X_5 \\
\dot{X}_8 &= X_{11} \\
\dot{X}_9 &= X_{12} \\
\dot{X}_{15} &= X_{17} \\
\dot{X}_{16} &= X_{18} \\
\dot{X}_{19} &= X_{22} \\
\dot{X}_{20} &= X_{23} \\
\dot{X}_{26} &= X_{29} \\
\dot{X}_{27} &= X_{30} \\
\dot{X}_{33} &= X_{35} \\
\dot{X}_{34} &= X_{36} \\
\dot{X}_{37} &= X_{40} \\
\dot{X}_{38} &= X_{41} \\
\dot{X}_{39} &= X_{42}
\end{aligned}
\qquad \text{(B-43)}
$$

WHEELSET SPIN [EQUATION (A-51)]

$$\dot{X}_3 = f(X_1, X_2, \ldots, X_{42})$$
$$\dot{X}_{10} = f(X_1, X_2, \ldots, X_{42})$$
$$\dot{X}_{21} = f(X_1, X_2, \ldots, X_{42})$$
$$\dot{X}_{28} = f(X_1, X_2, \ldots, X_{42})$$

WHEELSET LATERAL [EQUATION (A-45)]

$$\dot{X}_4 = f(X_1, X_2, \ldots, X_{42}$$
$$\dot{X}_{11} = f(X_1, X_2, \ldots, X_{42})$$
$$\dot{X}_{22} = f(X_1, X_2, \ldots, X_{42})$$
$$\dot{X}_{29} = f(X_1, X_2, \ldots, X_{42})$$

(B-43)
Continued

WHEELSET YAW [EQUATION (A-52)]

$$\dot{X}_5 = f(X_1, X_2, \ldots, X_{42})$$
$$\dot{X}_{12} = f(X_1, X_2, \ldots, X_{42})$$
$$\dot{X}_{23} = f(X_1, X_2, \ldots, X_{42})$$
$$\dot{X}_{30} = f(X_1, X_2, \ldots, X_{42})$$

RIGHT RAIL LATERAL [EQUATION (A-54)]

$$\dot{X}_6 = f(X_1, X_2, \ldots, X_{42})$$
$$\dot{X}_{13} = f(X_1, X_2, \ldots, X_{42})$$
$$\dot{X}_{24} = f(X_1, X_2, \ldots, X_{42})$$
$$\dot{X}_{31} = f(X_1, X_2, \ldots, X_{42})$$

LEFT RAIL LATERAL [EQUATION (A-53)]

$$\dot{X}_7 = f(X_1, X_2, \ldots, X_{42})$$
$$\dot{X}_{14} = f(X_1, X_2, \ldots, X_{42})$$
$$\dot{X}_{25} = f(X_1, X_2, \ldots, X_{42})$$
$$\dot{X}_{32} = f(X_1, X_2, \ldots, X_{42})$$

TRUCK FRAME/BOLSTER LATERAL [EQUATION (B-34)]

$$\dot{X}_{17} = f(X_1, X_2, \ldots, X_{42})$$
$$\dot{X}_{35} = f(X_1, X_2, \ldots, X_{42})$$

TRUCK FRAME YAW [EQUATION (B-35)]

(B-43)
Continued

$$\dot{X}_{18} = f(X_1, X_2, \ldots, X_{42})$$
$$\dot{X}_{36} = f(X_1, X_2, \ldots, X_{42})$$

CARBODY LATERAL [EQUATION (B-36)]

$$\dot{X}_{40} = f(X_1, X_2, \ldots, X_{42})$$

CARBODY/BOLSTER YAW [EQUATION (B-41)]

$$\dot{X}_{41} = f(X_1, X_2, \ldots, X_{42})$$

CARBODY ROLL [EQUATION (B-39)]

$$\dot{X}_{42} = f(X_1, X_2, \ldots, X_{42})$$

The first order equations of motion listed in equations (B-43) apply if single-point contact occurs at all wheels. If two-point contact occurs at a wheel (or wheels), these equations must be modified. For instance, if two-point contact occurs at the left wheel of the leading wheelset, the following modification are introduced in equations (B-43).

LEADING WHEELSET SPIN [EQUATION (A-62)]

$$\dot{X}_3 = f(X_1, X_2, \ldots, X_{42})$$

LEADING WHEELSET LATERAL [EQUATION (A-59)]

$$\dot{X}_4 = f(X_1, X_2, \ldots, X_{42})$$

LEADING WHEELSET YAW [EQUATION (A-63)] (B-44)

$$\dot{X}_5 = f(X_1, X_2, \ldots X_{42})$$

LEADING RIGHT RAIL LATERAL [EQUATION (A-65)]

$$\dot{X}_6 = f(X_1, X_2, \ldots, X_{42})$$

Also, the equation for the leading left rail lateral displacement, X_7, is eliminated. State X_7 is a known function of X_1 due to the contact constraint relation (A-56). Equations (B-43) are correct except for these modifications. If two-point contact occurs at other wheels, similar replacements are made.

TABLE B.2: STATES OF THE RAIL VEHICLE MODEL

FRONT TRUCK, LEADING WHEELSET

$X_1 = y_{w1}$

$X_2 = \psi_{w1}$

$X_3 = \dot{\theta}_{w1}$

$X_4 = \dot{y}_{w1}$

$X_5 = \dot{\psi}_{w1}$

$X_6 = y_{rail_{R1}}$

$X_7 = y_{rail_{L1}}$

FRONT TRUCK, TRAILING WHEELSET

$X_8 = y_{w2}$

$X_9 = \psi_{w2}$

$X_{10} = \dot{\theta}_{w2}$

$X_{11} = \dot{y}_{w2}$

$X_{12} = \dot{\psi}_{w2}$

$X_{13} = y_{rail_{R2}}$

$X_{14} = y_{rail_{12}}$

FRONT TRUCK

$X_{15} = y_{F1}$

$X_{16} = \psi_{F1}$

$X_{17} = \dot{y}_{F1}$

$X_{18} = \dot{\psi}_{F1}$

REAR TRUCK, LEADING WHEELSET

$$X_{19} = y_{w3}$$
$$X_{20} = \psi_{w3}$$
$$X_{21} = \dot{\theta}_{w3}$$
$$X_{22} = \dot{y}_{w3}$$
$$X_{23} = \dot{\psi}_{w3}$$
$$X_{24} = y_{rail_{R3}}$$
$$X_{25} = y_{rail_{L3}}$$

REAR TRUCK, TRAILING WHEELSET

$$X_{26} = y_{w4}$$
$$X_{27} = \psi_{w4}$$
$$X_{28} = \dot{\theta}_{w4}$$
$$X_{29} = \dot{y}_{w4}$$
$$X_{30} = \dot{\psi}_{w4}$$
$$X_{31} = y_{rail_{R4}}$$
$$X_{32} = y_{rail_{L4}}$$

REAR TRUCK

$$X_{33} = y_{F2}$$
$$X_{34} = \psi_{F2}$$
$$X_{35} = \dot{y}_{F2}$$
$$X_{36} = \dot{\psi}_{F2}$$

CARBODY

$$X_{37} = y_c$$
$$X_{38} = \psi_c$$
$$X_{39} = \phi_c$$
$$X_{40} = \dot{y}_c$$
$$X_{41} = \dot{\psi}_c$$
$$X_{42} = \dot{\phi}_c$$

In typical steady-state curving conditions, flanging occurs at the leading outer wheel of the vehicle (for practical vehicle suspension parameters and for negotiation of curves >2.5°). Thus, for wheel/rail profiles with steep flanges, such as new AAR 1 in 20 wheels, two-point contact develops at the leading outer wheel. Single-point contact occurs at all other wheels. In dynamic curving situations, flanging can occur at any wheel or combination of wheels. For a vehicle with new wheel profiles, two-point contact can develop at the outer or inner wheels of any of the wheelsets, especially during violent curve entry and exit, during negotiation of reverse curves, and during hunting.

For each wheelset of the vehicle, 3 distinct possibilities of wheel/rail contact exist. The possibilities are: (1) single-point contact at both wheels, (2) two-point contact at the outer wheel and single-point contact at the inner wheel, or (3) two-point contact at the inner wheel and single-point contact at the outer wheel. Thus, for a truck with 2 wheelsets, a total of 9 wheel/rail contact possibilities can be identified, as illustrated in Figure B.13. For a full vehicle with front and rear trucks, 81 contact combinations are possible. A separate set of vehicle equations of motion exists for each combination.

B.7.1 Dynamic Curving Program

The nonlinear vehicle equations of motion are numerically integrated to provide time histories of (1) all the state variables, (2) the wheel/rail contact forces, and (3) the contact patch work. A

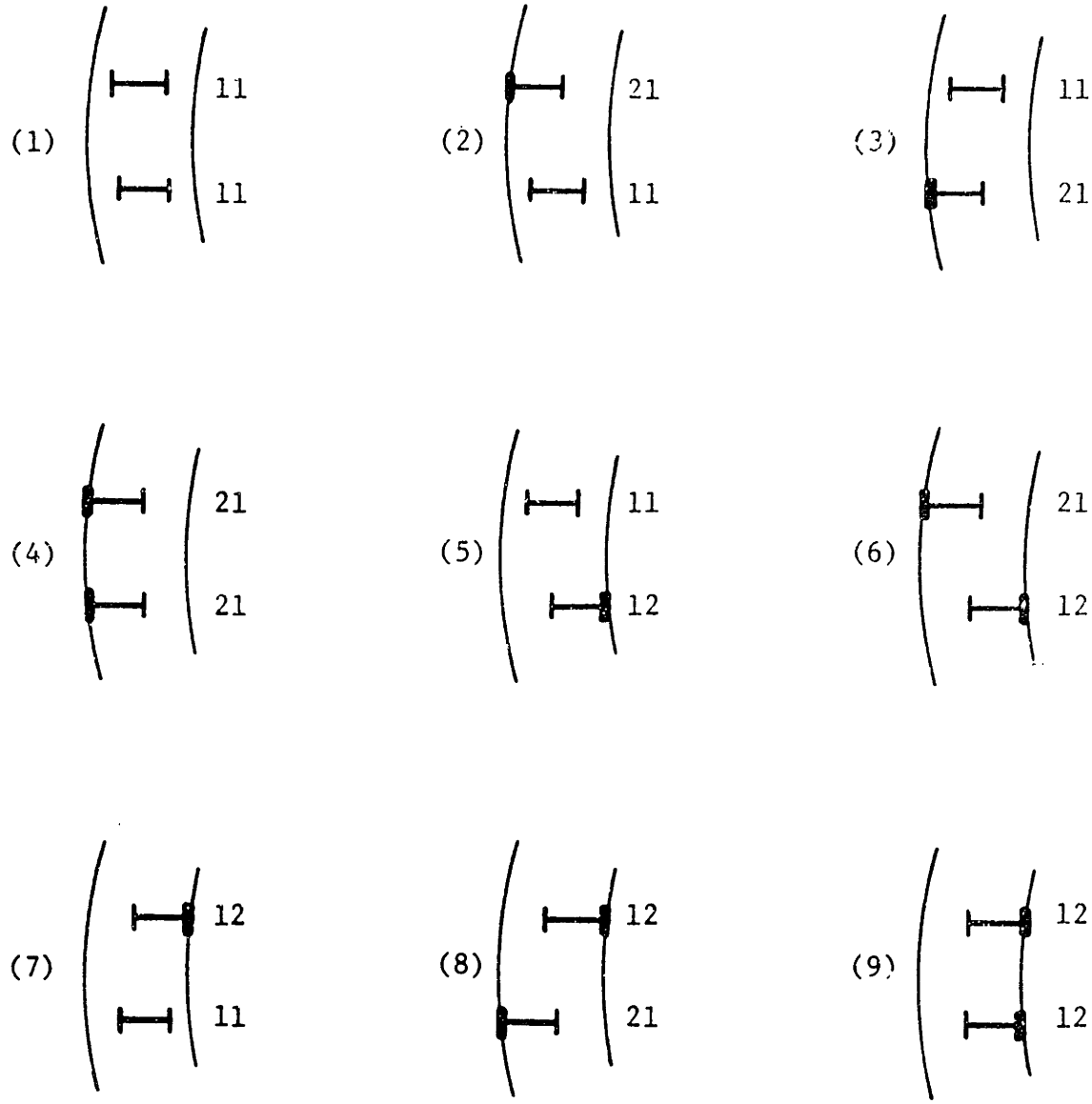

Key:

11 Single-Point Contact Outer and Inner Wheels.

21 Two-Point Contact Outer Wheel; Single-Point Contact Inner Wheel.

12 Single-Point Contact Outer Wheel; Two-Point Contact Inner Wheel.

Figure B.13: Wheel/Rail Contact Possibilities for Wheelsets of a Truck with New Wheels.

variable time-step, fourth order Runge-Kutta algorithm is employed for the integration. The dynamic curving analysis is coded in a FORTRAN program, entitled DYCURV (DYnamic CURVing). A flowchart of the program, the layout of the "equation" subroutines, and appropriate descriptions of the subroutines appear in Figures B.14, B.15, and Table B.3, respectively. Program DYCURV automatically determines the wheel/rail contact condition at each wheel. The program solves the single-point contact vehicle equations and evaluates whether or not a correct solution has been obtained. If a two-point contact wheel/rail profile is being used and the net wheelset lateral excursion at any wheel equals the flange clearance, the solution is not correct. Then, without incrementing the time-step, a different (appropriate) set of vehicle equations is solved and, again, checked for consistency. A consistent (i.e., correct) two-point contact solution is obtained if positive normal forces are predicted at the two contact points at each flanging wheel.

Program DYCURV requires a very small time-step generally for numerical stability. Previous dynamic curving analyses [16,26] have suggested a time-step of 0.00075 sec. This value is used in program DYCURV when tread contact occurs at all wheel/rail interfaces. When flange contact occurs at any wheel the program automatically reduces the time-step to 0.0005 sec. Thus, for a 1 second simulation in which flange contact occurs, 2,000 time-step iterations are required. The computer time required on a DEC VAX 1178 is about 1 CPU minute for a 1 second simulation, at a cost of $3.75/CPU minute at high priority.

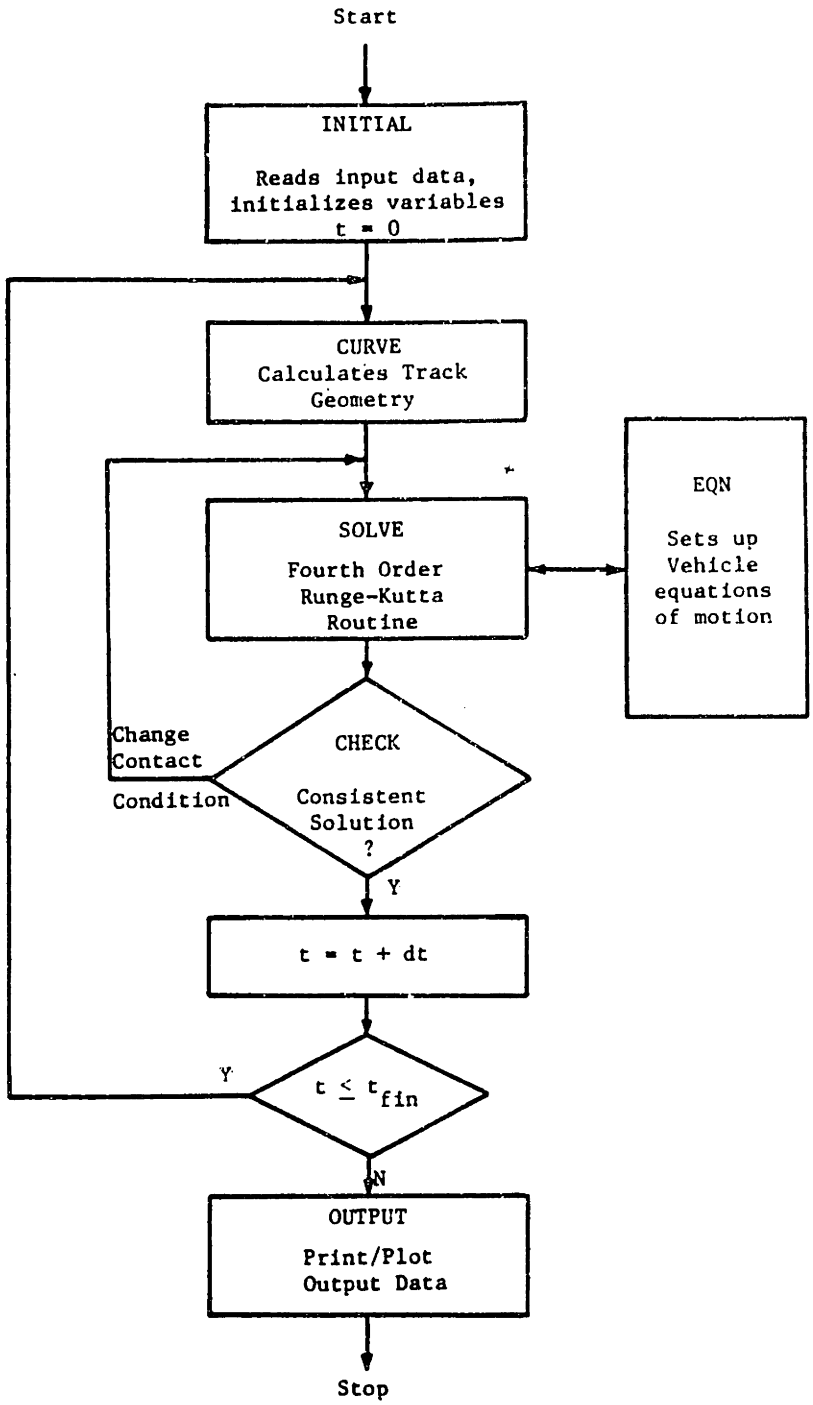

Figure B.14 Flowchart of Dynamic Curving Program

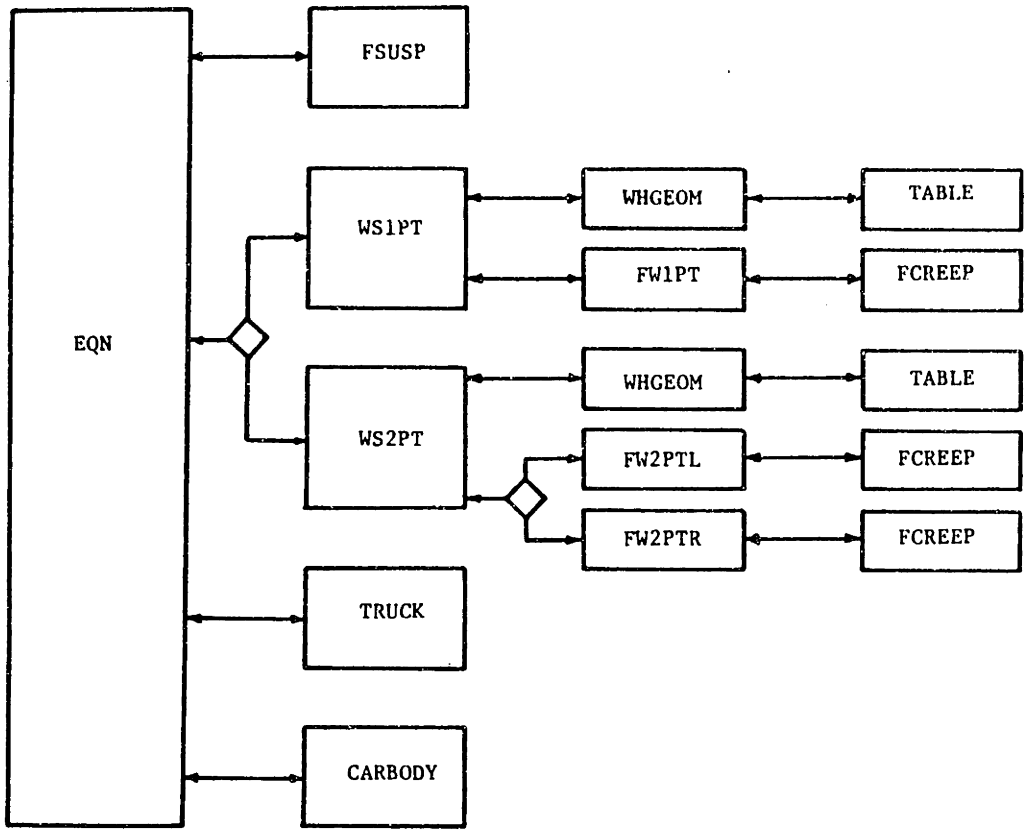

B.15 Layout of Equation Subroutines

TABLE B.3 SUBROUTINE DESCRIPTIONS FOR DYNAMIC CURVING PROGRAM

CARBODY	Sets up first order differential equations of motion of carbody.
CHECK	Checks consistency of solution (i.e., checks wheelset lateral excursions and signs of forces to determine if single-point or two-point contact occur at each wheel); if inconsistent, changes contact condition.
CURVE	Calculates track geometry: track curvature, superelevation angle, and rates.
EQN	Sets up appropriate first order differential equations of motion of vehicle (depending on contact conditions at wheels).
FCREEP	Determines creep forces and moment using "heuristic" scheme (Linear Kalker with Vermeulen-Johnson saturation).
FSUSP	Calculates suspension forces and moments acting on wheelsets, trucks, and carbody.
FW1PT	Calculates wheel/rail forces (creep and normal) using iterative approach assuming single-point contact occurs at both wheels.
FW2PTL	Calculates wheel/rail forces (creep and normal) using iterative approach assuming two-point contact occurs at left wheel and single-point contact occurs at right wheel.
FW2PTR	Calculates wheel/rail forces (creep and normal) using iterative approach assuming two-point contact occurs at right wheel and single-point contact occurs at left wheel.
INITIAL	Reads input data: system parameters, initial conditions, and wheel/rail geometry.
OUTPUT	Prints/plots output data: states, wheel/rail forces, contact work.
SOLVE	Standard fourth order Runge-Kutta integration routine.
TABLE	Interpolates wheel/rail contact geometry data from table.
TRUCK	Sets up first order differential equations of motion of truck.
WHGEOM	Determines wheel/rail contact geometry for net lateral excursion.

TABLE B.3 Continued

WS1PT	Sets up wheelset and rail equations of motion assuming single-point contact occurs at both wheels.
WS2PT	Sets up wheelset and rail equations of motion assuming two-point contact occurs at one wheel and single-point contact occurs at other wheel.

If the program is to be used for extensive parametric studies, optimal on-flange and off-flange time-steps should be determined. These values will be a function of the "stiffness" of the system of equations being integrated.

APPENDIX C: STEADY-STATE CURVING CONDITIONS

C.1 Introduction

This Appendix addresses analytical and computational methods that characterize rail vehicle steady-state curving behavior. Steady-state curving conditions are achieved when the wheelsets, trucks, and carbody satisfy force and moment steady-state equilibrium. The steady-state curving conditions represent a special case of the dynamic curving equations developed in Appendices A and B.

C.2 Wheelset Equilibrium Conditions

The steady-state equilibrium conditions for a wheelset negotiating a constant radius curve are expressed by eight algebraic equations. The equilibrium equations are:

$$\left.\begin{array}{ll} \text{Wheelset} & \left\{\begin{array}{l} \Sigma F_{x_T} = 0 \\ \Sigma F_{y_T} = 0 \\ \Sigma F_{z_T} = 0 \\ \Sigma M_{x_w} = 0 \\ \Sigma M_{y_w} = 0 \\ \Sigma M_{z_w} = 0 \end{array}\right. \\ \text{Left Rail} & \Sigma F_{y_T} = 0 \\ \text{Right Rail} & \Sigma F_{y_T} = 0 \end{array}\right\} \qquad \text{(C-1)}$$

where all forces (including inertial forces due to centrifugal acceleration) and moments are summed on the left. There are three wheelset

force equilibrium equations, three wheelset moment equilibrium equations, and a left and right rail lateral force equation.

The rails are assumed to have lateral freedom only. Overturning motion has been neglected. In steady-state curving, the rails are modeled as linear springs, as shown in Figure C.1. Each rail displaces laterally a distance related to the net lateral wheel force, i.e.,

$$\left.\begin{aligned} y_{rail_L} &= \frac{F_{YL}}{k_{rail}} \\ y_{rail_R} &= \frac{F_{YR}}{k_{rail}} \end{aligned}\right\} \qquad \text{(C-2)}$$

where F_{YL} and F_{YR} are the net lateral wheel forces and are composed of creep and normal forces. The typical range of effective lateral rail stiffnesses is 1.0×10^5 lb/ft for soft rail to 1.0×10^7 lb/ft for stiff rail [38].

A nonlinear model which considers the cases of single-point and two-point contact has been developed to predict the steady-state curving behavior of a single wheelset. The model assumes that the wheelset is in steady-state force and moment equilibrium. In one case, the model assumes that single-point contact occurs at both wheels of the wheelset. In the other case, the model assumes that two-point tread and flange contact occurs at the outer wheel and single-point contact occurs at the inner wheel of the wheelset. The following two sections formulate the equilibrium conditions for these two cases.

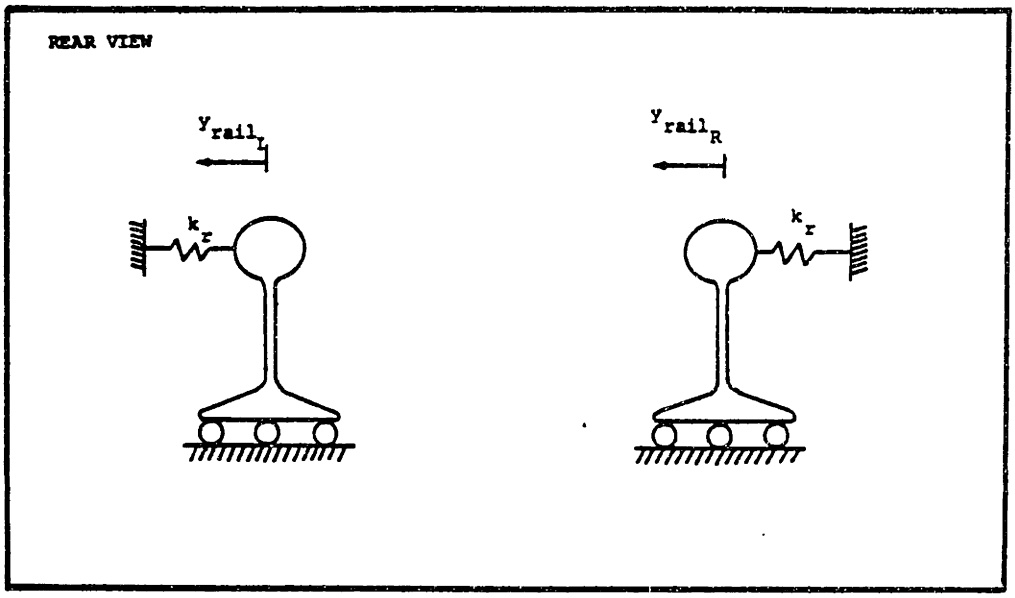

Figure C.1: Flexible Rail Model.

C.2.1 Single-Point Contact Conditions

A free-body diagram of a wheelset in single-point contact at both wheels is shown in Figure C.2. At each wheel/rail contact point, normal forces (denoted subscript N) and creep forces and moments (denoted subscript C) act. All forces and moments are resolved in track coordinates, except for the wheelset drive/brake torque, T_d, which acts about the spin axis. This drive/brake torque is a specified input. Other inputs are: (1) the vertical loads at the left and right wheels, V_L and V_R, respectively, acting in the negative z_T direction, (2) the thrust or drawbar force, F_t, acting at the wheelset center of mass in the x_T direction, (3) the wheelset lateral force, F_{lat}, acting in the track plane in the y_T direction, and (4) the wheelset yaw moment, M_{yaw}, acting about the z_W axis. Figure C.3 shows a rear view of the wheel and rail force equilibrium.

For a wheelset in single-point contact at the left and right wheels, the steady-state curving equilibrium conditions assuming small roll and yaw angles are given below.

WHEELSET

LONGITUDINAL

$$\Sigma F_{x_T} = 0 = F_{CXL} + F_{CXR} + F_t \qquad \text{(C-3)}$$

LATERAL

$$\Sigma F_{y_T} = 0 = F_{NYL} + F_{CYL} + F_{NYR} + F_{CYR} + F_{lat} \qquad \text{(C-4)}$$

VERTICAL

$$\Sigma F_{z_T} = 0 = F_{NZL} + F_{CZL} + F_{NZR} + F_{CZR} - V_L - V_R \qquad \text{(C-5)}$$

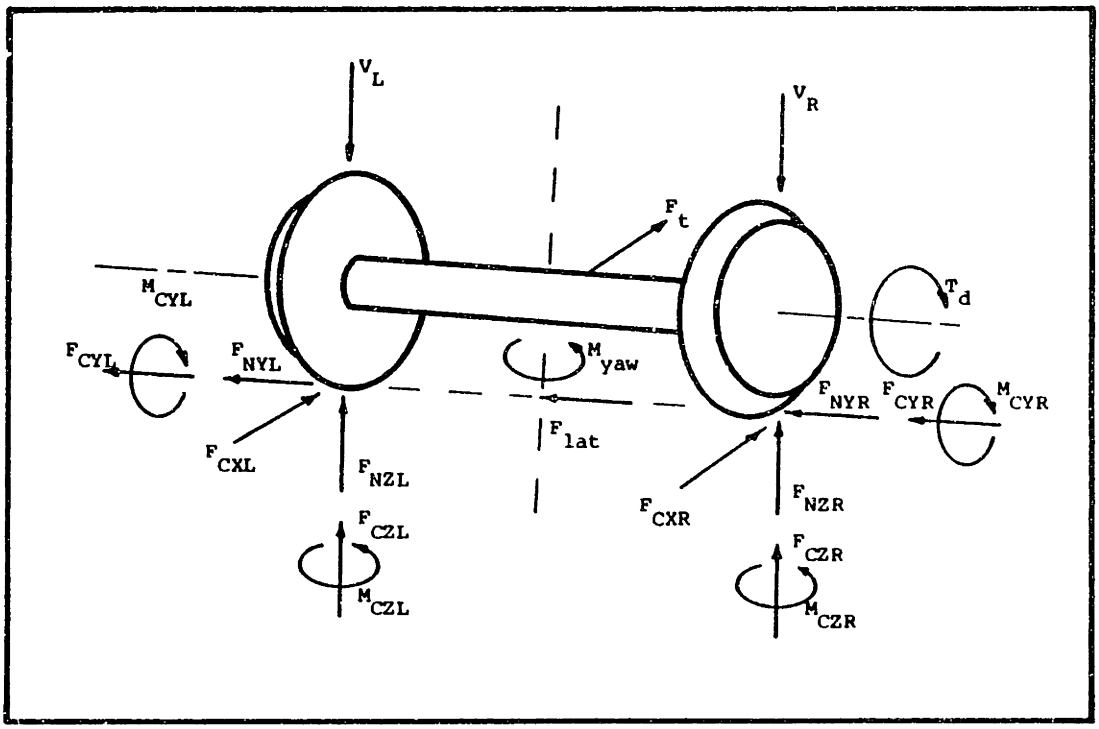

Figure C.2 Wheelset Free-Body Diagram: Single-Point Wheel/Rail Contact

REAR VIEW

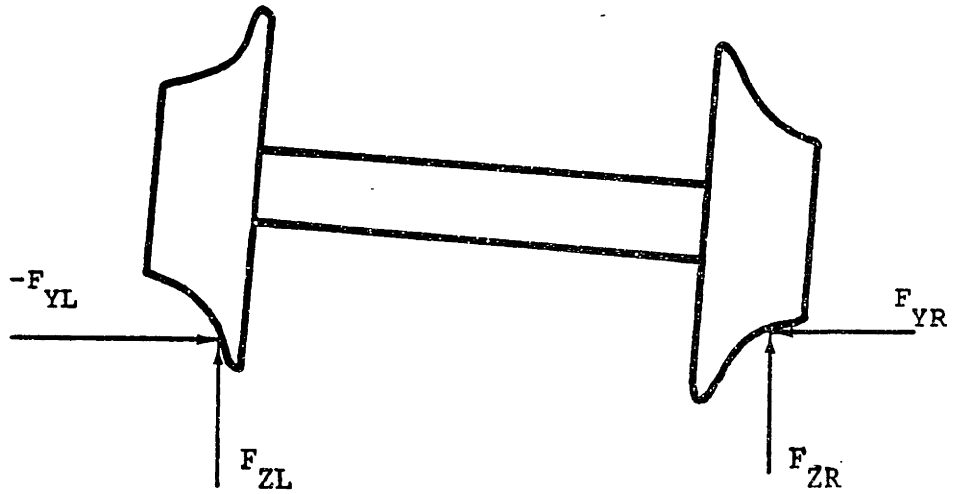

Wheel Forces

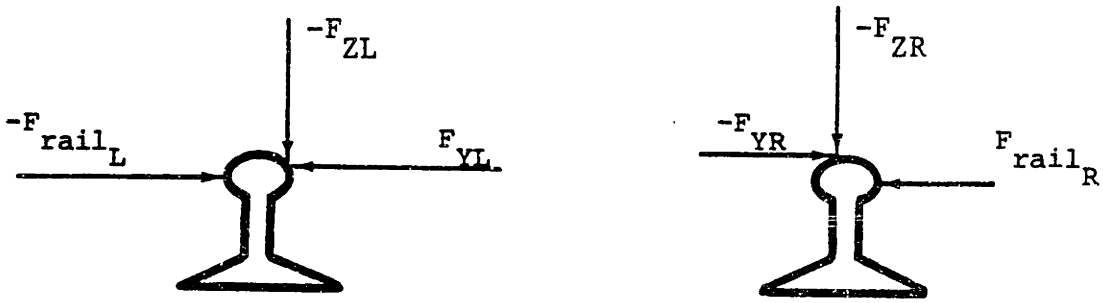

Rail Forces

Figure C.3 Wheel and Rail Forces for Single-Point Contact

ROLL

$$\Sigma M_{x_w} = 0 = (F_{NZL} + F_{CZL} - F_{NZR} - F_{CZR})a + (V_R - V_L)a \quad \text{(C-6)}$$

SPIN

$$\Sigma M_{y_w} = 0 = -r_L[F_{CXL} + \psi_w\{F_{CYL} + F_{CZL}\tan(\delta_L + \phi_w)\}]$$

$$-r_R[F_{CXR} + \psi_w\{F_{CYR} - F_{CZR}\tan(\delta_R - \phi_w)\}]$$

$$+M_{CYL} + M_{CYR} + \phi_w(M_{CZL} + M_{CZR}) + T_d \quad \text{(C-7)}$$

YAW

$$\Sigma M_{z_w} = 0 = -(F_{CXL} - F_{CXR})a - \psi_w\{(F_{NYL} + F_{CYL})(a - r_L\tan(\delta_L + \phi_w))$$

$$-(F_{NYR} + F_{CYR})(a - r_R\tan(\delta_R - \phi_w))\} + M_{CZL} + M_{CZR}$$

$$-\phi_w(M_{CYL} + M_{CYR}) + M_{yaw} \quad \text{(C-8)}$$

RAIL

LATERAL LEFT

$$\Sigma F_{y_T} = 0 = F_{NYL} + F_{CYL} + F_{rail_L} \quad \text{(C-9)}$$

LATERAL RIGHT

$$\Sigma F_{y_T} = 0 = F_{NYR} + F_{CYR} + F_{rail_R} \quad \text{(C-10)}$$

In equations (C-9) and (C-10) the lateral rail reaction forces, F_{rail_L} and F_{rail_R}, are functions of $y_w - y_{rail_L}$ and $y_w - y_{rail_R}$, respectively.

Equations (C-3) - (C-10) represent eight, coupled, nonlinear, algebraic equations. Assuming V_L, V_R, F_{lat}, and M_{yaw} are known, the equations can be solved for the following eight independent variables: F_t, y_w, F_{NZL}, F_{NZR} $\dot{\theta}_w$, ψ_w, y_{rail_L}, y_{rail_R}. These variables can be used to calculate all wheel/rail forces. The contact angles and roll angle are specified since $y_w - y_{rail_L}$ and $y_w - y_{rail_R}$ are known, and thus the resultant normal forces and the lateral components of the normal forces can be calculated from F_{NZL} and F_{NZR}. The creep forces at the left and right contact patches can be computed since the creepages (which are functions of $y_w - y_{rail_L}$, $y_w - y_{rail_R}$, $\dot{\theta}_w$ and ψ_w) and the normal forces are known. Equations (C-3) - (C-10) can alternatively be solved for the following variables if V_L, V_R, y_w, and ψ_w are specified: F_t, F_{lat}, F_{NZL}, F_{NZR}, $\dot{\theta}_w$, M_{yaw}, y_{rail_L}, y_{rail_R}. In Section C.3.1 of this Appendix, the numerical technique required to solve for this latter set of unknowns is described. Finally, for rigid rails, $y_{rail_L} = y_{rail_R} = 0$ and the wheelset equilibrium equations, equations (C-3) - (C-8), decouples from the lateral rail force equations, equations (C-9) and (C-10), leaving a system of six equations with six unknowns.

The thrust in the longitudinal track direction defines the drawbar force, F_t, which must be applied to the wheelset for it to traverse the curve in steady-state. The lateral force, F_{lat}, is provided by suspension and body (cant deficiency) forces. It equilibrates the

lateral components of creep and normal forces to yield steady-state equilibrium in the lateral direction. Suspension forces also give rise to the yaw moment, M_{yaw}, which balances the moments in the yaw direction due to creep and normal forces. The vertical loads at the left and right wheels, V_L and V_R, respectively, are provided by suspension and body forces. The sum and difference of the vertical and roll equations yield the following equations for the vertical loads:

$$V_L = F_{NZL} + F_{CZL} \tag{C-11}$$

$$V_R = F_{NZR} + F_{CZR} \tag{C-12}$$

The spin speed of the wheelset, $\dot{\theta}_w$, is determined by the spin equation, which balances the moments about the wheelset spin (bearing) axis. The wheelset drive/brake torque, T_d, is balanced principally by longitudinal creep forces.

C.2.2 Two-Point Contact Conditions

This section develops the equilibrium conditions for a wheelset assuming simultaneous tread and flange contact occurs at the left (flanging) wheel and single-point contact occurs at the right wheel. The lateral displacement of the wheelset with respect to the left rail equals the flange clearance and thus the contact geometry of the tread and flange contact points at the left wheel is fixed even though the forces may vary. Figure C.4 shows the free-body wheel and rail forces for two-point contact. The steady-state force and moment equilibrium equations for this case are similar to equations (C-3) - (C-1C) for single-point contact with new terms to account for the additional contact point. The

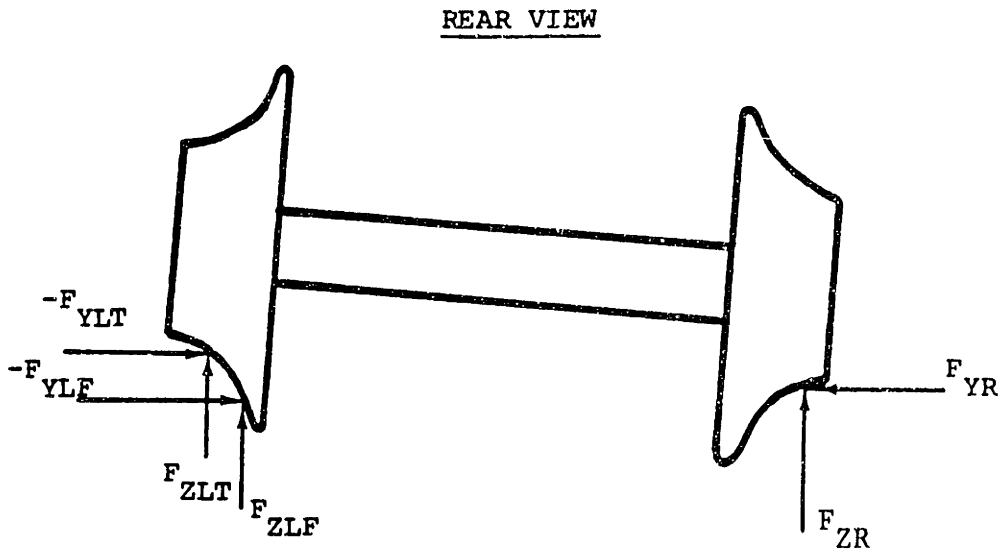

Wheel Forces

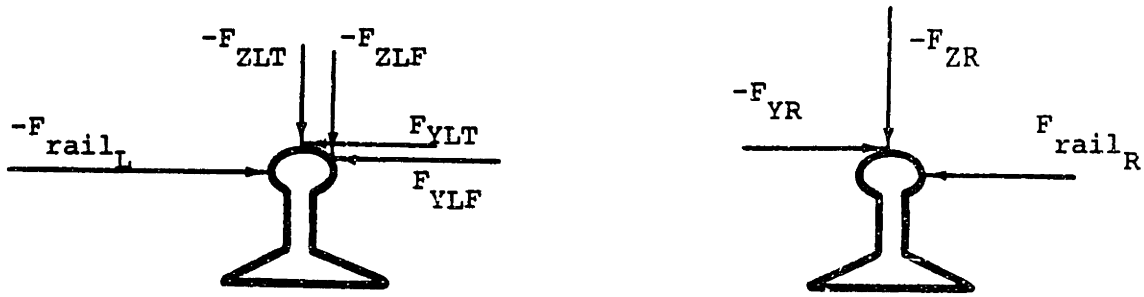

Rail Forces

Figure C.4 Wheel and Rail Forces for Two-Point Contact

two-point contact formulation is statically-determinate since (1) the net lateral excursion at the left wheel is constrained to equal the flange clearance, and (2) the normal forces have components in the lateral as well as vertical directions. The first reason implies that the contact geomtry at the tread and flange contact points of the flanging wheel is known. The second reason implies that the normal forces can be determined with the aid of the lateral force balance equation.

The steady-state curving equations for a wheelset in two-point contact at the left wheel and single-point contact at the right wheel are presented below.

WHEELSET

LONGITUDINAL

$$F_{x_T} = 0 = F_{CXLT} + F_{CXLF} + F_{CXR} + F_t \qquad \text{(C-13)}$$

LATERAL

$$F_{y_T} = 0 = F_{NYLT} + F_{CYLT} + F_{NYLF} + F_{CYLF} + F_{NYR} + F_{CYR} + F_{lat} \qquad \text{(C-14)}$$

VERTICAL

$$\Sigma F_z = 0 = F_{NZLT}+F_{CZLT}+F_{NZLF}+F_{CZLF}+F_{NZR}+F_{CZR}-V_L-V_R \qquad \text{(C-15)}$$

ROLL

$$\Sigma M_w = 0 = (F_{NZLT} + F_{CZLT} + F_{NZLF} + F_{CZLF} - F_{NZR} - F_{CZR})a - (V_R - V_L)a \qquad \text{(C-16)}$$

SPIN

$$\Sigma M_{y_w} = 0 = -r_{LT}[F_{CXLT} + \psi_w \{F_{CYLT} + F_{CZLT} \tan(\delta_{LT} + \phi_w)\}]$$

$$-r_{LF}[F_{CXLF} + \psi_w\{F_{CYLF} + F_{CZLF}\tan(\delta_{LF} + \phi_w)\}]$$

$$-r_R[F_{CXR} + \psi_w \{F_{CYR} - F_{CZR} \tan(\delta_R - \phi_w)\}]$$

$$+M_{CYLT} + M_{CYLF} + M_{CYR} + \phi_w(M_{CZLT} + M_{CZLF} + M_{CZR})$$

$$+T_d \qquad \text{(C-17)}$$

YAW

$$\Sigma M_{z_w} = 0 = -(F_{CYLT} + F_{CXLF} - F_{CXR})a$$

$$-\psi_w\{(F_{NYLT} + F_{CYLT})(a-r_{LT}\tan(\delta_{LT} + \phi_w))$$

$$+ (F_{NYLF} + F_{CYLF})(a - r_{LF}\tan(\delta_{LF} + \phi_w))$$

$$- (F_{NYR} + F_{CYR}) (a - r_R\tan(\delta_R - \phi_w))\}$$

$$+ M_{CZLT} + M_{CZLF} + M_{CZR} - \phi_w(M_{CYLT} + M_{CYLF} + M_{CYR}) + M_{yaw}$$

(C-18)

RAIL

LATERAL LEFT

$$\Sigma F_{y_T} = 0 = F_{NYLT} + F_{CYLT} + F_{NYLF} + F_{CYLF} + F_{rail_L} \qquad \text{(C-19)}$$

LATERAL RIGHT

$$\Sigma F_{y_T} = 0 = F_{NYR} + F_{CYR} + F_{rail_R} \tag{C-20}$$

Equations (C-13) - (C-20) represent eight, coupled, nonlinear, algebraic equations. Since two-point contact occurs, the relative wheelset excursion ($y_w - y_{rail_L}$) is fixed at the flange clearance (y_{fc}). Assuming V_L, V_R, F_{lat}, and M_{yaw} are known, the equations can be solved for: F_t, y_w, F_{NZLT}, F_{NZLF}, F_{NZR}, $\dot{\theta}_w$, ψ_w, y_{rail_R}. Alternatively, if V_L, V_R, y_w and ψ_w are specified, the equations can be solved for: F_t, F_{lat}, F_{NZLT}, F_{NZLF}, F_{NZR}, $\dot{\theta}_w$, M_{yaw}, y_{rail_R}. For rigid rails, the wheelset equations decouple from the rail force equations. The wheelset lateral excursion, y_w, equals the flange clearance, y_{fc}. If V_L, V_R, F_{lat}, and ψ_w are known, the following variables can be determined from equations (C-13) - (C-18): F_t, F_{NZLT}, F_{NZLF}, F_{NZR}, $\dot{\theta}_w$, M_{yaw}.

The equilibrium conditions are solved to determine the distribution of wheel/rail forces acting at the tread and flange contact points at the flanging wheel. Appropriate numerical methods are discussed in the following section.

The single-point contact or two-point contact equilibrium conditions can be manipulated to derive a useful relationship between the contact patch work index, W, defined in Table 2.1, and the external forces and moments on the wheelset. Summing the longitudinal equation, the yaw equation times (-1/R), and the spin equation times ($\dot{\theta}_w$/V) gives:

$$W_{TOT} = -F_t + \frac{M_{yaw}}{R} - \frac{\dot{\theta}_w}{V} T_d \tag{C-21}$$

where W_{TOT} represents the sum of the work at the contact patches:

$$W_{TOT} = \sum_{L,R} [F_{CPX}\xi_x + F_{CPY}\xi_y + M_{CP}\xi_{SP}] \tag{C-22}$$

If two-point contact occurs, $\sum_{L,R}$ represents the sum at the left tread, left flange, and right contact patches. Alternatively, equation (C-21) can be derived by writing a power balance for the wheelset:

$$P_{in} = P_{out} \tag{C-23}$$

$$P_{in} = V[F_t - \frac{M_{yaw}}{R} + \rho T_d] \tag{C-24}$$

$$P_{out} = -VW_{TOT} \tag{C-25}$$

From equation (C-3) and (C-13), the longitudinal thrust, F_t, balances the sum of the longitudinal creep forces:

$$F_t = -\sum_{L,R} F_{CXI} \tag{C-26}$$

Thus,

$$W_{TOT} = \sum_{L,R} F_{CXI} + \frac{M_{yaw}}{R} - \frac{\dot{\theta}_w}{V} T_d \tag{C-27}$$

Equation (C-27) is a useful check to ensure that a correct numerical solution of the equilibrium equations has been obtained.

In the full vehicle formulation, the wheelset yaw moment is not an external moment. Equation (C-27) reduces to

$$W_{TOT} = \sum_{L,R} F_{CXI} + \frac{M_{yaw}}{R} - \frac{\dot{\theta}_w}{V} T_d \qquad (C-27)$$

Equation (C-27) is a useful check to ensure that a correct numerical solution of the equilibrium equations has been obtained.

In the full vehicle formulation, the wheelset yaw moment is not an external moment. Equation (C-27) reduces to

$$W_{TOT} = \sum_{L,R} F_{CXI} - \frac{\dot{\theta}_w}{V} T_d \qquad (C-28)$$

which was obtained in [51].

C.3 Wheelset Numerical Methods

The coupled equilibrium equations for single-point and two-point contact have been incorporated into a general routine to analyze the wheelset steady-state curving behavior. The analysis distinguishes between single-point and two-point contact at the flanging wheel, and automatically solves for the appropriate wheel/rail contact condition. Figure C.5 shows an overview of the analysis procedure. First, the wheelset equations assuming single-point contact are solved. If a single-point contact wheel/rail profile has been used, the appropriate solution has been obtained. If a two-point contact profile has been used and the equilibrium net lateral excursion is less than or greater than the flange clearance, then the single-point contact solution is appropriate and corresponds to a single-point contact tread or flange solution, respectively. However, if the single-point contact solution gives a net excursion equal to the flange clearance, then the wheelset

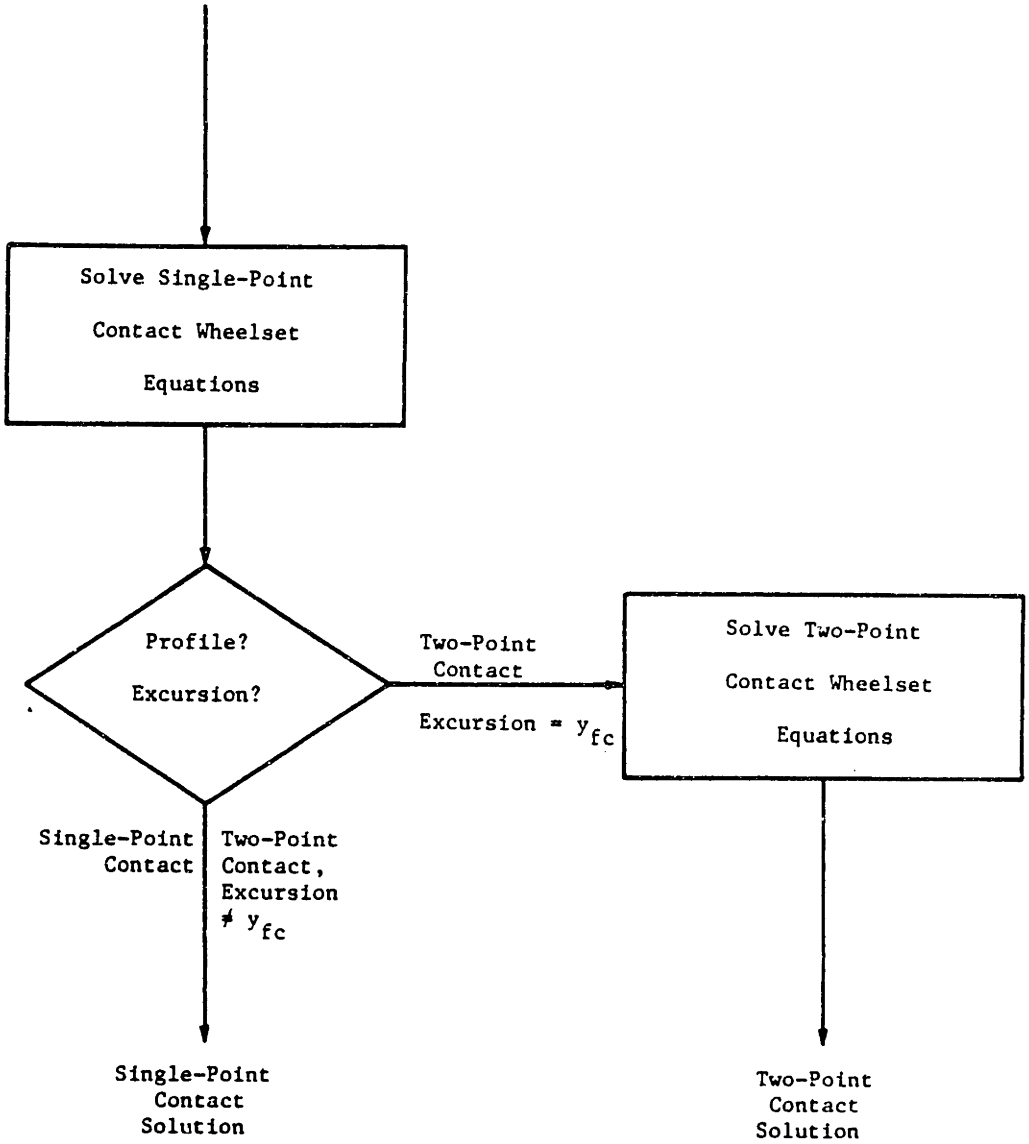

Figure C.5 Overview of Wheelset Steady-State Curving Analysis

equations for two-point contact must be solved. By necessity, the two-point contact solution is appropriate.

The following two sections address the numerical solution procedures used to solve the coupled equilibrium equations for single-point contact and two-point contact at the flanging wheel. The procedures assume that the wheelset lateral excursion and angle of attack, as well as the vertical loads at the left and right wheels are known. By solving the single-point contact equations, equilibrium values of lateral force and yaw moment are determined as functions of lateral excursion and angle of attack. Solution of the two-point contact equations yields the equilibrium yaw moment as a function of lateral force and angle of attack.

C.3.1 Methods for Single-Point Contact

For the case of rigid rails, the wheelset equilibrium conditions are specified by equations (C-3) through (C-8), and represent nonlinear algebraic equations coupled since the normal and creep forces depend upon each other. First, equations (C-7), (C-11) and (C-12) are solved simultaneously for the wheel/rail contact forces and moments. Then, equations (C-3), (C-4), and (C-8) are used to define the drawbar force, the lateral force, and the yaw moment, respectively, required for equilibrium.

Two nested iteration loops are used to solve simultaneously the spin, vertical and roll equations. The inner loop balances the torque about the wheelset rolling axis by adjusting the spin speed, $\dot{\theta}_w$, to satisfy the spin equation. The outer loop adjusts the vertical

component of creep force at each wheel to satisfy the sum and difference of the vertical and roll equations. The procedure is continued until vertical force convergence is achieved, as outlined in the flowchart in Figure C.6, and gives the equilibrium values of all contact forces and moments. The longitudinal, lateral, and yaw equations are then applied to solve for the equilibrium values of F_t, F_{lat}, and M_{yaw}, respectively.

A similar routine to solve the coupled wheelset equilibrium equations was developed by Sweet and Sivak [57] in which the two nested iteration loops are reversed. It should be noted that the creep forces are quite sensitive to small changes in the spin speed, $\dot{\theta}_w$.

To accommodate rail flexibility, the solution technique is to calculate the net lateral wheel force at each wheel assuming a rigid rail model. Then the lateral rail displacement at each wheel is calculated according to equations (C-2) and used to compute the effective lateral excursion at each wheel ($y_w - y_{rail_L}$, $y_w - y_{rail_R}$). These lateral excursions are used to update the wheel/rail contact geometry at the left and right contact points. The net lateral wheel force at each wheel is then re-computed, and the process is continued until convergence is achieved. Even with "soft" rail, convergence occurs rapidly, typically within several iterations.

C.3.2 Methods for Two-Point Contact

For some wheel/rail profiles, two-point contact occurs at the flanging wheel when the net lateral excursions equals the flange clear-

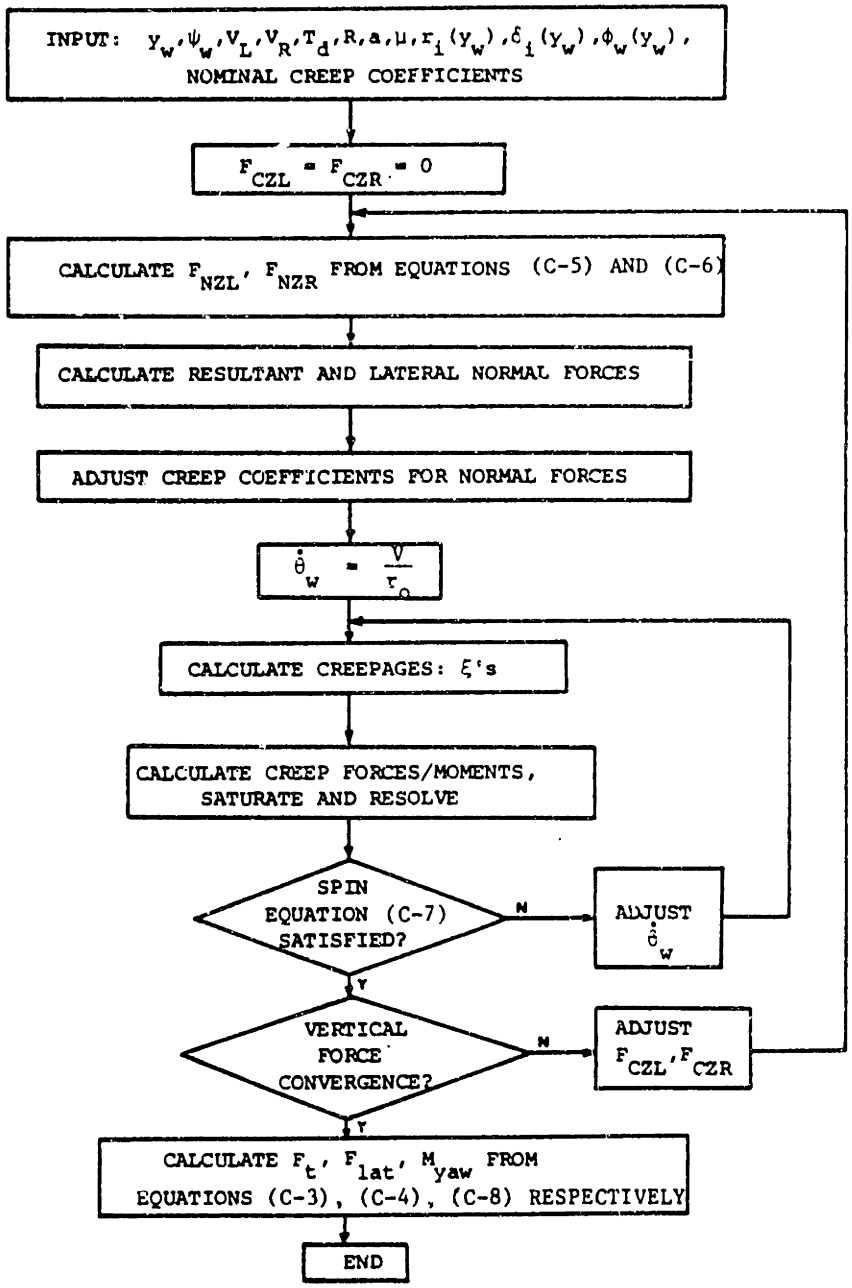

Figure C.6 Flowchart for Wheelset Equilibrium with Rigid Rails: Single-Point Contact Model

ance. Assuming rigid rails, the forces and moments at the three contact patches are determined by solving simultaneously the following four coupled equilibrium equations: the spin, vertical, roll, and lateral equations.

As before, the four coupled equations are solved using two nested iteration loops, as shown in Figure C.7. The inner loop adjusts the spin speed, $\dot{\theta}_w$, to satisfy the spin equation. The outer loop adjusts the vertical components of the creep forces at the tread and the flange of the outer wheel and the tread of the inner wheel to simultaneously satisfy the lateral equation and the sum and difference of the vertical and roll equations. Once vertical force convergence is achieved, equilibrium values of all contact forces and moments are known and the yaw equation is used to calculate the wheelset yaw moment which must act for equilibrium.

Rail flexibility is accounted for, as before, by solving first for the net lateral wheel forces assuming rigid rails. Equations (C-2) are used to calculate the lateral rail displacements, where $F_{YL} = F_{YLT} + F_{YLF}$. The net lateral excursion at the right, $y_w - y_{rail_R}$, is computed and used to update the right contact geometry. It is assumed that two-point contact at the left wheel is maintained and thus $y_w - y_{rail_L} = y_{fc}$. The net lateral wheel forces are then computed and the procedure is continued until convergence occurs.

C.4 Half-Carbody Model

The nonlinear wheelset model is coupled to the rail vehicle model by suspension elements. Two wheelsets are mounted via primary

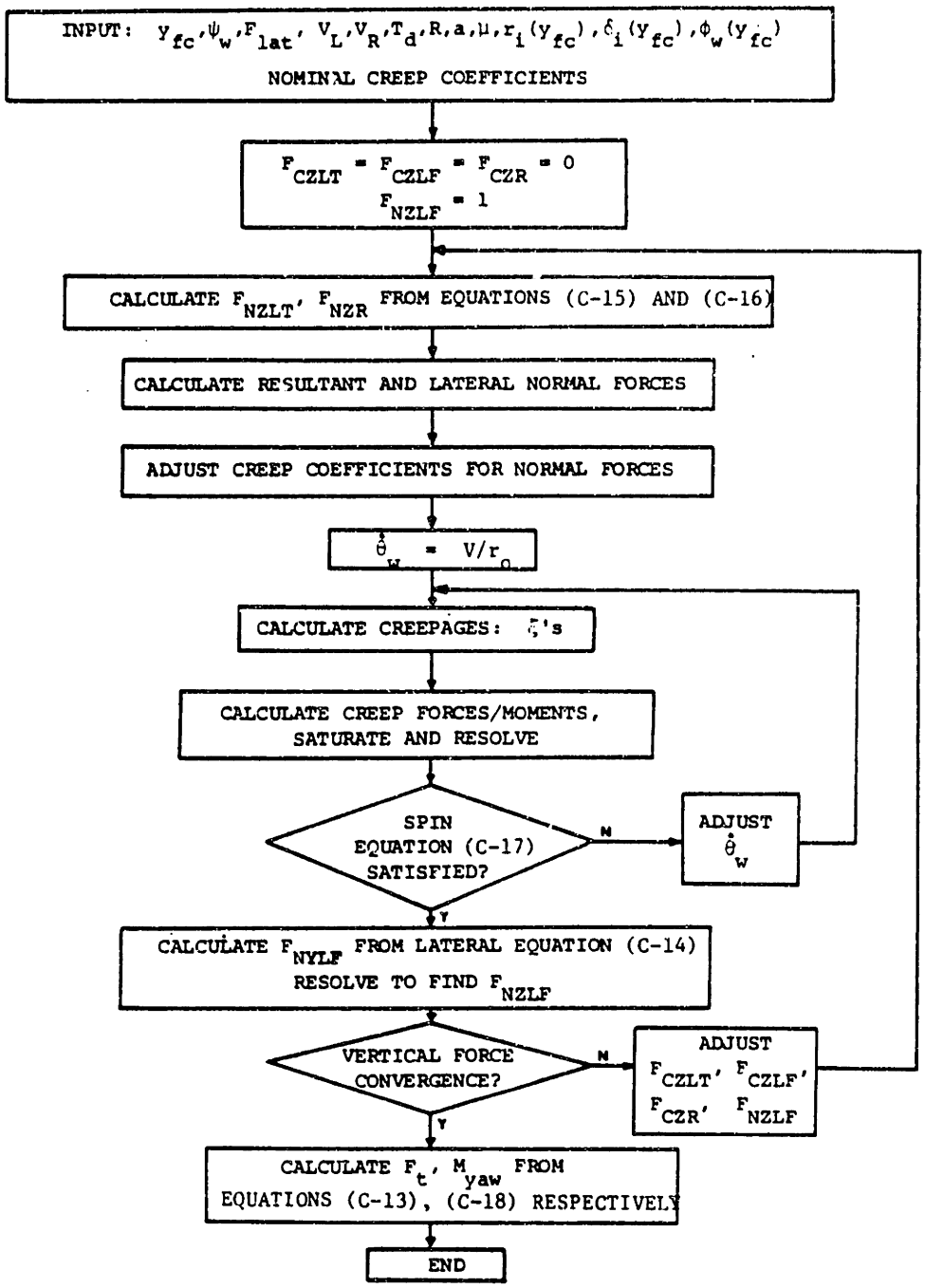

Figure C.7 Flowchart for Wheelset Equilibrium with Rigid Rails: Two-Point Contact Model

suspension elements to the truck frame which is attached via secondary suspension elements to the carbody. The generic truck model described in Section 2.5.4 is attached to the nonlinear wheelset model to formulate the nonlinear truck model.* In addition to wheel/rail nonlinearities, nonlinear suspension characteristics are included in the vehicle model.

In order to reduce the numerical computations required to solve the steady-state curving problem, a single truck/half carbody model has been developed. The model is used to solve separately for the front and rear truck solution. It is shown that a completely coupled full carbody solution can be obtained by iterating on the carbody yaw angle and secondary suspension lateral force; however, in general the decoupled solution is accurate due to the typically small secondary yaw torques.

The degrees of freedom of the decoupled half carbody model are:

- y_{w1} (y_{w3}) • lateral excursion of the leading wheelset of the front (rear) truck with respect to the track centerline
- ψ_{w1} (ψ_{w3}) • yaw angle of the leading wheelset of the front (rear) truck with respect to a radial line
- y_{w2} (y_{w2}) • lateral excursion of the trailing wheelset of the front (rear) truck
- ψ_{w2} (ψ_{w4}) • yaw angle of the trailing wheelset of the front (rear) truck)
- y_{FL} (ψ_{F2}) • lateral excursion of the front (rear) truck

*The bolster is assumed to be rigidly attached to the carbody in yaw and to the truck frame in all other directions.

- ψ_{F1} (ψ_{F2}) • yaw angle of the front (rear) truck
- y_{cs} • lateral excursion of carbody secondary connection point relative to the truck reference position
- ϕ_c • roll displacement of the carbody with respect to the track plane.

The model has eight degrees of freedom and is designed to represent a single truck with two wheelsets coupled to a half-carbody. The curving performance of either the front or the rear truck is computed separately under the assumption that coupling between the trucks is negligible for practical (typical) secondary suspensions. The assumption of decoupled trucks can then be checked as described below.

If the torque between the front truck and carbody is equal and opposite to the torque between the rear truck and carbody, the assumption of decoupling trucks is valid. However, if the torques on the front and rear trucks are not equal and opposite, coupling exists. To account for coupling between the front and rear trucks, the following relations must be satisfied:

$$\psi_c = (y_{cs_1} - y_{cs_2})/2\ell_s \tag{C-29}$$

$$F_{sec_1} = (T_{car_1} + T_{car_2})/2\ell_s \tag{C-30}$$

$$F_{sec_2} = -F_{sec_1} \tag{C-31}$$

where ψ_c = carbody yaw displacement

y_{cs_i} = lateral displacement of carbody at secondary suspension connection point, ith truck

F_{sec_i} = external lateral force on carbody at secondary suspension connection point, ith truck

T_{car_i} = torque acting on carbody, ith truck

ℓ_s = half of spacing between trucks

Subscripts: 1 = front truck

2 = rear truck

The full-vehicle solution can be obtained by iterating an ψ_c and F_{sec} in successive runs of the single truck model. This is rarely necessary, though, since ψ_c and F_{sec} are usually negligibly small with regard to coupling between the two trucks.

C.4.1 Primary Suspension Model

The primary suspension is modeled as a system of nonlinear (piecewise linear) springs connected in parallel in the lateral and longitudinal directions, and linear springs connected in parallel in the vertical direction. The arrangement is shown in Figure C.8. The longitudinal and vertical springs yield effective yaw and roll stiffnesses, respectively. The lateral stiffness, k_{py}, is modeled as a trilinear spring, as shown in Figure C.9 representing a hardening spring. Larger lateral forces are required to displace the suspension as the lateral stroke increases. Further, the effect of a "stop" at lateral clearance DY2 can be represented by making KPY3 much larger than KPY2. The longitudinal stiffness k_{px}, is modeled as a bilinear spring, as depicted in Figure C.10, and also represents a hardening spring. A "stop" can be modeled by making KPX2 much larger than KPX1.

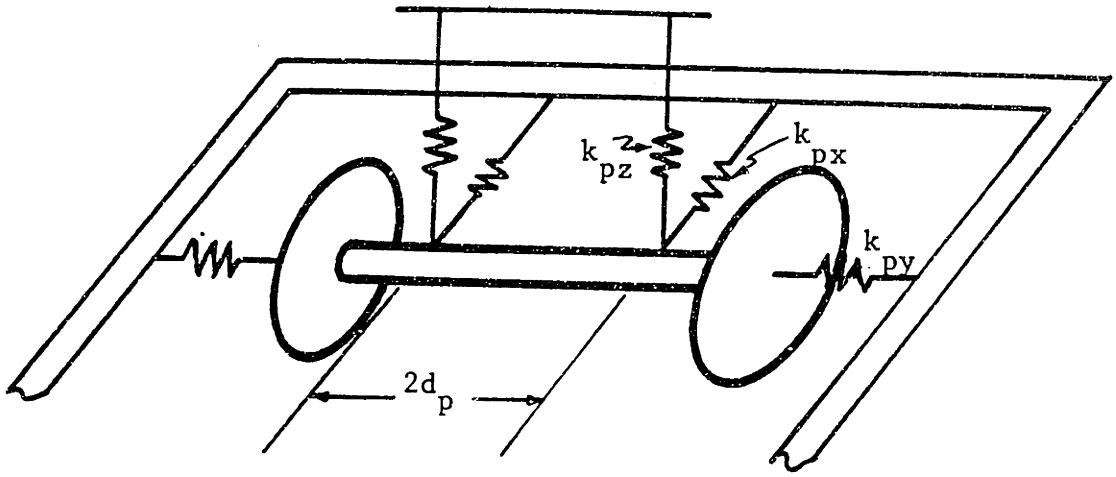

Figure C.8 Primary Suspension Stiffnesses

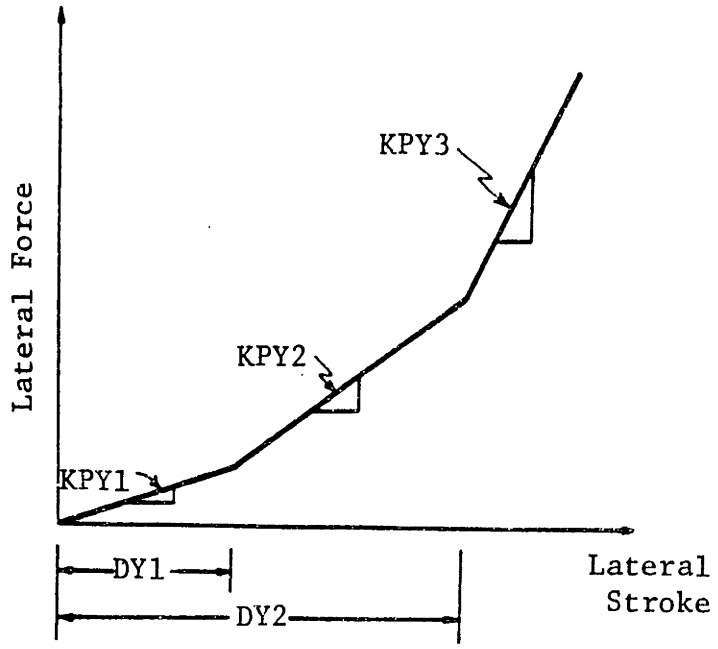

Figure C.9 Force-Displacement Characteristic For Primary Lateral Stiffness Model.

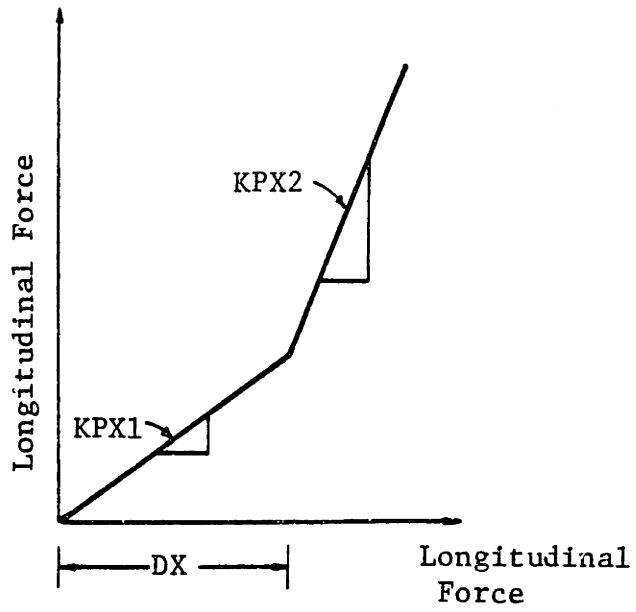

Figure C.10 Force-Displacement Characteristic for Primary Longitudinal Stiffness Model.

To bypass numerical convergence difficulties which can occur with very soft primary longitudinal stiffnesses, an auxiliary longitudinal suspension is introduced. This is shown in Figure C.11. An auxiliary primary longitudinal suspension, k_{pxaux}, is placed in parallel with a soft primary longitudinal stiffness, k_{px}, and is connected between the wheelset and the truck frame or between the wheelset and ground. An imposed extension, δ_{aux}, in series with a stiff k_{pxaux} is used to simulate a longitudinal clearance while maintaining a stiff primary suspension. A solution is obtained when δ_{aux} is selected such that all the force is transmitted through k_{px} and no force is transmitted through k_{pxaux}. When this occurs the longitudinal suspension is provided solely by the soft longitudinal stiffness k_{px}.

C.4.2 Secondary Suspension Model

The truck frame is connected to the carbody by secondary suspension elements. Connection in the longitudinal direction is provided by anchor rods between the carbody and each bolster, shown in Figure 2.15. Each bolster is fastened to a truck frame by a center pin so that it can rotate with respect to the truck frame. With the assumption of rigid anchor rods, each bolster follows the carbody motion in yaw and the truck motion in the lateral direction.

The secondary suspension model consists of linear springs connected in parallel in the lateral and vertical directions, two per truck for each direction. The secondary vertical stiffness, k_{sz}, provides roll stiffness between the truck and the carbody. The effect of k_{sz} is equivalent to a roll spring between the carbody and each truck frame:

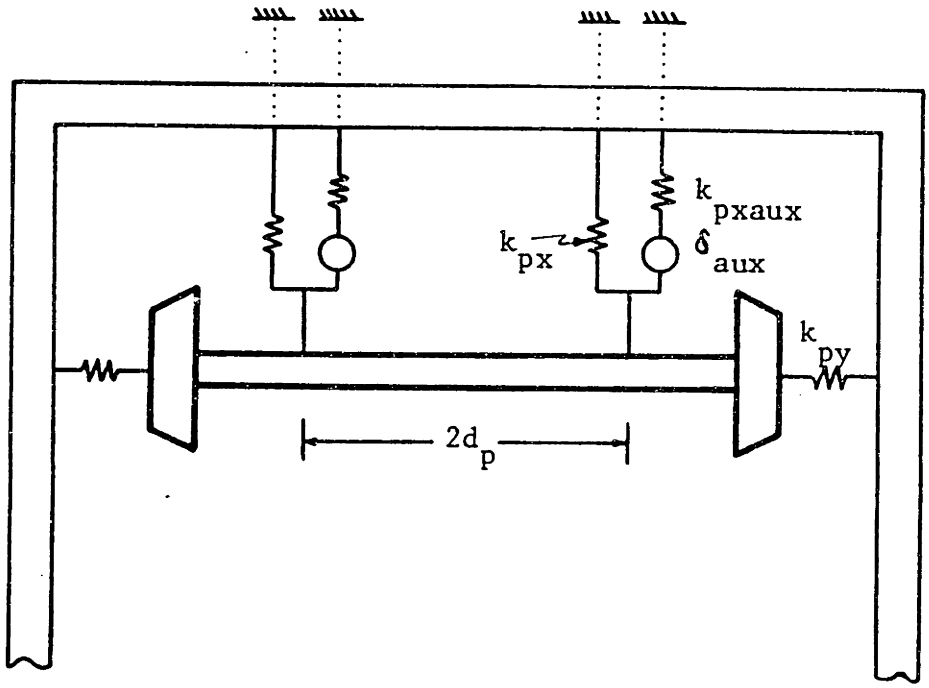

Figure C.11 Primary Suspension Arrangement with Auxiliary Suspension

$$k_{roll} = 2d_s^2 k_{sz} \qquad \text{(C-32)}$$

In yaw, the secondary suspension consists of anchor rods between the bolster and carbody which act in series with friction pads between the bolster and truck frame. The torque versus yaw stroke characteristic resulting from this series arrangement is shown in Figure 2.29. The breakaway torque, T_o, results from the Coulomb sliding force between the friction pads. In the curving analysis it is assumed that the maximum torque, T_o, is established between the carbody and the truck frame, which is realistic for negotiation of curves greater than 1°. The maximum torque is maintained regardless of any increase in the relative displacement between the two components.

C.4.3 Half-Carbody Model Equilibrium Conditions

The steady-state curving equations are conditions of simultaneous force and moment equilibrium of the wheelsets, truck, and half-carbody. The following equilibrium conditions apply for the half-carbody model.

1. Lateral Force Equilibrium 2. Yaw Moment Equilibrium	Leading Wheelset
3. Lateral Force Equilibrium 4. Yaw Moment Equilibrium	Trailing Wheelset
5. Lateral Force Equilibrium 6. Yaw Moment Equilibrium	Truck
7. Lateral Force Equilibrium 8. Yaw Moment Equilibrium 9. Roll Moment Equilibrium	Half-Carbody

Condition (8) is related to the interaction of the front and rear trucks in the analysis of a full vehicle, as expressed in relations (C-29) - (C-31). The carbody roll moment equation is a decoupled condition and is discussed in Section C.5.1. Conditions (1) through (7) represent a set of coupled, nonlinear, algebraic equations.

The forces and moments acting upon the vehicle can be characterized as internal arising from suspension and external arising from track curvature, cant deficiency, forced-steering (from carbody yaw), and imposed wheelset yaw offsets (δ_{aux}). Thus, the equilibrium equations can be cast as follows:

$$[K(\bar{x})]\{\bar{x}\} = \{\bar{B}(\bar{x})\} \qquad \text{(C-33)}$$

where the matrix produce $[K]\{\bar{x}\}$ represents a vector of internal suspension forces and moments and $\{\bar{B}\}$ represents the vector of all external forces and moments. The elements of $\{\bar{B}\}$ due to track curvature and cant deficiency are:

$$b_1 = F_{lat_1} + W_w\phi_d$$

$$b_2 = M_{yaw_1}$$

$$b_3 = F_{lat_2} + W_w\phi_d$$

$$b_4 = M_{yaw_2}$$

$$b_5 = W_F\phi_d$$

$$b_6 = \pm T_o$$

$$b_7 = F_{buff} \tag{C-34}$$

where F_{lat_1} and M_{yaw_1} represent the lateral force and yaw moment, respectively, acting on the leading (i = 1) and trailing (i = 2) wheelsets. The lateral force and yaw moment are both functions of the track curvature. The sixth element of $\bar{B}$ is the breakaway torque, T_o. The sign is positive for analysis of the front truck and negative for the rear truck.

The matrix product $[K]\{\bar{x}\}$ is composed of a stiffness matrix [K] due to primary and secondary suspensions, and a geometry state vector $\{\bar{x}\}$. When nonlinear suspension representations are used, the stiffness matrix is a function of the vehicle displacement vector. The elements of $\{\bar{x}\}$ are:

$$\begin{aligned} X_1 &= y_{w1} \\ X_2 &= \psi_{w1} \\ X_3 &= y_{w2} \\ X_4 &= \psi_{w2} \\ X_5 &= y_F \\ X_6 &= \psi_F \\ X_7 &= y_{cs} \end{aligned} \tag{C-35}$$

The seventh element represents the lateral excursion of the carbody at the secondary connection point.

For the case of the leading wheelset in two-point contact at the flanging (left) wheel, $X_1 = y_{w1}$ is fixed at the flange clearance (assuming rigid rails) and the lateral force, F_{lat_1}, becomes a state variable.

To account for initial wheelset misalignments, equation (C-33) can be modified to reflect the new "resting" (zero suspension force) state of the suspensions. The equilibrium equations can be written as

$$[K](\{\bar{x}\} - \{\bar{x}_m\}) = \{\bar{B}\} \tag{C-36}$$

where $\{\bar{x}_m\}$ represents a misaligned geometry state vector. For radial and lateral misalignment of each wheelset, the elements of $\{\bar{x}_m\}$ are:

$$X_{1m} = y_{w1m}$$

$$X_{2m} = \psi_{w1m}$$

$$X_{3m} = y_{w2m}$$

$$X_{4m} = \psi_{w2m}$$

$$X_{5m} = X_{6m} = X_{7m} = 0 \tag{C-37}$$

where the first four elements are the initial lateral and yaw misalignments of the leading and trailing wheelsets, shown in Figure C.12.

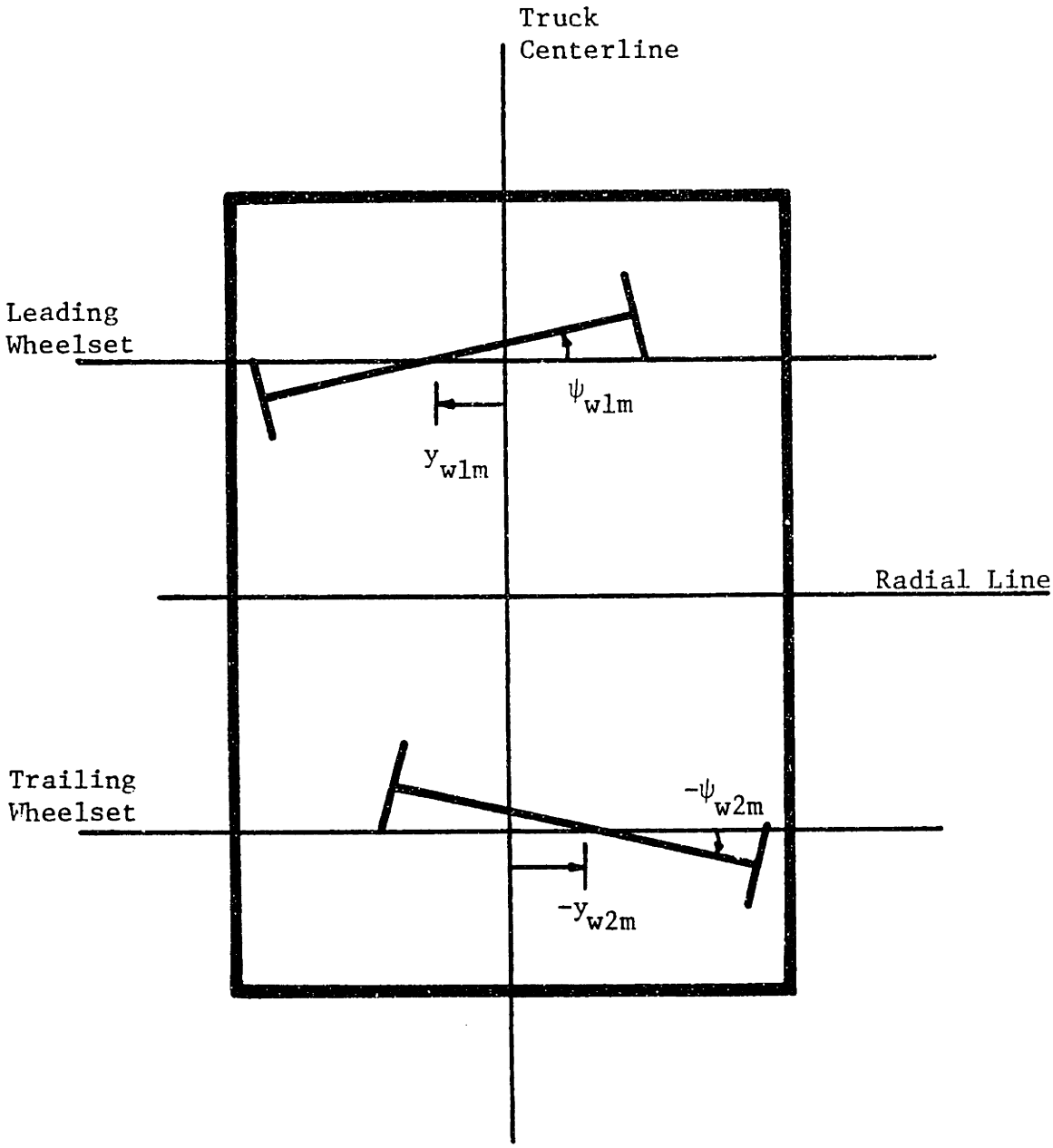

Figure C.12 Wheelset Misalignments

Assuming no wheelset misalignments, the seven coupled equilibrium equations for the half-carbody model are listed in equations (C-38) - (C-44). The following notation is used:

$$\pm = \begin{cases} + \text{ Front Truck} \\ - \text{ Rear Truck} \end{cases} \qquad \alpha = \begin{cases} 1 \text{ Truck Reference} \\ 0 \text{ Ground Reference} \end{cases}$$

$$\text{Subscript} = \begin{cases} 1 \text{ Leading Wheelset of Truck} \\ 2 \text{ Trailing Wheelset of Truck} \end{cases}$$

C.5 Half-Carbody Model Numerical Methods

The steady-state curving equations are used to determine the displaced steady-state geometry and the wheel/rail forces of the half-carbody model on a constant radius curve. The analysis assumes that the half-carbody model is dynamically stable.

C.5.1 Carbody Roll Calculation

The carbody roll angle can be calculated by summing the moments in the roll direction about the secondary connection point. The calculation accounts for the following influences: (1) carbody cant deficiency forces; (2) lateral buff forces; and (3) the inverted pendulum effect of carbody weight. From Figure C.13, expressions can be derived for: (1) the external roll moment about the secondary connection point (s) due to cant deficiency forces, $W_c\phi_d$, and buff, F_{buff}, and (2) the restoring moment due to the secondary vertical stiffness, k_{sz}, and the inverted pendulum effect. Equating these moment expressions yields the

Leading Wheelset Lateral

$$[-2k_{py_1} - \left\{ G_3 \pm (\frac{G_2+G_6}{b}) \right\}^2 (k_{b2} + k_{b3}) - (H_1 - H_3 + 1)^2 (k_{s2} + k_{s3}) - k_{s3}]y_{w1}$$

$$+ [\left\{ (G_3 \pm (\frac{G_2+G_6}{b}) \right\} \left\{ 1 \mp (G_1+G_5) \right\} (k_{b2} + k_{b3}) + b(H_1 + H_3 + 1)(k_{s2} + k_{s3}) + bk_{s3}](\psi_{w1} - \frac{b}{R})$$

$$+ [-\left\{ G_3^2 - (\frac{G_2+G_6}{b})^2 \right\} (k_{b2} + k_{b3}) - \left\{ (H_1 + H_3)^2 - 1 \right\} (k_{s2} + k_{s3}) - k_{s3}]y_{w2}$$

$$+ [\left\{ -G_3 \mp (\frac{G_2+G_6}{b}) \right\} \left\{ (1 \pm (G_1 + G_5) \right\} (k_{b2} + k_{b3}) + b(H_1 + H_3 + 1)(k_{s2} + k_{s3}) - bk_{s3}](\psi_{w2} + \frac{b}{R})$$

$$+ [2k_{py_1} + 2G_3 \left\{ G_3 \pm (\frac{G_2+G_6}{b}) \right\} (k_{b2} + k_{b3}) - 2(H_2 - H_3)(H_1 + H_3 + 1)(k_{s2} + k_{s3}) + 2k_{s3}]y_F$$

$$+ [2k_{py_1} b + 2(G_4 - G_5 - G_6) \left\{ \mp G_3 - (\frac{G_2+G_6}{b}) \right\} (k_{b2} + k_{b3})]\psi_F$$

$$+ [2(H_1 + H_2)(H_1 + H_3 + 1)(k_{s2} + k_{s3})]y_{cs}$$

$$+ [2(G_1 + G_2 + G_4) \left\{ \pm G_3 + (\frac{G_2+G_6}{b}) \right\} (k_{b2} + k_{b3})](\psi_c \pm \frac{\ell s}{R})$$

$$+ W_w \phi_d + F_{lat_1} = 0 \qquad (C-38)$$

Leading Wheelset Yaw

$$
\begin{aligned}
&\left[\left\{G_3 \pm \left(\frac{G_2+G_6}{b}\right)\right\}\left\{\left(1 \mp (G_1+G_5)\right\}(k_{b2}+k_{b3}) + b(H_1+H_3+1)(k_{s2}+k_{s3}) + bk_{s3}\right]y_{w1}\right.\\
&+ \left[-2d_p^2\,(k_{px_1}+k_{pxaux}) - (G_1+G_5 \mp 1)^2\,(k_{b2}+k_{b3}) - b^2(k_{s2}+k_{s3}) - k_{b3} - b^2k_{s3}\right](\Psi_{w1} - \tfrac{b}{R})\\
&+ \left[\left\{G_3 \mp \left(\frac{G_2+G_6}{b}\right)\right\}\left\{1 \mp (G_1+G_5)\right\}(k_{b2}+k_{b3}) + b(H_1+H_3-1)(k_{s2}+k_{s3}) + bk_{s3}\right]y_{w2}\\
&+ \left[\left\{1-(G_1+G_5)^2\right\}(k_{b2}+k_{b3}) - b^2(k_{s2}+k_{s3}) - k_{b3} + b^2k_{s3}\right](\Psi_{w2} + \tfrac{b}{R})\\
&+ \left[2G_3\left\{-1 \pm (G_1+G_5)\right\}(k_{b2}+k_{b3}) + 2b(H_2-H_3)(k_{s2}+k_{s3}) - 2bk_{s3}\right]y_F\\
&+ \left[2d_p^2\,(k_{px_1}+k_{pxaux}\,\alpha) + 2(G_4-G_5-G_6)\left\{\pm 1-(G_1+G_5)\right\}(k_{b2}+k_{b3}) + 2k_{b3}\right]\Psi_F\\
&+ \left[-2b(H_1+H_2)(k_{s2}+k_{s3})\right]y_{cs}\\
&+ \left[2(G_1+G_2+G_4)\,(G_1+G_5 \mp 1)\,(k_{b2}+k_{b3})\right]\left(\psi_c \pm \frac{\ell_s}{R}\right)\\
&+ 2\delta_{aux_1}\,d_p^2\,k_{pxaux} + M_{yaw_1} = 0
\end{aligned}
\tag{C-39}
$$

Trailing Wheelset Lateral

$$
\begin{aligned}
&\left[-\left\{G_3^2 - \left(\frac{G_2+G_6}{b}\right)^2\right\}(k_{b2}+k_{b3}) - \left\{(H_1+H_3)^2 - 1\right\}(k_{s2}+k_{s3}) - k_{s3}\right]y_{w1} \\
&+ \left[\left\{G_3 \mp \left(\frac{G_2+G_6}{b}\right)\right\}\left\{1 \mp (G_1+G_5)\right\}(k_{b2}+k_{b3}) + b(H_1+H_3-1)(k_{s2}+k_{s3}) + bk_{s3}\right](\psi_{w1} - \frac{b}{R}) \\
&+ \left[-2k_{py_2} - \left\{G_3 \mp \left(\frac{G_2+G_6}{b}\right)\right\}^2 (k_{b2}+k_{b3}) - (H_1+H_3-1)^2(k_{s2}+k_{s3}) - k_{s3}\right]y_{w2} \\
&+ \left[\left\{-G_3 \pm \left(\frac{G_2+G_6}{b}\right)\right\}\left\{1 \pm (G_1+G_5)\right\}(k_{b2}+k_{b3}) + b(H_1+H_3-1)(k_{s2}+k_{s3}) - bk_{s3}\right](\psi_{w2} + \frac{b}{R}) \\
&+ \left[2k_{py_2} + 2G_3\left\{G_3 \mp \left(\frac{G_2+G_6}{b}\right)\right\}(k_{b2}+k_{b3}) - 2(H_2-H_3)(H_1+H_3-1)(k_{s2}+k_{s3}) + 2k_{s3}\right]y_F \\
&+ \left[-2k_{py_2}b + 2(G_4-G_5-G_6)\left\{\mp G_3 + \left(\frac{G_2+G_6}{b}\right)\right\}(k_{b2}+k_{b3})\right]\psi_F \\
&+ \left[2(H_1+H_2)(H_1+H_3-1)(k_{s2}+k_{s3})\right]y_{cs} \\
&+ \left[2(G_1+G_2+G_4)\left\{\pm G_3 - \left(\frac{G_2+G_6}{b}\right)\right\}(k_{b2}+k_{b3})\right](\psi_c \pm \frac{\ell_s}{R}) \\
&+ W_w\phi_d + F_{lat_2} = 0
\end{aligned}
\tag{C-40}
$$

Trailing Wheelset Yaw

$$
\begin{aligned}
&\left[\left\{-G_3 \mp \left(\frac{G_2+G_6}{b}\right)\right\}\left\{1 \pm (G_1+G_5)\right\}(k_{b2}+k_{b3}) + b(H_1+H_3+1)(k_{s2}+k_{s3}) - bk_{s3}\right] y_{w1} \\
&+ \left[\left\{1-(G_1+G_5)^2\right\}(k_{b2}+k_{b3}) - b^2(k_{s2}+k_{s3}) - k_{b3} + b^2 k_{s3}\right]\left(\Psi_{w1} - \frac{b}{R}\right) \\
&+ \left[\left\{-G_3 \pm \left(\frac{G_2+G_6}{b}\right)\right\}\left\{1 \pm (G_1+G_5)\right\}(k_{b2}+k_{b3}) + b(H_1+H_3-1)(k_{s2}+k_{s3}) - bk_{s3}\right] y_{w2} \\
&+ \left[-2d_p^2\,(k_{px_2}+k_{pxaux}) - \left\{1 \pm (G_1+G_5)\right\}^2(k_{b2}+k_{b3}) - b^2(k_{s2}+k_{s3}) - k_{b3} - b^2 k_{s3}\right]\left(\Psi_{w2} + \frac{b}{R}\right) \\
&+ \left[2G_3\left\{1 \pm (G_1+G_5)\right\}(k_{b2}+k_{b3}) + 2b(H_2-H_3)(k_{s2}+k_{s3}) + 2bk_{s3}\right] y_F \\
&+ \left[2d_p^2\,(k_{px_2}+k_{pxaux}\alpha) + 2(G_4-G_5-G_6)\left\{\mp 1-(G_1+G_5)\right\}(k_{b2}+k_{b3}) + 2k_{b3}\right]\Psi_F \\
&+ \left[-2b(H_1+H_2)\,(k_{s2}+k_{s3})\right] y_{cs} \\
&+ \left[2(G_1+G_2+G_4)(G_1+G_5 \pm 1)\,(k_{b2}+k_{b3})\right]\left(\Psi_c \pm \frac{\ell_s}{R}\right) \\
&+ 2\delta_{aux_2}\, d_p^2\, k_{pxaux} + M_{yaw_2} = 0
\end{aligned}
\qquad \text{(C-41)}
$$

Truck Lateral

$$[2k_{py_1} + 2G_3\left\{G_3 \pm \left(\frac{G_2+G_6}{b}\right)\right\}(k_{b2} + k_{b3}) - 2(H_2 - H_3)(H_1 + H_3 + 1)(k_{s2} + k_{s3}) + 2k_{s3}]y_{w1}$$

$$+ [2G_3\left\{-1 \pm (G_1 + G_5)\right\}(k_{b2} + k_{b3}) + 2b(H_2 - H_3)(k_{s2} + k_{s3}) - 2bk_{s3}](\psi_{w1} - \frac{b}{R})$$

$$+ [2k_{py_2} + 2G_3\left\{G_3 \mp \left(\frac{G_2+G_6}{b}\right)\right\}(k_{b2} + k_{b3}) - 2(H_2 - H_3)(H_1 + H_3 - 1)(k_{s2} + k_{s3}) + 2k_{s3}]y_{w2}$$

$$+ [2G_3\left\{1 \pm (G_1 + G_5)\right\}(k_{b2} + k_{b3}) + 2b(H_2 - H_3)(k_{s2} + k_{s3}) + 2bk_{s3}](\psi_{w2} + \frac{b}{R})$$

$$+ [-2k_{py_1} - 2k_{py_2} - 2k_{sy} - 4G_3^2(k_{b2} + k_{b3}) - 4(H_2 - H_3)^2(k_{s2} + k_{s3}) - 4k_{s3}]y_F$$

$$+ [-2k_{py_1}b + 2k_{py_2}b \mp 4G_3(G_4 - G_5 - G_6)(k_{b2} + k_{b3})]\psi_F$$

$$+ [2k_{sy} + 4(H_1 + H_2)(H_2 - H_3)(k_{s2} + k_{s3})]y_{cs}$$

$$+ [\mp 4G_3(G_1 + G_2 + G_4)(k_{b2} + k_{b3})]\{\psi_c \mp \frac{\ell_s}{R}\}$$

$$+ W_F\phi_d = 0 \qquad (C-42)$$

Truck Yaw

$$[2bk_{py_1} + 2\left\{\mp G_3 - \left(\frac{G_2+G_6}{b}\right)\right\}(G_4 - G_5 - G_6)(k_{b2} + k_{b3})]y_{w1}$$

$$+ [2d_p^2(k_{px_1} + k_{pxaux}\alpha) + 2(G_4 - G_5 - G_6)\left\{\mp 1 - (G_1 + G_5)\right\}(k_{b2} + k_{b3}) + 2k_{b3}](\Psi_{w1} - \frac{b}{R})$$

$$+ [-2bk_{py_2} + 2\left\{\mp G_3 + \left(\frac{G_2+G_6}{b}\right)\right\}(G_4 - G_5 - G_6)(k_{b2} + k_{b3})]y_{w2}$$

$$+ [2d_p^2(k_{px_2} + k_{pxaux}\alpha) + 2(G_4 - G_5 - G_6)\left\{\mp 1 - (G_1 + G_5)\right\}(k_{b2} + k_{b3}) + 2k_{b3}](\Psi_{w2} + \frac{b}{R})$$

$$+ [-2k_{py_1}b + 2k_{py_2}b \mp 4G_3(G_4 - G_5 - G_6)(k_{b2} + k_{b3})]y_F$$

$$+ [-2d_p^2(k_{px_1} + k_{px_2} + 2k_{pxaux}\alpha) - 2b^2(k_{py_1} + k_{py_2}) - 4(G_4 - G_5 - G_6)^2(k_{b2} + k_{b3}) - 4k_{b3}]\Psi_F$$

$$+ [4(G_4 - G_5 - G_6)(G_1 + G_2 + G_4)(k_{b2} + k_{b3})](\Psi_c \mp \frac{\ell s}{R})$$

$$-2(\delta_{aux_1} + \delta_{aux_2})d_p^2 k_{pxaux}\alpha \mp T_o = 0 \qquad \text{(C-43)}$$

Carbody Lateral At Secondary

$$[2(H_1 + H_2)(H_1 + H_3 + 1)(k_{s2} + k_{s3})]y_{w1}$$

$$+ [-2b(H_1 + H_2)(k_{s2} + k_{s3})](\Psi_{w1} - \frac{b}{R})$$

$$+ [2(H_1 + H_2)(H_1 + H_3 - 1)(k_{s2} + k_{s3})]y_{w2}$$

$$+ [-2b(H_1 + H_2)(k_{s2} + k_{s3})](\Psi_{w2} + \frac{b}{R})$$

$$+ [2k_{sy} + 4(H_1 + H_2)(H_2 - H_3)(k_{s2} + k_{s3})]y_F$$

$$+ [-2k_{sy} - 4(H_1 + H_2)^2(k_{s2} + k_{s3})]y_{cs}$$

$$+ W_c\phi_d/2 + F_{buff} + F_{sec} = 0 \qquad \text{(C-44)}$$

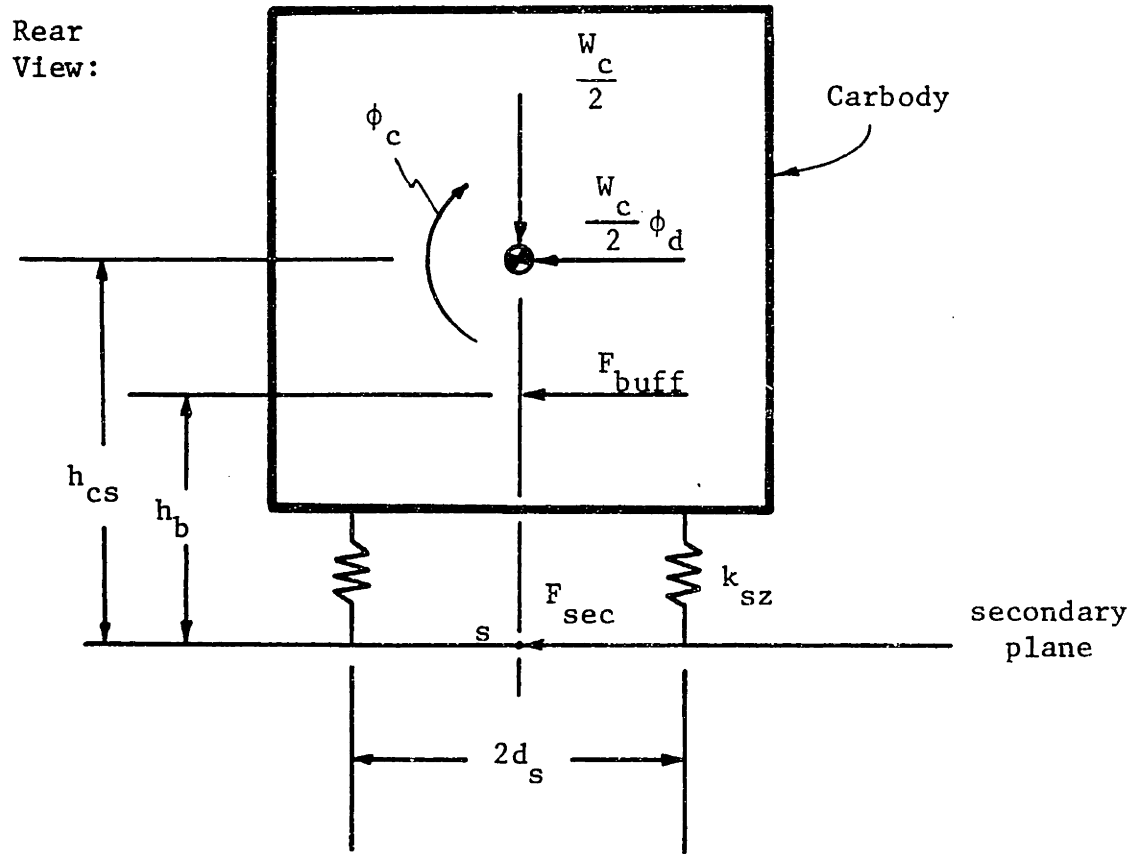

Figure C.13 Forces Acting at Secondary Suspension of a Truck

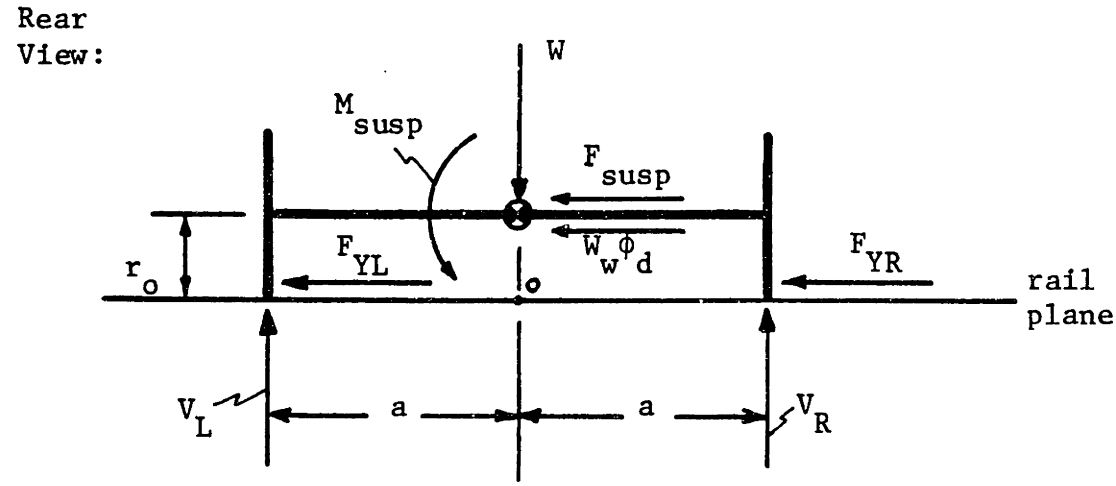

Figure C.14 Wheelset Free Body Diagram, Rear View

relation for the carbody roll:

$$\phi_c = \frac{-\frac{W_C}{2}\phi_d h_{cs} - F_{buff} h_b}{2k_{sz} d_s^2 - \frac{W_C}{2} h_{cs}} \qquad \text{(C-45)}$$

where $h_b = h_c - h_{ts} - h_{tp} - r_o$.

C.5.2 Vertical Wheel Load Calculation

The net vertical loads acting at the left and right wheels, V_L and V_R, respectively, are needed to solve the wheelset equilibrium equations. These vertical wheel loads are computed by considering the steady-state equilibrium of each wheelset in the roll direction. Figure C.14 shows the wheelset free-body diagram. Expressions for the vertical wheel loads are:

$$V_L = V_{avg} + \Delta V \qquad \text{(C-46)}$$

$$V_R = V_{avg} - \Delta V \qquad \text{(C-47)}$$

where the average vertical wheel load, V_{avg}, is due to wheelset, truck, and carbody weights:

$$V_{avg} = \frac{W_W}{2} + \frac{W_F}{4} + \frac{W_C}{8} \qquad \text{(C-48)}$$

and the vertical load shift, ΔV, arises from wheelset suspension force and moment loading. Summing moments about point 0 in Figure C.15 yields an expression for ΔV:

$$\Delta V = \frac{1}{2a}\left[M_{susp} + r_o(F_{susp} + W_W \phi_d)\right] \qquad \text{(C-49)}$$

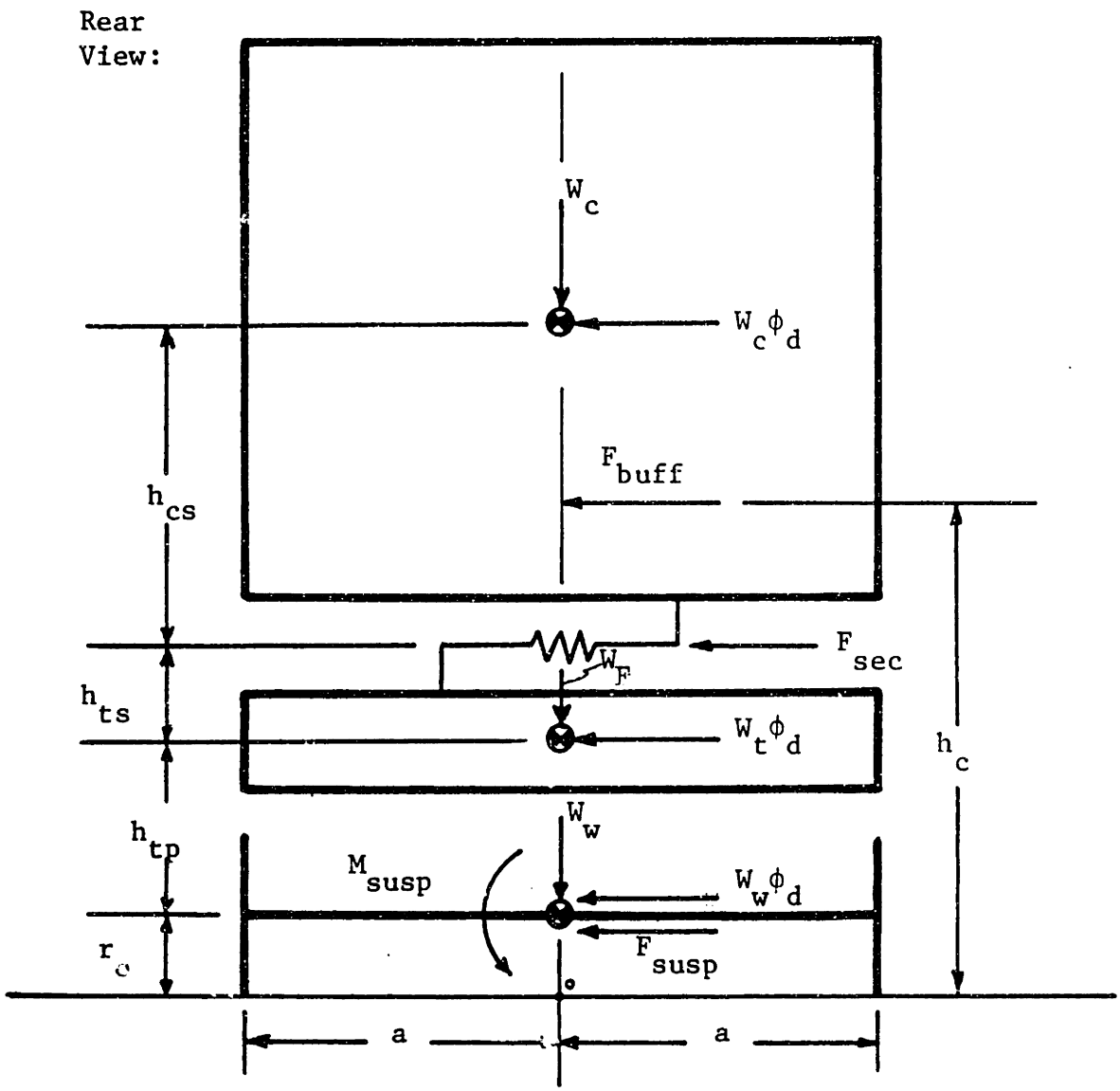

Figure C.15 Vehicle Free-Body Diagram, Rear View

The suspension force acting on each wheelset, F_{susp} is due to primary lateral stiffness, k_{py} and to any interaxle shear stiffness, k_{s2}. Assuming no initial wheelset misalignments, it is given by

$$F_{susp} = 2k_{py}(y_F + b\psi_F - y_{W1}) + k_{s2}\ y_{W2} - y_{W1} + b(\psi_{W1} + \psi_{W2}) + \delta_{fs} \qquad \text{(C-50)}$$

for the leading wheelset, and by

$$F_{susp} = 2k_{py}(y_T + b\psi_F - y_{w2}) - k_{s2}\ y_{W2} - y_{W1} + b(\psi_{W1} + \psi_{W2}) + \delta_{fs} \qquad \text{(C-51)}$$

for the trailing wheelset, where δ_{fs} represents the additional suspension stroke imposed by forced steering.

The suspension moment, M_{susp} is obtained by summing moments about the wheelset center of gravity. From Figure C.15,

$$M_{susp} = \frac{W_C}{\phi}\ \phi_d\ (h_{cs} + h_{ts} + h_{tp}) + \frac{W_F}{2}\ \phi_d h_{tp} + \frac{F_{buff}}{4}\ (h_c - r_o) + \frac{F_{sec}}{2}\ (h_{ts} + h_{tp}) + \frac{W_C}{4}(y_{cs} - h_{cs}\phi_c - \frac{y_{W1}+y_{W2}}{2}) + \frac{W_F}{2}(y_F - \frac{y_{W1} + y_{W2}}{2}) \qquad \text{(C-52)}$$

C.5.3 Solution Method for Coupled Equations

Equations (C-38) - (C-44) represent a set of coupled, nonlinear, algebraic equations. These equations are solved numerically using an iterative algorithm entitled SROOTS [49]. The major features of the method are: (1) the iterations do not include any searches along lines in the space of the variable so most situations require only one evaluation of the set of algebraic equations, and (2) the correction vector, δ, interpolates between the classical Newton-Raphson and the steepest descent corrections in a way that generally yields fast convergence. These two features make the algorithm computationally fast. A schematic of an iteration in SROOTS is shown in Figure C.16.

The standard form of the equations to be solved is:

$$F_i = 0, \quad i = 1, 2, \ldots\ldots, N \tag{C-53}$$

where N is the total number of equations. The method requires the following information:

(1) an initial estimate or guess of the solution vector

(2) a step-length, DSTEP, to approximate the first-derivatives of the functions, i.e.,

$$\frac{f_1}{X_1} \simeq \frac{f_1(X_1 + \text{DSTEP}, X_2, X_3, \ldots, X_N) - f_1(X_1, \ldots\ldots, X_N)}{\text{DSTEP}} \tag{C-54}$$

(3) A generous estimate of the distance between the initial guess and the final solution where the distance, DMAX, is

$$\text{DMAX} = d(\bar{X}, \bar{Y}) = \sum_{i=1}^{N} [(X_i - Y_i)^2]^{1/2} \tag{C-55}$$

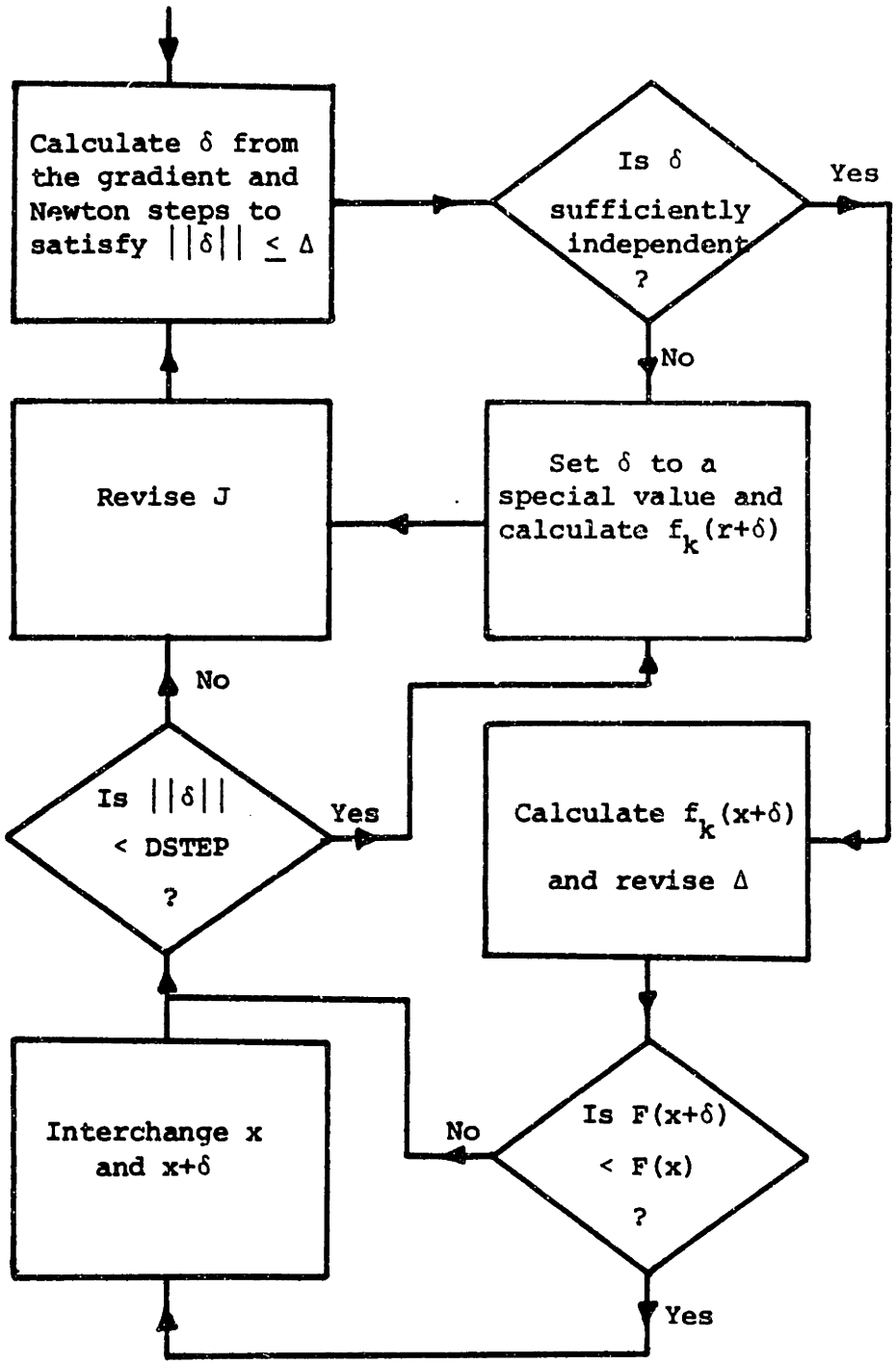

Figure C.16 Schematic of one Iteration in SROOTS, from Rabinowitz, [49]

(4) The required accuracy of the solution, ACC, with iterations stopping when $\sum_{i=1}^{N}[f_i(\bar{X})]^2 = ACC$

(5) The maximum number of allowable iterations, MAX.

When SROOTS cannot find a solution of the equations consistent with the value of ACC, it reports one of the following errors:

(1) The number of iterations exceeds MAX.

(2) A stationary point is predicted since no solutions exist within distance DMAX of X.

(3) N + 4 calls of the residual function fail to improve X indicating that DSTEP may be too large, or that rounding errors prevent the desired accuracy from being obtained.

(4) A completely new evaluation of the partial derivatives (Jacobian) does not decrease F. This may occur for reasons indicated in (3).

C.5.4 Program SSCURV

The steady-state curving analysis is coded in a Fortran program entitled SSCURV (Steady-State CURVing). A flowchart of program SSCURV is shown in Figure C.17. The main program reads the vehicle and curving input data, calls SROOTS which solves the equilibrium state equations, and appropriately formats the output. SROOTS calls CALFUN N times to set up the system Jacobian matrix (matrix of partial derivatives). In each iteration it calls MINV to invert the system matrix. CALFUN sets up the vehicle equations each time it is called. It does this by calling KMAT for the stiffness matrix and by calling WHLST1 or WHLST2 once for each wheelset to obtain the wheel/rail forces and moments. WHLST1 (for WHeeLSet 1 point) solves for wheelset contact forces and

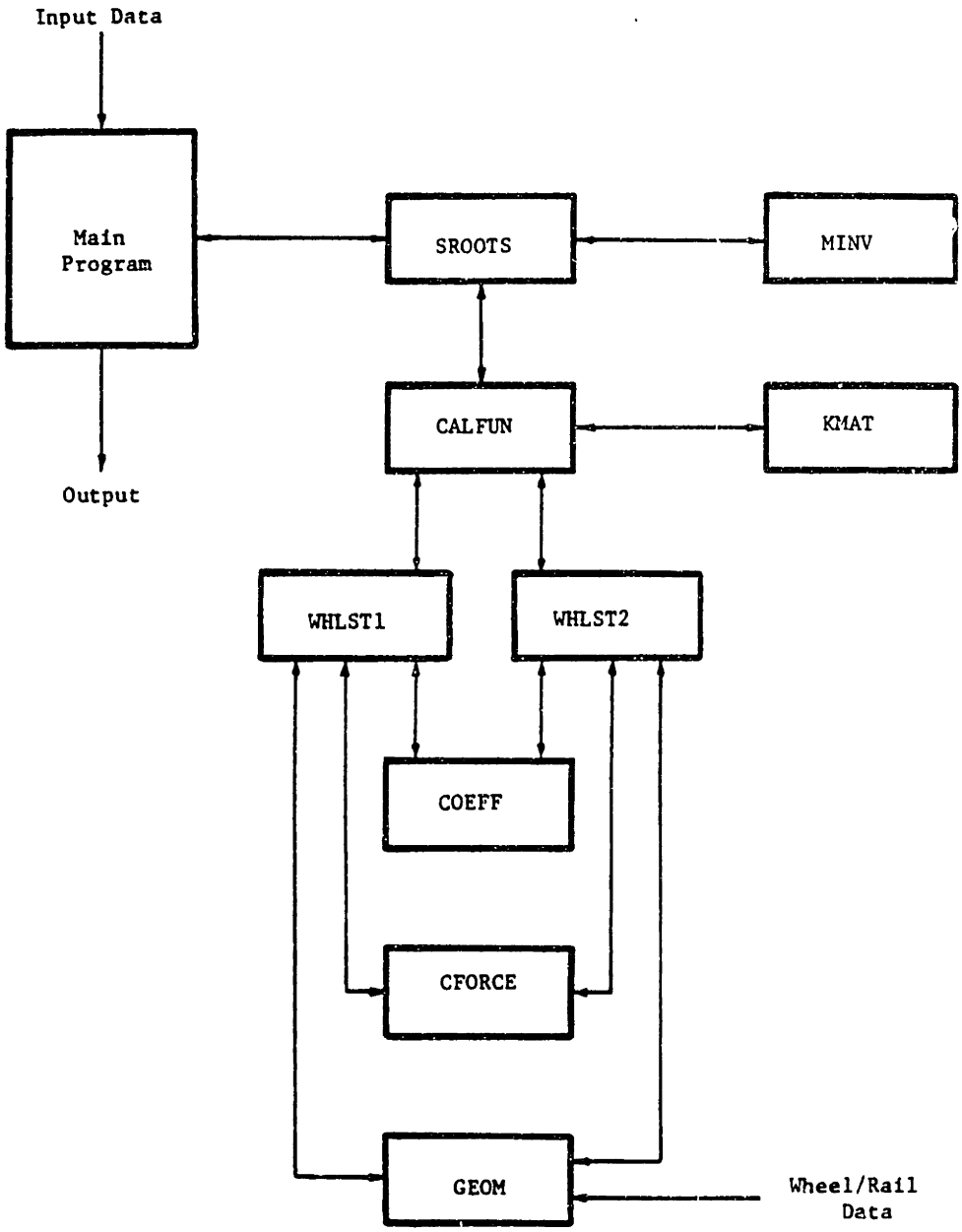

Figure C.17 Steady-State Curving Program SSCURV Layout

moments assuming single-point contact occurs at both wheels; WHLST2 (for WHeeLSeT 2 point) solves for contact forces and and moments assuming two-point contact occurs at the flanging wheel and single-point contact occurs at the inner wheel. Both WHLST1 and WHLST2 call GEOM, COEFF, and CFORCE. GEOM obtains the wheel/rail geometry from the profile data table. Creep forces at each wheel are computed in CFORCE using the Kalker creep coefficients obtained from COEFF, which adjusts the coefficients based on the normal forces. COEFF and CFORCE are called iteratively by the wheelset routines (WHLST1, WHLST2) until the appropriate creep and normal forces are obtained to satisfy the wheelset equilibrium conditions.

In summary, program SSCURV solves the coupled, nonlinear, algebraic, equilibrium equations representing steady-state curving by subroutine SROOTS, which has proved to be a very robust equation solver.

Rail/Vehicle Inputs

Wheel/Rail profile geometry data

Vehicle system inputs such as geometry, weights

Forcing Inputs:

D	degree curve
ϕ_d	cant deficiency
Buff	lateral component of buff force, per truck
T_d	wheelset drive torque (same for all wheelsets)
F_{sec}	lateral force or carbody at secondary suspension connection point
ψ_c	carbody yaw displacement

Outputs

The primary output of the steady-state curving program is the vector of steady-state displacements which satisfies the nonlinear vehicle equations. From this solution vector, the following outputs are obtained.

- Wheelset lateral excursions, y_{wi}
- Wheelset angles of attack, ψ_{wi}
- Net wheelset forces and moments
- Wheel/rail forces (creep and normal)
- Suspension strokes
- Work at wheel/rail contact patches
- Equilibrium check

Program Usage Notes

1. The number of SROOTS iterations required to obtain the final solution is relatively sensitive to the initial guess of the solution vector. An initial guess which is close to the final result speeds convergence. Previous solutions can be used effectively as initial guesses to help avoid convergence difficulties.

2. Care should be taken to ensure that the initial guess of the state vector does not violate the range of the wheel/rail profile geometry data. If guessed wheelset excursions fall outside the tabulated range, program execution will be stopped in the first call to CALFUN.

3. Lateral rail flexure at each wheel is determined iteratively in the wheelset subroutines (WHLST1, WHLST2). The rail flexibility feature makes convergence more difficult, and requires more computation time. A typical lateral rail stiffness is 1.0×10^6 lb/ft. The flexibility analysis can be bypassed by using large lateral rail stiffnesses, i.e., greater than 1.0×10^{10} lb/ft, simulating rigid rails. Runs which do not converge using the flexibility option should be rerun with rigid rails until convergence is achieved. Softer stiffnesses should then gradually be introduced using previous solutions as initial guesses.

Program Costs

Program SSCURV is efficient and inexpensive to run. A typical solution for single-point contact analysis requires about 10-20 iterations, although sometimes up to 50 iterations are required. In

general, more iterations are required for two-point contact solutions. The computer execution time on a DEC VAX 1178 is about 1 CPU second for 2 iterations, at a cost of 6 cents per CPU second at high priority.